

The background of the cover is a grid of squares. The top-left portion is a solid dark blue. A diagonal line of squares, starting from the top-right and moving towards the bottom-left, is filled with various colors including yellow, orange, light blue, and a single red square. The bottom-right portion is a solid dark blue.

# ESRF HIGHLIGHTS

## 2012



# Highlights 2012

EUROPEAN SYNCHROTRON RADIATION FACILITY

Pages

3	<b>Introduction</b>
5	<b>Status of the Upgrade Programme</b>
9	<b>Scientific Highlights</b>
9	<i>Structural Biology</i>
32	<i>Dynamics and Extreme Conditions</i>
50	<i>X-ray Imaging</i>
65	<i>Soft Condensed Matter</i>
81	<i>Electronic Structure and Magnetism</i>
94	<i>Structure of Materials</i>
120	<b>Enabling Technologies</b>
128	<b>Accelerator and X-ray Source</b>
136	<b>Facts and Figures</b>

**Cover**

Cytoskeletal network structure studied by X-ray nanodiffraction. The image shows an overlay of the calculated structure orientation, indicated by black lines, on the corresponding X-ray dark-field image of the keratin-rich extension of a cell. Each square represents an area of 250 x 250 nm.

From B. Weinhausen *et al.*, p 75. Image courtesy of S. Köster, Georg-August-Universität Göttingen.

Back cover photo credit: ESRF/P. Ginter.



## Dear Reader

2012 was an important year for the future of the ESRF. It was marked by activities that aimed at preserving the ESRF in the long term, in particular to maintain its leading role in synchrotron science on both a European and a worldwide level, and to guarantee that its user programme remains attractive and continues to strengthen in the foreseeable future.



Credit: ESRF / Molyneux Associates.

### Halfway through Phase I of the Upgrade Programme

The difficulties we were confronted with in 2010-2011 imposed a timely re-thinking of the whole Upgrade Programme. A beneficial consequence is that the Upgrade Programme will now deliver a substantially enhanced suite of instruments capable of addressing major scientific challenges where prime X-ray science is expected to provide new insights, particularly in the domains of condensed matter, materials science, and life sciences. This opportunity to develop a substantially new X-ray science - coupling diffraction and spectroscopy methods with real space imaging and microscopy techniques at resolutions well below those obtainable with optical wavelengths - is already offering both interesting and promising results in areas of basic and applied research, including innovative industrial studies. New instruments at the ESRF promise to improve diffraction and spectroscopy experiments further by increasing beam brightness, overall experiment stability and reliability, with gains of several orders of magnitude foreseen. The full revision of the beamline portfolio has now been completed and already new and revised beamlines are being made available to our users. Similarly, important accelerator upgrades have been commissioned this year, while others have been put through their proof of principle testing. These include the successful commissioning of the new solid-state amplifier towers, the lattice modifications to install 6-metre and 7-metre vacuum chambers in the storage ring straight sections and the new radio-frequency HOM-damped cavities. Following the firm recommendation from the SAC at the end of 2011, the new topping-up injection strategy is currently in progress.

### Return to user operation after an exceptionally long shutdown

2012 started with an exceptionally long five-month shutdown of the accelerator complex to allow extensive and disruptive works for the construction of the new EX2 experimental halls as well as major interventions in the

storage ring tunnel. This was the longest interruption in beam delivery since the start of operation of the ESRF's storage ring in 1992. As a consequence, user operation was reduced, with approximately 30% less beam time available compared to a normal year. The restart was successful and user operation (USM) resumed according to the most optimistic expectations despite the many "unknowns" linked to the works. Major realignment of the storage ring and beamlines had to be implemented following the disruptive work, ground excavations and ground subsidence. Approximately 32,000 tonnes of earth were displaced on the site provoking relative movements of the X-ray beams of up to 10 mm peak-to-peak.

Taking advantage of the long shutdown, a new structure for the Beam Time Allocation Panels (BTAPs) was set up with the aim of increasing the efficiency and transparency of the whole beam time allocation process. This major change was successfully implemented by the User Office with the support of the ESRF's IT Support Services in October 2012 for proposals for the 2013-I period. Comments received from the panels and the Science Advisory Committee members about this new system have been very positive.

### The Long-Term Strategic Mission of the ESRF was reviewed by the *ad hoc* working group created by the ESRF Council

This working group, chaired by the Vice-Chairman of Council, Prof Michel van der Rest, was composed of experts nominated directly by the ESRF Council. The mission of the working group was to provide a critical review and assessment of the long-term strategic mission and role of the ESRF in X-ray science. The report was presented to the ESRF Council at its plenary meeting in November 2012, at which time it was adopted. It has since been published on the ESRF web site and is available for downloading. With its far-reaching and very exciting recommendations for the ESRF, this document is now a key reference to inspire and define the scope of the ESRF in the foreseeable future; it will serve as a guide for the ESRF Management when implementing



the scientific and technical policy over the coming years. The report takes into account the very competitive European and international environment of synchrotron science, including analytical research infrastructures such as XFELs and new neutron sources. The fundamental questions being addressed concern the strategic choices that the ESRF needs to make in order to remain attractive to its increasingly large and diversified user community, and to continue to represent an undisputable added value for all contributing countries. During 2012 this working group compiled information from experts, ESRF users and staff, and from other synchrotron laboratories in Europe and abroad.

## Preparation has started for the Upgrade Programme Phase II

Important work started in 2012 on the preparation of the technical and scientific case of the Upgrade Programme Phase II, with new ideas for unique and innovative technical implementations driven by the very strong and broad scientific case developed in detail in 2007, which is presented in the Purple Book. In this respect, the ESRF's commitment to studying realistic possibilities that could qualitatively improve the X-ray source has allowed scientists of the Accelerator and Source Division to identify a new storage ring lattice design that would considerably reduce the horizontal emittance (from the present 4 nm to ~0.1 nm). This would lead to an increase in brightness and degree of coherence of the X-ray beams almost inversely proportional to the proposed reduction of horizontal emittance. Contrary to vertical emittance, the horizontal emittance is far from being diffraction-limited. This work has refuelled, once again, the long-standing worldwide reflection on how to build a new generation of "diffraction-limited" storage ring lattices. The proposal from the Accelerator and Source Division consists of a major upgrade of the present storage ring, leading to a brightness even greater than a factor of 50 in the ESRF's specific hard X-ray region. A white paper laying down the fundamentals of Phase II of the Upgrade Programme was prepared and presented to the ESRF Council in November 2012. This document was well-received by the ESRF Council and is now available on the ESRF's web site. It constitutes the basis for the preparation of a full scientific and technical case study to be included in a Technical Design Study (TDS). This TDS will be prepared by the ESRF Management with the help and advice of the ESRF users, Science Advisory Committee and Administrative and Finance Committee, and will be submitted for decision to the ESRF Council in June 2014. According to the present preliminary planning, Phase II could be launched as initially foreseen in 2015 for a five-year period ending in 2019. During this period the ESRF would operate with the present source until the third quarter of 2018 when it would be closed to user operation for approximately one year, until autumn 2019. Following a commissioning period, USM would resume with the new source at the end of 2019.

## New and present partners invest in the bright future of the ESRF

The attraction of the ESRF continues to grow and can be seen in the interest shown by new countries to set up formal associations despite the difficult economic situation worldwide. The ESRF Council and Management are working hard to develop these relations and are reviewing the level of participation of the existing partners with a view to improving the present balance between the partners' financial contributions and their scientific use of the ESRF. This is not only a very important condition for ensuring the long-term stability of the ESRF's financial resources, but it should also ensure that the fundamental principle of access to beam time is open to everybody and is based on the scientific excellence of the proposals.

The structure of this scientific highlights report is similar to last year's. It emphasises the dual mission to which the ESRF is committed over the next few years: the Upgrade Programme and the operation of the facility. As in previous years, it contains many examples of the impressive science carried out at the ESRF. Despite the reduced amount of beam time available, 2012 was a very productive year with almost two thousand refereed publications in scientific journals. In particular, in May 2012, the total number of publications from work carried out at the ESRF since the beginning of USM in 1994 reached the record value of 20,000 publications!

On behalf of the ESRF user community and staff, I wish to congratulate the laureates of the 2012 Nobel Prize for Chemistry, Robert J. Lefkowitz and Brian K. Kobilka who jointly received the award for "*studies of G-protein-coupled receptors*". I also wish to proudly share with you the information that key structural studies on this fundamentally important family of proteins were carried out by Prof. Kobilka as a user of the ESRF's beamlines ID13 and ID23-2, where he amply benefited from these *at-the-time-unique* structural biology microfocus beamlines!

This report also provides a summary of the main activities carried out at the ESRF in 2012. A large part of this work was centred around, and was intimately linked to, the points briefly outlined above.

Some important changes took place within the ESRF's Management, with key players leaving the ESRF and new ones arriving. I am pleased to announce that the ESRF Management is once again complete. I am very glad to welcome the new Director of Administration, Dr. Luis Sanchez Ortiz, and the new Director of Research for Life Sciences, Prof. Bauke Dijkstra from the University of Groningen. Both started their terms of office at the ESRF in September 2012. Similarly, I wish to warmly thank Dr. Harald Reichert, Director of Research for Physical Sciences, who assumed the role of acting Director of Research for Life Sciences until the arrival of Bauke. Finally, in 2012, the ESRF welcomed a new Science Advisory Committee made up of many new members with a very impressive range of scientific



expertise, headed by its Chairman Prof. K. Hämäläinen from the University of Helsinki.

All things considered, the ESRF is in good shape, and has very *bright* plans for the future which, if carried out, will ensure world-class scientific opportunities for its strong and diversified user community for many years to come.

The year 2012 was significant in that it laid down the first stones of the path towards the ESRF of the next twenty years. Continuing on from these important decisions, I wish to highlight that of all the actions that will shape the future ESRF, a very important one – perhaps the most important one – will be, in my opinion, to ensure that the ESRF remains attractive for the younger generations of scientists, engineers, technicians and administrators. Therefore the ESRF is engaged in rendering the facility as attractive as possible to them. This includes our

commitment, in the context of a worldwide effort, to increase opportunities for students at both graduate and undergraduate levels in scientific and technical disciplines.

I wish to conclude this foreword by thanking the very many people who contributed to the successes of the ESRF in 2012. In particular, I wish to thank the members of the scientific, technical, administrative, and financial panels for their help and advice, and the Council delegates for their guidance and continued support. Special thanks go to all ESRF users for their wonderful scientific work and critical engagement in supporting the ESRF, and to all my colleagues at the ESRF for their particularly hard work and exceptional motivation in supporting simultaneously the operation of the facility and the realisation of the Upgrade Programme.

Francesco Sette,  
ESRF Director General

## Status of the Upgrade Programme

As the most visible part of the Upgrade Programme, the new buildings for the EX2 project are taking shape and have started to dominate the new landscape of the ESRF. The unique opportunity provided by the long shutdown in the first half of 2012 has been used for the renewal and installation of many systems and components that could not have been easily upgraded or replaced during regular shutdown periods. The facility came back into full operation in May, returning almost instantly to the high performance our users expect. The upgrade of the accelerator complex as well as the renewal of the beamline portfolio continues to be on track and in line with the master plan laid out in 2009. With the continued support from our funding bodies, we are confident to deliver the Upgrade Programme in its totality.

### The EX2 project

In 2005, the first scenario of the EX2 project envisaged the creation of as many long beamlines as possible, with added laboratory and office space, and without shutdown of the facility. The constraints were already known: site topological features, continuing operation of the existing site and, most of all, extremely stringent thermal and vibration requisites well beyond those generally found in the building industry.

To address these key issues and to satisfy urban planning restrictions, a sustainable quality environment programme was incorporated into the design phase. This included measures to economise energy such as controlled air flow and the use of green roofs to boost the thermal stability of the buildings, the use of natural light to ensure the comfort

of future users, building accessibility and a judicious choice of materials.

The construction project should reach completion within the next three or four months. The current advancement of the project has enabled us to measure the constraints related to the targets, and we are pleased to report that the milestones set for 2012 have all been achieved. Major works impacting the accelerator complex and the beamlines were completed as scheduled which permitted the machine restart that went ahead as planned on 19 April 2012. Most of the works on premises impacted by the project in the existing buildings are now complete. New buildings include the ID16 satellite building, which was accepted on 10 October. Since then, the first results of thermal and vibration stability of the satellite building confirm the validity of the technical design choices. Core and shell works on the new Belledonne and Chartreuse experimental halls are complete (**Figure 1** and **Figure 2**) and work is underway to render the air treatment units operational before the “high quality slab” is poured, thus allowing the thermal effects on the cement to be controlled during the drying period.

Targets for 2013 span the completion of the technical work packages, the pouring of the high quality slabs and acceptance of installations and buildings. The final stage will be to check compatibility with specifications and to close the contracts (financial and contractual matters).

Needless to say, the stakes are high and we are confident that the project will come to fruition on time, within budget and fit for purpose thanks to the unflinching support of all



**Fig. 1:** The Laboratory and Office Building (LOB) in front of the EX2 Belledonne extension. In the background to the left, the ILL/ESRF Science Building is also under construction. The picture was taken on 23 November 2012.

those involved. Pulling the strings to coordinate a project of this scope is no mean feat. For the project manager, E. Bruas, *“Management of this project will remain an impressive venture rich in human interactions. From the outset, with the identification of needs and throughout the design and construction phases, it was necessary to seek out, control and process information and strike a fine balance between technical compromises and financial and timescale constraints. The success of the trio quality, budget and timescale will be in great part due to the mobilisation of the ESRF experts whose skills allowed the design and building contractors to be guided.”*

The time span of the project covers four years, starting with the architectural design competition and ending with the acceptance of the buildings. Over such a period there were many differences in interest, human resource movements, budget cuts and, inevitably, technical hitches. Project management tools, notably a collegial risk management system (technical, timescale and financial) were implemented to anticipate problems, analyse them and, whenever possible, turn them into opportunities. A good example of this was when an international panel of experts was set up to study the risk relating to the delivery of the high quality slab to required specifications. The expert advice given by this panel throughout the design phase meant the ESRF was able to benefit from experience gained in the construction of recent synchrotron facilities including ALBA, PETRA, SOLEIL and DIAMOND.

## Upgrade of the source

The upgrade of the accelerator system is progressing well and as planned. An improved orbit stabilisation system – the Fast Orbit Correction – was put into service during the May restart. Users will benefit from a beam stability better than 100 nm, effectively damping the disturbances due to insertion device gap changes and magnet vibrations.

The extension of the ID23 straight section to 7 metres is in progress. This change in magnet configuration has the consequence of breaking the symmetry of the lattice, however, this will allow tests of low  $\beta_y$  optics and new RF HOM-damped cavities. The installation of in-house designed permanent magnet steerers on ID16 brings this beamline one step closer to the canted configuration that will enable the two end stations - nano-imaging and nano-analysis - to operate in parallel.

Four solid state amplifiers now power the booster RF system. Compared to the klystron transmitter, the new system uses about one third of the power that was required previously.

A technical design study has been launched for the upgrade of the existing storage ring to increase the brilliance by more than a factor of 30, through the implementation of a 7-bend achromat lattice.

## Renewal of beamlines

The Instrumentation Services and Development Division (ISDD) and the Experiments Division (ExpD) continue to



be intimately involved in all upgrade beamline (UPBL) projects throughout their design, implementation and commissioning phases. In general terms, ISDD provides resources and expertise during the implementation of the Upgrade Programme for both the Experiments Division and the Accelerator and Source Division (ASD). Finding a fair balance between regular operation and new projects is still the most challenging aspect of resource monitoring. Special efforts to deploy new practices have been pursued, with particular focus given to project management in order to facilitate accurate resource allocation and monitoring. In 2012, more than 200 projects were carefully monitored.



Fig. 2: The EX2 Chartreuse hall. The picture was taken on 23 November 2012.

The main projects for beamline renewal are as follows:

- **UPBL1 – Diffraction for nano-analysis.** The TDR has been completed. The general architecture of the beamline has been finalised and the main design solutions for most major components have been selected. The detailed design of the mirrors and multilayer devices is underway.

- **UPBL4 – Nano-imaging and nano-analysis.** The assembly of the nano-analysis double mirror is in progress. Components for slits and attenuators and for the nano-imaging multilayer mirror have been delivered. For the nano-imaging nanotomography endstation, the sample stage based on a piezo hexapod with capacitive metrology is in the assembly phase. First lab tests were done in October 2012. The design of the large motion sample stages is being finalised.

- **UPBL6 – Hard X-ray spectroscopy (RIXS & XRS).** The mechanical parts for the assembly of the white beam and focussing mirrors have been received and assembly is underway. The modified pre-monochromator has been successfully tested at ID20. Lab tests demonstrated 100 nrad resolution with the commercial high precision stages of the high resolution post-monochromator. The mechanical parts are being assembled. For the assembly of the RIXS and Raman spectrometers (Figure 3), the first carbon fibre chamber has been tested successfully. Acceptance tests of large positioning stages and of large granite structures are underway.

- **UPBL7 – Soft X-ray spectroscopy (RIXS & XMCD).** The parts required for the white beam double mirror, deflecting mirror and refocussing optics have been delivered, or are soon to be delivered, and assembly has been scheduled. The design of the entrance and exit slits is complete. Calculations to optimise the vibration stability of the RIXS spectrometer (11 m arm, integrating a collimating mirror and a grating monochromator) have been completed. The detailed design and drawings of most sub assemblies is underway.

- **UPBL9A – Time-resolved ultra-small-angle scattering.** Components for beamline optics have been received.

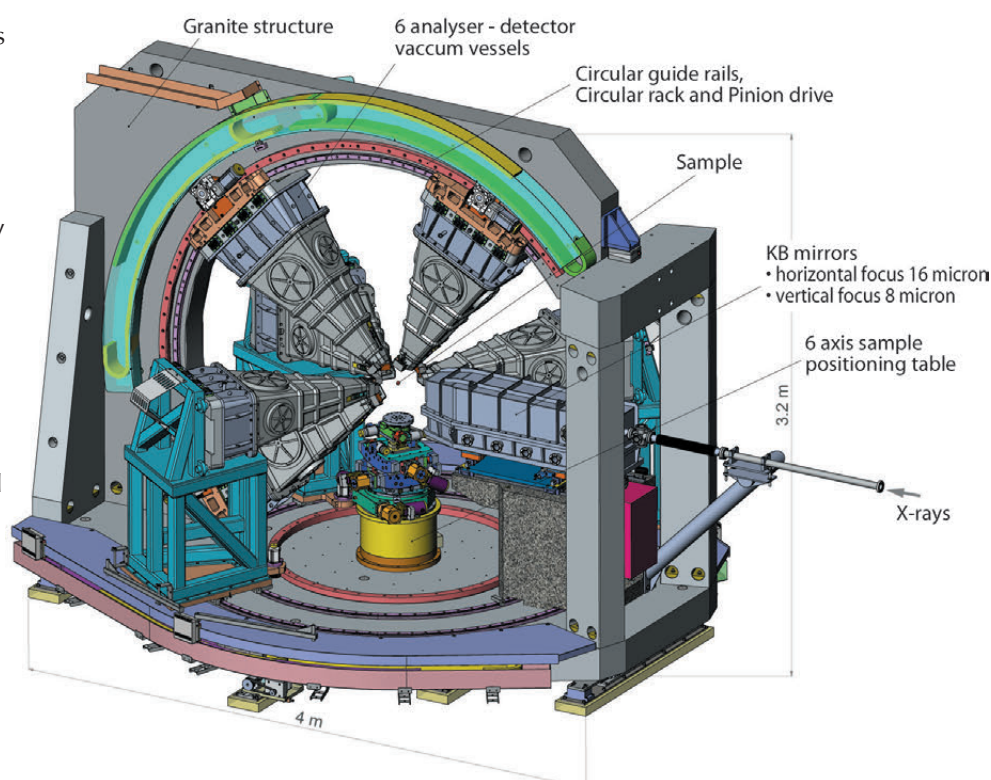


Fig. 3: UPBL6 - X-ray Raman spectrometer / 4 m x 3.2 m.



The SAXS detector vacuum tube (2 m diameter, 32 m long) and internal long translation mechanism have been ordered.

• **UPBL10-ID30 – Automated crystallographic evaluation.**

Promising first results have been obtained for the beam splitters and silicon side bounce monochromator. The optics for the three ID30A branch lines for macromolecular crystallography have been commissioned. Heat-load tests await completion. LN<sub>2</sub> large sample dewars have been delivered and will be tested soon.

• **UPBL11 – Time-resolved and extreme conditions X-ray absorption spectroscopy.**

EDXAS / S and L branches have accepted their first user experiments. Instrumentation was shown to be reliable and easy to use. Development has started on a Laue polychromator and pulsed magnetic fields. Other items include the installation and commissioning of a new FReLoN detector equipped with custom optics, the collaborative development and testing of a new version of the XH germanium microstrip detector from the STFC and the integration and initial tests of a linear Hamamatsu CCD sensor for energy-dispersive XAS (**Figure 4**).

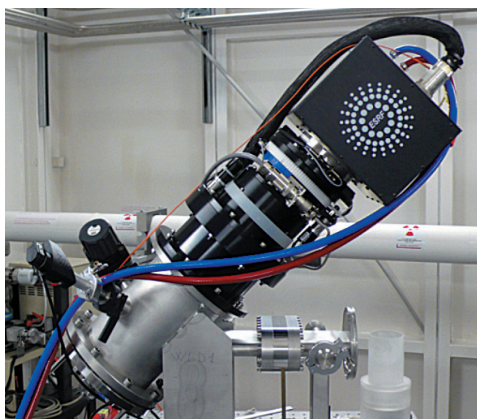


**Fig. 4:** UPBL11 - New back-thinned Hamamatsu CCD / 13.7 bits @ 10 Mhz, 4200 fps.

• **ID10 refurbishment.** The main stage of the ID10 refurbishment was successfully completed and the beamline is back to full user operation. The white beam double mirror has been installed and awaits commissioning.

• **ID19 refurbishment.** The first step of the ID19 refurbishment has been successfully completed. The second stage has started with the design for the secondary source.

The most noteworthy activities of the ISDD in 2012 included the procurement of 44 X-ray mirrors – from tender exercises to qualification testing and final installation, the delivery of several customised X-ray detectors and the design of highly-complex large-structure scientific instruments. Furthermore, the long shutdown provided the opportunity to put into operation several upgraded software packages and to deploy new generic solutions over our entire beamline portfolio. This included the upgrade of the beamline vacuum control and insertion device control on most of the beamlines, the production of standard beam viewers for twelve beamlines, the tender procedure for a large volume order of IcePAP motor controllers, the design and production of new electronic modules for beamline control such as new V2F100 voltage-to-frequency converters, the final commissioning of the fast orbit feedback for the storage ring, continuation of beamline control modernisation (vacuum and insertion device controls), the implementation of new online data analysis algorithms (MX auto-processing and spectro-imaging) and special projects in parallelisation of modelling and data analysis software packages as well as the upgrade of the Debian operating system and the batch systems (OAR). Despite the very high workload on the UPBLs, a number of R&D programmes have made good progress. A few examples are: MEDIPIX3-based modules, APD-based 2D detector XNAP and a new scintillator material, development of a silicon-to-glass bonding machine for mass fabrication of high resolution X-ray spherical analysers and a new hexapod support for mirror positioning.

*B. Dijkstra, R. Dimper, H. Reichert,  
P. Raimondi and J. Susini*



# Structural Biology

Following the long shutdown needed for the preparation and construction work required for Phase I of the ESRF Upgrade Programme, user service at the ESRF's structural biology facilities was restored in May. Following a week or two of frenetic activity, the beamlines were ready and operational as planned.

Despite the relatively short year of operation, 2012 has been a busy year with much activity devoted to the construction of new beamlines and the deployment of new equipment. The ESRF's BioSAXS facility has been re-opened, with a completely new optical configuration, at the refurbished beamline BM29. The use of a high-bandpass multilayer monochromator system combined with new focusing optics means a smaller focal spot and increased flux. This, coupled with energy tunability, allows for greater flexibility in the experiments that can be performed. Moreover, while maintaining the operation of the automated liquid sample handler, we have extended the range of options available at BM29 by including an HPLC system for the study of proteins and protein complexes "straight off the column". SAXS experiments at BM29 now also benefit from an advanced beamline control GUI and automatic data processing via software developed at EMBL Hamburg. We have also extended the functionality of our crystallography database ISPyB with enhancements specifically designed for bioSAXS measurements.

The newest of our macromolecular crystallography beamlines, ID30A, continues to make good progress. Optics and experimental hutches have been constructed and the commissioning of the X-ray optics has begun. Initial results are promising with all components conforming to expectations. X-rays have also been successfully delivered to the experimental hutches - a major milestone en route to user operation. The automation of sample handling has been a key success of the ESRF Structural Biology Group for more than a decade. ID30A will extend this capability, bringing new opportunities for structural biology. Automatic sample changing will remain a core element of beamline operation and will be enhanced by the availability of high capacity sample dewars and faster, more robust robots. In the longer term, and to further increase capacity, it will be necessary to update the sample holder itself. Work is underway to provide a new sample holder that is compatible with present standards but which will allow

higher precision mounting and greater reliability. This development is being undertaken in cooperation with our colleagues at other synchrotron sites and with the appropriate user communities.

The work presented in this highlights chapter represents only a very small fraction of the science reported by the ESRF's structural biology user community. Nevertheless, even a brief perusal of the articles presented here makes it clear that we continue to facilitate extremely high-quality research over a broad range of topics of fundamental biological interest. As usual, the space available means that we limit ourselves to highlighting some general themes and have not been able to include a very large number of deserving cases. Approximately 30% of the articles presented in the chapter concern the crystal structures of membrane proteins, illustrating the continuing importance of this research area throughout Europe. Today, however, we are seeing more sophisticated sets of experiments that provide an understanding, at an atomic level, of how these crucial cellular components function. We are proud, as a group, to have helped in a small way with the work that led to the award for the 2012 Nobel Prize in Chemistry.

By the time next year's ESRF Highlights appears we expect the first components of the ID30A complex to be in user operation. These will be a beamline (ID30A1) for the completely automatic analysis of the diffraction properties of protein crystals and the second of our dedicated microfocus beamlines for MX (ID30A3). However, this will not be the end of our efforts to continue to produce world leading instruments for MX and ideas are under discussion to further enhance, or even revolutionise, the practice of structural biology at synchrotron sources. These ideas may crystallise in the coming year and will form part of Phase II of the ESRF Upgrade Programme.

*S. McSweeney and G. Leonard*



### Principal publication and authors

M. Gelin (a,b), G. Poncet-Montange (a,b), L. Assairi (c,d), L. Morellato (e,f), V. Huteau (e,f), L. Dugué (e,f), O. Dussurget (g,h,i), S. Pochet (e,f) and G. Labesse (a,b), *Structure* **20**, 1107–1117 (2012).  
 (a) CNRS, UMR5048, Universités Montpellier 1 et 2; Centre de Biochimie Structurale, Montpellier (France)  
 (b) INSERM, U1054, Montpellier (France)  
 (c) Institut Curie, Orsay (France)  
 (d) INSERM, U759, Orsay (France)  
 (e) Unité de Chimie et Biocatalyse, Institut Pasteur, Paris (France)  
 (f) CNRS, UMR3523, Paris (France)  
 (g) Unité des Interactions Bactéries-Cellules, Institut Pasteur, Paris (France)  
 (h) INSERM U604, Paris (France)  
 (i) INRA USC2020, Paris (France)

## Ligand screening and *in situ* synthesis using protein crystals

Drug discovery is an active field of research in which medicinal chemistry remains a key player and X-ray crystallography is of increasing importance. Indeed, crystal structures of protein targets bound to ligands are providing essential guidelines for chemical structure optimisation. X-ray crystallography can also be used to screen for so-called fragments, *i.e.* weak and small binders, that can be built up step-by-step to produce larger and better ligands [1]. In parallel, organic chemistry has witnessed the emergence of soft reactions which work efficiently at room temperature (and pressure) and in aqueous solvent making them *a priori* compatible with biological samples. Such biocompatible chemical reactions have been used to link together fragments taking advantage of the protein target to template ligand growth [2]. However, this approach has been limited by the size of the combinatorial libraries one can deconvolute after *in situ* reaction, and by the number of biocompatible reactions. Surprisingly, structure-based fragment screening and *in situ* chemistry have not been combined extensively, despite a clear complementarity and proof-of-concept [3]. Moreover, molecular targets of drugs have long been viewed as static and inert structures and not as potential catalysts of new *in situ* reactions despite a seminal example of so-called epitaxial selection [4].

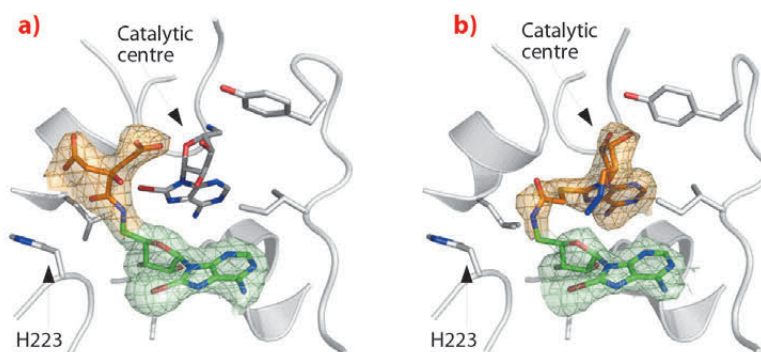
In this context, we were interested in studying bacterial NAD kinases that are essential enzymes and represent attractive therapeutic targets for the development of new antibiotics. So far, little knowledge has been gathered for these proteins as

their coding genes have only recently been discovered and no inhibitor was known. In order to rapidly obtain new ligands, we carried out focused screening using adenosine derivatives as mimics of the two nucleotidic moieties of NAD, the natural substrate. Our expectation was to map the active site and to introduce a chemical ‘handle’ to which we could tether additional fragments. Accordingly, some adenosine congeners were designed, synthesised, and then co-crystallised with the enzyme. Among the seven 5′-adenosine derivatives tested, only two gave rise to well-diffracting crystals while crystal soaking added two new structures (recorded at beamlines **ID14-4** and **ID14-2** at resolutions between 1.75 Å and 2.03 Å). The refined structures showed perfect mimicry of the biologically relevant substrate NAD, and revealed a central hydrophobic sub-pocket. This suggested that the diphosphate moiety of NAD could be substituted by a short, rather hydrophobic linker between two adenosines in order to design a novel inhibitor.

Subsequently, we analysed the binding of 8-bromo-adenosines and discovered an unanticipated amidation catalysed by NAD kinase. Soaking the crystals with a new compound (5′-amino-8-bromo-5′-deoxyadenosine) revealed extra electron density corresponding to a citrate molecule (a crystallisation agent) attached covalently to the bound adenosine (**Figure 5a**). According to the clear electron density, an amide bond was formed. This chemical reaction is distinct from the biologically relevant activity of this enzyme, and occurs at a position 7 Å away from the actual catalytic centre.

**Fig. 5:** *In situ* amidation. Crystal structures of NAD kinase in complex with two products of *in situ* chemistry:

a) 8-bromo-5′-amino-5′-deoxyadenosine (green) with covalently linked citrate (orange); b) 8-bromo-5′-amino-5′-deoxyadenosine (green) covalently linked *in situ* with 8-thioglycolic-5′-azido-5′-deoxyadenosine (orange). Data recorded on **ID14-2** and **ID14-4** at resolutions of 2.38 Å and 2.29 Å respectively.





This unexpected reactivity prompted us to bridge two adenosine derivatives *in situ* in order to completely fill the protein active site (**Figure 5b**). Then, a closely related compound with no labile bromide atom was synthesised chemically, and was shown to inhibit *in vitro* the growth of the human pathogen *Staphylococcus aureus*.

Interestingly, the *in situ* formation of the amide bond is reminiscent of the removal of the 5'-thioacetyl group of another adenosine derivative by the same enzyme [5]. This led to a model where a nearby histidine (H223), normally interacting with a phosphate group of the natural ligand, stabilises the tetragonal intermediate of

the amidation and deacetylation reactions. Indeed, mutation of the histidine abolishes the amidation confirming the role of the protein in the reaction.

Structure-based drug design is a promising method but its combination with *in situ* chemistry is still in its infancy. Here, we have shown the possible use of a protein to build up its own ligands following focused ligand screening by X-ray crystallography. This approach takes advantage of the power of high-quality beamlines and automated crystal handling that allow rapid and efficient crystal screening (100–200 datasets collected per day).

#### References

- [1] G. Chessari and A.J. Woodhead, *Drug Discov Today*, **14**, 668–675 (2009).
- [2] M.F. Schmidt and J. Rademann, *Trends Biotechnol.* **27**, 512–521 (2009).
- [3] M.S. Congreve *et al.*, *Angew Chem Int Ed Engl.* **42**, 4479–4482 (2003).
- [4] B.A. Katz *et al.*, *Biochemistry* **34**, 8264–8280 (1995).
- [5] G. Poncet-Montange, *et al.*, *J. Biol. Chem.* **282**, 33925–33934 (2007).

## ■ The molybdenum storage protein combines protein and inorganic polyoxometalate cluster chemistry

Molybdenum plays an essential role in many vital biochemical processes, for which organisms have developed a complete Mo metabolism including uptake/transport, gene regulation, homeostasis and storage. Mo is used within complex cofactors (molybdopterin in diverse oxygen-transferring redox enzymes and an FeMo cofactor in nitrogenases) or simply as single molybdate ions bound to proteins. Recent studies on a Mo storage protein (MoSto) of the N<sub>2</sub> fixing bacterium *Azotobacter vinelandii* revealed that Nature also uses Mo in the form of polyoxometalate clusters. Inorganic polyoxometalate chemistry is a long-standing research field. Polyoxometalate clusters are characterised by their huge variety culminating in “giant clusters” of up to 368 Mo atoms.

The MoSto protein in *A. vinelandii* is related to the Mo-dependent nitrogenase: it supplies the nitrogenase cofactor with Mo to ensure nitrogenase functionality under molybdenum-deficient conditions. Storage as polyoxomolybdate allows the organism to compactly deposit more than 100 Mo ions in a single MoSto molecule. Molybdate uptake is an ATP hydrolysis driven process; molybdate release is ATP-independent but pH-regulated, occurring stepwise above pH 6.8 [1]. X-ray structure analysis of the MoSto

protein at 1.6 Å resolution revealed a cage-like ( $\alpha\beta$ )<sub>3</sub> protein complex with a central cavity approximately 7250 Å<sup>3</sup> in volume (**Figure 6**). Well-defined pockets on the surface of the cavity form the binding sites for various polyoxometalate clusters. To correctly assign the type of each cluster atom at the corresponding position we performed X-ray fluorescence scans (0.6–2.1 Å) and single-wavelength anomalous dispersion experiments (1.73 Å) on MoSto crystals at beamline **ID29**. Elements (such as magnesium and phosphorous) with absorption edges outside the wavelength spectra of the scans could be distinguished from Mo by their low anomalous dispersion signal. On this basis we detected about 100 Mo atoms in the cavity, 70 of them in defined polynuclear Mo–O aggregates. The ten polymolybdate clusters observed were subdivided into four distinct types: one Mo<sub>3</sub>, three Mo<sub>5–7</sub> clusters and six structurally identical Mo<sub>8</sub> clusters. Three of the Mo<sub>8</sub> clusters are bound covalently, while the other three are bound non-covalently (see **Figure 6**). Interestingly, MoSto can also be loaded with polynuclear tungsten-oxygen clusters [2].

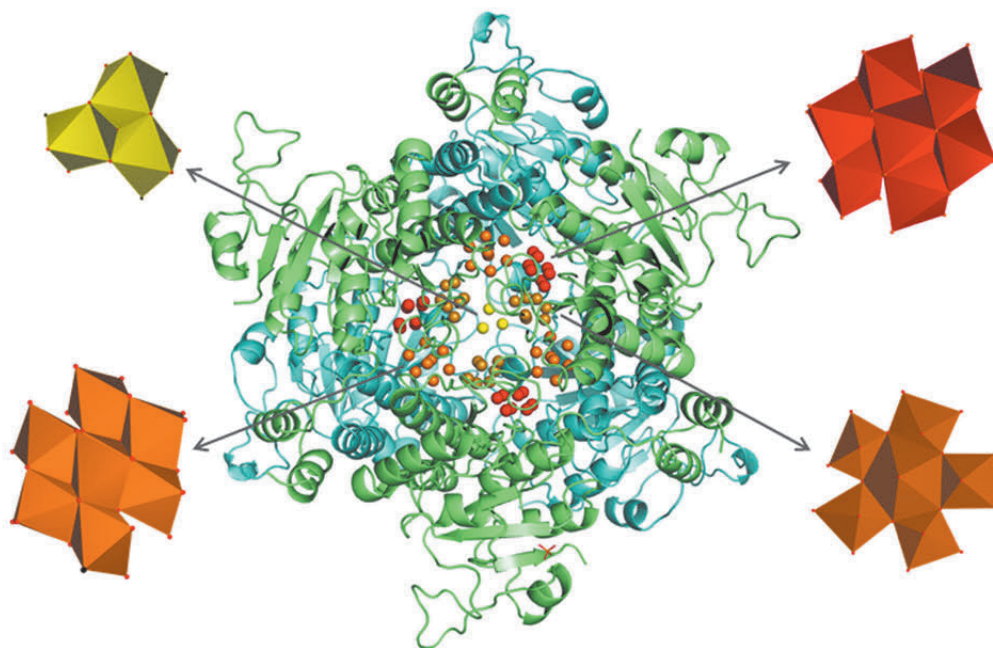
Since polyoxomolybdate clusters are not formed spontaneously at neutral or weakly acid pH values, molybdate polymerisation to larger polyoxometalate

#### Principal publication and authors

B. Kowalewski (a), J. Poppe (b), U. Demmer (b), E. Warkentin (b), T. Dierks (a), U. Ermler (b) and K. Schneider (a), *J. Am. Chem. Soc.* **134**, 9768–9774 (2012).  
(a) Department of Biochemistry I, University of Bielefeld (Germany)  
(b) Max-Planck-Institute for Biophysics, Frankfurt am Main (Germany)



**Fig. 6:** The heterohexameric ( $\alpha\beta$ )<sub>3</sub> protein complex ( $\alpha$  subunit blue,  $\beta$  subunit green) builds up a large occluded cavity in its interior occupied with different types of polyoxomolybdate clusters (Mo<sub>3</sub> yellow, covalent Mo<sub>8</sub> red, non-covalent Mo<sub>8</sub> orange, Mo<sub>5-7</sub> brown). In the Mo<sub>3</sub> cluster, each of the three triangularly arranged Mo atoms is octahedrally coordinated to five O atoms and to His $\alpha$ 140 imidazole N<sub>e2</sub>. The three covalent and three non-covalent Mo<sub>8</sub> clusters present a three-layer structure of two, four and two MoX<sub>n</sub> octahedra that are displaced relative to each other by a half octahedron. In the covalent Mo<sub>8</sub> clusters, Mo coordinates to the proteinogenic ligands His $\alpha$ 156 imidazole N<sub>e2</sub> and Glu $\alpha$ 129 carboxylate O<sub>e1</sub> in addition to the inorganic oxygens. In comparison, the non-covalent Mo<sub>8</sub> clusters are characterised by significantly more interactions with the protein scaffold including the involvement of three consecutive histidines and a metal ion (probably Mg<sup>2+</sup>). The electron densities of the Mo<sub>5-7</sub> cluster reveal an inhomogeneous Mo composition interpreted as the superposition of several polyoxometalate clusters. Architecturally, the core of the Mo<sub>5-7</sub> cluster can be described as a distorted (Mo)Mo<sub>5</sub> building block which is also found in inorganic Mo<sub>36</sub> and Mo<sub>57</sub> clusters.



aggregates must occur inside the protein cavity. Two scenarios of polyoxometalate cluster synthesis can thus be distinguished: (a) the protein binding pocket acts as template, nucleation site and catalyst of the polymerisation reaction thus predetermining the type (size, shape) of the cluster and (b) small clusters are spontaneously and transiently formed under bulk conditions (perhaps promoted by special electrostatic conditions in the solvent-filled cavity) and selectively stabilised by the protein matrix in a subsequent process. In both cases the protein matrix protects/stabilises the metal clusters by binding them and preventing them from rapid degradation.

The protein/template-induced and self-assembly contributions differ from cluster to cluster.

MoSto is unique in biology and extends the competences of proteins in general, by synthesising/binding/protecting polynuclear metal-oxide clusters of different types. It combines macromolecular biochemistry with supramolecular inorganic chemistry, both characterised by a tremendous structural diversity. This quality could eventually be exploited by using the protein cavity with its tailor-made pockets as a bioreactor for synthesising novel polyoxometalate clusters in a controllable and tunable way.

#### References

- [1] J. Schemberg, K. Schneider, D. Fenske and A. Müller, *ChemBioChem* **9**, 595-602 (2008).
- [2] J. Schemberg, K. Schneider, U. Demmer, Warkentin, A. Müller and U. Ermler, *Angew. Chem.* **119**, 2460-2465 (2007).

#### Principal publication and authors

J. Kellosoalo (a), T. Kajander (a), K. Kogan (a), K. Pokharel (a,b) and A. Goldman (a), *Science* **337** 473-476 (2012).  
 (a) *Structural Biology and Biophysics Program, Institute of Biotechnology, University of Helsinki (Finland)*  
 (b) *Department of Biochemistry and Food Chemistry, University of Turku (Finland)*

## ■ The structural basis for ion pumping by integral membrane pyrophosphatases

Plants, parasitic protozoa, bacteria and archae contain membrane-integral pyrophosphatases (M-PPases). These are novel primary transmembrane pumps with 14-17 transmembrane (TM) helices that link pyrophosphate (PP<sub>i</sub>) hydrolysis to sodium or proton pumping [1]. PPases are essential, they make it possible for anabolic reactions like DNA synthesis to be driven to completion. Unlike the soluble PPases, M-PPases recycle part

of the free energy of PP<sub>i</sub> hydrolysis to generate an electrochemical potential across biological membranes. In plants, they are vital for maturation and enhance survival under abiotic stress conditions such as drought, anoxia and cold [2]. They are also important for proliferation of disease causing protozoa [3].

M-PPases have neither sequence, structural nor functional similarity to the F<sub>0</sub>F<sub>1</sub> or

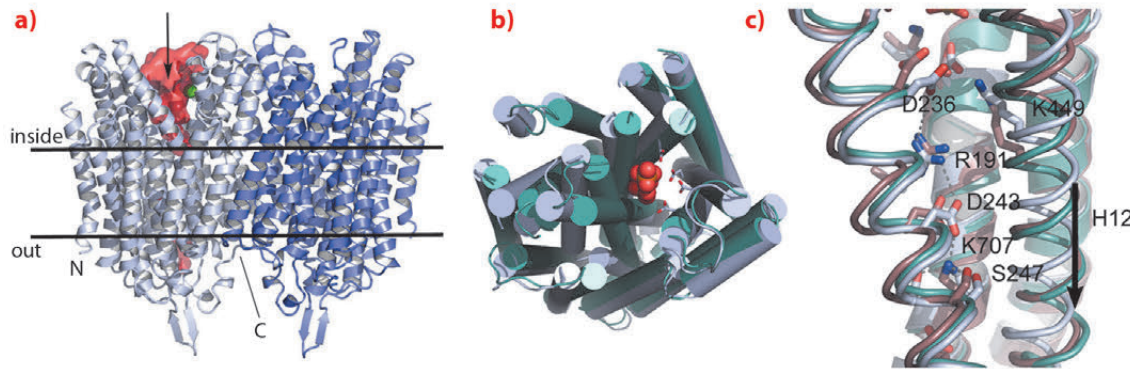


**Fig. 7:** Structure of *Thermotoga maritima* membrane bound pyrophosphatase and a comparison of different catalytic states. a) The dimer structure of Tm-PPase in relation to the lipid bilayer: one active site is indicated by the green metal ion ( $Mg^{2+}$ ), the cavity space in red, with an arrow indicating substrate binding. b) Comparison of the apo-structure (light blue) and  $P_i$ -product complex (active site viewed from above) of Tm-PPase (green), showing the contraction of the structure around the active site with bound ligand ( $2 \times P_i$ , shown as red spheres). c) Comparison of the Tm-PPase apo-structure (light blue), product complex (green), and mung bean PPase inhibitor complex (brown) around the gate region, showing the salt bridges involving R191 and the downward movement of TM-helix 12 (a and c, adapted from Kellosalo *et al.* 2012).

P-type ATPases. They can either be proton or sodium pumps, and some require  $K^+$  for maximal activity. The resting enzyme state is  $EMg_2$ , and two more metal ions bind with substrate,  $Mg_2PP_i$  [2].

We have solved the structure of the  $Na^+$ -pumping M-PPase of *Thermotoga maritima* (TmPPase) in the resting state (TmPPase:Ca:Mg) at 2.6 Å resolution and with product bound (TmPPase: $P_i_2$ : $Mg_4$ ) at 4.0 Å. TmPPase is a homodimer with 16 TM-helices per monomer (Figure 7). The helices extend up to 25 Å from the membrane bilayer on the cytoplasmic side so that the hydrolytic centre is held some 20 Å above the membrane plane.

The protein has a completely novel fold and its unusual active site has four distinct regions: the hydrolytic centre, a “coupling funnel”, the gate (closed in our structure) just below the membrane surface, and an exit channel for  $Na^+$ -ions. The distance from the hydrolytic centre to the gate is about 20 Å. Six helices (5-6, 11-12 and 15-16) form the hydrolytic centre and the coupling funnel on the cytoplasmic face of the protein. However, just four helices (5, 6, 12 and 16) form the gate and channel, creating an internal “symmetry mismatch” between the two sides of the protein.

Below the hydrolytic centre is the “coupling funnel” (Figure 7) containing eight absolutely conserved charged residues that couple hydrolysis to ion pumping. Some of the interactions observed in the resting structure suggest that the funnel is poised to switch into an alternate conformation to pump the sodium ion, especially the residue R191, which is almost equidistant between D243 and D236. Alignment of our structures and that of the substrate complex of the related mung bean PPase [4] shows that TM12 moves downwards by about 2 Å, concomitant with R191 switching up and

down in a locked and released spring movement.

As the conformational changes observed in the inhibited and product-bound states are similar, with the exit channel closed in both, we suggest that ion pumping in M-PPases occurs via a “binding change” mechanism as in the  $F_0F_1$  ATP synthase, and that the full conformational change that opens the gate involves a downwards piston-like motion of TM12 (Figure 8). This is driven by a concerted contraction during substrate binding. This change destroys a high-affinity sodium-binding site above the gate, leading to transfer of

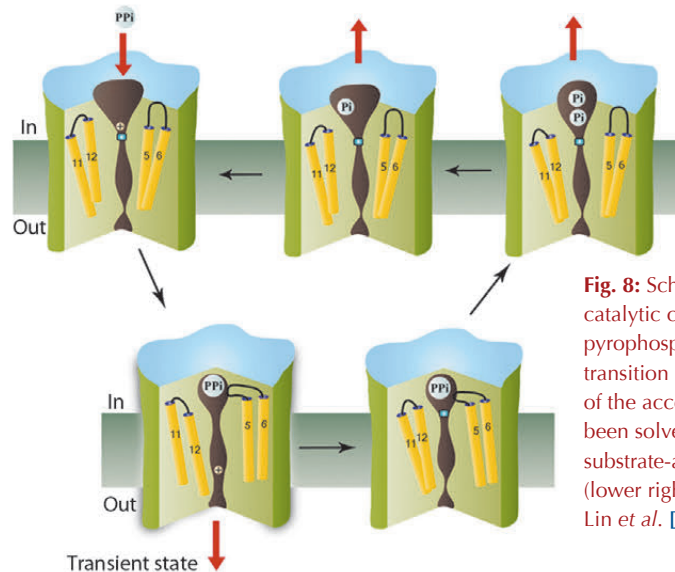


**Fig. 8:** Schematic showing the catalytic cycle of membrane pyrophosphatases, with the transition state indicated. Three of the accessible states have been solved by us, while the substrate-analogue complex (lower right) was solved by Lin *et al.* [4].

the ion into the exit channel, followed by its rapid diffusion into the periplasm. Consistent with this model, there are no conserved polar residues below the gate. Release of the sodium ion would allow the gate to close, hydrolysis to occur, product to leave, and the protein to revert to its resting state.

Our work and the related mung bean structure provide the first steps in understanding the structure and mechanism in this novel family of ion pumps.

#### References

- [1] A.M. Malinen, G.A. Belogurov, A.A. Baykov and R. Lahti, *Biochemistry* **46**, 8872–8878 (2007).
- [2] M. Maeshima, *Biochim. Biophys. Acta* **1465**, 37–51 (2000).
- [3] M.T. McIntosh and A.B. Vaidya, *Int. J. Parasitol.* **32**, 1–14 (2002).
- [4] S.M. Lin, J.Y. Tsai, C.D. Hsiao, Y.T. Huang, C.L. Chiu, M.H. Liu, J.Y. Tung, T.H. Liu, R.L. Pan and Y.J. Sun, *Nature* **484**, 399–403 (2012).



**Principal publication and authors**

B. Billen (a), R. Spurny (a), M. Brams (a), R. van Elk (b), S. Valera-Kummer (c), J.L. Yakel (d), T. Voets (e), D. Bertrand (c) and A.B. Smit (b), C. Ulens (a), *Proc Natl Acad Sci U S A* **109**, 9173-9178 (2012).

(a) *Laboratory of Structural Neurobiology, KULeuven (Belgium)*

(b) *Department of Molecular & Cellular Neurobiology, VU University (The Netherlands)*

(c) *HiQScreen, Geneva (Switzerland)*

(d) *Laboratory of Neurobiology, NIEHS (USA)*

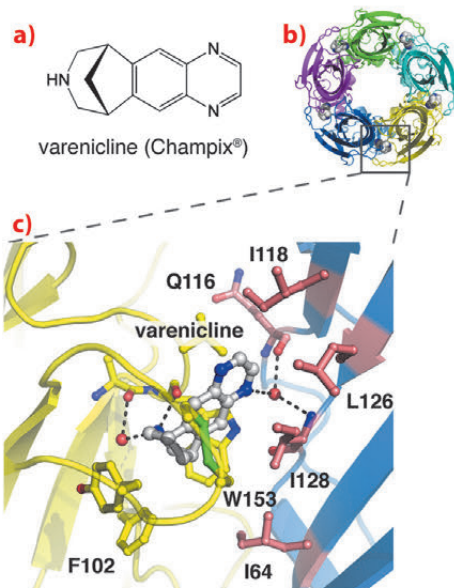
(e) *Laboratory of Ion Channel Research, KULeuven (Belgium)*

**Three-dimensional structures reveal molecular action of anti-smoking drug**

Nicotine is the chemical substance in tobacco responsible for smoking addiction, which causes major public health risks. The effects of nicotine are mediated through specific nicotinic acetylcholine receptors (nAChRs) that function as heteropentameric ligand-gated ion channels composed of  $\alpha$ - and  $\beta$ -subunits. These  $\alpha$ 4 $\beta$ 2 nAChRs trigger downstream dopamine signalling in the mesolimbic system, which is an area in the brain that plays an important role in pleasure and reward sensation. Consequently, the  $\alpha$ 4 $\beta$ 2 nAChR has

become a key target for the development of therapeutic agents for smoking cessation. Recently, a partial agonist for the  $\alpha$ 4 $\beta$ 2 nAChR, varenicline (Champix®), has been approved for clinical use as a smoking cessation aid (Figure 9a). This drug derives its therapeutic effect from two fundamental molecular actions. First, it binds to  $\alpha$ 4 $\beta$ 2 nAChRs with higher affinity, but lower efficacy than nicotine. This effect is thought to antagonise the reward sensation of smoking. Second, varenicline activates and desensitises  $\alpha$ 4 $\beta$ 2 nAChRs, thereby minimising withdrawal symptoms and increasing the success rate of smoking cessation attempts. Understanding the molecular mechanism of partial agonism of the nAChR has great potential for designing novel smoking cessation compounds but is currently hampered by the absence of a high-resolution structure of a eukaryotic nicotinic receptor.

**Fig. 9:** X-ray crystal structure of Ct-AChBP in complex with varenicline.



Current structural insight into ligand recognition by nAChRs derives from acetylcholine binding proteins (AChBPs), which are homologous to the extracellular ligand binding domain of nAChRs [1]. In this study, we demonstrate that a newly discovered AChBP from *Capitella teleta*, Ct-AChBP, binds partial agonists such as varenicline with high affinity, similar to  $\alpha$ 4 $\beta$ 2 nAChRs. We determined X-ray crystal structures of Ct-AChBP in complex with varenicline (Figure 9b) or lobeline, which are both partial agonists at  $\alpha$ 4 $\beta$ 2 nAChRs. These structures highlight the binding pocket architecture for molecular recognition of these ligands, revealing the contact residues that potentially mediate their molecular actions in  $\alpha$ 4 $\beta$ 2 nAChRs (Figure 9c). The ligand binding site of Ct-AChBP is found at the interface between two subunits and ligands interact with amino acids from both the principal face (historically designated as 'loops' A, B, and C) and the complementary face ('loops' D, E, and F) of the binding pocket. On the principal face, varenicline interacts with aromatic amino acids (W153 in loop B and Y201 in loop C), which are highly conserved among different nAChR subtypes. These interactions include cation- $\pi$  interactions and multiple hydrogen bonds that converge on residues of loop B.

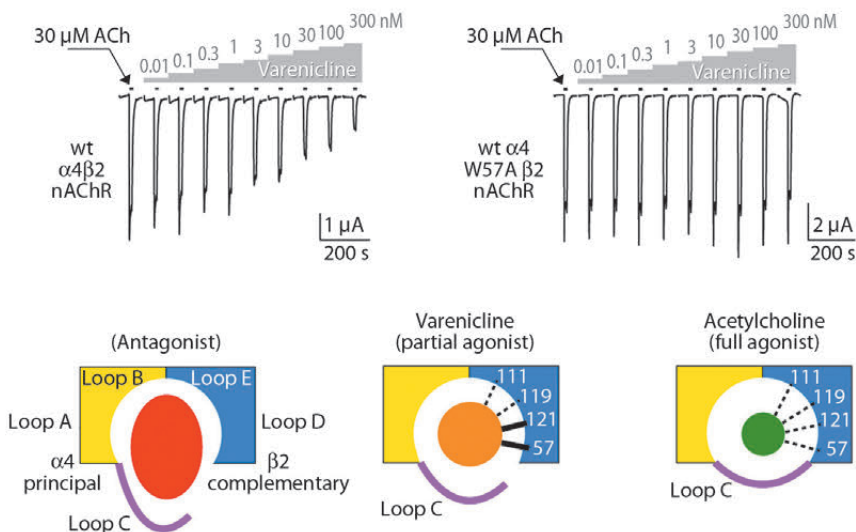


**Fig. 10:** Ligand-activated currents of nAChRs.



On the complementary face of the binding site, varenicline forms mostly hydrophobic interactions with residues that are weakly conserved among different nAChR subtypes. In Ct-AChBP, these residues are I118, L126, and I128 in loop E and I64 in loop D. A water molecule forms hydrogen bonds between the varenicline pyrazino nitrogen and the backbone nitrogen and oxygen of I128 and Q116, respectively. Remarkably, this water molecule occupies a position that is almost identical to the water molecule observed in the complex between AChBP and nicotine [2].

Employing structure-based mutagenesis, we investigated the functional role of several homologous contact residues in human  $\alpha 4 \beta 2$  nAChRs expressed in *Xenopus* oocytes. Using the two-electrode voltage-clamp technique, we measured ligand-activated currents of nAChRs and compared relative affinity and efficacy for varenicline and desensitisation by varenicline and the full agonist acetylcholine on wild type and mutant receptors. We found that mutations at two positions, namely W57

and L121, have remarkable effects on channel function. First, we observed that the mutations abolish varenicline-mediated desensitisation of  $\alpha 4 \beta 2$  nAChRs (Figure 10). This result suggests that the loop D residue W57 (I64 in Ct-AChBP) and loop E residue L121 (I128 in Ct-AChBP) form critical interactions with varenicline to mediate transitions to a desensitised state of the  $\alpha 4 \beta 2$  nAChRs. Second, we observed that mutations at these positions eliminate the relative difference in efficacy of channel opening between varenicline and the full agonist acetylcholine. Together, these results demonstrate the predictive value of the X-ray crystal structure and highlight the key role of specific amino acid residues in mediating receptor desensitisation and channel opening with limited efficacy, which both are effects thought to facilitate smoking cessation.

In summary, our results help to understand the effects of smoking cessation drugs in a structural context and provide a novel entry into drug discovery programmes aimed at developing better smoking cessation aids.

#### References

- [1] K. Brejc, W.J. van Dijk, R.V. Klaassen, M. Schuurmans, J. van Der Oost, A.B. Smit and T.K. Sixma, *Nature*. **411**, 269-276 (2001).
- [2] P.H. Celie, S.E. van Rossum-Fikkert, W.J. van Dijk, K. Brejc, A.B. Smit and T.K. Sixma, *Neuron* **41**, 907-914 (2004).

## ■ Endo- $\alpha$ -mannosidase: an alternative route to N-glycan processing

Asparagine-linked (N-linked) glycans direct the folding and targeting, as well as influencing the stability and function of mature glycoproteins. Transfer and biosynthetic modification of a conserved 14-oligosaccharide precursor occurs within the endoplasmic reticulum and features the sequential hydrolysis and transfer of individual glycoside moieties. Aberrant glycosylation, through modification of this process, is strongly associated with cellular dysfunction and disease, including the metastatic progression of cancer and congenital disorders. Furthermore, N-glycans are known to play significant roles in viral proliferation, rendering the various enzymes involved in their maturation as potential therapeutic targets.

Treatment strategies to regulate diseases of glycoprotein biosynthesis have, to date, focussed largely on the use of inhibitors of the 'trimming' glycosidases

acting early in the N-glycan processing pathway, such as glucosidase I. The limited efficacy of such compounds to provide effective disease control has arisen, in part, due to the existence of a unique "bypass" enzyme acting within the same pathway, *endo*- $\alpha$ -mannosidase. *Endo*- $\alpha$ -mannosidase circumvents the well-known N-glycan processing pathway, specifically hydrolysing an internal bond within the precursor oligosaccharide to liberate a mannose moiety flanked by at least one glucosyl moiety. Using ESRF data, we have recently revealed the first native 3-D structures of a bacterial *endo*- $\alpha$ -mannosidase enzyme (Figure 11a). Data collected at beamline ID14-1 revealed an initial protein-ligand complex allowing the first view of the enzyme active site (Figure 11b).

As might be expected given its unique activity, the 3-D structure of *endo*- $\alpha$ -mannosidase appears relatively novel

#### Principal publication and authors

A.J. Thompson (a), R.J. Williams (b), Z. Hakki (b), D.S. Alonzi (c), T. Wennekes (d), T.M. Gloster (a), K. Songsrirote (a,e), J.E. Thomas-Oates (a,e), T.M. Wrodnigg (f), J. Spreitz (f), A.E. Stütz (f), T.D. Butters (c), S.J. Williams (b) and G.J. Davies (a), *Proc. Natl. Acad. Sci. (USA)* **109**, 781-786 (2012).  
(a) Department of Chemistry, University of York (UK)  
(b) School of Chemistry and Bio21 Molecular Science and Biotechnology Institute, University of Melbourne (Australia)  
(c) Oxford Glycobiology Institute, Department of Biochemistry, University of Oxford (UK)  
(d) Laboratory of Organic Chemistry, Wageningen University (The Netherlands)  
(e) Centre of Excellence in Mass Spectrometry, University of York (UK)  
(f) Institute of Organic Chemistry, Graz University of Technology (Austria)



compared to those within the 120+ currently known glycoside hydrolase families. The active site appears to be located within a long solvent-accessible cleft, consistent with the linear, elongated nature of the N-glycan substrate. The majority of amino acids comprising this region are highly conserved among *endo- $\alpha$* -mannosidases from different species. Highly unusual within these structures is the apparent absence of divalent metal ions, or even a site available for metal coordination, a feature typically

synonymous with  $\alpha$ -mannosidase activity. These observations, together with further structural complexes and kinetic analysis, have led us to propose a novel, substrate-assisted mechanism for catalysis via a 1,2 epoxide intermediate (**Figure 12**).

Given that detailed knowledge of enzymatic mechanisms is of central importance to the rational design of inhibitors and potential drug compounds, future work will focus on the complete mechanistic dissection of *endo- $\alpha$* -

**Fig. 11:** a) 3-D structure and b) electron density for BIS-TRIS-Propane bound in the *endo- $\alpha$* -mannosidase active site, both determined using data collected at the ESRF.

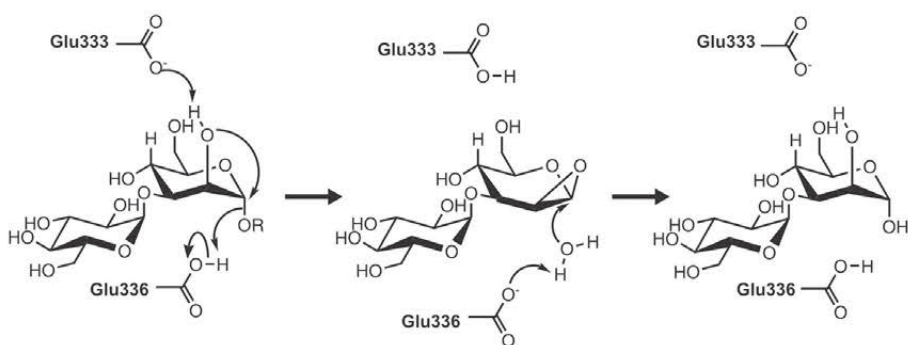
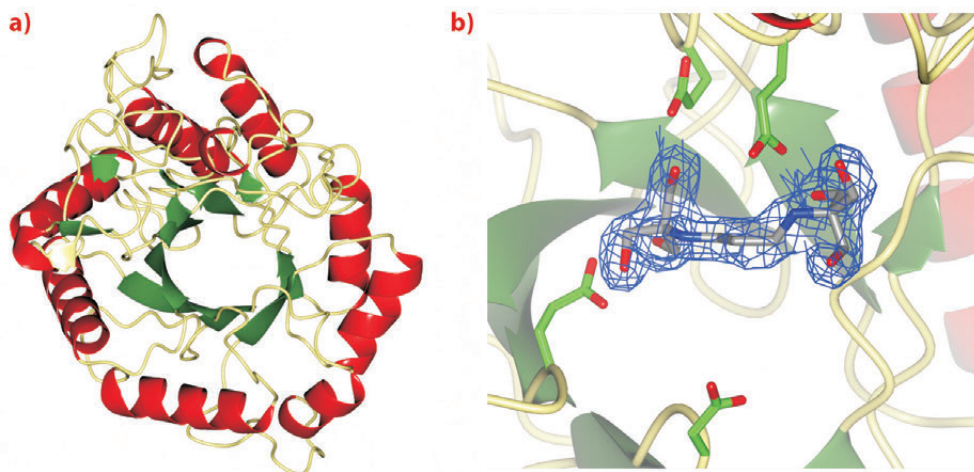


**Fig. 12:** Potential *endo- $\alpha$* -mannosidase reaction mechanism via an epoxide-like 1,2-anhydro sugar intermediate.

*mannosidase* activity, together with further structural analysis of complexes. Inhibitors that block the early processing stages of N-glycan biosynthesis have been shown to provide some promise as novel treatment strategies to a wide range of pathologies including cancer and viral infections. As such, the elucidation of the structure of *endo- $\alpha$* -mannosidase provides a valuable rationale for the development of novel compounds, which might form part of combinatorial antiviral therapies together with existing  $\alpha$ -glucosidase I/II inhibitors.

## ■ The structure of an 'alternative' respiratory complex I

Mitochondria are "cellular power plants" that generate most of the cellular supply of adenosine triphosphate (ATP), which is used as a source of energy. The first reaction of the mitochondrial respiratory system is carried out by complex I. Many organisms possess alternative enzymes that can bypass or replace the complexes of the mitochondrial respiratory chain.

These include the alternative NADH-quinone oxidoreductase enzymes (NDH-2), which can bypass complex I. NDH-2 enzymes catalyse the transfer of an electron from NADH via FAD to quinone.

Ndi1, an NDH-2-type enzyme, is found in the mitochondria of *Saccharomyces cerevisiae* (Baker's yeast). Ndi1 can



functionally replace complex I of the mitochondrial respiratory chain both in *Caenorhabditis elegans* (round worm) and in cultured human cells. Recently, the expression of yeast Ndi1 in *Drosophila melanogaster* (fruit fly) mitochondria conferred protection against toxins and the usually lethal complex I knockdown [1]. Importantly, Ndi1 has been shown to increase lifespan, independently of the effects of diet, by mitigating mitochondrial ROS production in ageing flies and limiting the accumulation of markers of oxidative damage. NDH-2 enzymes are also important targets for drug design, since their activity is crucial to the life cycles of the causative agents of malaria (*Plasmodium falciparum*) and tuberculosis (*Mycobacterium tuberculosis*).

To understand the molecular basis of the activities of NDH-2 enzymes and as a starting point for drug development, we need to know the crystal structure of Ndi1. Ndi1 is a monotopic membrane protein (possessing an integrated structure that does not cross the membrane bilayer). Monotopic membrane proteins include a significant fraction of their structure that is soluble, therefore their structural characterisation involves a delicate balance between the requirements for membrane protein stabilisation (for example, the presence of detergents) and traditional techniques applied in soluble protein structural elucidation.

We were able to solve the crystal structure of Ndi1 to 2.7 Å resolution, with much of the diffraction data collected on beamlines

ID29 and ID23-1. The structure (Figure 13) reveals three domains: the FAD-binding domain (residues 43-178 and 342-442), the NADH-binding domain (residues 179-341) and a C-terminal membrane-anchor domain (residues 443-513). The FAD- and NADH-binding domains show typical Rossmann folds and significant structural similarity to soluble FAD-dependent oxidoreductase-type enzymes. The C-terminal membrane-anchor domain is composed of a contiguous 70-residue stretch, with a three-stranded  $\beta$ -sheet connected to a helix-turn-helix structure. The crystals of Ndi1 contained dimeric assemblies of the protein. The membrane-anchor domains from each monomer associate in the dimer to create a contiguous apolar ridge across the centre of the complex. The base of this ridge is the part of the protein most deeply inserted into the membrane. It is comprised of the C-terminal helix of the membrane-anchor domain and presents predominantly aromatic residues to the membrane (Figure 13).

To investigate the location of the active site of Ndi1 and in particular, its substrate-binding properties, we crystallised the protein in the presence of NAD<sup>+</sup> and UQ2 (ubiquinone-2). The resulting crystal structures show that these molecules bind in overlapping positions, stacking approximately 3.0 Å from the *re*-face of the FAD cofactor. This common binding site lies at the intersection of two channels in the protein structure – one leading from the matrix and the other from the membrane. Ndi1 therefore accommodates

#### Principal publication and authors

M. Iwata (a,b), Y. Lee (a,b,c), T. Yamashita (d,e), T. Yagi (d), S. Iwata (a,b,c,f,g,h), A.D. Cameron (a,b,c,f) and M.J. Maher (a,i), *Proc. Natl. Acad. Sci. USA* **109**, 15247-15252 (2012).

(a) Division of Molecular Biosciences, Membrane Protein Crystallography Group, Imperial College, London (UK)

(b) Membrane Protein Laboratory, Diamond Light Source, Harwell Science and Innovation Campus, Oxfordshire (UK)

(c) Human Receptor Crystallography Project, Japan Science and Technology Agency, Kyoto (Japan)

(d) Department of Molecular and Experimental Medicine, The Scripps Research Institute, La Jolla, CA (USA)

(e) Department of Cardiovascular Physiology, Faculty of Medicine, Kagawa University (Japan)

(f) Rutherford Appleton Laboratory, Research Complex at Harwell, Didcot (UK)

(g) Department of Cell Biology, Graduate School of Medicine, Kyoto University, (Japan)

(h) Systems and Structural Biology Centre, RIKEN, Kanagawa (Japan)

(i) La Trobe Institute for Molecular Science, La Trobe University, Melbourne (Australia)

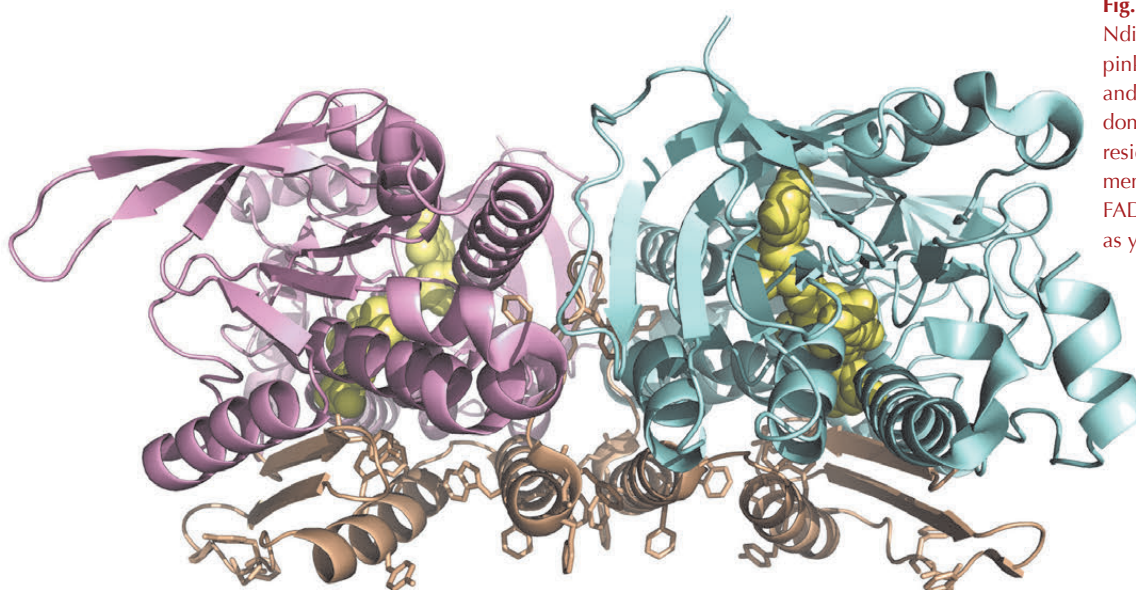


**Fig. 13:** Dimeric structure of Ndi1: Molecule A is shown in pink, molecule B in pale blue and the membrane-anchor domains in brown. Aromatic residues, which present to the membrane are highlighted. The FAD cofactors are represented as yellow spheres.



### References

- [1] A. Sanz *et al.*, *Proc. Natl. Acad. Sci. USA* **107**, 9105-9110 (2010).  
 [2] M.H. Bracey *et al.*, *FEBS Lett.* **567**, 159-165 (2004).

the passage of both lipid- and water-soluble substrates to a common binding site (**Figure 14**).

Monotopic membrane proteins lie at the bilayer's aqueous interface and integrate into the membrane, without crossing the membrane bilayer. This type of membrane

insertion is crucial in biology as it allows protein active sites of widely varying activity to engage the lipid core, without the constraints of pure  $\alpha$  or  $\beta$  folds that are features of integral membrane proteins [2]. The Ndi1 structures presented here are in some ways the ultimate example of this type of adaptation. Ndi1 brings essential activity (NADH-quinone oxidoreduction) to the membrane such that the binding sites for its water-soluble (NADH) and lipid-soluble (ubiquinone) substrates overlap. This highlights Ndi1 as an example of the evolution of a membrane protein from an ancestor soluble protein, explaining how the protein adopted membrane soluble substrates.

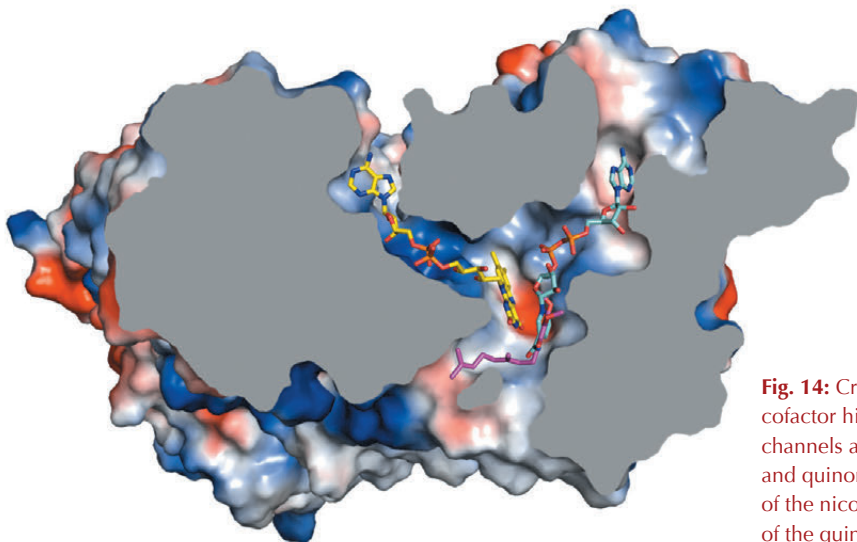


**Fig. 14:** Cross-section of a Ndi1 monomer with the FAD cofactor highlighted in yellow. The substrate binding channels are occupied by NAD<sup>+</sup> (cyan carbon atoms) and quinone (pink carbon atoms). The binding positions of the nicotinamide ring of NAD<sup>+</sup> and the head group of the quinone overlap.

### Principal publication and authors

J. Reguera (a,b), C. Santiago (a), G. Mudgal (a), D. Ordoño (a), L. Enjuanes (a) and J.M. Casasnovas (a), *PLoS Pathogens* **8**, e1002859 (2012).  
 (a) Centro Nacional de Biotecnología, CNB-CSIC, Madrid (Spain)  
 (b) Present address: European Molecular Biology Laboratory, Grenoble Outstation (France)

## ■ Structural view of coronavirus cell entry and neutralisation

Virus particles formed in infected cells transmit the viral genome and the infection from cell to cell. Viruses must therefore enter into host cells to initiate the replicative infective cycle. In their extracellular transit stage, via distinct proteins or motifs, virus particles attach to specific cell surface molecules (receptors) to penetrate into cells. Receptor-binding virus proteins are targets for immune responses that would prevent virus entry and infection. The study of virus-receptor interactions and virus neutralisation is important for the development of therapies preventing virus infections.

The coronaviruses are a large family of enveloped viruses mostly responsible of enteric and respiratory diseases, such as the severe acute respiratory syndrome and 10-20% of all common colds [1]. Coronavirus infections cause important economic losses, and high mortality rates were witnessed in recent outbreaks. Coronavirus particles display large surface projections (17–20 nm

in length) comprised of homotrimers of the spike glycoproteins (S), which generate a characteristic crown-like appearance (**Figure 15**). These spike glycoproteins mediate particle attachment to cell surface receptors and entry into host cells. In addition, they contain antigenic sites, recognised by antibodies neutralising coronaviruses. The cell surface aminopeptidase N (APN), a target for cancer therapy, is a major cell entry receptor for coronaviruses. A subset of coronaviruses, the alphacoronavirus, attach to the APN to penetrate into host cells. A fragment of the S protein, the receptor binding domain (RBD), bears the APN recognition motifs. These motifs overlap with antigenic sites recognised by neutralising antibodies that prevent coronaviruses binding to APN. We employed X-ray crystallography with the aim to identify how alphacoronaviruses attach to the APN and how neutralising antibodies prevent coronaviruses binding to the receptor and infection. We determined the crystal structures of the

RBD of porcine coronavirus in complex with either its APN receptor or with a neutralising antibody (nAb) (**Figure 15**). Diffraction data extending to about 3Å resolution for structure determination was collected at beamline **ID29**.

The APN is a type II membrane protein and thus, the N-terminus of its ectodomain is located near the cell membrane (**Figure 15**). The APN ectodomain structure revealed this to be composed of four domains (DI to DIV). APN forms dimers on the cell surface and in the crystals. The dimerisation surface comprises about 1000 Å<sup>2</sup> of DIV (green in **Figure 15**). In the virus-receptor complex, each RBD molecule (blue in **Figure 15**) contacts the membrane distal region of a single APN molecule. The protruding tip of the RBD, which bears two exposed aromatic residues (Tyr and Trp) in loops (red in **Figure 15**), docks into recessed APN surfaces. The Tyr residue fits between an α helix and a glycan, whereas the Trp sits in a cavity formed by DII and DIV of APN (not shown). The receptor binding tip of the RBD is also targeted by the crystallised nAb (**Figure 15**), which mostly binds to the Tyr residue. Other coronavirus neutralising antibodies recognise also the APN-binding tip of the RBD, showing that this region is a major antigenic site in the envelope S. These results indicate that antibodies neutralise coronavirus infections by blocking virus binding to its APN receptor. Efficient coronavirus vaccines must elicit immune responses focused toward the

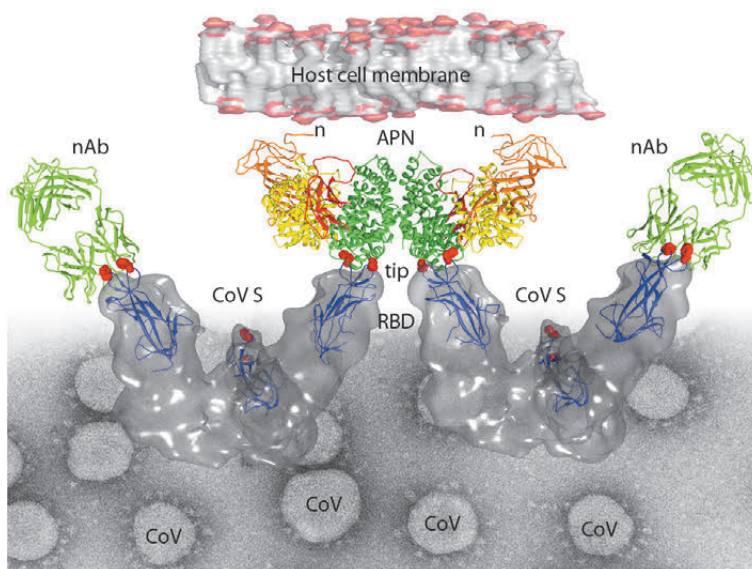


**Fig. 15:** Structural view of coronavirus (CoV) binding to its host cell aminopeptidase N (APN) receptor and its inhibition by neutralising antibodies. Ribbon representations of the crystal structures of a porcine coronavirus spike (CoV S) receptor-binding domain (RBD), shown in blue, in complex with the cell surface dimeric pig APN ectodomain, or with a CoV neutralising antibody (nAb, green). APN domains are orange (DI), yellow (DII), red (DIII) and green (DIV). The N-terminus of the APN connects to the membrane. Two coronavirus residues (Tyr and Trp) exposed to the APN and nAb contact tip of the RBD are shown as red spheres. The coronavirus RBD was fitted into the cryo-EM (EMD-1423) structure of a trimeric CoV S fragment [2], shown as a grey surface. An EM-micrograph of CoV particles with their characteristic projections formed by homotrimers of the S glycoprotein that binds to the APN for cell entry is also shown.

identified receptor binding motifs in the envelope S protein. These structural results provide a compelling view of coronavirus cell entry and immune neutralisation, and may aid the design of antivirals or coronavirus vaccines. APN is also a target for cancer therapy and its structure could facilitate the development of anti-cancer drugs.

#### References

- [1] P.S. Masters, *Adv. Virus Res.* **66**, 193-292 (2006).
- [2] D.R. Beniac, A. Andonov, E. Grudski and T.F. Booth, *Nat. Struct. Mol. Biol.* **13**, 751-752 (2006).

## ■ Capturing a closed conformation of an ion channel

Pentameric ligand-gated ion channels (pLGICs) are a major family of neurotransmitter receptors in the brain and its periphery that encompasses acetylcholine, serotonin, glycine and γ-aminobutyric acid receptors. All these receptors share a common pentameric architecture with a large extracellular domain (ECD) and a transmembrane domain (TMD) that is composed of four α-helices, named M1 to M4, that form a funnel-shaped pore defined by the M2 helices of each of the subunits. pLGICs are dynamic proteins that couple neurotransmitter binding in the ECD to the

opening of the ion channels embedded in their TMD. This coupling involves global conformational reorganisations, thereby generating discrete allosteric states including a basal closed state, an active open state stabilised by agonists and several desensitised closed states. A prerequisite for understanding the gating mechanism of pLGICs at the molecular level is to obtain structural information on each of these different allosteric states.

GLIC is a pH-gated bacterial homologue of the family [1] of which the structure has

#### Principal publications and authors

M. Prevost (a), L. Sauguet (a,b), H. Nury (a,b), C. Van Renterghem (a), C. Huon (a), F. Poitevin (b), M. Baaden (c), M. Delarue (b) and P.J. Corringer (a), *N.S.M.B.* **19**, 642-9 (2012).  
 (a) Institut Pasteur, Groupe Récepteurs-Canaux, CNRS, Paris (France)  
 (b) Institut Pasteur, Unité de Dynamique Structurale des Macromolécules, CNRS, Paris (France)  
 (c) Laboratoire de Biochimie Théorique, CNRS, Univ Paris Diderot, Paris (France)



been solved in the presence of saturating concentrations of agonist protons in an open conformation (**Figure 16**) [2]. In the present work, our aim was to solve the X-ray structure of a closed conformation of GLIC. In order to do so, we generated four different cross-links between the ECD and the TMD. The four distinct mutants crosslink ECD loop 2 to four positions in the TMD M2-M3 loop. Electrophysiology experiments revealed that 3 out of 4 cross-linking mutations produce no current in their oxidised form suggesting that these channels are unable to open in the membrane context.

with DTT prior to crystallisation returned to the known open conformation. In addition, we observe that a phospholipid binding site identified in the GLIC wild-type open structure is lost in all the locally-closed structures. For the reduced double mutants that crystallise in the open form, residual electron density in the  $F_o - F_c$  map clearly identified again the presence of phospholipids. This suggests that the binding of phospholipids could be part of the molecular determinants that stabilise the open form of the channel, in line with the possibility that some phospholipids may act as allosteric effectors of pLGICs.

We performed similar cross-linking mutations on the human glycine  $\alpha 1$  receptor and observed that they display similar phenotypes to that of the corresponding GLIC mutants. This suggests that our findings can be extended to eukaryotic pLGICs. In addition, we showed that the locally-closed form can be adopted by a fully functional GLIC cross-linked mutant suggesting that these conformations may also occur in the membrane for a functional channel, outside of the crystal and detergent context. This idea is supported by molecular dynamics simulations showing that the locally-closed state is stable in a membrane environment, and also by cross-linking and SCAM experiments (substituted cysteine accessibility method) that are compatible with the locally-closed to open state transition. The locally-closed form we observed could thus correspond to a late intermediate in the course of activation or to an early intermediate in the course of desensitisation of GLIC. In our structures, the locally-closed form is also associated with a reshaping of the cavities located behind M2, known to mediate the effect of allosteric effectors, including general anaesthetics and alcohols. The locally-closed conformation might thus constitute a valid template for mechanistic investigations of the gating process and in the design of novel classes of pharmacological effectors targeted to neurotransmitter receptors.

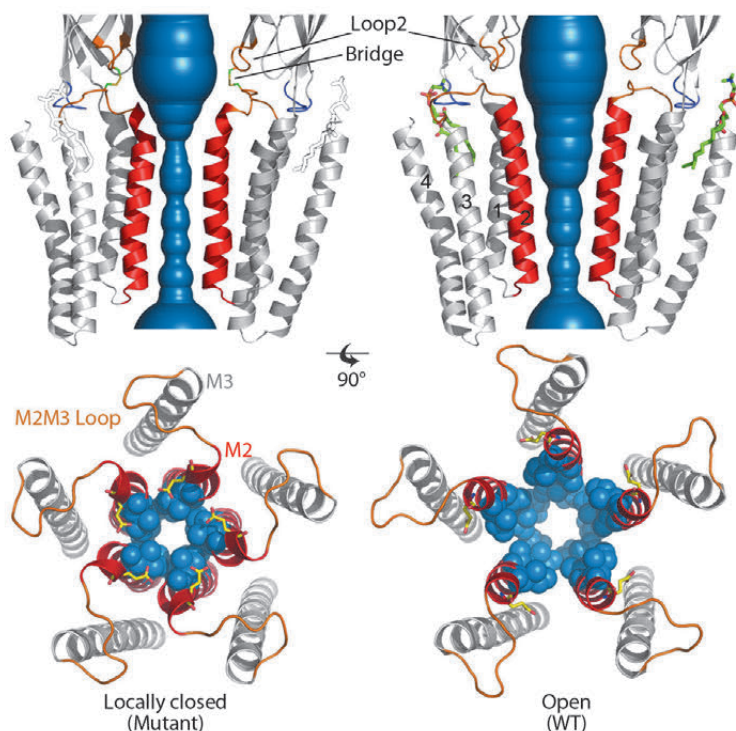


**Fig. 16:** Comparison of the X-ray structures of a GLIC cross-linked mutant in the locally-closed conformation (left) and wild-type GLIC in the open conformation (right). The water accessible region of the pore of locally-closed and open forms is shown in blue. The lipid molecule seen only on the open structure is shown in green sticks and drawn on the locally-closed structure for reference. The bottom panels present top-views of the pores. M2 helices are coloured in red, and side chains of constricting residues are shown as blue spheres.

We solved the structures of these four mutants by X-ray crystallography at 2.6-3.3 Å resolution. All four mutants display a common locally-closed conformation of the protein characterised by: i) an overall conformation very similar to the open form, with nearly identical conformations of the ECD, M1, M3 and M4 helices, ii) a locally-closed pore. The open to locally-closed conformational reorganisation involves an iris-like, symmetrical closure of the pore, where each M2 helix is bent and its upper part is tilted by 17° (**Figure 16**). In this process, the upper part of M2 detaches from M3 to interact with each other in a tightly packed bundle of five short helices that obstructs the pore. As a control, we checked that the X-ray structures of every mutant reduced

#### References

- [1] N. Bocquet *et al*, *Nature* **445**, 116-119 (2007).
- [2] N. Bocquet *et al*, *Nature* **457**, 111-114 (2009).

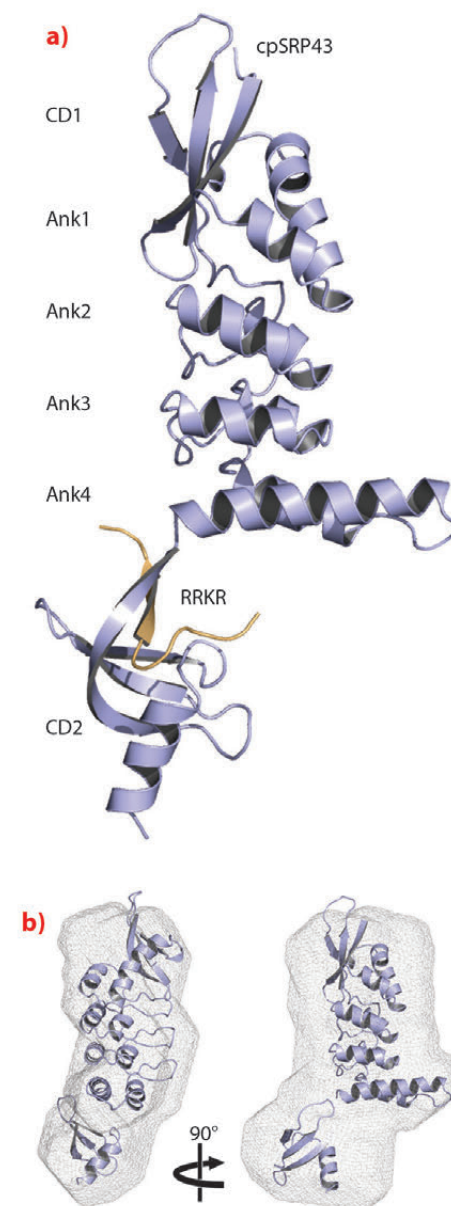
## Chromodomains in the chloroplast signal recognition particle read a twin-arginine motif

Chromodomain (CD) containing proteins play important roles in the regulation of gene expression and chromatin remodelling. CDs typically recruit protein complexes to chromatin and read the epigenetic ‘histone code’ by recognising lysine methylation in histone tails. While these canonical CDs all localise to the nucleus, a few are found as cytosolic proteins. The chloroplast signal recognition particle protein 43 (cpSRP43) represents the only known example of CDs implicated in protein targeting.

The signal recognition particle (SRP) is a universally conserved protein-RNA complex that mediates the co-translational targeting of secretory and membrane proteins. Its counterpart in chloroplasts lacks the SRP RNA and is responsible for the post-translational transport of light-harvesting antenna proteins (LHCPs) to the thylakoids [1]. The cpSRP43 protein is a unique addition to the chloroplast SRP (cpSRP) system. It forms a stable complex with cpSRP54 in the stroma and serves as a chaperone for its membrane protein substrate LHCP. Together, these three proteins form the soluble ‘transit complex’ which allows delivery of LHCPs to the thylakoid membrane and subsequent insertion.

cpSRP43 consists of three chromodomains and four ankyrin repeats [2]. The second chromodomain (CD2) of cpSRP43 binds to the C-terminal tail of cpSRP54, which comprises a conserved arginine-rich motif (RRKR motif). We determined the crystal structure of cpSRP43 from *Arabidopsis thaliana* in complex with a peptide including the RRRK motif at a resolution of 3.2 Å with data collected remotely at beamline ID14-2 (Figure 17). The structure of the complex in solution was studied by NMR spectroscopy and by small-angle X-ray scattering (SAXS), the latter performed at the BioSAXS beamline ID14-3. CD2 adopts the typical chromodomain fold and the SAXS analysis confirms the overall domain arrangement and indicates flexibility concerning the position of CD2.

The cpSRP54 tail binds to CD2 via  $\beta$ -completion closing a five-stranded



$\beta$ -barrel. The pattern of  $\beta$ -completion is basically identical to the one observed in canonical, nuclear CDs when binding to histone tails. Methylated lysines in histone tails are accommodated within an aromatic cage formed by three aromatic residues (Figure 18). Cation- $\pi$  stacking interactions between the positively charged lysine and the electron-rich aromatic ring systems decode the level of methylation (e.g. HP1 recognises the histone H3 tail containing trimethylated lysine 9). The corresponding cage in CD2 is modified and is formed by a single aromatic (Trp291) and two charged residues (Glu268 and Asp293). All three

### Principal publication and authors

I. Holdermann (a), N.H. Meyer (b,c), A. Round (d), K. Wild (a), M. Sattler (b,c) and I. Sinning (a), *Nature Structural and Molecular Biology* **19**, 260-263 (2012).

(a) Heidelberg University Biochemistry Center (BZH), Heidelberg (Germany)

(b) Institute of Structural Biology, Helmholtz Zentrum München, Neuherberg (Germany)

(c) Munich Center for Integrated Protein Science and Chair Biomolecular NMR, Technische Universität München, Garching (Germany)

(d) European Molecular Biology Laboratory, Grenoble (France)

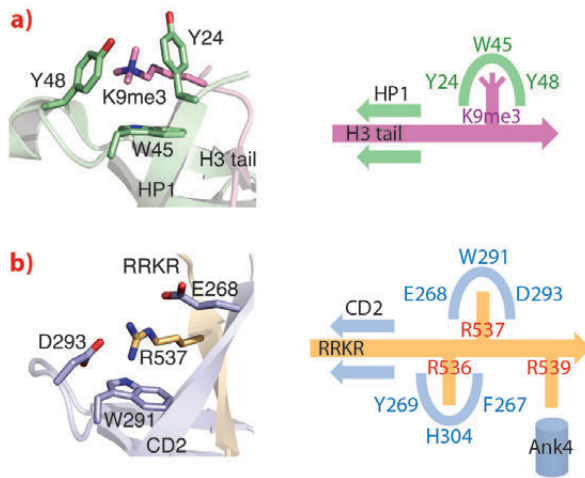
**Fig. 17:** Structure of cpSRP43 in complex with the cpSRP54 tail. a) Ribbon presentation of cpSRP43 (ankyrin repeats, Ank1 to 4; chromodomains, CD1 and CD2) and the RRRK peptide in orange. b) Structure of cpSRP43 in solution obtained using SAXS data. The rigid-body model from the crystal structure is superposed within the SAXS *ab initio* envelope.



### References

- [1] P. Grudnik, G. Bange and I. Sinning, *Biol Chem* **390**, 775-782 (2009).  
 [2] K.F. Stengel, I. Holdermann, P. Cain, C. Robinson, K. Wild and I. Sinning, *Science* **321**, 253-256 (2008).

residues are highly conserved and this adaptation of the cage reflects the change in the substrate, with the methylated lysine being replaced by a non-methylated arginine (Arg537). As a unique addition to CD interactions, an adjacent arginine (Arg536) is accommodated in a second aromatic cage formed by three aromatic residues (Phe267, His304 and Tyr269). Therefore, CD2 employs a “twinned cage” to read out a twin-arginine motif using two neighbouring arginines in the cpSRP54 tail. Replacing any of the conserved arginines abolishes complex formation and drastically reduces LHCP insertion.



The evolutionary origin of these non-nuclear CDs is not clear. The earliest occurrences of cpSRP43 in chlorophytes coincide with the appearance of chromovirus retrotransposons in plants. However, strong sequence dissimilarities do not allow for valid conclusions. The transition of chromodomains from reading the epigenetic ‘histone code’ to the recognition of arginines in protein targeting allows employing both chromodomains and the SRP system in a novel functional context. cpSRP43 adapts the universally conserved SRP system to a post-translational function and our structure of cpSRP43 in complex with the C-terminal tail of cpSRP54 demonstrates how the spectrum of chromodomain interactions can be extended.

**Fig. 18:** Substrate recognition by chromodomains. a) An aromatic cage in classical CDs decodes lysine methylation (HP1 with H3K9me3). b) A modified cage in cpSRP43 CD2 reads the second arginine in the RRKR motif (R537). The scheme visualises the twin-arginine motif in the cpSRP54 tail and its read-out by two cages in CD2.

### Principal publication and authors

V. Krenn (a), A. Wehenkel (a,b), X. Li (a), S. Santaguida (a) and A. Musacchio (a,b), *J Cell Biol.* **196**, 451-467 (2012).

(a) Department of Experimental Oncology, European Institute of Oncology, Milan (Italy)

(b) Department of Mechanistic Cell Biology, Max Planck Institute of Molecular Physiology, Dortmund (Germany)

## ■ Structural analysis reveals features of the spindle checkpoint kinase Bub1-kinetochore subunit Knl1 interaction

The spindle assembly checkpoint, or mitotic checkpoint, coordinates mitotic timing with chromosome-spindle interactions during mitosis, restricting mitotic exit to cells that have achieved bi-orientation of all their chromosomes [1]. Cells in which the checkpoint is artificially inactivated undergo precocious mitotic exit in the presence of unattached or incorrectly attached chromosomes. Alterations of checkpoint function might be relevant for tumour development, possibly by rendering cells more susceptible to the development of aneuploidies and to consequent genetic instability.

The Bub1 (budding uninhibited by benzimidazole 1) serine/threonine kinase

is a conserved component of the spindle assembly checkpoint. During mitosis, Bub1 localises to kinetochores, large scaffolds that bridge chromosomes to spindle microtubules to ensure faithful chromosome segregation. It is believed that kinetochore recruitment of Bub1, where the protein displays slow exchange dynamics that probably reflect its specific activities there, is essential for its function. In our studies, we decided therefore to investigate the mechanism of kinetochore recruitment of the Bub1 kinase.

Kinetochore recruitment of Bub1 has been proposed to rely on the interaction of the Bub1 tetratricopeptide repeats (TPR) with a short sequence motif of the outer kinetochore protein Knl1 known as



K11 [2,3]. To test this possibility formally, we reconstituted a construct of the TPR repeats of Bub1 with the K11 motif of Kn1 and crystallised it. X-ray diffraction data from a single crystal were collected at beamline **ID14-1** to a resolution of 2.6 Å in spacegroup P2<sub>1</sub>. Four independent monomers were placed in the asymmetric unit by molecular replacement using the model of the Bub1 TPRs from *S. cerevisiae* (PDB ID 3ESL) as a search probe [4].

The crystal structure revealed that the interaction of Bub1 with Kn1 develops along the convex surface of the TPR assembly (**Figure 19**). Alanine mutations at residues Phe75, Asn79, Gln84 and Phe85 of Bub1 led to complete disruption of the Bub1:K11 interaction *in vitro*. We generated stable inducible cells expressing EGFP-tagged wild type Bub1 and a mutant carrying the alanine mutations. Surprisingly, kinetochore recruitment of the Bub1(4A) mutant appeared to be largely normal. This observation confuted the hypothesis that the interaction of the TPR region of Bub1 with the K11 motif of Kn1 is important for kinetochore recruitment of Bub1.

Next, we sought to identify the minimal segment of Bub1 required for kinetochore recruitment. After showing that residues 190 and 284 of human Bub1 are sufficient for kinetochore recruitment, we refined our analysis by expressing additional constructs, including Bub1(209-270) and Bub1(227-270). The latter construct matched almost exactly the segment of budding yeast Bub1 that was previously co-crystallised with Bub3 [4], while the former is preceded by an 18-residue N-terminal extension of unknown function. While Bub1(209-270) localised robustly to kinetochores, Bub1(227-270) was unable to reach kinetochores (**Figure 20**). These results suggest that efficient kinetochore recruitment requires the Bub3 binding domain and a short N-terminal extension.

Our studies exploited the crystal structure of the Bub1-K11 complex to design a set of simple and insightful functional experiments that led us to question a previously proposed mechanism for kinetochore recruitment of Bub1. On the basis of these negative results, we went on to identify the precise determinants for Bub1 kinetochore recruitment [4].

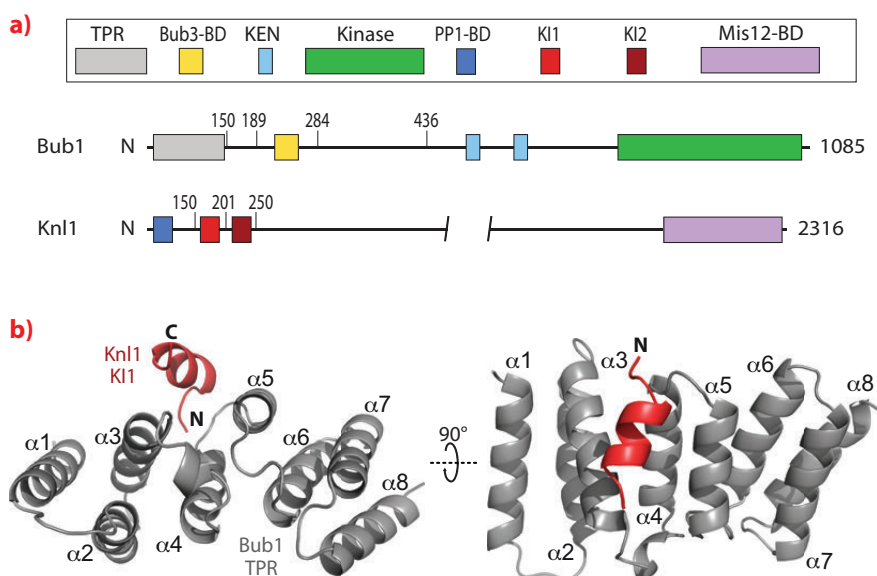


**Fig. 19:** a) Schematic representation of the domain structures of Bub1 and Kn1. b) Cartoon diagram of the TPR (grey):K11 (red) interaction. The K11 peptide binds the convex surface of the TPR helical array.

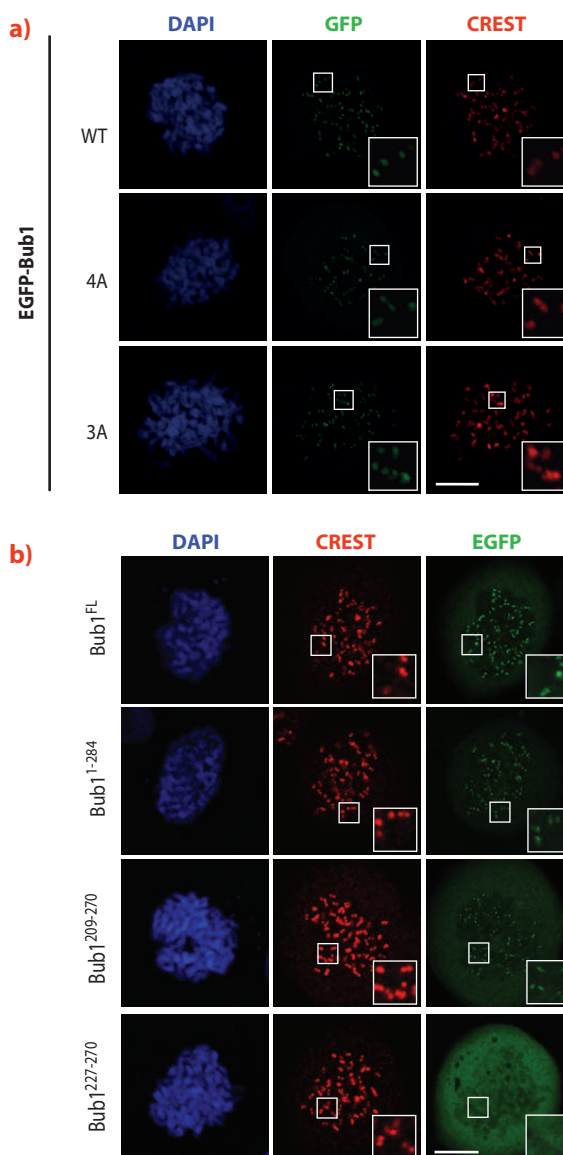


**Fig. 20:** a) Two combinations of multiple alanine point mutants of Bub1, indicated by 4A and 3A, leave kinetochore recruitment of Bub1 unaltered. CREST is a kinetochore marker. The inset shows enlarged kinetochores. b) Identification of a minimal kinetochore-binding segment of Bub1. Bub1(209-270) localised normally to kinetochores, whereas Bub1(227-270) failed to be recruited.

#### References

- [1] A. Musacchio and E.D. Salmon, *Nat Rev Mol Cell Biol* **8**, 379–393 (2007).
- [2] T. Kiyomitsu, C. Obuse and M. Yanagida, *Dev Cell* **13**, 663–676 (2007).
- [3] T. Kiyomitsu, H. Murakami & M. Yanagida, *Mol Cell Biol* **31**, 998–1011 (2011).
- [4] N.A. Larsen, J. Al-Bassam, R.R. Wei and S.C. Harrison, *Proc Natl Acad Sci USA* **104**, 1201–1206 (2007).



### Principal publication and authors

P. Szwedziak, Q. Wang,  
S.M. Freund and J. Löwe, *EMBO J*  
31, 2249-60 (2012).  
MRC Laboratory of Molecular  
Biology, Cambridge (UK)

## Bacterial cell division protein FtsA forms actin-like filaments

The divisome is the inner membrane protein complex performing bacterial cell division, leading to two daughter cells. It consists of more than a dozen proteins, with one component being FtsZ, the bacterial tubulin homologue forming the Z-ring [1,2]. In many bacteria, FtsZ is assisted by FtsA, which displays structural similarities to actin but shows an altered subdomain architecture when compared to actin, ParM or MreB [3]. FtsA contains an amphipathic helix for its attachment to the inner membrane and it has been shown that the two proteins, FtsA and FtsZ, interact directly [4]. Whether FtsA is able to polymerise, given its unusual actin-like fold, has been a long-standing question.

We employed a combination of biochemical and structural techniques, including X-ray crystallography at the ESRF. First, we set out to define the minimal portion of FtsZ that interacts with FtsA and reconstituted the FtsA:FtsZ:membrane system *in vitro*. By means of co-pelleting assays we demonstrated that the last 8-16 residues of *Thermotoga maritima* FtsZ (TmFtsZ) are necessary and sufficient to interact with *T. maritima* FtsA (TmFtsA) *in vitro*. We also confirmed that the C-terminal amphipathic helix of FtsA is required for membrane binding. We then co-crystallised full-length TmFtsA with the peptide corresponding to the last 16 residues of TmFtsZ. A high-resolution structure, solved from a dataset obtained at beamline ID29, revealed that the peptide bound within the 2B subdomain of TmFtsA between helices H6 and H8,

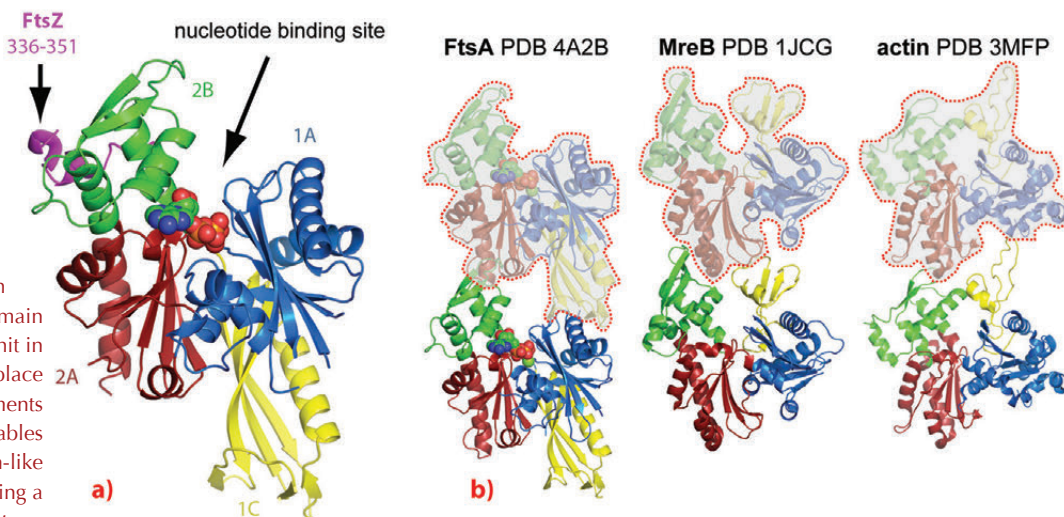
adopting a predominantly alpha-helical conformation (Figure 21a). The protein was present as a translational dimer in the asymmetric unit and when co-crystallised with ATP $\gamma$ S, TmFtsA produced new crystals containing continuous protofilaments that closely resemble the dimer.

Importantly, these filaments are related in their architecture and subunit arrangement to all known actin-like protofilaments, including actin itself, ParM and MreB (Figure 21b). In order to investigate FtsA's polymerising abilities biochemically, we took advantage of FtsA's membrane affinity and utilised an electron microscopy monolayer assay. This revealed filaments several hundred nanometres in length, often present as doublets. Occasionally we could observe two-dimensional sheets. Computational Fourier transformation of the images of the sheets provided us with a longitudinal spacing of around 48 Å, which matches the spacing found in the crystals.

To investigate FtsA polymerisation in a broader range of bacterial species we turned to electron cryotomography and structured illumination fluorescence microscopy (SIM) and over-expressed FtsA from *Thermotoga*, *Escherichia coli* and *Bacillus subtilis* in *E. coli* cells. This confirmed our previous *in vitro* studies and we were able to visualise FtsA filaments in cells. Interestingly, full-length TmFtsA bound to the inner surface of the cytoplasmic membrane through its C-terminal amphipathic helix thereby distorting the membrane and forming

**Fig. 21:** a) the FtsZ peptide (purple) is bound to the surface of subdomain 2B (green) of FtsA. b) FtsA, MreB

and actin filaments with the protofilament axis vertical. The three proteins adopt a similar subdomain architecture, however, the 1B subdomain of MreB and actin (yellow) is missing in FtsA and instead subdomain 1C in FtsA is located on the other side of the molecule. When forming filaments, FtsA's subdomain 1C of the preceding subunit in the protofilament takes the place of subdomain 1B in the filaments of actin and MreB. This enables FtsA to form canonical actin-like protofilaments, despite having a different domain architecture.





lipid structures, coated with FtsA protein filaments. Finally, we investigated whether FtsA polymers are of biological significance *in vivo*. For this, we first rationally designed polymerisation-deficient mutants based on our high-resolution crystal structure of the polymer. Then we confirmed lack of polymerisation by means of SIM and performed a complementation assay in a *B. subtilis* FtsA temperature sensitive (ts) background, in which the ts-FtsA protein is unable to support cell division at elevated temperatures and this endogenous tsFtsA is complemented with a series of mutant versions of FtsA, polymerising and non-

polymerising. We were able to observe that the polymerisation-deficient mutants did not rescue the wild-type phenotype and cells were elongated and filamentous. We therefore concluded that FtsA polymerisation has an important role in bacterial cell division.

In this work, we showed that FtsA appears to be a domain-swap of the canonical actin fold that is capable of forming protofilaments because the swapped 1C domain appears in the correct place in the protofilament, shifted by one subunit (**Figure 21b**).

#### References

- [1] D.W. Adams and J. Errington, *Nat Rev Microbiol* **7**, 642 (2009).
- [2] J. Löwe and L.A. Amos, *Nature* **391**, 203 (1998).
- [3] F. van den Ent and J. Löwe, *EMBO J* **19**, 5300 (2000).
- [4] S. Pichoff and J. Lutkenhaus, *Mol Microbiol* **64**, 1129 (2007).

## ■ An unexpected role in coffee beans for a protein normally associated with lignin biosynthesis

Functional food research is a new scientific discipline that focuses on using food for both sustenance and as a delivery vehicle for bioactive molecules. Coffee is an example of such a functional food as it can be used both as a drink and to deliver the well-known bioactive molecule caffeine. However, coffee also contains other less well-known bioactive molecules, including the chlorogenic acids (CGAs). The CGAs are a group of soluble secondary metabolite esters that have been implicated in biotic and abiotic stress responses in plants, while the related shikimate esters are key intermediates for lignin biosynthesis. One or more CGAs are found in important food species such as potatoes, tomatoes, apples and pears, with a particularly high level of 5-caffeoylquinic (5-CQA) and 3,5-O-dicaffeoylquinic acid (3,5-diCQA) found in coffee beans (**Figure 22**). In addition to their role as secondary metabolites in plants, there is growing evidence that the CGAs can act as dietary antioxidants and that their consumption can have beneficial effects for human health. So, enjoying your morning cup of coffee not only invigorates your mind but could also be beneficial for your overall health.

The CGA and shikimate esters are synthesised via the phenylpropanoid pathway and the last step is catalysed by the hydroxycinnamoyl-CoA shikimate/quinic hydroxycinnamoyl-transferases

(HCT/HQT). HCT and HQT can reversibly shuttle hydroxycinnamoyl units between their CoA- and shikimate/quinic-esterified forms, but have a preference for shikimate and quinic respectively. HCT and HQT belong to the plant specific BAHD acyltransferase family. Despite their generally low sequence identity, these enzymes possess a sequence conserved catalytic HXXXD motif and can be further phylogenetically distributed into eight distinct clades. While some structural information was available for several BAHD family members, no structural information was available for the clade containing HCT/HQT. Members of this large family are involved in the biosynthesis of a large array of secondary metabolites, including a number of important therapeutic drugs. In an effort to understand the remarkable substrate diversity of the BAHD superfamily, we performed structural, biochemical and mutagenesis studies of HCT and HQT from *Coffea canephora* (robusta) in collaboration with groups at Nestlé R&D in Tours, France and Washington University in St. Louis Missouri, USA.

Native crystals of HCT appeared only once in initial crystal trials and access to the microfocus capability of beamline **ID23-2** were crucial to successful data collection from very thin plates. We then designed a more proteolytically stable variant of HCT that readily crystallised. We subsequently

#### Principal publication and authors

- L.A. Lallemand (a), C. Zubieta (a), S.G. Lee (b), Y. Wang (c), S. Acajjaoui (a), J. Timmins (a), S. McSweeney (a), J.M. Jez (b), J.G. McCarthy (d) and A.A. McCarthy (e), *Plant Physiology* **160**, 249–260 (2012).
- (a) ESRF  
(b) Department of Biology, Washington University, St. Louis (USA)  
(c) Donald Danforth Plant Science Center, St. Louis (USA)  
(d) Nestlé Research and Development, Notre-Dame d’Oé, Tours (France)  
(e) UVHCI, UJF-EMBL-CNRS, Unité Mixte Internationale 3265 and EMBL, Grenoble (France)



solved several structures of HCT from different conditions using data collected at beamline **ID14-4**. A comparison of these different structures revealed a remarkably plasticity in and around the active site. Unfortunately, we were never able to obtain a structure of HQT or a substrate bound HCT structure. Nevertheless, using ligand docking algorithms, structural and sequence comparisons, as well as the

molecular modelling of HQT we were able to identify putative residues important in substrate recognition (**Figure 22**). Several of these were mutated and characterised biochemically to validate the docking results. In particular, Leu400 and Phe402, of which the side chains were predicted to be important for shikimate binding in HCT, were mutated to the Thr and Tyr residues found in HQT, and resulted in a shift of the substrate preference to quinate, as expected. We also unexpectedly showed for the first time that, *in vitro*, HCT is capable of synthesising the 3,5-*O*-diCQA. This novel activity is consistent with our ligand docking experiments and helps explain why green coffee beans contain such a large quantity of diCQAs. During our mutagenesis studies we also identified a new HCT mutant, His-153-Asn, designed to mimic the catalytic loop of HQT, which resulted in a significantly increased 3,5-diCQA production (**Figure 22**).

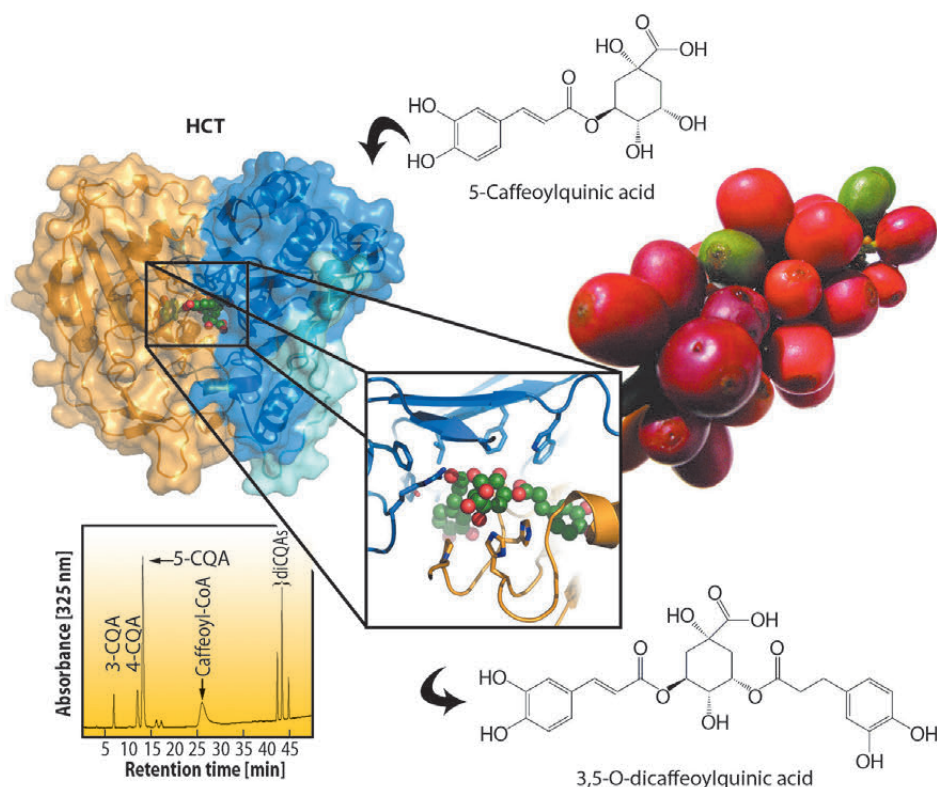


**Fig. 22:** Coffee beans contain large quantities of beneficial compounds such as 5-CQA and 3,5-diCQA that are predominantly synthesised by HQT and HCT respectively. The lower left panel shows a chromatogram illustrating the synthesis of 3,5-diCQA catalysed by a HCT mutant. The central inset shows the best docking result of 3,5-diCQA in HCT.

These results provide the first structural characterisation of a hydroxycinnamoyl transferase from the BAHD family and in conjunction with our docking, biochemical and mutagenesis studies reveal the molecular level determinants for the substrate specificity of this important family of proteins. This work has potential applications in altering the level of the beneficial CGAs and diCGAs compounds in other food plant species or in the generation of novel target compounds. As HCT is central to the biosynthesis of complex lignins, our results could also be used to modulate the substrate specificity of HCT and form the basis for new research directions in the area of biofuel production from non-food plant biomass.

#### Principal publication and authors

A. Palencia (a), T. Crépin (a), M.T. Vu (b), T.L. Lincecum (b), S.A. Martinis (b) and S. Cusack (a), *Nat Struct Mol Biol.* **19**, 677-84 (2012).

(a) European Molecular Biology Laboratory (EMBL), Grenoble Outstation and Unit of Virus Host-Cell Interactions, University of Grenoble-EMBL-Centre National de la Recherche Scientifique, Grenoble (France)  
(b) Department of Biochemistry, University of Illinois, Roger Adams Laboratory, Urbana (USA)

## Structural dynamics of the aminoacylation and proof-reading functional cycle of bacterial leucyl-tRNA synthetase

The aminoacyl-tRNA synthetases are responsible for attaching a particular amino acid to its cognate transfer-RNA. The accuracy of this reaction is essential to the fidelity of protein synthesis and thus for cell survival. However, distinguishing structurally related amino

acids with sufficient accuracy presents a fundamental challenge for the molecular recognition of the aminoacylation active site. To overcome this problem, at least six different aminoacyl-tRNA synthetases, for example LeuRS, IleRS and ValRS, have developed highly evolved, proof-reading



and editing mechanisms, which reduce the error rate to better than 1 in 3000. For example, LeuRS possesses a robust editing mechanism to hydrolytically deacylate tRNA<sup>Leu</sup> that has been mischarged with non-cognate amino acids such as isoleucine or methionine. LeuRS, a ~100 kDa protein, comprises a synthetic enzyme body including the Rossmann-fold catalytic domain, which activates the amino acid with ATP and then ligates it to the tRNA 3' end, and the anticodon binding domain. In addition, there are four flexibly linked domains, denoted zinc (ZN1), editing, leucine-specific (LS) and C-terminal (Figure 23a). Proof-reading requires that the tRNA 3' end, initially charged (or mischarged) in the synthetic site, translocates to the editing site, located ~35 Å away in the independently folded editing domain. Although the LeuRS complex with the tRNA bound in the editing site ('editing state') has been previously reported, structural information about the aminoacylation state and how the tRNA translocates between the two sites, and about the roles of each of the externally linked domains, was lacking.

Making extensive use of the ERSF high intensity beamlines, we have now determined the crystal structure of the functional aminoacylation complex of *E. coli* LeuRS (LeuRSEC) at 2.5 Å resolution. In this ternary complex, the 3' end of *E. coli* tRNA<sup>Leu</sup> is bound in the synthetic site and poised to interact with leucyl-adenylate (present as a non-hydrolysable analogue), the intermediate aminoacylation reaction (Figure 23b). To complement this, we have also determined the crystal structure of the same system at 2.1 Å resolution but with the tRNA 3' end bound in the editing site (Figure 23c). Comparison of the two structures reveals substantial domain and active site rearrangements that accompany tRNA translocation between the two functional conformations (Figure 24; also see the movie: <http://www.cgl.ucsf.edu/chimera/animations/tRNA/leucyl-tRNA.mov>). A hypothesis for the mechanism of translocation is as follows. We suppose that the aminoacylation state is a high energy state, under strain due to the unusual conformation of the 3' end of the tRNA, the distorted state of the adenylate and the fully closed conformation of the catalytic 'KMSKS' loop (Figure 24a). Formation of this state is possible due

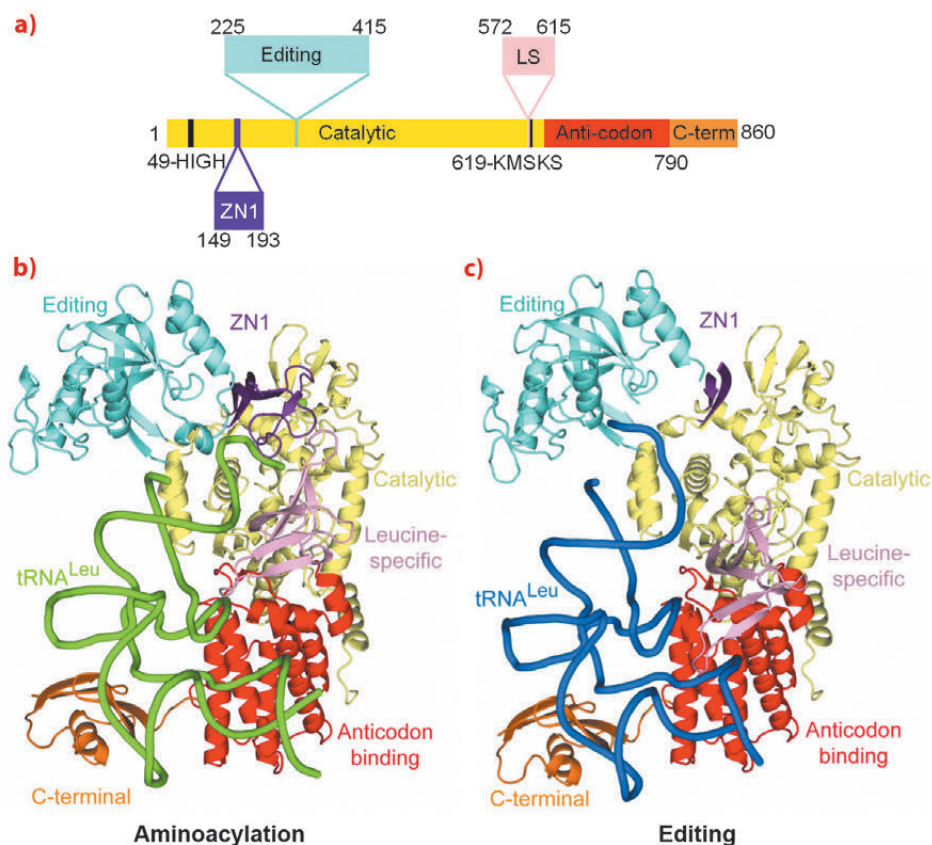


**Fig. 23:** a) The domain structure of LeuRSEC. The colour code for the various domains is: catalytic (yellow), ZN1 (purple), editing (cyan), leucine-specific (pink), anticodon-binding (red) and C-terminal (orange). The catalytic motifs HIGH and KMSKS are represented in black. b) Aminoacylation conformation with the tRNA in green and the zinc ion represented as a sphere. c) Editing conformation with the tRNA in blue. In this state, ZN1 is partially disordered.

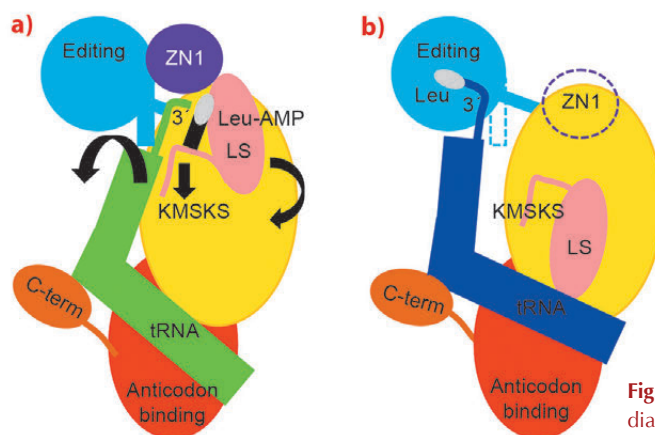


**Fig. 24:** Schematic diagram of the structural changes between the aminoacylation (a) and proof-reading (b) conformations of the LeuRSEC-tRNA<sup>Leu</sup> complex. Colour code as in Figure 23 (dotted regions are disordered in the crystal structure). Leucine is represented as a white oval and AMP as a black rectangle. The black arrows in (a) indicate direction of movement during translocation to the editing state.

to a high binding energy of the tRNA 3' end as a result of its numerous contacts to various domains of the enzyme, including the editing domain. Once the covalent integrity of the adenylate is broken by transfer of the amino acid moiety to the tRNA, the strain is released by relaxation of the KMSKS loop into its open conformation, dissociation of AMP and the flip of the leucine-specific domain (Figure 24b). Concomitantly,



the KMSKS loop, the ZN1 and editing domain lose their interactions with the tRNA, destabilising the binding of the acceptor end of the now charged tRNA. This allows the tRNA 3' end to flip to its preferred low energy conformation in the editing active site (**Figure 24b**). Globally, the editing domain slightly rotates as the tRNA pivots around its fixed contact points on the anti-codon binding domain and the C-terminal domain moves synchronously, maintaining its contacts to the tRNA. In this conformation the tRNA has far

fewer contacts and is already partially disassociated from the catalytic domain. This favours total tRNA release in the case of correctly charged Leu-tRNA<sup>Leu</sup> or possibly direct re-aminoacylation, without full release, of hydrolysed and recycled, mischarged tRNA.

Our results provide new insight into the dynamic mechanism of aminoacylation and proof-reading in LeuRS, a molecular machine essential for accurate protein synthesis.

#### Principal publication and authors

M.J. Wheeler (a), S. Russi (a,b), M.G. Bowler (c) and M.W. Bowler (a,b), *Acta Cryst.* **F68**, 111-114 (2012).

(a) ESRF

(b) EMBL, Grenoble (France)

(c) Department of Physics, University of Oxford (UK)

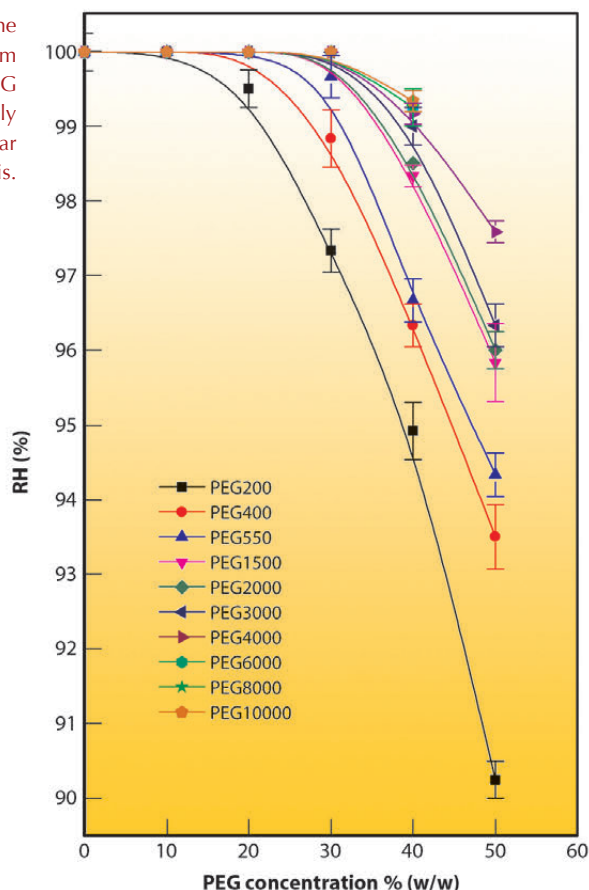
## Predicting relative humidity equilibria for dehydration experiments

The diffraction quality of crystals of macromolecules can be improved by controlled dehydration. A number of methods exist to change the relative humidity that surrounds crystals, but for reproducible results, with complete characterisation of the changes induced, a precise humidity control device coupled with an X-ray source is required. The EMBL Grenoble has developed a

humidity control device, the HC1, now available on the ESRF MX beamlines [1,2]. Using this device, many systems have shown significant improvements in their diffraction quality. The first step of a dehydration experiment is to determine the relative humidity (RH) in equilibrium with the mother liquor of the crystal being studied. If the RH to which the crystal is exposed is too high it will dissolve and if too low, changes may be induced in the crystal. Until now, the equilibrium RH has been found experimentally by placing a drop of the mother liquor in a loop and monitoring the size of the drop using specific image processing software. This stage of the experiment can be quite time consuming as an initial starting point is often unknown. In order to simplify this process, we have measured the equilibrium RH for a range of concentrations of the most commonly used precipitants (salts and polymers such as polyethylene glycol – PEG). The data provide a starting point for most dehydration experiments and Raoult's Law for the equilibrium vapour pressure of water above a solution [3] can be used to understand the observations and make predictions for precipitant concentrations commonly in use.

We found that increasing the molecular weight of the PEG (for a given w/w concentration) increased the RH in equilibrium with the solution and observed a steep increase in RH equilibrium point with decreasing PEG concentration (**Figure 25**). Measurements were also

**Fig. 25:** Plot showing the measured equilibrium relative humidity for PEG concentrations commonly used in macromolecular crystallogensis.





made of typical buffer solutions (100 mM) and detergents (1% (w/v)) and these were found to have an RH equilibrium point of 100%; therefore, only the main precipitant affects the RH equilibrium point. Using Raoult's Law, the equilibrium relative humidity can be predicted for many of the precipitants used in macromolecular crystallogensis. Raoult's Law has two aspects that are counter intuitive and lead to some surprising observations. The first is that the number of equivalent molecules in solution must be accounted for. This means that for sodium chloride, each ion in solution counts as a molecular equivalent. The second is that it is the number of species, and not the nature of the species, in solution that affects the equilibrium vapour pressure. This means that one molecule of PEG 200 has the same contribution as, for example, a sodium ion. Raoult's law starts to break down for PEG solutions over a molecular weight of 1000 Da, but this can be corrected using the Flory-Huggins model for the entropy of mixing of polymers as shown in **Equation 1**. In this equation, RH represents relative humidity,  $x$  is the mass fraction of solute and  $n$  is the molecular weight of the polymer (as in PEG  $n$ ). The parameter  $m$  comes from the Flory-Huggins model for

$$RH = \frac{1}{1 + \frac{18x}{(1-x)m}} e^{\{(1-m/n) / (1 + \frac{(1-x)m}{18x})\}} \quad \text{Eq. 1}$$

the entropy of mixing of polymers. This is such that the ratio  $n/m$  is the number of polymer segments, each of which takes up one space in the disordered lattice. For  $n \gg m$  the dependence on  $n$  diminishes – therefore, the RH equilibria for all PEGs of >1000 Da will be equal. For the precipitants most often used in crystal growth experiments (typically 10-30% PEG (w/w)), the equilibrium point will be around 99.5%.

An online RH calculator is available, based on the equations derived from this work, to allow users to predict RH starting points in advance of experiments [4] and has made these experiments much faster as well as being useful for vapour diffusion crystallisation experiments. Determining the starting point for these experiments is the first step in automation. A new workflow interface [5] for these experiments, through the beamline GUI MXCuBE, coupled to on-line data analysis, is also available and should increase the use of the device and the number of successful cases.

#### References

- [1] J. Sanchez-Weatherby *et al.*, *Acta Cryst.* **D65**, 1237-1246 (2009).
- [2] S. Russi *et al.*, *J. Struct. Biol.* **175**, 236-243 (2011).
- [3] F.-M. Raoult, *C. R. Acad. Sci. Paris*, **104**, 1430-1433 (1887).
- [4] <http://go.esrf.eu/RH>
- [5] S. Brockhauser *et al.*, *Acta Cryst.* **D68**, 975-984 (2012).

## ■ The application of hierarchical cluster analysis to the selection of isomorphous crystals

The amount of diffraction data that can be obtained from a single crystal of a biological macromolecule is limited by radiation damage, due to a resolution-dependent reduction in diffraction intensity. This limitation cannot be overcome. We can optimise the conditions of measurements [1] but there is an absolute limit of resolution and data quality that can be obtained from a single crystal. Furthermore, less data can be obtained from a small crystal before significant radiation damage occurs because the diffracting volume is lower. In cases where several crystals of the same type are available, the result of a crystallography study can be substantially improved by using a multicrystal data collection strategy. However, this effect is only valid if the subdata sets used are from crystals that are structurally identical.

Unfortunately, it has been observed that frozen single crystals of the same biological macromolecule often have relatively low structure identity (and are therefore not isomorphous), thus, to obtain a real gain from multicrystal data sets, we need to be able to make an appropriate selection of isomorphous crystals.

In this study, we evaluated the possibility of using hierarchical cluster analysis as a tool for the identification of isomorphous data sets. About hundred multicrystal data sets were collected with the goal of solving the structures of four test proteins using the weak anomalous signal from sulphur atoms. The results of the hierarchical cluster analysis (based on the intensity correlation coefficients for complete data sets) are shown in **Figure 26**. The data sets constituting the principal clusters were

#### Principal publication and authors

R. Giordano (a,b), R.M.F. Leal (a,c), G.P. Bourenkov (d), S. McSweeney (a) and A.N. Popov (a), *Acta Cryst.* **D68**, 649-658 (2012).  
(a) ESRF  
(b) Present address: SLS, PSI, Villigen (Switzerland)  
(c) Present address: ILL, Grenoble (France)  
(d) EMBL Hamburg Outstation, c/o DESY, Hamburg (Germany)



**Fig. 26:** Hierarchical cluster analysis dendrograms. a) Bovine Zn-free insulin (INS), b) thaumatin (THA), c) bovine pancreatic trypsin (TRY), d) chorismate synthase (AroF) from *Mycobacterium tuberculosis* multicrystal data sets.

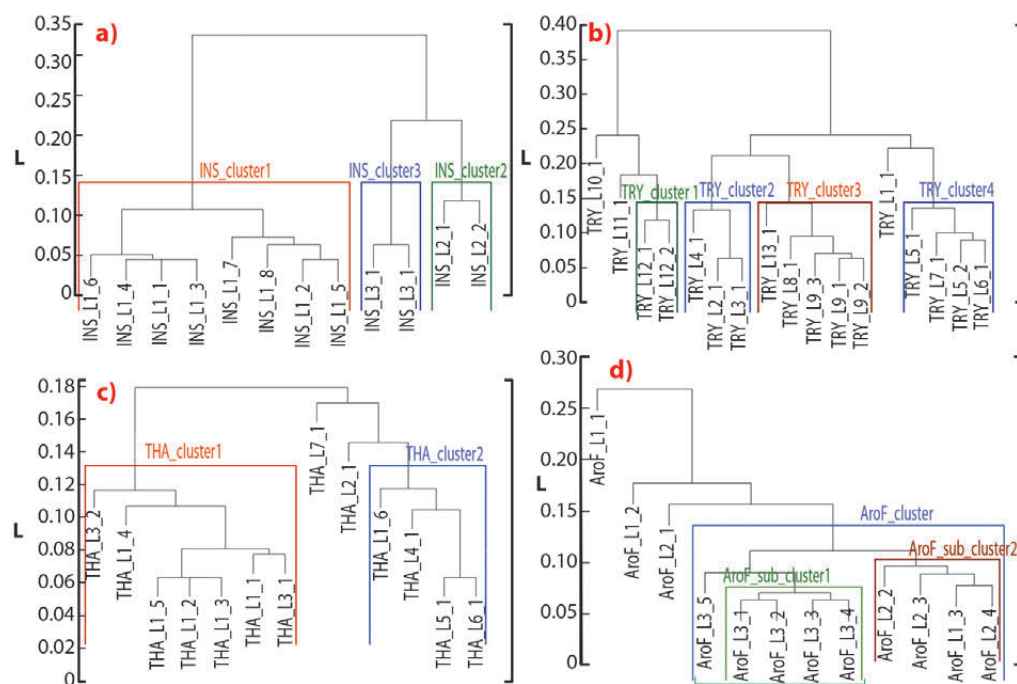
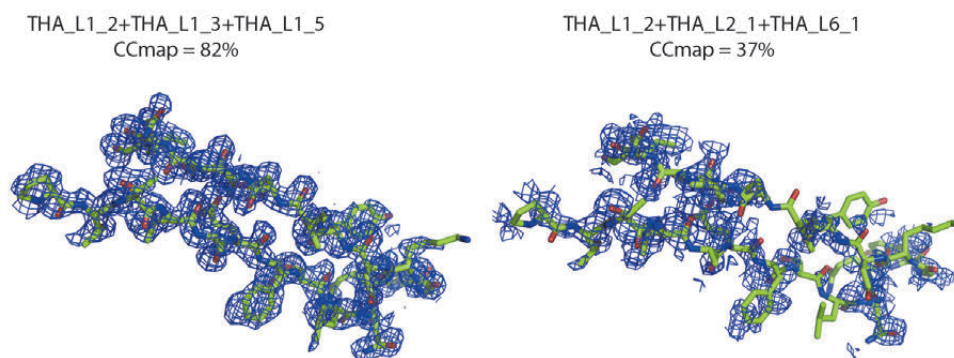


**Fig. 27:** Experimentally phased electron density maps for thaumatin obtained using combined data sets. a) A very high quality map was obtained by merging data sets from the principal cluster shown in **Figure 26c**. In contrast, the map resulting from merging data sets selected arbitrarily is uninterpretable.



merged together and analysed. The results clearly show improvement in the quality of multicrystal anomalous difference data sets created on the basis of cluster analysis as compared to blindly merging all data sets. As an illustration of the impact, **Figure 27** represents electron-density maps for thaumatin.

Our study demonstrates the importance of hierarchical cluster analysis in understanding non-isomorphism of single crystals of biological macromolecules, in particular hierarchical cluster analysis can help in the selection of sets of isomorphous crystals. The results of this study illustrate that for SAD data collection where the anomalous signal is small (~1%) it is of great importance to use a protocol that helps to appropriately merge data sets from different crystals. In difficult cases, this method could permit structure solution when individual data sets are insufficient.

This research shows that the combination of multi-crystal data collection techniques with advanced statistical data analysis methods has a clear potential to expand the applicability of sulphur-SAD phasing techniques towards more complex structures. The methodology could be further extended to aid other applications such as heavy-atom derivative phasing or, possibly, resolution enhancement for poorly ordered systems. The development of automated and reproducible sample handling techniques providing better control over the sample state throughout the experiment is likely to become another important component of multicrystal data collection methods.

#### References

- [1] G.P. Bourenkov and A.N. Popov, *Acta Cryst. D66*, 409-419. (2010).



## Cisplatin treatment as a route to remove SOD1 aggregates in ALS

Protein aggregates are found in the neurons of patients with several fatal, incurable neurodegenerative conditions, including amyotrophic lateral sclerosis (ALS). In ALS patients, superoxide dismutase (SOD1) aggregates, found in the cytoplasm and in mitochondria, have been repeatedly proposed as a major cause of motoneuron degeneration [1]. Although the exact mechanism of cytotoxicity is still debated, these aggregates contribute to the pathogenesis and their removal is thought to be a promising target for new therapeutic approaches.

It was previously shown that these aggregates are the result of the disulphide bond formation between SOD1 molecules involving the two free cysteines that are normally reduced in native conditions [2, 3]. In the present work, we show that cisplatin (cisPt), a drug commonly employed in cancer treatment, is able to solubilise aggregates of SOD1 present in cell lines which overexpress ALS-related SOD1 mutants. Furthermore we have shown that cisPt inhibits the oligomerisation of human SOD1 by forming an adduct with the apo- form of the enzyme (Figure 28). The structural basis for this behaviour has been elucidated both through X-ray crystallography and X-ray absorption spectroscopy (EXAFS); in particular we have shown that a Pt(II) ion of the cisPt moiety binds the sulphur atom of the free Cys111 residue of each subunit of SOD1, thus preventing the Cys111-dependent trans oligomerisation occurring (Figure 29). The dissociation constant of this binding is  $37 \pm 3 \mu\text{M}$ . CisPt is also able to bind the metalated forms  $\text{Cu}_2\text{-Zn}_2$  and  $\text{Zn}_2\text{-Zn}_2$  of hSOD1.

The structural studies have rationalised the mode of action of cisPt against SOD1 oligomerisation *in vitro*. On one hand, the binding of cisPt to the solvent exposed Cys111 in SOD1 sequesters this site and prevents the formation of intermolecular disulphide bonds. On the other, the high affinity binding of cisPt to the cysteine sulphur drives the break and reduction of the intermolecular disulphide bonds in already formed oligomers, thus dissolving the aggregates. Therefore cisPt is able not only to block but also to reverse the formation of the SOD1 aggregates through selective target of Cys111, without affecting the normal functional pathway of SOD1 maturation and enzymatic activity. The present findings can contribute to the background knowledge for designing lead compounds capable of preventing SOD1 aggregation and can contribute to the development of treatments for ALS.

### Principal publication and authors

L. Banci (a,b,c), I. Bertini (a,b), O. Blažević (a), V. Calderone (a,b), F. Cantini (a,b), J. Mao (a), M. Vieru (a,c), I. Amori (d), M. Cozzolino (d) and M.T. Carrì (d,e), *J Am Chem Soc.* **134**, 7009-7014 (2012).  
(a) Magnetic Resonance Center CERM, University of Florence (Italy)  
(b) Department of Chemistry, University of Florence (Italy)  
(c) Fondazione Fiorgen, Florence (Italy)  
(d) Fondazione Santa Lucia, IRCCS, Rome (Italy)  
(e) Department of Biology, University of Rome "Tor Vergata" (Italy)

### References

- [1] M. Cozzolino, M.G. Pesaresi, I. Amori, C. Crosio, A. Ferri, M. Nencini and M.T. Carrì, *Antioxid Redox Signal.* **11**, 1547-58 (2009).  
[2] L. Banci, I. Bertini, M. Boca, V. Calderone, F. Cantini, S. Giroto, M. Vieru, *Proc. Natl. Acad. Sci. USA* **106**, 6980-5 (2009).  
[3] L. Banci, I. Bertini, M. Boca, S. Giroto, M. Martinelli, J.S. Valentine, M. Vieru, *PLoS One* **3**, e1677 (2008).

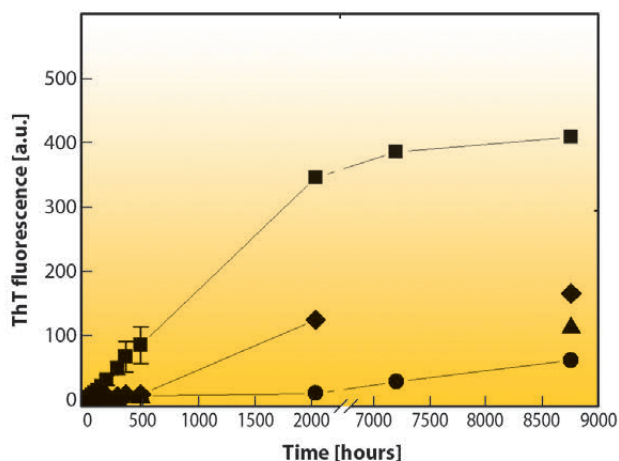


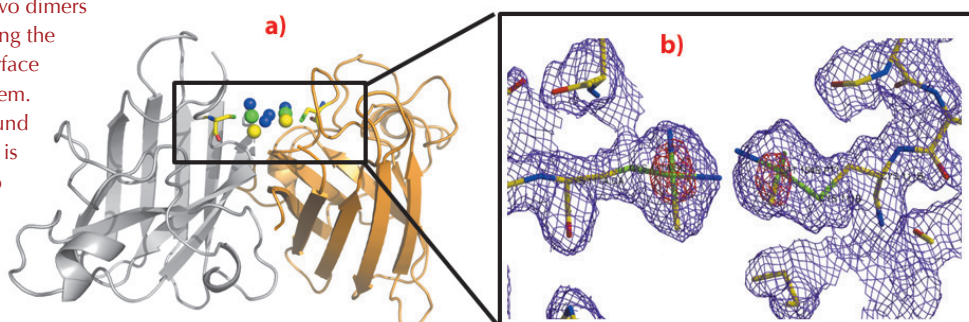
**Fig. 28:** Inhibition of formation of apo SOD1 high molecular weight oligomers by cisplatin monitored by ThT fluorescence measurements over 9000 hours. ThT fluorescence for 0.1 mM apo hSOD1 (■); 0.1 mM apo hSOD1 and 0.8 mM cisplatin (●); 0.1 mM apo hSOD1 and 0.4 mM cisplatin (▲); 0.1 mM apo hSOD1 and 0.2 mM cisplatin (◆). Adapted with permission from *J. Am. Chem. Soc.* **134**, 7009-7014. Copyright (2012) American Chemical Society.

**Fig. 29:** Crystal structure of cisplatin-bound apo hSOD1.

a) ribbon representation of one of the two dimers present in the asymmetric unit highlighting the two Cys111 facing each other at the interface and cisplatin bound to each of them.

b) insert showing the two Cys111 bound to cisplatin and their electron density. It is evident the lack of the space to host two cisplatin moieties at the same time. (N – blue; Pt – green; Cl – yellow).

Adapted with permission from *J. Am. Chem. Soc.* **134**, 7009-7014. Copyright (2012) American Chemical Society.





# Dynamics and Extreme Conditions

This year's Highlights contributions cover the fields of earth and planetary science, functional materials, and water and biological systems. As in previous years, the combination of different experimental techniques and/or theoretical simulations is an important ingredient. This is exemplified by the study of volcanic hotspots (X-ray diffraction and X-ray fluorescence), diluted magnetic semiconductors (EXAFS, hard X-ray photoemission spectroscopy, X-ray emission spectroscopy, and density functional theory (DFT)),  $\text{PbZr}_{1-x}\text{Ti}_x\text{O}_3$  (inelastic X-ray and diffuse scattering), and supramolecular Pt-tpy complexes (resonant X-ray emission spectroscopy and DFT). The X-ray diffraction studies of silicate perovskite and dolomite to 80 GPa witness the impressive progress in single crystal structure determination at very high pressures. The real-time observation of nanocrystalline growth and the ability to distinguish bulk and surface contributions illustrates the capabilities of nuclear resonance techniques. The temperature-dependent study of the oxygen K-edge in liquid water further fuels the controversial discussion on the number of hydrogen bonds in water, and gives a flavour of the kind of experiments which can be performed on the X-ray Raman spectrometer at ID20.

As in previous years, besides supporting a cutting edge scientific programme, substantial effort went into new instrumental and methodological developments. Many of these have been undertaken in close collaboration with groups of the Instrumentation Services and Development Division. To mention only a few of them: establishment of silicon crystal processing techniques to achieve close to theoretical performance of (high-energy resolution) crystal monochromators, a resistively heated diamond anvil cell for temperatures up to 1200 K, a new low-temperature ( $T = 5 - 300$  K) high-pressure cryostat, and the implementation of a new Perkin-Elmer 2D detector for ID27.

The large volume press (LVP) was opened for public user access in September 2012, and first user experiments were successfully conducted. At present, the available beam time for peer-reviewed experiments with the LVP is 30% of the standard allocation time for an ESRF beamline,

but it is planned to increase this amount to 50% in the near future.

The Upgrade Programme Beamline Project UPBL06 - Inelastic X-ray Scattering - located at ID20 has made excellent progress. The radiation tests of the lead hutches have been completed and all the main optical elements have been installed. The two spectrometers, for resonant IXS and X-ray Raman scattering, are in place and commissioning of the various beamline components is on-going. The current planning foresees the first user experiments in June 2013.

ID28 was reviewed in the autumn 2012 and received very positive feedback. The panel made several pertinent suggestions which are being taken into account by the beamline staff.

Finally, discussions started on the perspectives offered by a new storage ring with a largely reduced horizontal emittance. For the high-pressure beamlines ID09A and ID27, a flux increase of about 20 at the sample location is expected, while for the other beamlines of the group it is in particular the reduced horizontal source size (from 970 to 66  $\mu\text{m}$ ) which will offer new possibilities in the investigation of even smaller samples.

*M. Krisch*



## Earth and Planetary Science

### X-rays illuminate the origin of volcanic hotspots

Melting processes in the deep Earth's mantle may be the origin of the deep-derived plumes believed to feed hotspot volcanoes such as those in Hawaii. Zones in the lowermost mantle where seismic waves have ultra-low velocities have been interpreted as indicative of partial melting [1]. Between 5% and 30% partial melting could reduce the velocities of P and S seismic waves in agreement with seismological observations. The consequences of partial melting on the formation of distinct geochemical reservoirs could be major. Nevertheless, it is the density contrast between solid and melt fractions that controls the dynamic behaviour of the deep, partially molten mantle. Ascent or descent of liquids can have drastically different geodynamical consequences such as surface volcanism or production of a deep magma ocean, respectively.

We carried out experiments at beamlines **ID27** and **ID21** to determine the liquid buoyancy in the deep mantle. We used synthetic samples of chondritic composition, which is believed to be the most suitable for the deep and primitive mantle. After compression to target pressures between 40 GPa to 120 GPa, samples were heated by two infrared lasers with a spot diameter of more than 20  $\mu\text{m}$ . Melting of our samples was then achieved at temperatures up to 4,150 K. Temperatures were measured by analysing the pyrometric signal emitted over a sample area of 3  $\mu\text{m} \times 3 \mu\text{m}$ . Melting criteria are based on the use of *in situ* X-ray diffraction [2].

We analysed the recovered samples using simultaneous X-ray diffraction (XRD) and X-ray fluorescence (XRF), generating XRD and XRF maps with resolutions down to around 500 nm. XRD analyses revealed circular zoning in the laser hotspot: the centre contained the quenched liquid, as evidenced by the presence of several phases. The surrounding band of minerals consisted exclusively of aluminium-bearing (Mg,Fe)SiO<sub>3</sub> perovskite (Mg-Pv), the most refractory phase in the lower mantle (Figure 30). From the XRF

maps, we obtained the iron partition coefficient ( $D_{\text{Fe}}$ ) between the two different regions.  $D_{\text{Fe}}$  was between 0.45 and 0.6, indicating that iron was roughly twice as concentrated in the liquid compared to solid Mg-Pv (Figure 31). Our findings contrast strongly with a previous study suggesting a liquid 10 times more concentrated in Fe compared to Mg-Pv, at the core-mantle boundary pressure of 135 GPa [3]. This discrepancy could be attributed to the difference in composition of the starting materials: olivine in the previous study and an aluminium-bearing silicate glass in the present one. Furthermore, our samples were sufficiently thin to avoid any additional manipulation after their synthesis, while in the previous study the samples were thicker and may have encountered larger thermal gradients; they were also cut into slices for electron microprobe analyses.

On the basis of thermodynamic calculations [4], our results provide evidence that melt generated at the

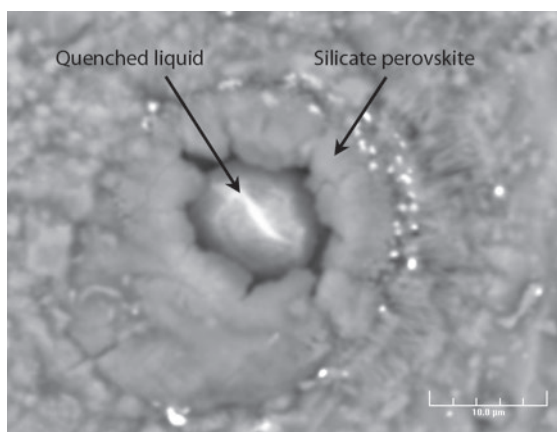


**Fig. 30:** Electron photomicrograph of a sample recovered after synthesis at 55 GPa and 2900 K. At the centre, the molten region is about 10  $\mu\text{m}$  in diameter.

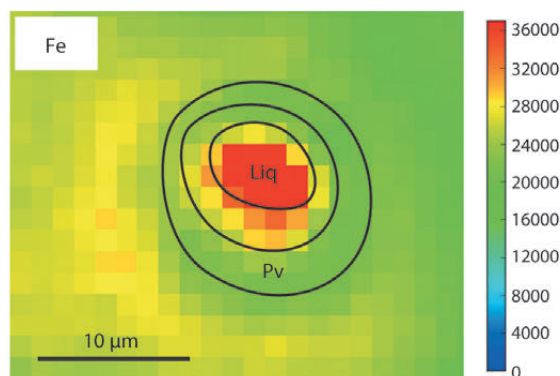
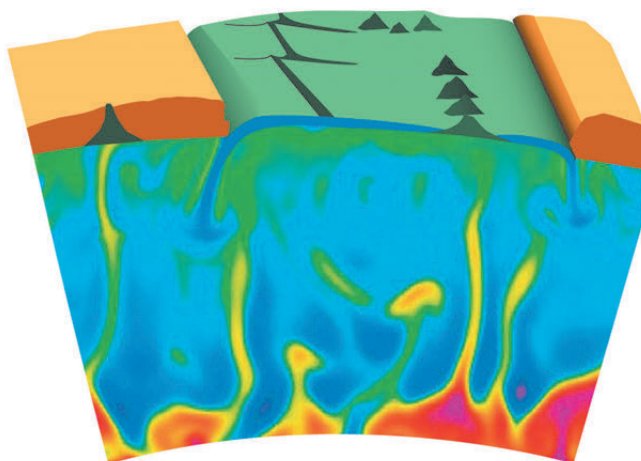


**Fig. 31:** Spatial distributions of the Fe XRF-intensity for the sample synthesised at 78.5 GPa and 3650 K. The intensity in the liquid (Liq) is about twice that in the silicate perovskite (Pv).



**Fig. 32:** Illustration of mantle plumes from the core-mantle boundary region reaching the Earth's crust. Due to the lateral displacement of the tectonic plates at the surface, the mantle plumes can create a series of aligned hot spot volcanoes.



core-mantle boundary should be buoyant, and hence should segregate upwards. This observation gives support to the theory that volcanic hotspots like the Hawaiian Islands originate from mantle plumes at the Earth's core-mantle boundary (**Figure 32**). The results of the experiment are also of great significance for the understanding of the early history of the Earth. Within the hypothesis of magma oceans induced by large meteoritic impacts on the early Earth, our results suggest that magma crystallisation should push the liquids towards the surface and form a deep solid residue depleted in incompatible elements.

#### Principal publication and authors

T. Boffa Ballaran (a),  
A. Kurnosov (a), K. Glazyrin (a,b),  
D.J. Frost (a), M. Merlini (c,d),  
M. Hanfland (d) and R. Caracas (e),  
*Earth and Planetary Science Letters*  
**333–334**, 181–190 (2012).

(a) Bayerisches Geoinstitut,  
Universität Bayreuth (Germany)

(b) Present address: Kline  
Geoscience Lab., Yale University  
(USA)

(c) Dipartimento di Scienze della  
Terra, Università degli Studi di  
Milano (Italy)

(d) ESRF

(e) CNRS, Ecole Normale  
Supérieure de Lyon, Laboratoire de  
Sciences de la Terre (France)

### Single-crystal study of silicate perovskites at conditions of the Earth's lower mantle

High-pressure experiments have shown that at the top of the lower mantle (above 20 GPa or 660 km depth)  $(\text{Mg,Fe})_2\text{SiO}_4$  ringwoodite and majoritic garnet, with a composition between  $(\text{Mg,Fe,Ca})_3\text{Al}_2\text{SiO}_{12}$  and  $(\text{Mg,Fe})_4\text{Si}_4\text{O}_{12}$ , transform to an assemblage of Al and Fe-bearing  $\text{MgSiO}_3$ -perovskite and  $(\text{Mg,Fe})\text{O}$  ferropericlasite [1]. In spite of its simple mineral composition, measurements of seismic wave velocities reveal a complex structure of the Earth's lower mantle. For example, a number of studies have identified seismic velocity anomalies (called large low-shear velocity provinces) extending from the base to the middle of the lower mantle. Such

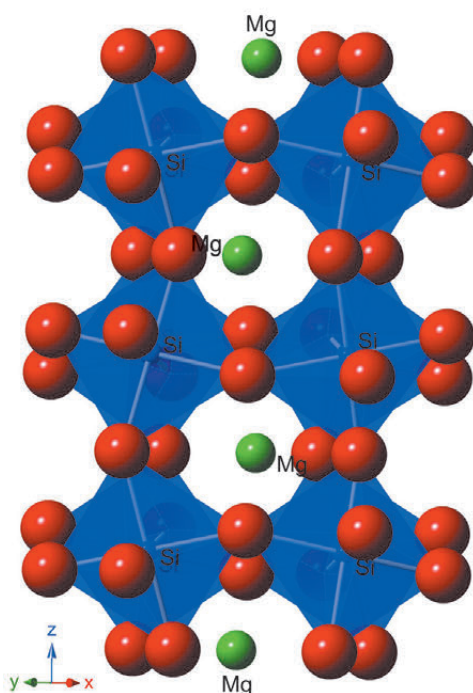
anomalies are likely to have a chemical origin suggesting that these regions contain a silicate perovskite with a composition distinct from that of the surrounding mantle. An understanding of the plausible chemical variation of perovskite in addition to its effect on density and elastic properties is, therefore, seminal for constraining geophysical models.

$\text{MgSiO}_3$  perovskite is orthorhombic, space group  $Pbnm$ , and consists of a framework of tilted  $\text{SiO}_6$  octahedra with Mg occupying the larger dodecahedral sites (**Figure 33**). Mg can be substituted by  $\text{Fe}^{2+}$ , whereas Mg and Si can be replaced by  $\text{Fe}^{3+}$  and Al usually as coupled substitution.

Three different magnesium silicate perovskite samples, one with compositions of the pure end-member  $\text{MgSiO}_3$ , one containing 4 mole% of  $\text{Fe}^{2+}$  substitution  $[(\text{Mg,Fe})\text{SiO}_3]$  (as expected for a peridotitic sample), and one with 37 mole% of  $\text{Fe}^{3+}$ -Al substitution  $[(\text{Mg,Fe})(\text{Al,Si})\text{SiO}_3]$  (as expected for a perovskite formed within subducted oceanic crust in the lower mantle) have been synthesised using a multi-anvil press and accurately characterised.

We have used the novel setup at beamline **ID09A** that allows data to be collected from a single crystal of any material at extreme conditions. The use of a single-crystal instead of powdered material has the advantage of providing very high-

**Fig. 33:** Room pressure structure of  $\text{MgSiO}_3$  perovskite viewed down the [110] direction. The distortion of the octahedral framework increases with pressure.





quality data since deviatoric stresses due to grain-grain interactions are absent. As a result, one can obtain very accurate and precise unit-cell lattice parameters and thus better constrain the compressibility behaviour of the material investigated.

The perovskite single-crystals were loaded in membrane-driven diamond anvil cells with He as the pressure-transmitting medium. Diffraction intensities were collected up to 75 GPa. No significant broadening of the diffraction spots was observed suggesting that the crystals were not subjected to large non-hydrostatic stresses. The high quality of the collected data allows a detailed examination of the effect of the two different chemical substitutions on the compression mechanism of  $\text{MgSiO}_3$  perovskite, and on the density and seismic velocities at depths of the Earth's lower mantle.

Since a high-spin to low-spin transition at high-pressure had been observed in ferropiclasite, there has been an intense debate about whether such a transition also occurs in Fe substituting into the  $\text{MgSiO}_3$ -perovskite structure. Opinion is still divided, especially because powder data collected for  $\text{MgSiO}_3$  perovskite with different amounts of Fe lack the necessary resolution to observe such a transition. We were able to observe a clear difference in the variation of the lattice strain (calculated from the measured unit-cell lattice parameters) between  $\text{MgSiO}_3$  and  $(\text{Mg,Fe})\text{SiO}_3$  perovskites above 40 GPa for the first time (Figure 34). Such a tiny effect can probably only be detected in very high-quality data, and it supports the suggestion of an intermediate spin state of  $\text{Fe}^{2+}$  in perovskite at lower mantle conditions.

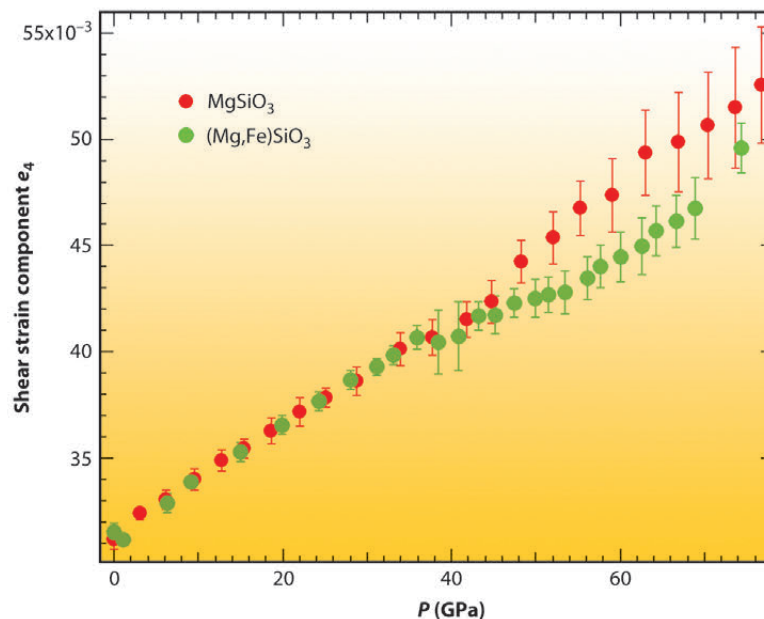


**Fig. 34:** Variation with pressure of the shear strain component,  $e_4$  (as defined for orthorhombic perovskite in [2]) for  $\text{MgSiO}_3$  (open circles) and  $(\text{Mg,Fe})\text{SiO}_3$  (filled circles) perovskites. Above 40 GPa there is a clear difference between the behaviour of the two samples as a result of a possible spin transition of  $\text{Fe}^{2+}$ .

The coupled substitution of  $\text{Fe}^{3+}$  and Al into the  $\text{MgSiO}_3$ -perovskite structure gives rise to a major change in the compression behaviour of this material. The unit-cell c-axis becomes much more compressible than that of the  $\text{MgSiO}_3$  end-member, as a result of an initial larger compression of the octahedral site due to the substitution of Si by Al. As a consequence,  $(\text{Mg,Fe})(\text{Si,Al})\text{O}_3$  perovskite is more compressible than the  $\text{MgSiO}_3$  end-member.

The two types of substitutions also affect the elastic properties of  $\text{MgSiO}_3$  perovskite differently.  $\text{Fe}^{2+}$  has a large negative effect on the bulk sound velocity and a large increase in density in contrast with  $\text{Fe}^{3+}$ -Al which have a very modest effect both on the bulk sound velocity and on density. Therefore, of the two, the latter would be the most probable cause of the observed seismic anomalies in the lower mantle.

#### References

- [1] T. Irifune, *Nature*, **370**, 131-133 (1994).
- [2] M.A. Carpenter, C.J. Howard, K.S. Knight and Z. Zhang, *J. Phys. Condens. Matter*, **18**, 10725-10749 (2006).

## New structures of carbonates at high pressures and their relevance for the deep carbon cycle

Calcite,  $\text{CaCO}_3$ , and dolomite,  $\text{CaMg}(\text{CO}_3)_2$  are two very common minerals on the Earth's surface. They are probably formed in the deep sea sediments and coral reefs. The chemical equilibria regulating their precipitation is recognised as being affected by the  $\text{CO}_2$  content in the oceans and atmosphere, two parameters which are directly related to the Earth's actual and past climate [1].

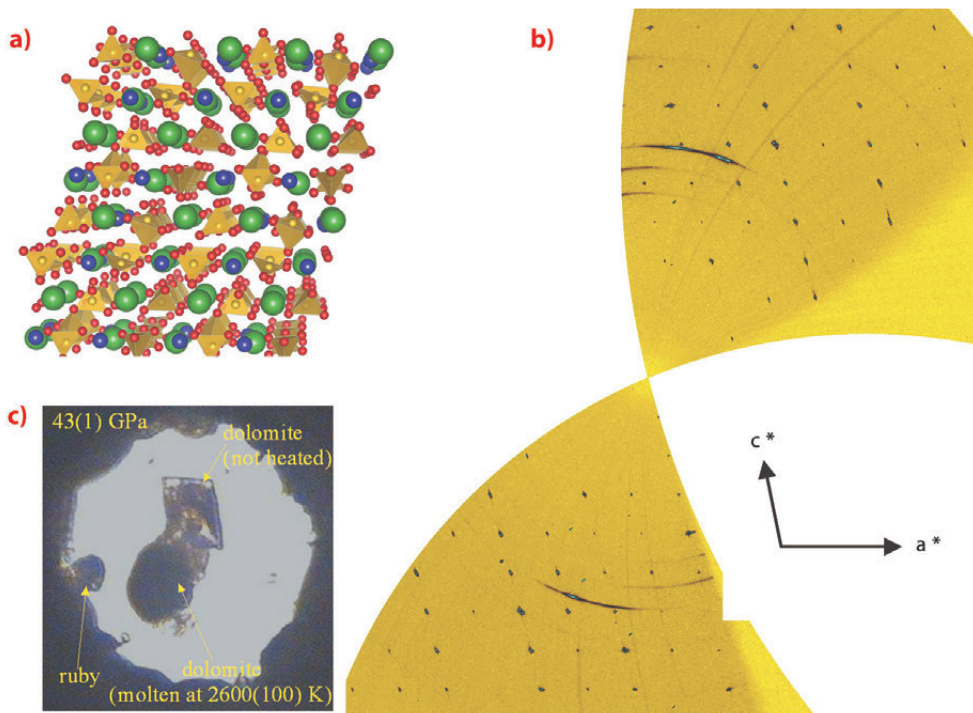
Nevertheless, not all the marine carbonate sediments are transformed into limestone and preserved at the Earth's surface because a significant portion of the oceanic carbonate sediments are transferred into deep Earth through the subduction mechanism of the oceanic crust and its overlying sediment layers. Therefore, in order to understand the whole Earth carbon cycle, it is

#### Principal publication and authors

M. Merlini (a), W.A. Crichton (b), M. Hanfland (b), M. Gemmi (c), H. Müller (b), I. Kupenko (d) and L. Dubrovinsky (d), *Proc. Natl. Acad. Sci. U.S.A.* **109**, 13509-13514 (2012).  
(a) Dipartimento di Scienze della Terra, Università degli Studi di Milano (Italy)  
(b) ESRF  
(c) Center for Nanotechnology Innovation@NEST, Istituto Italiano di Tecnologia, Pisa (Italy)  
(d) Bayerisches Geoinstitut, Universität Bayreuth (Germany)



**Fig. 35:** a) Crystal structure of dolomite-III at 55 GPa. b) Reconstructed h0l reciprocal space of dolomite-III with diffraction data collected at 55 GPa. c) A picture of the sample after the high-pressure and high-temperature experiment up to melting point.



fundamental to take into account the transformation of carbonates within the Earth’s mantle as well. In such a way, carbon may be transported and stored at depth, and it may also return back to the Earth’s surface through volcanic processes. The first step in any of these investigations, however, is assessing the structures of these carbon-rich materials at extreme conditions. Here we focussed in particular on the phase behaviour of dolomite, in order to study the phase evolution at the high pressures and temperatures expected in the Earth’s mantle. Very tiny single crystal samples ( $20 \times 20 \times 5 \mu\text{m}^3$ ) were pressurised in diamond anvil cells up to 80 GPa, and the structure evolution of dolomite was monitored by X-ray single crystal diffraction.

The experiments were performed at beamline **ID09A**, employing the recently optimised single-crystal diffraction setup, well-suited to the investigation of samples as small as a few  $\mu\text{m}^3$  in size and to pressures in excess of a megabar. Dolomite undergoes two structural transitions above 17 GPa (dolomite-II) and 35 GPa (dolomite-III), respectively. The first one is a displacive transition towards a lower symmetry structure, very similar to the one encountered in  $\text{CaCO}_3$  at much lower pressures [2]. The density of dolomite-II (triclinic,  $a = 4.7407(10) \text{ \AA}$ ,  $b = 5.3885(10) \text{ \AA}$ ,  $c = 6.7430(10) \text{ \AA}$ ,  $\alpha = 101.42(1)^\circ$ ,  $\beta = 89.27(1)^\circ$ ,  $\gamma = 95.72(1)^\circ$ ,  $V = 168.01(5) \text{ \AA}^3$ ) is similar to dolomite-I. The second transition (**Figure 35**) exhibits a first-order character, towards a different triclinic phase ( $a = 6.2346(9) \text{ \AA}$ ,  $b = 9.3025(11) \text{ \AA}$ ,  $c = 10.9893(12) \text{ \AA}$ ,  $\alpha = 75.89(1)^\circ$ ,  $\beta = 81.05(1)^\circ$ ,  $\gamma = 89.48(1)^\circ$ ,  $V = 610.32(14) \text{ \AA}^3$ ). Despite the significant volume changes (5%) upon transition (**Figure 36**), a single-crystal domain with quality suitable for structural investigation was preserved. The structure was solved with the charge-flipping method and Fourier analysis and was found to consist of 80 atoms in the unit cell. The main structural features are the presence of non-coplanar  $\text{CO}_3$  groups, a feature also present in the recently solved  $\text{CaCO}_3$ -III structure [3]. Moreover, the presence of a further chemically bonded oxygen close to the carbon positions (**Figure 36**) indicates that

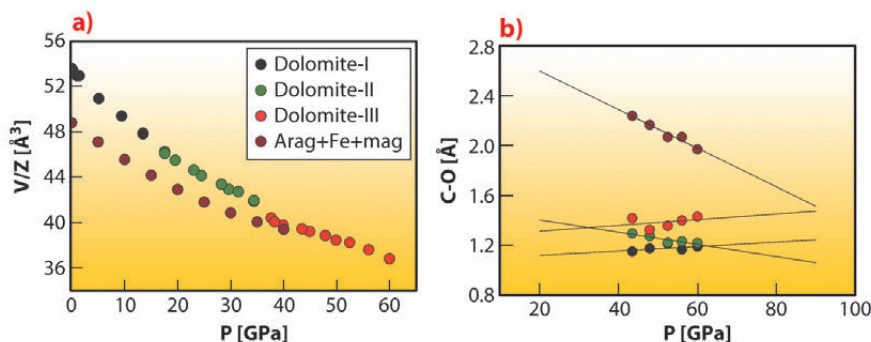


**Fig. 36:** a) Volume behaviour of dolomite, dolomite-II and dolomite-III, compared to the volume of a chemically-identical mixture of aragonite (the high pressure polymorph of  $\text{CaCO}_3$ ) and Fe-magnesite ( $\text{Mg,FeCO}_3$ ). b) Evolution of C-O distances as a function of pressure for selected C atoms. The presence of a fourth C-O chemical bond that progressively shrinks as a function of pressure is particularly evident, pointing towards a tetrahedrally coordinated carbon at extreme pressures.



this structure represents an intermediate topology between the low pressure carbonates and the predicted ultrahigh pressure carbonates, with tetrahedral coordinated carbon. The thermodynamic stability of dolomite-III at combined ultrahigh pressures and temperatures was investigated using the recently developed laser heating system for single crystal diffraction. These results indicate that single-phase dolomite-III is stable at the high pressures and temperatures existing in the lower mantle, also in agreement with another recent experimental study [4]. Dolomite-III may therefore act as

an important carbon repository in the lowermost mantle. The similarity between dolomite-III and calcite-III even suggests the possibility of an extended solid-solution between  $\text{CaCO}_3$  and  $\text{CaMg}(\text{CO}_3)_2$ , with this new structure acting therefore as the main vehicle for carbon transport in subduction environments, where experimental investigations reveal that a Mg-calcite, a composition intermediate between the calcite and dolomite compositional join, is the main carbon-bearing phase in multicomponent systems representative of the chemistry of the oceanic crust and sediment layer.

#### References

- [1] A. Ridgwell and R.E. Zeebe, *Earth Planet. Sci. Lett.* **234**, 299–315 (2005).
- [2] L. Merrill and W.A. Bassett, *Acta Cryst.* **B31**, 343–349 (1975).
- [3] M. Merlini, M. Hanfland and W.A. Crichton, *Earth Planet. Sci. Lett.* **333–334**, 265–271 (2012).
- [4] Z. Mao et al. *Geophys. Res. Lett.* **38**, L22303 (2011).

## Dense molten rocks in the interior of the Moon

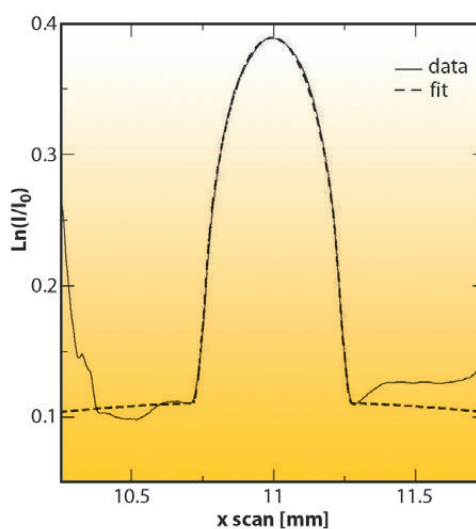
A 2011 NASA study [1] of moonquakes, based on seismometer measurements made during the Apollo missions, revealed a surprising new view of the lunar interior: the deepest parts of the rocky mantle of the Moon, at depths between 1200 and ~1350 km, appear to contain large amounts of molten rock (magma). In fact, up to 30 per cent of this deep layer may be molten. On Earth, such melt percentages would be accompanied by the formation of volcanoes, because magma formed in the interior of the Earth is less dense than the rock it originates from. This density difference provides a driving force for upward transport, leading to volcanic eruptions at the surface. However, despite the presence of large amounts of magma in its interior, the Moon has no active volcanoes. We have found an explanation for this apparent discrepancy by subjecting synthetic Moon rocks to extreme pressures and temperatures and measuring the density of the resulting magma using *in situ* techniques at beamline ID27.

Volcanic rocks on the Moon, sampled by Apollo astronauts, show a range in chemical composition that is much wider than that found on Earth. In particular, they show a very large range in titanium content, from less than 1 weight percent (wt%) in  $\text{TiO}_2$  to approximately 16 wt%. We measured the effect of this compositional variation on magma densities at lunar interior pressure and temperature conditions.

Magma densities were determined *in situ* by combining Paris-Edinburgh high-

pressure equipment with synchrotron X-ray absorption techniques [2]. Finely-powdered synthetic lunar rocks, inserted into natural diamond cylinders, were subjected to lunar interior pressures and heated to extreme temperatures inducing sample melting. Molten sample densities were obtained by measuring the absorption of synchrotron X-rays by the sample (Figure 37). *In situ* measurements were combined with computer simulations [3] to constrain lunar melt densities.

Results, summarised in Figure 38, show that virtually all magma in the Moon is less dense than the rocks they originate from, as is the situation on Earth. There is one exception: the most Ti-rich magmas become neutrally buoyant (as dense as their surroundings) at the deepest levels in the lunar mantle – exactly where the NASA study [1] detected magma.



#### Principal publication and authors

- M. van Kan Parker (a), C. Sanloup (b,c), N. Sator (d), B. Guillot (d), E.J. Tronche (a), J-P. Perrillat (e), M. Mezouar (f), N. Rai (a) and W. van Westrenen (a), *Nature Geoscience* **5**, 186-189 (2012).  
(a) Faculty of Earth and Life Sciences, VU University Amsterdam (the Netherlands)  
(b) UPMC Université Paris 06 and CNRS, UMR 7193, Paris (France)  
(c) SUPA, School of Physics and Astronomy, and Centre for Science at Extreme Conditions, The University of Edinburgh (UK)  
(d) Laboratoire de Physique Théorique de la Matière Condensée (UMR7600), Université Pierre et Marie Curie (Paris 6) (France)  
(e) Laboratoire de Sciences de la Terre, Université Claude Bernard Lyon 1, UMR5570 CNRS ENS Lyon (France)  
(f) ESRF

**Fig. 37:** X-ray absorption as a function of X-ray beam position in the x-direction (in mm) for molten low-titanium lunar glass at  $P = 16000$  bar,  $T = 1908 \pm 50$  K (solid line); Units  $\ln(I/I_0)$  with  $I$  the intensity of the X-ray beam after passing through the sample assembly, and  $I_0$  the intensity before passing through the assembly. The dotted curve shows the best fit to the data, giving a magma density  $2.87 \pm 0.03$  g  $\text{cm}^{-3}$ . The enhanced absorption at low x values shows the position of platinum-bearing pressure-temperature calibrants touching the outside of the diamond sample capsule.



**References**

- [1] R.C. Weber, P.Y. Lin, E.J. Garnero, Q. Williams and P. Lognonne, *Science* **331**, 309-312 (2011).
- [2] M. van Kan Parker, C. Sanloup, E.J. Tronche, J-P. Perrillat, M. Mezouar, N. Rai and W. van Westrenen, *High Pres. Res.* **30**, 332-341 (2010).
- [3] B. Guillot and N. Sator, *Geochim. Cosmochim. Acta* **71**, 4538-4556 (2007).

Such titanium-rich melts are formed by partial melting of titanium-rich solid rocks. Lunar sample analysis previously showed such rocks originally formed at shallow depths (<100 km) during the early evolution of the Moon. Our results therefore suggest that significant vertical rock transport occurred before magma generation, providing new constraints on lunar interior evolution.

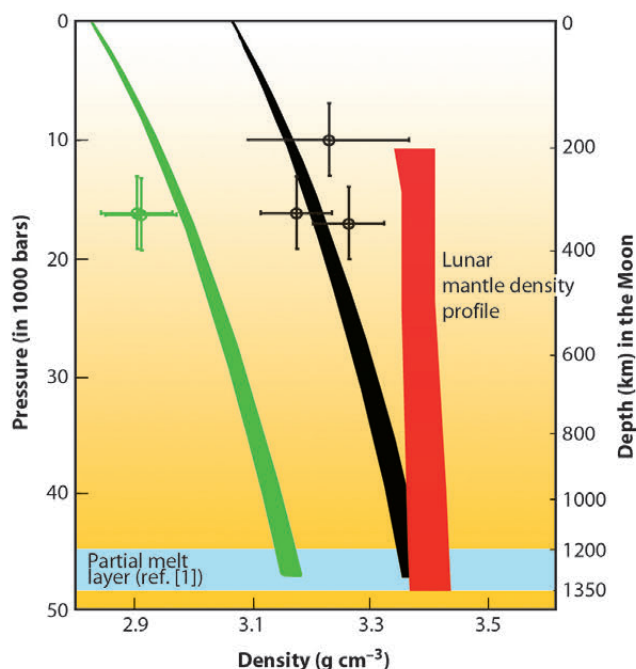


**Fig. 38:** Compilation of our *in situ* data (circles) and densities obtained from computer simulations (coloured curves). Green: lunar magma with < 1 wt% TiO<sub>2</sub>. Black: lunar magma with 16 per cent by weight TiO<sub>2</sub>. The blue bar indicates the area of partial melt according to ref. [1]. The red area represents estimates of the present-day density profile in the lunar mantle.

**Functional materials**

**Principal publication and authors**

- J. Fujii (a), M. Sperl (b), S. Ueda (c), K. Kobayashi (c), Y. Yamashita (c), M. Kobata (c), P. Torelli (a) F. Borgatti (d), M. Utz (b), C.S. Fadley (e,f), A.X. Gray (e,f), G. Monaco (g), C.H. Back (b), G. van der Laan (h) and G. Panaccione (a), *Phys. Rev. Lett.* **107**, 187203 (2011).
- (a) CNR-IOM, TASC Laboratory, Trieste (Italy)
- (b) Inst. Experimentelle Physik, Univ. Regensburg (Germany)
- (c) NIMS beamline Station at SPring-8, NIMS, Sayo, Hyogo (Japan)
- (d) CNR-ISMN, Bologna (Italy)
- (e) Dep. of Physics, University of California, Davis (USA)
- (f) Material Sciences Division, LBNL, Berkeley, California (USA)
- (g) ESRF
- (h) Diamond Light Source, Chilton, Oxfordshire (UK)

**Disentangling bulk and surface electron screening behaviour in (Ga,Mn)As**

The worldwide effort to understand the mechanisms at the origin of ferromagnetic order in diluted magnetic semiconductors (DMS) has resulted in a wealth of new concepts in spintronics. In the case of (Ga,Mn)As, fundamental questions persist regarding the spatial homogeneity of the coupling between Mn ions and the influence of surface and interface effects on the bulk electronic properties [1,2]. Recent advances in research on diluted

magnetic semiconductors (DMS) have demonstrated that the properties of the first few atomic layers play a fundamental role for future spintronics applications, hence, the understanding and control of the carrier density in (GaMn)As may have great technological significance. While many experimental and theoretical efforts have focused on reaching a reliable control and description of surface and interface effects of DMS, a basic understanding of the differences between surface and bulk electronic properties is still lacking.

Within an international collaboration, we performed high-resolution hard X-ray photoemission spectroscopy (HAXPES) at SPring-8 beamline BL15XU and at ESRF beamline ID16 on well-characterised (Ga,Mn)As films. Thanks to the unusually high bulk sensitivity achieved by HAXPES (probing depth > 100 Å), the presence of a distinct electronic screening channel in the bulk, hitherto undetected in surface sensitive analysis, has been revealed, thus demonstrating that the electronic structure of the bulk and the surface of (Ga,Mn)As is profoundly different. Comparison with

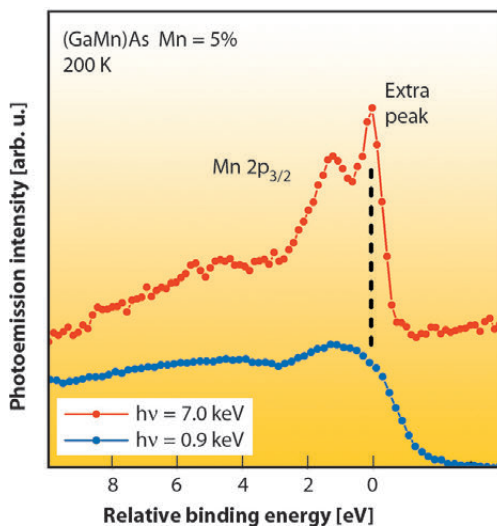


**Fig. 39:** Mn 2p<sub>3/2</sub> photoemission spectra from a (Ga,Mn)As film (5% Mn, T<sub>c</sub> = 60 K), after HCl chemical etching, measured using soft and hard X-ray energies. Spectra have been aligned to the same relative binding energy scale without background subtraction.



model calculations identifies the character of the Mn 3d electronic states and clarifies the role of hybridisation in mediating the ferromagnetic coupling.

**Figure 39** compares soft X-ray (surface sensitive) and HAXPES (bulk sensitive) Mn 2p spectra of (GaMn)As. The surface sensitive spectrum agrees well with previous Mn 2p PES reports [3]. In contrast, the Mn 2p HAXPES spectrum reveals an additional sharp feature at the onset of the main  $2p_{3/2}$  peak which is completely absent in the surface-sensitive one. Similar low binding energy peaks have recently been reported in HAXPES from 3d-based transition metal oxides, and are generally associated with a metallic-like, i.e. delocalised, character [4].

Using model calculations we were able to ascribe these changes to the electron screening process, which highlights the importance of the d-electron hybridisation.

**Figure 40** explains the difference in the screening ability of the electrons: each Mn atom carries a cloud of partially localised d electrons. A difference in the spatial extension of the electronic cloud, which is indicated by a change in the radius of the sphere, corresponds to a

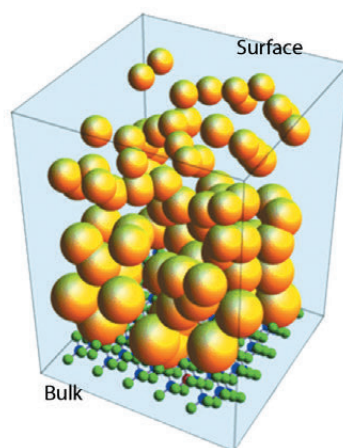


**Fig. 40:** The (GaMn)As electronic structure. Randomly-substituted Mn atoms on the Ga sites are shown at the bottom of the figure. The electronic clouds of partially localised Mn d electrons are approximated by spheres, with a radius proportional to the screening length. Near the surface (top) the d electrons are more localised (smaller radius) than in the bulk (bottom, larger radius).

different hybridisation. Near the surface the d electrons are more localised (smaller radius) than in the bulk (larger radius), corresponding to a different screening ability, a fundamental parameter to set ferromagnetism in the system.

Our results not only confirm the remarkable change of the screening properties in diluted systems when going from the surface to the volume, but also confirm that adequate knowledge of the electronic structure of the surface/interface in comparison to the bulk one is essential for any real applications.

#### References

- [1] T. Dietl, *Nature Mater.* **9**, 965 (2010).
- [2] I. Zutic, J. Fabian and S. Das Sarma, *Rev. Mod. Phys.* **76**, 323 (2004).
- [3] J. Okabayashi *et al.*, *Phys. Rev. B* **58**, R4211 (1998).
- [4] G. Panaccione *et al.*, *Phys. Rev. Lett.* **97**, 116401 (2006).

## Magnetic complexes: a way to combine magnetism and photonics in semiconductors

Due to their unique photonic properties and to the possibility of tuning the band gap over an exceptionally wide energy range, gallium nitride (GaN) and related compounds are considered as technologically outstanding semiconductors. Most of the commercial light emitting diodes (LEDs) are currently based on GaN. Moreover, this material – once homogeneously doped with transition metal ions and with a considerable amount of free holes – has been predicted to be the ideal candidate for ferromagnetic semiconductor with spintronic functionalities above room temperature [1]. The epitaxial growth of these systems can be reliably directed by taking advantage of specific features of magnetic impurities in semiconductors. This can result in either a *dilute*, homogeneous alloy [2] or a *condensed*, inhomogeneous system with the self-organised aggregation of magnetically robust nanocrystals embedded in the host

paramagnetic matrix and with specific signatures crucially depending on the crystallographic phase of the specific nanocrystals [3].

The examples given above have been only possible through the development of a protocol of comprehensive structural, magnetic and chemical characterisation supported by an extensive theoretical investigation and feedback. In particular, synchrotron absorption and diffraction, and advanced electron microscopy have permitted significant advances.

These advances have led recently to the discovery of magnetic nitride complexes involving one magnetic impurity and one or more electrically active dopants. Using synchrotron radiation methods supported by *ab initio* computations, it has been possible to show that the codoping of GaN with Mn (magnetic species) and Mg (acceptors) results in the formation of

#### Principal publication and authors

- T. Devillers (a), M. Rovezzi (b), N. Gonzalez Szewacki (c), S. Dobkowska (d), W. Stefanowicz (d), D. Sztenkiel (d), A. Grois (a), J. Suffczyński (e), A. Navarro-Quezada (a), B. Faina (a), Tian Li (a), P. Glatzel (b), F. d'Acapito (f), R. Jakiela (d), M. Sawicki (d), J.A. Majewski (c), T. Dietl (c) and A. Bonanni (a), *Scientific Reports* **2**, 722 (2012).
- (a) Institut für Halbleiter und Festkörperphysik, Johannes Kepler University, Linz (Austria)  
(b) ESRF  
(c) Institute of Theoretical Physics, Faculty of Physics, University of Warsaw (Poland)  
(d) Institute of Physics, Polish Academy of Sciences, Warsaw (Poland)  
(e) Institute of Experimental Physics, Faculty of Physics, University of Warsaw (Poland)  
(f) Consiglio Nazionale delle Ricerche, IOM-OGG c/o ESRF GILDA CRG, Grenoble (France)



**Fig. 41:** Number of Mg atoms neighbouring each Mn in the first cation coordination sphere ( $Mg_{Gd}$ ), extracted from EXAFS analysis and compared to the energetically most favourable configurations found by *ab initio* computations. The arrows correlate the theoretical and experimental values to the corresponding Mn-Mg complexes.

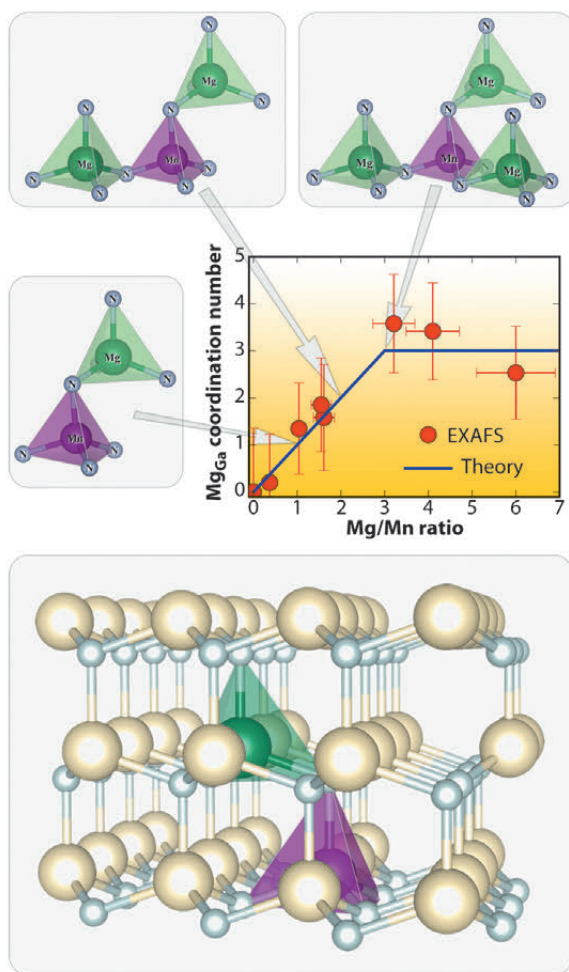
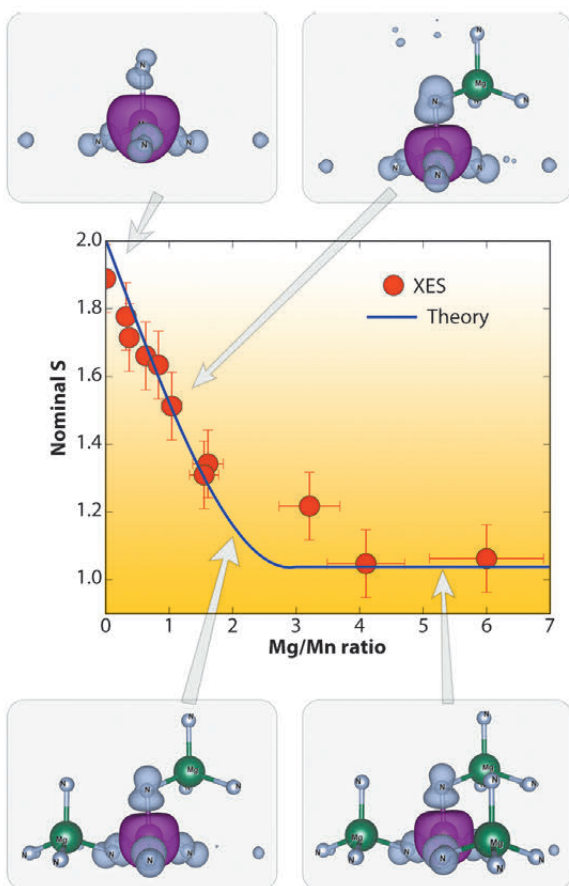


**Fig. 42:** Nominal spin state *S* as a function of the ratio between the Mg and Mn concentration, extracted from the analysis of XES spectra and supported by *ab initio* computations. The arrows correlate the experimental values to the corresponding calculated spin polarisation densities.



**References**

[1] T. Dietl, H. Ohno, F. Matsukura, J. Cibert and D. Ferrand, *Science* **287**, 1019 (2000).  
 [2] M. Sawicki, T. Devillers, S. Gałeski, C. Simserides, S. Dobkowska, B. Faina, A. Grois, A. Navarro-Quezada, K.N. Trohidou, J.A. Majewski, T. Dietl and A. Bonanni, *Phys. Rev. B* **85**, 205204 (2011).  
 [3] A. Bonanni, A. Navarro-Quezada, T. Li, M. Wegscheider, Z. Matej, V. Holy, R.T. Lechner, G. Bauer, M. Rovezzi, F. D’Acapito, M. Kiecana, M. Sawicki and T. Dietl, *Phys. Rev. Lett.* **101**, 135502 (2008).

cation complexes  $Mn-Mg_k$  where the number of ligands  $k$  is dictated by the synthesis conditions.

From extended X-ray absorption fine structure (EXAFS) measurements carried out at beamline **BM08** (GILDA Italian beamline) at the Mn K-edge and by *ab initio* computation based on density functional theory (DFT), a correlation was found between the positions occupied by Mn and Mg in the host lattice, instead of uniform distribution. As summarised in **Figure 41**, the number of Mg cations neighbouring each Mn follows the Mg/Mn ratio in the sample, it increases linearly up to Mg/Mn = 3 and then becomes saturated. This configuration corresponds to the energetically most favourable cation complexes identified by DFT.

The theoretical expectations are also confirmed by following the evolution of the Mn spin state *S* as a function of Mg codoping. This is obtained *via* the  $K\beta$  X-ray emission spectroscopy (XES) technique, which – by probing the  $3p \rightarrow 1s$  transitions – is sensitive to the magnitude of the exchange interaction between the Mn  $3p$  core-hole and the net magnetic moment in the Mn  $3d$  valence shell. From the XES spectra, collected at beamline **ID26**, the values of *S* are obtained. These are reported in **Figure 42** together with calculated spin-polarisation densities. With this analysis, it was possible to demonstrate that, upon Mg codoping, the Mn spin state first decreases linearly from 2 to 1, and then saturates for Mg/Mn > 3.

The formation of the paramagnetic complexes has two surprising consequences: (i) in the combination 1 Mn – 1 Mg, the observed delocalisation of the hole-states holds promise for the realisation of the long-pursued carrier-mediated high-temperature ferromagnetic interaction between magnetic spins in a semiconducting matrix, and (ii) in the case of complexes involving three Mg ligands, photoluminescence revealed a broad infrared band covering two of the principal telecommunication windows, namely 1.33  $\mu m$  and 1.55  $\mu m$ .



## RXES investigation of d-d states in a self-aggregating supramolecular Pt-tpy complex

In the photophysics and photochemistry of transition metal complexes d-d (ligand field), transitions are of fundamental importance because they are often responsible for deactivating radiative (emissive) relaxation pathways to the ground state and for promoting ligand release photochemical reactions [1]. Despite their fundamental importance, it is difficult to characterise such states since they are spectroscopically silent to most conventional laboratory techniques. Nevertheless, it has been demonstrated in several cases that RXES (Resonant X-ray Emission Spectroscopy) can effectively provide specific information on d-d states for metal-containing systems. RXES is an element selective technique which probes both the unoccupied and occupied orbitals involved in electronic transitions at the metal centre by combining XANES and XES (Figure 43).

At beamline ID26, we have extended the use of RXES to the study of d-d states in the self-aggregating square planar [Pt(tpy)Cl]Cl complex. In solution Pt-tpy (tpy = 2,2':6',2''-terpyridine) derivatives form oligomers of various sizes depending on their concentration (see for example Figure 43 where a model stacked structure is shown). The intermolecular Pt...Pt and  $\pi$ - $\pi$  interactions that drive the formation of these supramolecular structures in polar solvents produce dramatic changes in their absorption and emission profile, as for example a luminescence shift to the near infrared. For these attractive optical features, Pt-tpy complexes have found application as sensors for biomolecules (e.g. glucose) and as probes for DNA G-quadruplex formation [2].

Collection of 2D RXES maps for [Pt(tpy)Cl]Cl at the Pt-L<sub>3</sub> edge was achieved both on a solid sample (Figure 44) and on an aqueous solution. Aided by DFT calculations, simulation of the maps evidenced the nature of the orbitals involved in the d-d transitions. The main peak ( $E_I = 11567.7$  eV,  $E_T = 5.1$  eV) and the shoulder ( $E_T = 6.7$  eV) arise from Pt-based molecular orbitals with prevalent Pt 5d and Cl 3p character, while the tail (ca.  $E_T = 7.5$  eV) is attributed to transitions between molecular orbitals where the

Pt 5d atomic orbitals are mostly mixed with N 2p and C 2p atomic orbitals of the tpy ligand.

Notably, measurements performed on [Pt(tpy)Cl]Cl aqueous solutions of different concentrations (5–40 mM) retain these RXES features, but show a shift of the major peak to higher energy transfer values (up to 0.5 eV) as the sample concentration decreases. Such significant change in energy is associated with the concentration-dependent size decrease of the supramolecular structure of [Pt(tpy)Cl]Cl in diluted solutions. The filled d orbitals that extend perpendicular to the molecular plane ( $d_{xz}$ ,  $d_{yz}$  and  $d_z^2$ ) interact along the

### Principal publication and authors

C. Garino (a), E. Gallo (a,b), N. Smolentsev (b,c), P. Glatzel (b), R. Gobetto (a), C. Lamberti (a), P.J. Sadler (d) and L. Salassa (d,e), *Phys. Chem. Chem. Phys.* **14**, 15278-15281 (2012).

(a) Department of Chemistry and NIS Centre of Excellence, University of Turin (Italy)

(b) ESRF

(c) Research Center for Nanoscale Structure of Matter, Southern Federal University, Rostov-on-Don (Russia)

(d) Department of Chemistry, University of Warwick, Coventry (UK)

(e) CIC biomaGUNE, Donostia-San Sebastian (Spain)

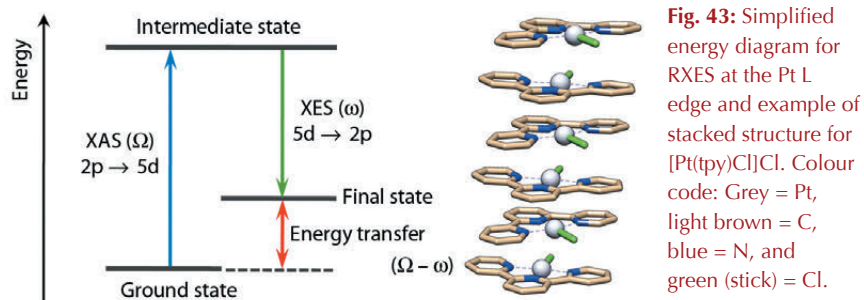


**Fig. 43:** Simplified energy diagram for RXES at the Pt L edge and example of stacked structure for [Pt(tpy)Cl]Cl. Colour code: Grey = Pt, light brown = C, blue = N, and green (stick) = Cl.

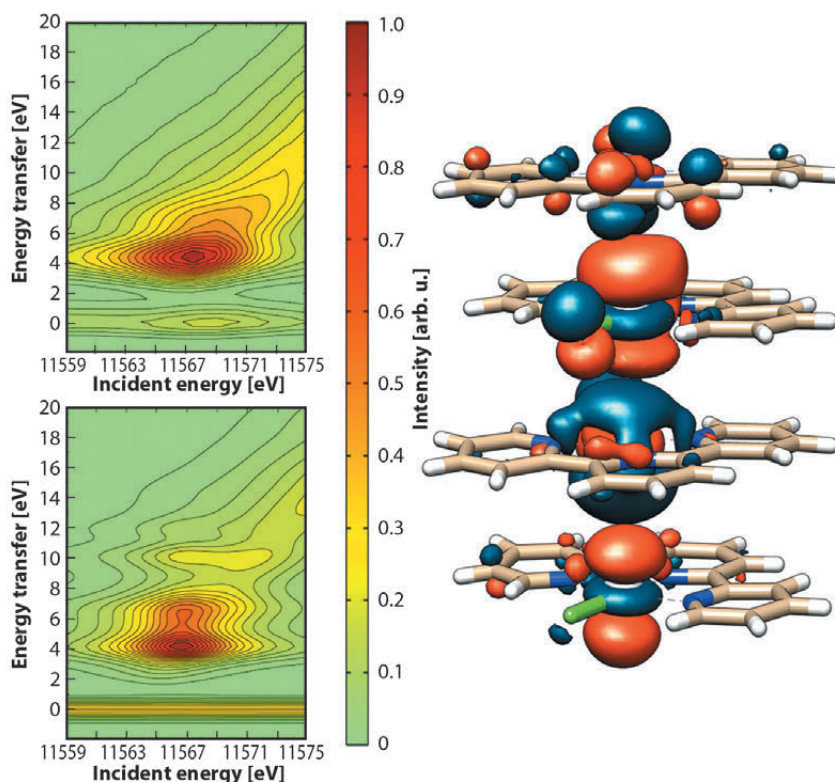


**Fig. 44:** Contour plots of experimental (top) and simulated (bottom) Pt-L<sub>3</sub> ( $2p_{3/2}$ ) RXES planes for solid [Pt(tpy)Cl]Cl and selected antibonding molecular orbital for {[Pt(tpy)Cl]<sup>+</sup>}<sub>4</sub>.



### References

- [1] P.S. Wagenknecht and P.C. Ford, *Coord. Chem. Rev.* **255**, 591-616 (2011).  
 [2] V.W.-W. Yam and K.M.-C. Wong, *Chem. Commun.* **47**, 11579-11592 (2011).

axial direction, splitting into bonding and antibonding combinations which lower the energy of d–d ligand field transitions. This is reflected in the shift of the RXES main band to higher energies at lower concentration.

Our findings help to rationalise the considerable changes in the optical properties of Pt-tpy derivatives with the substitution of a Cl ligand in [Pt(tpy)Cl]Cl and suggests that favouring the formation of supramolecular interactions in the plane

of the ligands allows full control of the d–d states to be achieved by directly affecting the  $d_{x^2-y^2}$  orbital energy.

For the first time we demonstrated how this powerful technique can be used to characterise spectroscopically d-d states in high-order metal-based systems in solution. A complete understanding of the energy and orbital nature of these states is key to guide the design and synthesis of functional supramolecular architectures based on transition metal complexes.

### Principal publication and authors

M. Miglierini (a,b),  
 V. Prochazka (b), S. Stankov (c,d),  
 P. Svec, Sr. (e), M. Zajac (f),  
 J. Kohout (g), A. Lancok (h),  
 D. Janickovic (e) and P. Svec (e),  
*Phys Rev B* **86**, 020202(R) (2012).  
 (a) Slovak University of Technology  
 in Bratislava (Slovakia)  
 (b) RCPTM, Palacky University  
 (Czech Republic)  
 (c) Institute for Synchrotron  
 Radiation, Karlsruhe Institute of  
 Technology (Germany)  
 (d) Laboratory for Applications of  
 Synchrotron Radiation, Karlsruhe  
 Institute of Technology (Germany)  
 (e) Institute of Physics, Slovak  
 Academy of Sciences (Slovakia)  
 (f) ESRF  
 (g) Charles University (Czech  
 Republic)  
 (h) Institute of Inorganic Chemistry,  
 AS CR (Czech Republic)

## Exploring the formation of nanocrystallites

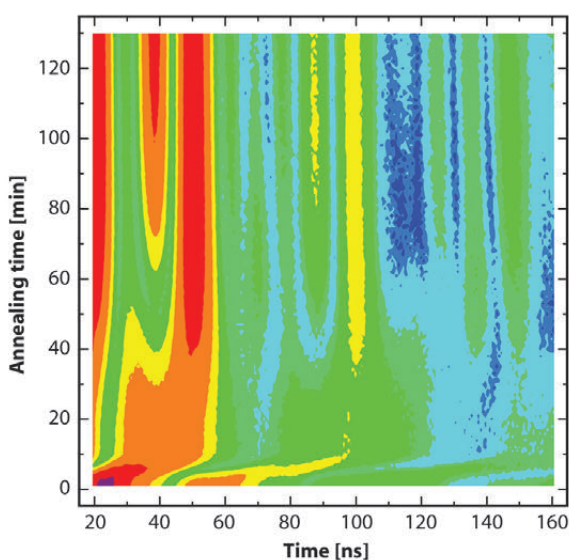
Iron-containing metallic glasses exhibit unique soft magnetic properties that are attractive for a variety of practical applications including transformer cores, magnetic sensors and magnetic shielding. The beneficial magnetic parameters are closely related to the amorphous state of the material. However, their prolonged operation at elevated temperatures leads to a partial crystallisation which produces a deterioration of the advanced magnetic features.

Nanocrystalline alloys represent a new class of materials that offer a rich variety of new physical properties. They can be tailored by tuning the chemical and structural compositions by controlling the size and morphology of the crystalline nanograins. These nanocrystalline materials are prepared by controlled crystallisation of metallic glasses at defined conditions (temperature, time).

The presence of nanocrystalline grains embedded in the residual amorphous matrix stabilises the structure, preserving and even enhancing the performance of these materials.

The transformation of the structure via crystallisation is one of the mechanisms that considerably affects the macroscopic physical properties of these materials. In order to further optimise these properties, it is necessary to understand the microstructure and the processes that are taking place during the crystallisation. The behaviour of metallic glasses is usually investigated under static external conditions in relatively long time windows over several tens of minutes. In contrast, the information derived by rapid data acquisition techniques is averaged over the entire volume of the sample and is limited only to one specific feature such as structural order or magnetic behaviour. Therefore, further elucidation of the nanocrystallisation kinetics requires a thorough understanding of the nanograin growth by disentangling the evolution of structurally different components, *i.e.* nanograins, interfaces, and the residual amorphous precursor, that takes place during thermal annealing. To reach this goal we have used the method of nuclear forward scattering (NFS) at the Nuclear Resonance Station ID22N. Choosing iron atoms as probes, information on their magnetic states (hyperfine interactions), consequently on the structural arrangements, is simultaneously obtained. The high brilliance of third-generation synchrotron radiation sources allows NFS spectra to be collected with sufficiently high statistics for very short time intervals. This made *in situ* monitoring possible

**Fig. 45:** Contour plot of the NFS spectra showing the appearance of magnetic hyperfine interactions after about 45 minutes of annealing. Note also progressive changes in the spectra immediately after the beginning of the heat treatment.





for the temperature driven process of crystallisation demonstrated in this work.

The time spectra of nuclear forward scattering were collected during isothermal heat treatment at a temperature close to the onset of crystallisation of the investigated NANOPERM alloy. The obtained NFS spectra reveal rapid development that takes place shortly after the beginning of the annealing process (Figure 45). This is a direct consequence of the changes in the hyperfine interactions due to modifications of the nearest neighbourhood of the iron atoms connected with the emerging ferromagnetic nanocrystalline grains.

By performing a quantitative analysis of the NFS spectra (Figure 46) we were able to disclose the nucleation and growth of the iron nanograins to fine details by accessing separately atoms located in their interior (bulk), at their surfaces as well as those that belong to the residual amorphous matrix. The crystallisation model we developed (solid lines in Figure 46b) gave complete explanation of the experimental data (open symbols in Figure 46b).

By using NFS experiments, it is now possible to identify the interface regions formed by the atoms located at the surfaces of the nanograins. The interface component in the NFS spectra prevails at the stages of early crystallisation when the majority of atoms are located at the nanograin surface. At advanced crystallisation stages, the bulk fraction, resulting from the growth of the

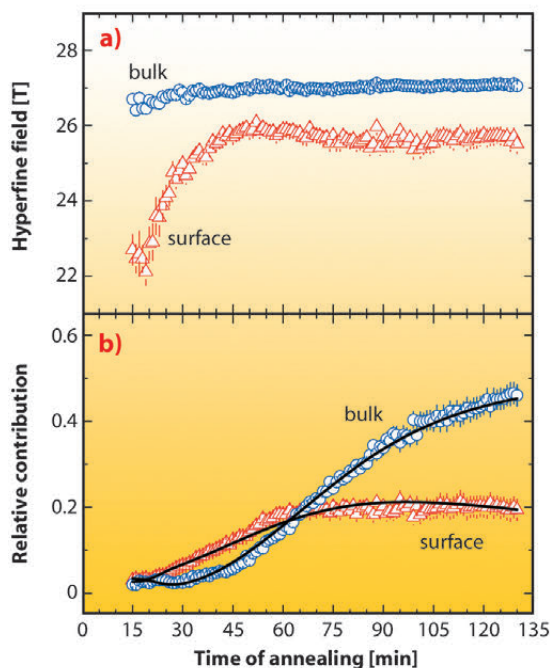


**Fig. 46:** Magnetic hyperfine fields (a) corresponding to the bulk and surface iron atoms in the newly born nanocrystals are stabilised once their structure is well developed. During this grain growth process, the relative contribution of the surface atoms dominates that of the bulk atoms, which appears later (b).

nanograins size as well as of their number, increases.

Employing *in situ* nuclear forward scattering during isothermal crystallisation, the process of nanograin formation was investigated in real time revealing how the nanograins are formed, especially at the very early stages of isothermal annealing. Even though the overall formation of nanocrystals can also be deduced from other analytical techniques, our approach provides the possibility to study independently iron atoms positioned at different structural sites within the alloy owing to their site-specific hyperfine interactions.

## Microscopic and mesoscopic structure of functional perovskite ferroelectrics

Piezoelectric materials change their physical dimensions under application of an electric voltage and generate voltage under mechanical stress. Today they are widely used as sensors and actuators in various industries. In general, the most efficient piezoelectrics are mixed perovskites with composition close to the so-called morphotropic phase boundary (MPB). Near the MPB the ferroelectric phases of different symmetry have nearly the same energy and are separated by a rather small potential barrier. As a result, the different states can be easily switched by a small electrical

or mechanical signal providing high electromechanical coupling. The exact structure and switching mechanisms are, however, challengingly complex and not yet understood. We combine diffuse and inelastic X-ray scattering experiments to reveal the character of structural heterogeneity in the most extensively used MPB piezoelectric – PZT.

Lead zirconate-titanate  $\text{PbZr}_{1-x}\text{Ti}_x\text{O}_3$  (PZT) holds about 80% of the piezoelectric market. It is also a model system for studying the MPB phenomenon, which is observed for compositions when  $x$  is

### Principal publications and authors

R.G. Burkovsky (a,b),  
Y.A. Bronwald (a),  
A.V. Filimonov (a), A.I. Rudskoy (a),  
D. Chernyshov (c), A. Bosak (b),  
J. Hlinka (d), X. Long (e),  
Z.-G. Ye (e) and S. Vakhruhev (f,a),  
*Phys. Rev. Lett.* **109**, 097603 (2012).  
(a) St. Petersburg State Polytechnical University (Russia)  
(b) ESRF  
(c) SNBL at ESRF (France)  
(d) Institute of Physics, Academy of Sciences of the Czech Republic, Prague (Czech Republic)  
(e) Department of Chemistry and 4D LABS, Simon Fraser University, Burnaby (Canada)  
(f) Ioffe Physical-Technical Institute, St. Petersburg (Russia)



around 0.48. Many diffraction studies have been devoted to understanding the structure of PZT near the MPB, but despite these efforts, the results and their interpretation remain controversial [1]. This is mainly due to the fact that diffraction studies reveal in almost all cases a structure, which is more complex than the single phase long-range ferroelectric order. The real microscopic structure can be studied effectively by analysing the scattering outside Bragg peaks by diffuse and inelastic scattering methods. We used these methods at beamlines **BM01A** and **ID28**, respectively. PZT single crystals of sufficient size and quality were grown at the Simon Fraser University (Canada).

Our diffraction measurements reveal the appearance of strong anisotropic diffuse scattering around Bragg spots

(**Figure 47 a,c**) at temperatures just below the transition between two different ferroelectric phases (about  $T = 430$  K). The observed scattering does not correspond to the polarisation fluctuations near the phase transition because it is absent on the high-temperature side of the ferroelectric-ferroelectric transition and also near the ferroelectric-paraelectric transition (about  $T = 663$  K). Consequently, we have to assume another mechanism, which takes into account some structural inhomogeneity.

To further understand the origin of diffuse scattering we used inelastic X-ray scattering (IXS). This technique allows static and dynamic components of diffuse scattering to be disentangled due to the meV energy analysis of the scattered photons. **Figure 48** schematically shows the IXS intensity maps along the inspected directions in reciprocal space. We observe strong quasielastic scattering (centred at zero energy-transfer) in diagonal and longitudinal directions, while in transverse directions the scattering is almost purely inelastic. Therefore, the observed diffuse scattering (**Figure 47a**) is a superposition of two contributions: one is due to phonons and the other one is due to static deviations from long-range order. The important feature of this second component is the absence of any intensity along the transverse direction. To reproduce this feature with models by considering the diffuse scattering as a Fourier image of real-space objects or 3D correlators was not possible. In contrast, it is consistent with Huang scattering – scattering due to inhomogeneous deformations of the lattice. More specifically, we note a very good agreement (**Figure 47 b,d**) with experimental data when the deformations are modelled as being due to tetragonal-symmetry point defects in a matrix that is nearly cubic. From the anisotropy of the diffuse scattering, it can be deduced that these defects produce very small volume strain due to the specific ratio between tensile strain along the main tetragonal direction and compressive strain along the two other directions. The emerging physical picture behind this model assumes that small clusters of the tetragonal phase remain in the matrix of the new average structure below the ferroelectric-ferroelectric phase transition temperature. In this model

**Fig. 47:** Experimental diffuse scattering maps (a,c) and corresponding calculations (b,d).

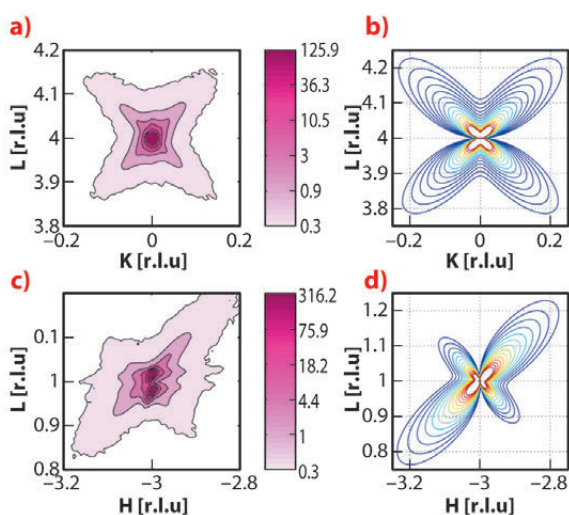
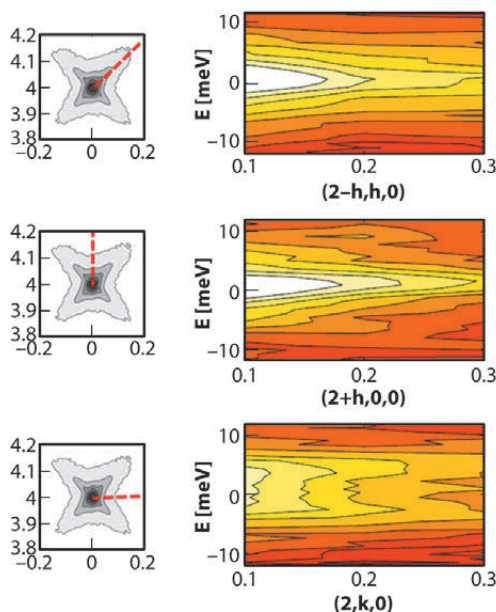


**Fig. 48:** Inelastic X-ray scattering maps along the three key directions of the (0 0 2) Brillouin zone.





we associate the diffuse scattering with the scattering by the matrix surrounding the clusters (not with the scattering by the clusters themselves, which are too small for direct observation) because the matrix is deformed on a larger, mesoscopic scale.

Last, but not least, the observed morphotropic PZT diffuse scattering appears at first sight to be very similar in shape to that of relaxor ferroelectrics [2] – a different and special class of disordered perovskites. However there are

clear topological differences with respect to the relaxor case – in (0 0 L) Brillouin zones of PZT the transverse diffuse scattering component is suppressed, while for diffuse scattering in relaxors, the minimum of intensity appears along the longitudinal direction. This forms a solid basis for the assumption that the origin of diffuse scattering in these two classes of materials is also different. We believe that the present work on PZT will further stimulate the development of a common understanding of disorder phenomena in functional perovskite ferroelectrics.

#### References

- [1] J. Kreisel, B. Noheda and B. Dkhil, *Phase Transitions* **82**, 633 (2009).  
[2] A. Bosak, D. Chernyshov, S. Vakhrushev and M. Krisch, *Acta Crystallographica* **A68**, 117 (2012).

## ■ Water and biological systems

### Water: mixture or continuum?

Water is one of the most well-studied substances, yet we still do not have a complete description of its structure. The complex hydrogen-bond network that gives rise to water's remarkable properties is transient, requiring different descriptions at different time and length scales. Spectroscopic studies of water provide compelling but often conflicting information on the local structure and dynamics. One of the recurring questions that surfaces periodically is whether the liquid is best described as a continuum or a mixture at the molecular scale.

The earliest descriptions of water were mixture models, of miniature icebergs mixed with a “normal” liquid, which helped explain some of the anomalous properties of water like the density maximum at 4°C. Since the advent of molecular dynamics, simulations of varying complexity have regularly suggested a continuum model of liquid water. In this view, hydrogen bonds in the liquid are distorted, broken and reformed continuously, but the liquid itself is composed of a single component.

However, spectroscopic data can often be modelled by assuming the existence of distinct species with different local structures: a modern version of a mixture model with a tetrahedrally-coordinated ice-like component and a dense component with distorted or broken hydrogen bonds. While these mixture

models are not supported by molecular dynamics simulations, they do have one very attractive feature: they establish a direct correspondence between the structure in the liquid phase and that of low-density and high-density amorphous ices, the existence of which is another peculiar and much discussed property of water. X-ray spectra in particular have recently been used to support the mixture model view of water structure [1]. Existing X-ray and neutron diffraction techniques are relatively insensitive to the details of hydrogen bonding in water. Therefore, further spectroscopic investigations are of interest in order to test the validity of the different models.

One particular spectroscopic result is often taken as direct evidence of a two-component structure: van't Hoff behaviour, in which temperature-induced spectral changes can be viewed as changes in the populations between two components. Importantly, a van't Hoff fit of temperature-dependent spectra gives a value for the enthalpy change in the conversion between the two components.

Using an in-house-developed temperature-controlled liquid flow setup at beamline **ID16**, we measured the oxygen near-edge spectrum of liquid water at various temperatures using X-ray Raman scattering. Thanks to excellent statistical accuracy and stability we can see a subtle and systematic evolution with

#### Principal publication and authors

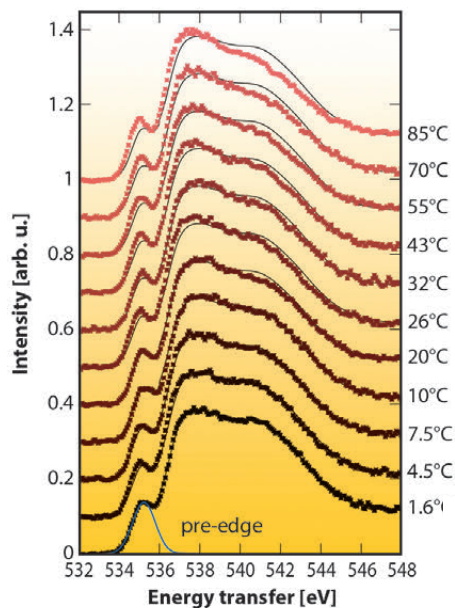
T. Pytkäinen (a,b), A. Sakko (a), M. Hakala (a), K. Hämäläinen (a), G. Monaco (b) and S. Huotari (a,b), *J. Phys. Chem. B* **115**, 14544-14550 (2011).  
(a) Department of Physics, University of Helsinki (Finland)  
(b) ESRF



temperature (Figure 49). We focused our attention on the pre-edge feature that has been discussed extensively in the literature [1]. In particular, it has been connected to distorted and broken hydrogen bonds, and has been used to support a two-component model.

We find that the temperature dependence of the pre-edge intensity in our data does indeed display van't Hoff

**Fig. 49:** The temperature dependence of the oxygen near-edge spectrum. A smoothed version of the 1.6°C spectrum is shown for reference throughout.



behaviour (Figure 50). However, the enthalpy difference,  $\Delta H$ , between the two assumed components obtained from a van't Hoff fit to our data is small, only  $0.9 \pm 0.2$  kcal/mol. This is of the order of the latent heat of melting from ice lh to liquid (1.43 kcal/mol), but much smaller than the strength of one hydrogen bond (out of two per molecule) in ice, 5.5 kcal/mol. In terms of hydrogen bond strengths, the two populations are found to be very similar. In our earlier work we showed that the near-edge region in various ice polymorphs is sensitive to non-hydrogen-bonded neighbours [2]. The current results indicate that the pre-edge in liquid water is sensitive to distortions that leave hydrogen bonds intact. Earlier studies proposing that severe distortion and breaking of hydrogen bonds is needed to produce the pre-edge feature should be revisited. Our results are furthermore consistent with the continuum models of molecular dynamics simulations, bridging an important gap between computer simulation and X-ray spectroscopy experiments.

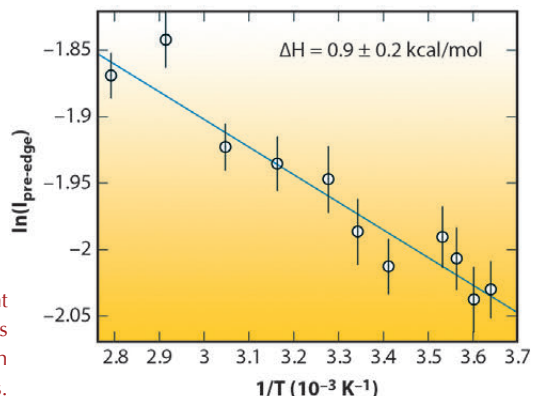


**Fig. 50:** The intensity of the pre-edge component displays van't Hoff behaviour. A fit to the data gives an enthalpy change  $\Delta H$  in the conversion between two components.

#### References

- [1] For a recent review, see A. Nilsson and L. G. M. Pettersson, *Chem. Phys.* **389**, 1-34 (2011).  
 [2] T. Pytkänen, V. M. Giordano, J.-C. Chervin, A. Sakko, M. Hakala, J. A. Soininen, K. Hämäläinen, G. Monaco and S. Huotari, *J. Phys. Chem. B* **114**, 3804-3808 (2010).

#### Principal publication and authors

R.H. Coridan (a), N.W. Schmidt (a), G.H. Lai (a), P. Abbamonte (b) and G.C.L. Wong (a), *Physical Review E* **85**, 031501 (2012).

(a) University of California, Los Angeles (USA)

(b) University of Illinois at Urbana-Champaign (USA)

## Femtosecond movies of confined water reconstructed from IXS data

An understanding of nanoconfined water and structure water has been a fundamental challenge to physics and chemistry and has important consequences in molecular biology and environmental sciences. Recent experimental and computational results have given interesting but conflicting results, ranging from liquid-like water to solid-like water.

The dynamical structure factor  $S(q, \omega)$  measured by inelastic X-ray scattering (IXS)

contains detailed information regarding the interactions of a system. This can be seen in the dispersion relations directly derived from IXS measurements, but it can also be seen in other ways. The electrodynamic response function  $\chi(q, \omega)$  can be extracted from measurements of  $S(q, \omega)$  by Kramers-Kronig relations. Recently, we showed that the portion of  $\chi(q, \omega)$  that encapsulates the solvent response on molecular time and length scales in liquid water can be extracted from meV-IXS measurements of  $S(q, \omega)$



performed at beamline ID28 [1] (Figure 51). The Fourier-transformed real space Green's function  $\chi(r-r', t-t')$  can be used to image density fluctuations to resolutions of roughly 20 fs in time and 0.4 Å in space.

Using this measured response function we examined how a 'bulk' homogeneous fluid responds to nanoconfinement. In doing so, we distinguish confinement effects from the termination of a bulk fluid from effects that originate in confinement-induced phase transitions. We computationally reconstructed the dynamical hydration structure of water between two hydrophilic sheets, modelled as semi-infinite slabs separated by a distance  $D$  and decorated with charge dipole interaction sites [2]. Here, we show the dynamics of a confined water layer when one slab is sheared while the other remains stationary.

We found a variety of distinct hydration structures that changed both with the degree of confinement and the dipole density on each surface. For large  $D$ , the hydration structure in between the sheets is essentially bulk-like, and the influence of one sheet on the other is imperceptible. Even at roughly 1 nm away from the surface, the density fluctuations are still indistinguishable from bulk-like water. As the intermolecular bond length between molecules is only about 0.3 nm, only a few layers of water interact with the surface.

Of particular interest is the nanoconfined water dynamics observed as the hydrophilic slabs are sheared past one another. When  $D$  approaches 10 Å, these few layers of water decorating each sheet begin to interact more strongly with one another. However, water remains bulk-like between the two distorted surface-associated hydration layers. When  $D$  decreases to 6 Å (nominally two water molecular thicknesses), the two surface-associated hydration layers are forced to reconstruct into a single, frustrated layer. A series of "freeze-melt" behaviour is observed in this layer of water: As one hydrophilic slab shears past the other, this layer transforms from a well-defined layer bridging the two surfaces, called "freeze" (Figure 52a), to completely amorphous, delocalised layer, "melt" (Figure 52c), as the dipoles across the gap become out of register. Interestingly, as the dipole

density increases, the hydration structures between nearest neighbour dipole sites on the same slab begin to interfere, creating a continuous hydration structure on that slab. In this limit, the "freeze-

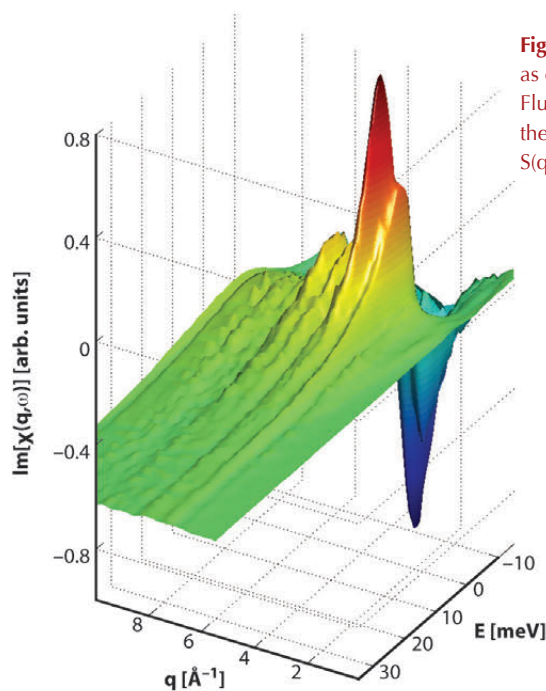


Fig. 51: The imaginary part of  $\chi(q, \omega)$ , as determined by applying the Fluctuation-Dissipation theorem to the measured dynamic structure factor  $S(q, \omega)$ :  $\text{Im}[\chi(q, \omega)] = -\pi[S(q, \omega) - S(q, -\omega)]$ .

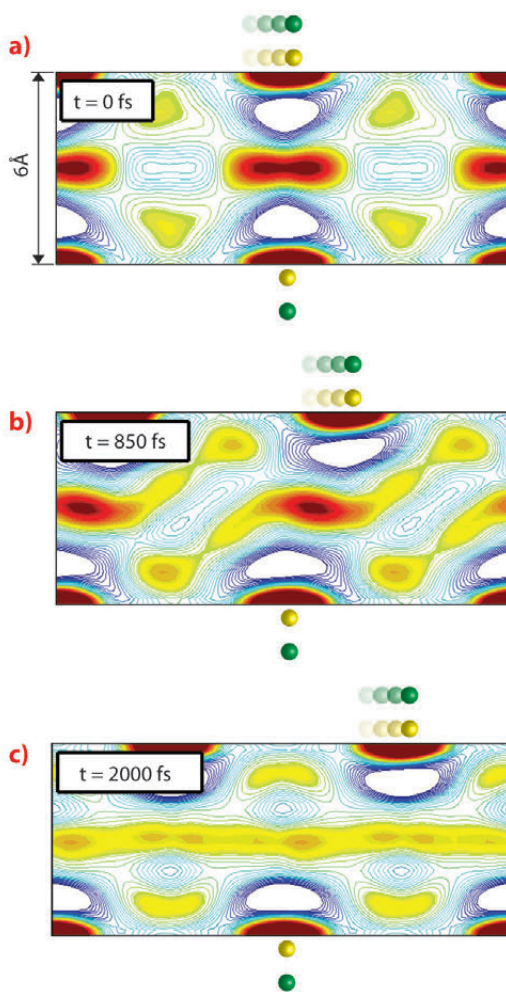


Fig. 52: The shear dynamics of water confined between hydrophilic slabs separated by  $D = 6$  Å and decorated by dipoles (green/yellow spheres) with inter-dipole distance  $a = 7$  Å. In this reconstruction, the top slab is being sheared with a velocity of 200 m/s past the stationary bottom slab. Red and blue contours indicate regions of water density that are respectively greater than or less than bulk. When the shearing dipoles are in register with the stationary ones (a), the water density is localised, bridging the static hydration shells of the nearest dipole sites on each slab, as if they were "frozen". As the top slab becomes out of register with the bottom, this structure transforms (b) and begins to become amorphous. When the slabs are completely out of register (c), the layer between them "melts" into a disordered, one-dimensional fluid layer. The process is reversed as the sites come back into register, leading to periodic "freeze-thaw" dynamics.



### References

- [1] R.H. Coridan, N.W. Schmidt, G.H. Lai, R. Godawat, M. Krisch, S. Garde, P. Abbamonte and G.C.L. Wong, *Physical Review Letters* **103**, 237402 (2009).  
 [2] R.H. Coridan, N.W. Schmidt, G.H. Lai and G.C.L. Wong, *Journal of Physics: Condensed Matter* **21**, 424115 (2009).

melt” dynamics disappear as the slabs are sheared.

These results have interesting implications. We found that a broad range of observations from our system agree with other experimental and computational studies of confined water, and may reconcile disparate results on confined water – this is surprising since we

started with bulk response functions. That the “freeze-melt” behaviour is seen to essentially disappear may have implications for high lubricity surfaces, such as those found in biology (ex: the highly charged and disordered polymer brushes found in mammalian joints). We hope to apply our hybrid technique to reconstructing water dynamics in other interesting geometries.

### Principal publication and authors

B. Moeser (a), A. Janoschka (a), J.A. Wolny (a), H. Paulsen (b), I. Filipov (c), R.E. Berry (c), H. Zhang (c), A.I. Chumakov (d), F.A. Walker (c) and V. Schönemann (a), *J. Am. Chem. Soc.* **134**, 4216 (2012).  
 (a) Department of Physics, University of Kaiserslautern (Germany)  
 (b) Institute of Physics, University of Lübeck (Germany)  
 (c) Department of Chemistry and Biochemistry, University of Arizona, Tucson (USA)  
 (d) ESRF

## Nuclear resonance scattering enlightens binding of cardiovascular regulatory NO to heme proteins

The diatomic molecule nitric oxide, NO, plays an essential role as a signal molecule for cardiovascular regulation, the regulation of cell function and as a neurotransmitter in vertebrates, as well as a toxic defence substance for eliminating invading organisms [1]. NO is toxic in high concentration, its production and transport are strongly regulated. Insects such as the Amazon river-based kissing bug *Rhodnius prolixus* have developed the strategy of causing vasodilation by injecting the suite of NO-transporter heme proteins, the nitrophorins (NP), into the tissues and capillaries of their victims [2]. NO dissociates upon dilution and pH rises from ~5–6 in the salivary glands of the insect to ~7.3–7.4 when the saliva is injected into the victim’s tissues.

We have found that nuclear inelastic scattering (NIS) could not only pin down heme NO binding modes in nitrophorins, but also possibly functionally relevant low-energy modes at energies down to  $10\text{ cm}^{-1}$ , and all this in one experiment. The experimental iron vibrational density of states (DOS) shown in **Figure 53a** exhibits a broad dominant peak around  $600\text{ cm}^{-1}$  and has also been calculated by quantum mechanical (QM) density functional theory (DFT) coupled with molecular mechanics (MM) methods. The simulations identify this dominant peak as caused by iron-NO binding modes with major stretching character. The simulation shown in **Figure 53b** was performed with the heme carboxylates of NP2-NO both being protonated. This was motivated by the low pH of the NP2-NO sample (pH 5.5), which was chosen to be similar to that of the saliva of *R. prolixus*. The calculations in **Figure 53c** show that deprotonation of the heme carboxylates significantly reduces the iron-NO stretching frequencies. This indicates an unexpected effect, namely a weakening of the iron-NO bond, which might occur even *in vivo* when, after being bitten, the nitrophorins are injected into the neutral pH blood of the victim.

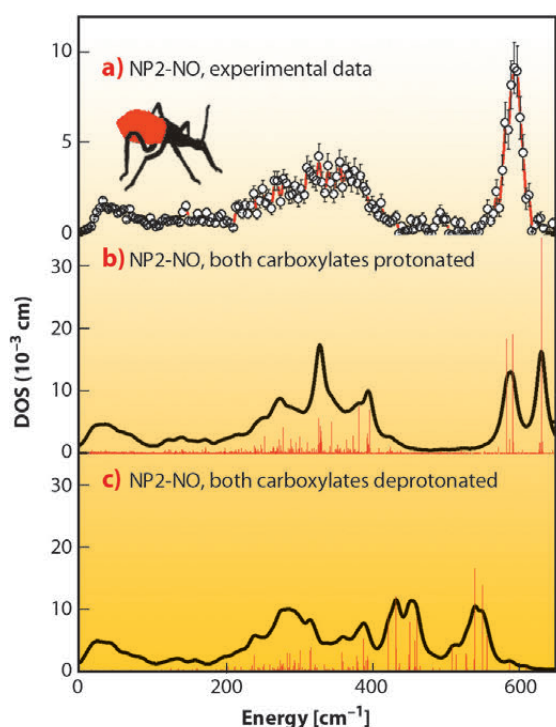


**Fig. 53:** Iron vibrational density of states (DOS) for NP2-NO: a) experimental data, b) simulation with both heme carboxylates protonated, and c) with both heme carboxylates deprotonated. Reprinted with permission from B. Moeser *et al.* *J. Am. Chem. Soc.* **134**, 4216. Copyright (2012) American Chemical Society.



At energies below  $100\text{ cm}^{-1}$  about 300 protein modes have been calculated. Among the most intense are 4 modes around  $70\text{ cm}^{-1}$  all of which involve considerable heme doming. It is also striking that the experimental NIS spectrum of NP2-NO has a band at  $68\text{ cm}^{-1}$  (Figure 54). The remaining three modes with the highest iron displacement below  $100\text{ cm}^{-1}$  are at 17, 36, and  $29\text{ cm}^{-1}$ . These modes represent mainly a heme sliding motion [3], which is around  $36\text{ cm}^{-1}$  coupled to a twisting of the  $\beta$ -barrel subunits. Indeed, there is also an experimentally observed band at around  $32\text{ cm}^{-1}$ . These low-energy heme modes are believed to be functionally relevant and may support NO capture and release, not only in nitrophorins but also in other heme proteins as well.

The presented results may be important with regard to a potential application of these type of NO carrier proteins and also other heme-containing systems such as cardiovascular drugs. The binding of NO to heme iron can obviously be affected by the pH-value of the fluid environment, an effect which has not been considered before.

#### References

- [1] S. Moncada, R.M.J. Palmer and E.A. Higgs, *Pharmacol. Rev.* **43**, 109-142 (1991).
- [2] J.M.C. Ribeiro, J.M.H. Hazzard, R.H. Nussenzweig, D.E. Champagne and F.A. Walker, *Science* **260**, 539-541 (1993).
- [3] K. Achterhold and F.G. Parak, *J. Phys: Condens. Matter* **15**, S1683-S1692 (2003).

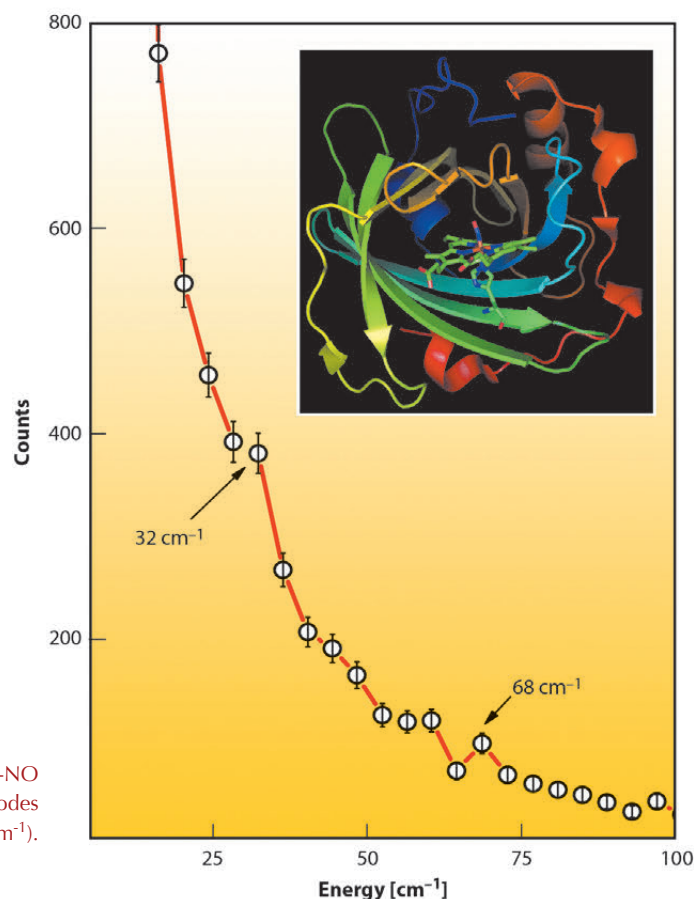


**Fig. 54:** Low-energy region of the raw NIS data of NP2-NO with indicated peaks caused by translational heme modes ( $32\text{ cm}^{-1}$ ) and by heme doming modes ( $68\text{ cm}^{-1}$ ).



## X-ray Imaging

The set of highlights presented in this chapter shows, as usual, that the application of X-ray imaging techniques at the ESRF covers a very wide range of scientific domains: from biomedical applications and life sciences to materials, cultural heritage and environmental science. We are constantly striving to further improve the imaging capabilities, in particular lateral resolution, detection limits and speed of acquisition. Imaging is indeed one of the five flagships of Phase I of the ESRF Upgrade Programme. A set of upgrade beamlines (UPBL) are under construction, among which the NINA beamline composed of two independent branches: NI for nano-imaging, NA for nano-analysis. Its satellite building was inaugurated in October 2012 and hutches are currently being constructed. The ID19 beamline is also benefitting from a complete refurbishment partially carried out in conjunction with developments at ID17 and in the so-called paleontology facility. One of the numerous objectives of this refurbishment is to facilitate the transfer of samples between ID17 and ID19 to allow the combination of large field of view/medium resolution (ID17) with medium field of view/high resolution (ID19). This was achieved through the installation of four identical large sample stages (one at ID17, two at ID19, and also one at BM05) and the development of a standardised control system. Generally speaking, the combination of techniques, whether on a single beamline or on several, is an increasing trend. In the following examples, the elucidation of degradation processes affecting Van Gogh's paintings was done by combining  $\mu$ XRF/ $\mu$ XRD at ID18F and  $\mu$ FTIR,  $\mu$ XRF/ $\mu$ XANES at ID21, and the study of geometrical carrier confinement within a single nanowire was carried out by collecting simultaneously optical luminescence and X-ray fluorescence.

Another general issue, illustrated by several of the following highlights, is the dose and the different approaches to limit possible radiation damage. At ID17, Zhao *et al.* implemented the so-called "EST based PCT" method, for equally sloped tomography based phase contrast X-ray tomography, which allows a simultaneous increase in resolution and decrease in the dose and acquisition time relative to conventional phase contrast tomography. Their work is illustrated by application to diagnosis of human breast cancers. Similar efforts to improve data acquisition and processing methods permitted further development of the X-ray grating interferometry technique at ID19, which offers a real trimodal

(phase contrast, absorption contrast and scattering "dark-field" contrast) low-dose X-ray tomography.

Focusing the beam to micro and even nano probes makes dose and the consequent radiation damage even more critical. The use of a cryo-environment is a common solution, in particular for the study of biological samples. For the future NINA end-stations, the implementation of such environments is both mandatory and challenging. At ID21, different instrumental developments were recently implemented to improve the preparation and analysis of samples under cryoconditions. The study of TiO<sub>2</sub> uptake in cucumber plants presented hereafter was carried out a few months ago at room temperature but would clearly have benefitted from these new cryo devices, judging from the success of similar recent experiments. The cryo-environment was also a necessity for the experiments of Deville *et al.* to follow the freezing of colloidal suspensions and subsequently observe the frozen microstructure, as done at ID19.

A room temperature alternative to cryo-microscopy was demonstrated in the article by Beerlink *et al.* where a native lipid bilayer membrane of less than 5 nm was imaged using an intense nanofocused beam in relatively low-dose conditions. This was made possible by positioning the sample a few millimetres downstream of the focal plane and by exploiting the contrast formed by the free space propagation of hard X-rays. Such an approach opens the way to many new investigations like membrane fusion, membrane phase transitions, and the transport of molecules through bilayers.

As in previous years, this chapter contains only a sub-set of many interesting results published during the year and obviously there are many omissions due to lack of space. In particular, two domains are not represented, which regularly use the X-ray imaging instruments: palaeontology (e.g. fossil bone 3-D virtual histology [Sanchez *et al.*, *Microscopy and Microanalysis* 18, 1095-1105 (2012)]) and evolutionary biology (e.g. *in ovo* 3-D embryology on crocodiles, **Figure 55**); and Earth sciences, where the micrometric resolution and imaging capabilities are regularly associated to X-ray absorption spectroscopy in order to identify and localise different speciations of key elements such as iron, and consequently monitor fundamental redox processes [Borfecchia, *J. Anal.*



*At. Spectrom.* 27, 1725 (2012); Beck, *Geochimica et Cosmochimica Acta* 99, 305 (2012)].

2013 will be a fundamental year for X-ray imaging at the ESRF. Work will continue for the phase I projects of UPBL4-NINA and the ID19/ID17/paleontology refurbishment with various steps of implementation and commissioning being scheduled. Discussions will also

start regarding phase II.

While phase I was oriented towards improved resolution (in particular nanoscopy), phase II could be the opportunity to explore temporal resolution. Hence the name of the workshop, satellite to the 2013 Users meeting: “X-ray cinematography with the new coherent source”.

M. Cotte



**Fig. 55:** 3-D imaging of various developmental stages of Nile crocodile embryos *in ovo* (from la Ferme aux crocodiles, Pierrelatte, France) using long distance propagation phase contrast tomography at beamline ID19. In addition to the skeleton development highlighted here, this approach allows the anatomy of the soft tissue to be visualised. These samples were studied within a research project on archosaur phylogeny (crocodiles, dinosaurs, birds). By studying the embryological development of modern crocodiles and birds, it is possible to derive information to better understand the evolutionary transition from dinosaurs to birds. Credits: Martin Kunderát (Uppsala University) / Paul Tafforeau (ESRF).

## ■ Towards reduced radiation dose for 3-D breast cancer scans

Early detection of breast cancer contributes to an improved prognosis and results in reduced disease mortality. The breast cancer screening technique used today in clinics is “dual-view digital mammography”. Its limitation is that it only provides two images of the breast, which can explain why up to 20% of breast tumours are not detectable on mammograms. Mammograms can also sometimes appear abnormal, when no breast cancers are actually present. Computed tomography (CT) allows a precise 3-D visualisation of the human body but it cannot be routinely applied in breast cancer diagnosis because of the high radiosensitivity of the breast, which significantly reduces the benefit-risk ratio. The potential induction of tumours due to the exam itself is considered too high. Recognising these limitations, we

have developed a way to produce three-dimensional X-ray images of the breast at a radiation dose that is lower than the 2D radiographies used in clinics. Phase contrast X-ray tomography at 60 keV of a whole human breast has been performed at ID17. Images were reconstructed applying the so-called “equally sloped tomography” (EST) algorithm using 512 projections to produce 3-D images of the organ at a resolution higher than that used in clinical CT (pixel size of 92  $\mu\text{m}$  vs more than 200  $\mu\text{m}$  for clinical CT scanners) and at a lower dose than that of dual view mammography (which is typically about 3 mGy). The new method allows a clear and precise identification of a malignant cancer. According to a blind evaluation by five experienced radiologists, this method can reduce the radiation dose and acquisition time by ~74% relative

### Principal publication and authors

Y. Zhao (a), E. Brun (b,c), P. Coan (c,d), Z. Huang (a), A. Sztrókay (d), P. C. Diemoz (c), S. Liebhardt (d), A. Mittone (c), S. Gasilov (c), J. Miao (a) and A. Bravin (b), *PNAS* 109, 18290-18294 (2012).

(a) Department of Physics and Astronomy and California NanoSystems Institute, University of California, Los Angeles (USA)

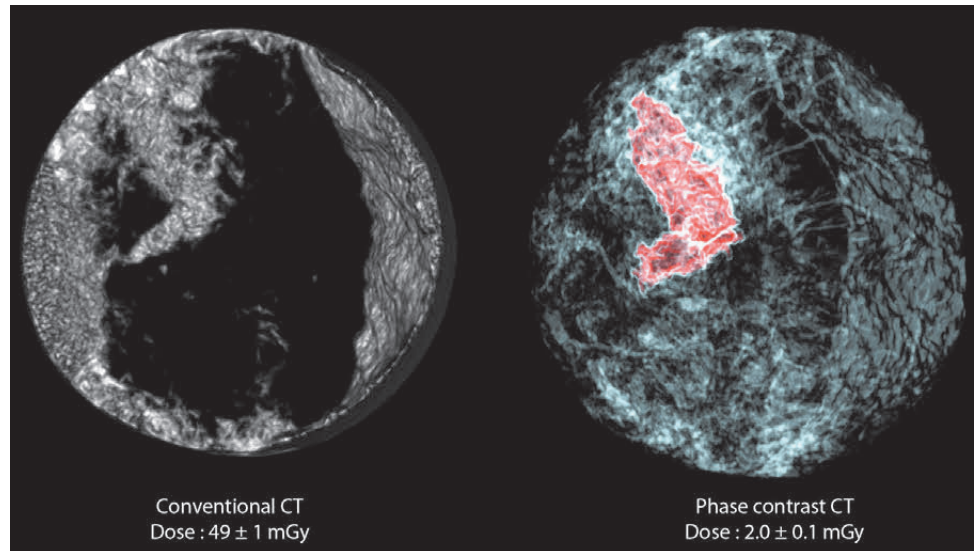
(b) ESRF

(c) Faculty of Physics, Ludwig Maximilians University, Garching (Germany)

(d) Department of Clinical Radiology, Ludwig Maximilians University, Munich (Germany)



**Fig. 56:** Comparison between a conventional CT scan of the breast sample and a scan using EST with phase contrast imaging. In the latter image, the tumour is highlighted in red. The radiation dose needed for the scans is indicated at the bottom.



to conventional phase-contrast X-ray tomography, while maintaining high resolution and contrast. Despite the significant reduction in the number of projections used (corresponding to an important saving in dose and acquisition time), radiologists ranked the generated images as having the highest sharpness, contrast, and overall image quality compared to 3-D images of breast tissue created through other standard methods (based on the filtered back projection algorithm (FBP)) (**Figure 56**).

CT scans for early detection of breast cancer may now become possible thanks to the combination of three ingredients: high energy X-rays, phase contrast imaging and the use of a sophisticated novel mathematical algorithm, the EST, to reconstruct the CT images from X-ray data. Tissues are more transparent to high energy X-rays and therefore less dose is deposited (a factor of 6 in radiation dose reduction). The phase contrast imaging technique may allow contrast to be observed due to the phase modulation of X-rays, even if the amplitude (*i.e.* absorption) modulation is weak or absent, with a dose to the tissues similar or even reduced compared to conventional absorption radiography. Finally, the EST method is a Fourier-based iterative method that iterates back and forth between real and Fourier space using the pseudo-polar fast Fourier transform. At each iteration, physical constraints, including the sample boundary and the non-negativity of the sample structure, are enforced in real space, while the Fourier transform of the measured projections are imposed in Fourier space. As a result, the EST

needs 4 times less radiation than FBP to produce images of the same quality (**Figure 57**).

It was therefore demonstrated that diagnostic CT images can be produced with a spatial resolution 2-3 times higher than present hospital scanners, but with a radiation dose that is about 25 times lower. This new technique can open the doors to the clinical use of CT in mamography, which would be a powerful tool in the fight against breast cancer.

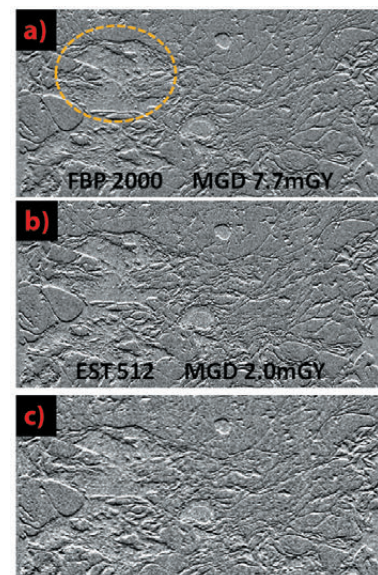


**Fig. 57:** Image quality comparison of the phase contrast CT images of the whole breast (9 cm diameter), reconstructed using the conventional (Hamming filtered) FBP algorithm or the EST. a) A 92- $\mu$ m-thick sagittal slice of the FBP reconstruction using 2000 projections, b) EST using 512 projections or c) EST 200. The yellow ellipse indicates a tumour region. FBP 2000 and EST 512 have the highest image quality, EST 200 (with 1/10 of the dose necessary to reconstruct the FBP2000) still shows a high contrast.

## Brain tumour localisation and destruction facilitated by gadolinium-based nanoparticles in microbeam radiation therapy

Microbeam radiation therapy (MRT) can be enhanced by the prior administration of gadolinium-based nanoparticles to the patient. The nanoparticles have a radiosensitising effect that is activated by X-ray microbeams [1]. The nanoparticles also improve contrast in magnetic resonance imaging (MRI) permitting localisation of the tumour [2]. These two beneficial properties allow theranostic applications to be envisaged using the same drug as contrast and dose media.

The new technique has been tested at the ESRF's biomedical beamline ID17. Following treatment, rats bearing very aggressive brain tumours survived five times longer than non treated rats. **Figure 58** presents a summary of the results. The median survival time of non-treated tumour bearing rats was around 19 days while it reached 47 days for those treated by MRT alone. The median survival time increased even further to 93 days when the MRT treatment was carried out 20 minutes after an intravenous injection of gadolinium oxide nanoparticles.

For treatments combining MRT with gadolinium based nanoparticles, the time delay between the administration of the nanoparticles and the subsequent MRT irradiation proved critical. When the time delay was 5 minutes, the median survival time fell to 35 days, *i.e.* lower than the survival time achieved with MRT alone. The variation in the survival time is most probably caused by the non-uniform distribution of the nanoparticles within the brain. MRI images reveal that the nanoparticles concentrate within and around the tumour tissue (**Figure 59**). The dependency of the survival time on the time delay post injection leads to the conclusion that the difference in gadolinium nanoparticle concentration between the tumour and healthy tissue is highly significant, and more important than achieving the ultimate dose within the tumour because healthy tissue can be equally damaged by the dose enhancement induced by the nanoparticles. In other words, even if the total concentration of nanoparticles

in the tumour affected tissue (**Figure 59**, right hemisphere) is lower 20 minutes after injection than at 5 minutes after injection, the higher contrast between the nanoparticle concentration in tumour affected tissue and non affected tissue (**Figure 59**, left hemisphere) dominates by prolonging the survival time.

The gadolinium nanoparticles have also proven beneficial for MRI, which is the standard imaging technique used for the diagnosis of a brain tumour. The nanoparticles help to delineate the tumour and its surrounding vasculature because the nanoparticles leak from the vascular bed to the interstitial space between the tumour cells. This is demonstrated by **Figure 59** where the tumour has better contrast than the healthy tissue. Gadolinium nanoparticles are therefore appealing as dual modality drugs for their beneficial effect on the treatment as well as for the possibility of performing imaging-guided therapy.

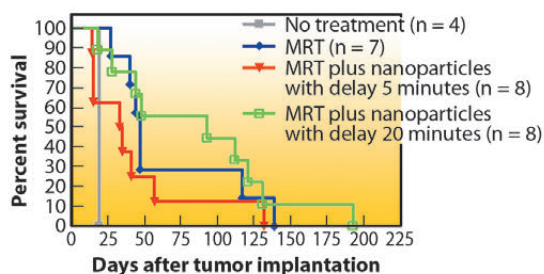


**Fig. 58:** Survival curves for tumour bearing rats. Without treatment (grey curve,  $n=4$  rats), treated by MRT only (blue curve,  $n=7$ ) and treated by MRT following intravenous injection of nanoparticles with delays of 5 minutes (red curve,  $n=8$ ) and 20 minutes (green curve,  $n=8$ ). The MRT irradiation was done in cross fire mode, using  $50\ \mu\text{m}$  wide X-ray beams with a spacing of  $211\ \mu\text{m}$  between the beams. The skin entrance dose was set up at 400 Gy for the peak and 20 Gy for the valley.

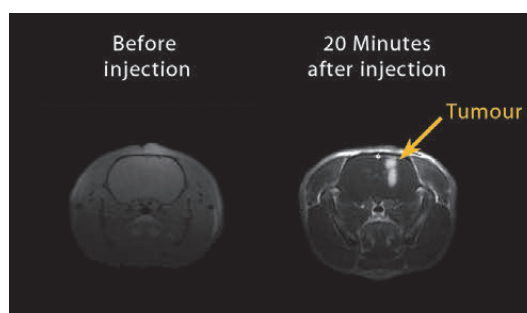


**Fig. 59:** MRI images of rat brain glioma before and 20 minutes after injection of gadolinium nanoparticles. The tumour and surrounding tissues are revealed by the effect of the particles on the MRI signal.

### Principal publication and authors

G. Le Duc (a), I. Miladi (b), C. Alric (b), P. Mowat (b), E. Brauer Krisch (a), A. Bouchet (a), E. Khalil (c), C. Billotey (b), M. Janier (b), F. Lux (b), T. Epicier (d), P. Perriat (e), S. Roux (b,d) and O. Tillement (b), *ACS Nano* **5**, 9566-74 (2011).

(a) ESRF

(b) Laboratoire de Physico-Chimie des Matériaux Luminescents, UMR 5620 CNRS – Université Claude Bernard, Lyon (France)

(c) Faculty of Pharmacy, University of Jordan, Amman (Jordan)

(d) Institut UTINAM, UMR6213 CNRS-UFC, Université de Franche-Comté, Besançon (France)

(e) Matériaux, Ingénierie et Sciences, UMR 5510 CNRS-INSA, Université Claude Bernard, Lyon (France)



The nanoparticles were designed and produced by the Laboratoire de Chimie des Matériaux Luminescents (Université Claude Bernard, Lyon, France). First *in vivo* trials were performed at the ESRF in 2007 in preparation for the experiments

presented here. Ongoing studies aim at a treatment where one injection will serve both diagnosis and therapy, using the remanence of the nanoparticles in the tissue up to and over 24 hours following injection.

#### References

- [1] O. Tillement, S. Roux, G. Le Duc, P. Perriat, C. Mandon, B. Mutelet, C. Alric, C. Billotey, M. Janier and C. Louis, Utilisation de nanoparticules à base de lanthanides comme agents radiosensibilisants, Patent FR N 07 58348, 17 Oct 2007.
- [2] F. Lux, A. Mignot, P. Mowat, C. Louis, S. Dufort, C. Bernhard, F. Denat, F. Boschetti, C. Brunet, R. Antoine, P. Dugourd, S. Laurent, L. Vander Elst, R. Muller, L. Sancey, V. Josserand, J.L. Coll, V. Stupar, E. Barbier, C. Rémy, A. Broisat, C. Ghezzi, G. Le Duc, S. Roux, P. Perriat and O. Tillement, *Angew Chem Int Ed Engl.* **50**, 12299-303 (2011).

#### Principal publication and authors

I. Zanette (a, b), M. Bech (b), A. Rack (a), G. Le Duc (a), P. Tafforeau (a), C. David (c), J. Mohr (d), F. Pfeiffer (b) and T. Weitkamp (e), *Proc. Natl. Acad. Sci. USA* **109**, 10199–10204 (2012).

(a) ESRF

(b) Department of Physics and Institute for Medical Engineering, Technische Universität München, Garching (Germany)

(c) Laboratory for Micro- and Nanotechnology, Paul Scherrer Institut, Villigen (Switzerland)

(d) Karlsruhe Institute of Technology, Institute for Microstructure Technology, Karlsruhe (Germany)

(e) Synchrotron Soleil, Gif-sur-Yvette (France)

## ■ Trimodal X-ray tomography with reduced dose

Many areas of modern medicine, such as diagnosis, treatment planning, and fundamental research rely heavily on imaging techniques. However, the different methods currently used in medical imaging have their own limitations. Histological methods, for example, provide hardly any three-dimensional information. The most common 3-D methods, on the other hand, are limited either in soft-tissue contrast (conventional absorption X-ray imaging) or spatial resolution (magnetic resonance imaging).

A new X-ray imaging technique known as “grating interferometry” (XGI), which uses interactions between X-rays

and matter other than absorption to obtain contrast, provides images with unprecedented density contrast and high spatial resolution of a few micrometres. The superb density sensitivity down to  $0.5 \text{ mg/cm}^3$  in the phase-contrast images obtained with XGI allows soft tissues with very tiny differences in composition to be discerned, see [1,2] and **Figure 60**. Moreover, XGI also yields the so-called “dark-field” signal, which reveals the presence of sub-pixel-size scattering structures in the object, such as fibres, cracks or nanosized pores.

Depending on the properties of the source, the interferometer consists of two or three line grids with high aspect ratios and periods of a few micrometres. One of these gratings is scanned transversally to obtain the different image signals [2]. An important advantage of this method over other phase-contrast X-ray techniques is that XGI also performs well for low-brilliance laboratory sources. The possibility of transferring this technique to clinical practice is under investigation in Europe and Japan, where prototypes of small animal scanners and preclinical machines using XGI are being developed.

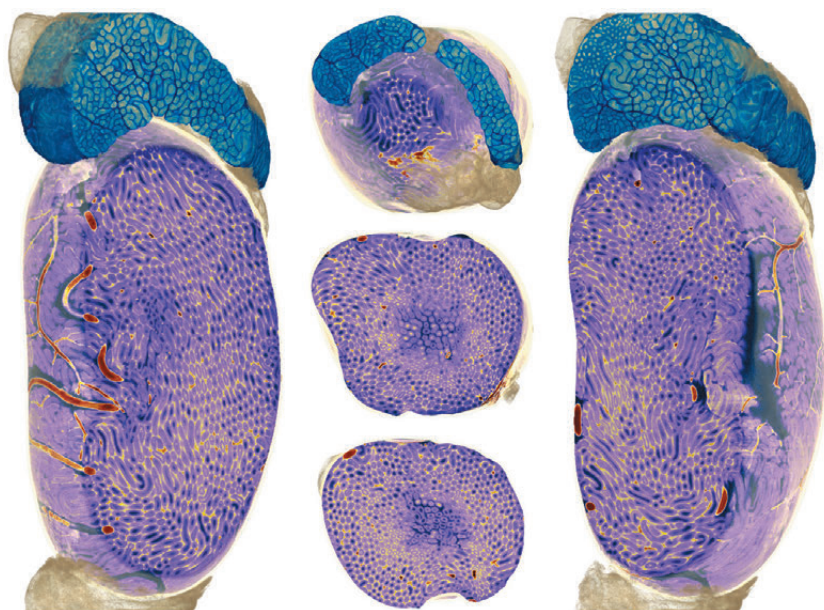


**Fig. 60:** Different sections through the phase tomogram of a rat testicle obtained with XGI. The epididymis is shown in blue and the adipose tissue is coloured yellow. Inside the testis, the seminiferous tubules and the vessels (in dark red) are clearly visible.

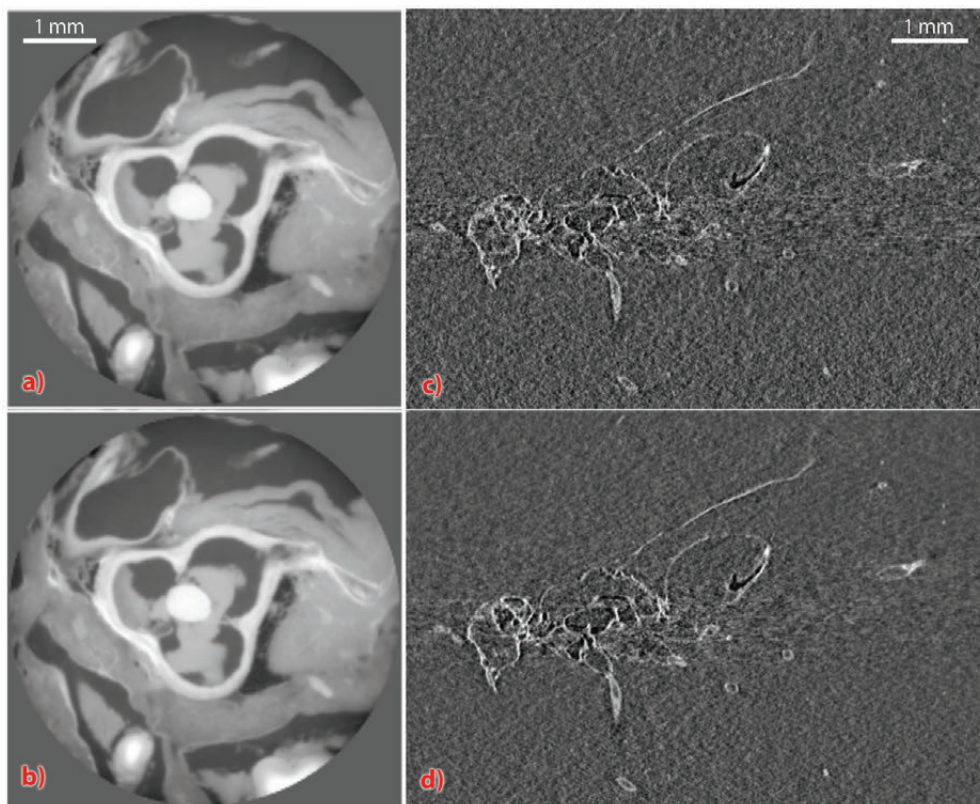


**Fig. 61:** Comparison between grating-based tomograms obtained with the standard method (top) with tomograms of the same specimen obtained with the sliding window protocol (bottom). Further information is given in the text.

One of the main challenges when irradiating patients with X-rays is to keep the radiation dose low. We have made an important step forward in optimising the application potential of this technique. The high-performance grating interferometer used in this study has been installed at beamline **ID19**.

Our development consists of a new measurement protocol for XGI-based tomography called the “sliding window” technique. Through simultaneous grating stepping and sample rotation, combined with advanced data analysis, phase and dark-field images of a given quality can be obtained faster and with much less dose than before. Moreover, this new protocol makes XGI compatible with continuous tomographic scans, in which the rotation of the detector and source relative to the sample does not stop or slow down as images are acquired. This mode is employed in most medical tomography scanners, unlike the stop-and-go mode used so far in XGI tomography.

The sliding window method has been demonstrated with simulations and experimental data collected at **ID19**. In **Figure 61** images taken with the sliding-window method are compared to images obtained with the standard procedure. The pictures on the left show phase

tomography slices of a mouse heart; the aortic valve is clearly visible at the centre of these images. **Figure 61a** was obtained with the standard procedure, **Figure 61b** with the sliding window method and 5 times less dose. Thanks to the advantages of the new protocol, these two images show very similar quality despite the large difference in dose. **Figure 61c** and **Figure 61d** show dark-field slices of a wasp in amber, obtained with the standard and the sliding-window methods, respectively. These two tomograms were obtained with the same radiation dose delivered to the sample. Their comparison demonstrates that the new method can significantly reduce image noise. It should also be noticed that the wing of the animal, corresponding to a small crack in the amber that is almost invisible in absorption as well as phase contrast, can be clearly revealed with the dark-field signal.

The complementarity of the image signals accessed with X-ray grating interferometry and the new simple and fast acquisition procedure make X-ray grating interferometry an attractive technique for high-sensitivity biomedical imaging and possibly also for future hospital CT scanners. The potential of this method should also be further investigated for materials science and palaeontology.

#### References

- [1] G. Schulz, C. Waschkies, F. Pfeiffer, I. Zanette, T. Weitkamp, C. David and B. Müller, *Scientific Reports*, **2**, 826 (2012).
- [2] I. Zanette, M. Bech, F. Pfeiffer and T. Weitkamp, *Applied Physics Letters* **98**, 094101 (2011).



### Principal publications and authors

A. Lasalle (a), S. Deville (a),  
C. Guizard (a), E. Maire (b) and  
J. Adrien (b), *Acta Materialia* **60**,  
4594–603 (2012).

(a) *Laboratoire de Synthèse et  
Fonctionnalisation des Céramiques,  
CNRS, Cavaillon (France)*

(b) *MATEIS, Université de Lyon,  
Villeurbanne (France)*

## Particle redistribution and defect development during the freezing of colloidal suspensions

The solidification of colloidal suspensions is commonly encountered in our everyday life through a variety of natural processes such as the freezing of soil and the growth of sea ice. It is also seen in engineering applications including food engineering, cryobiology, filtration and water purification. In materials science, the freezing of colloidal suspensions is finding applications in the processing of porous materials, usually referred to as ice templating or freeze-casting. This simple process, where a colloidal suspension is simply frozen under controlled conditions and then sublimated before sintering, provides materials with a unique porous architecture, where the porosity is a replica of that of ice crystals.

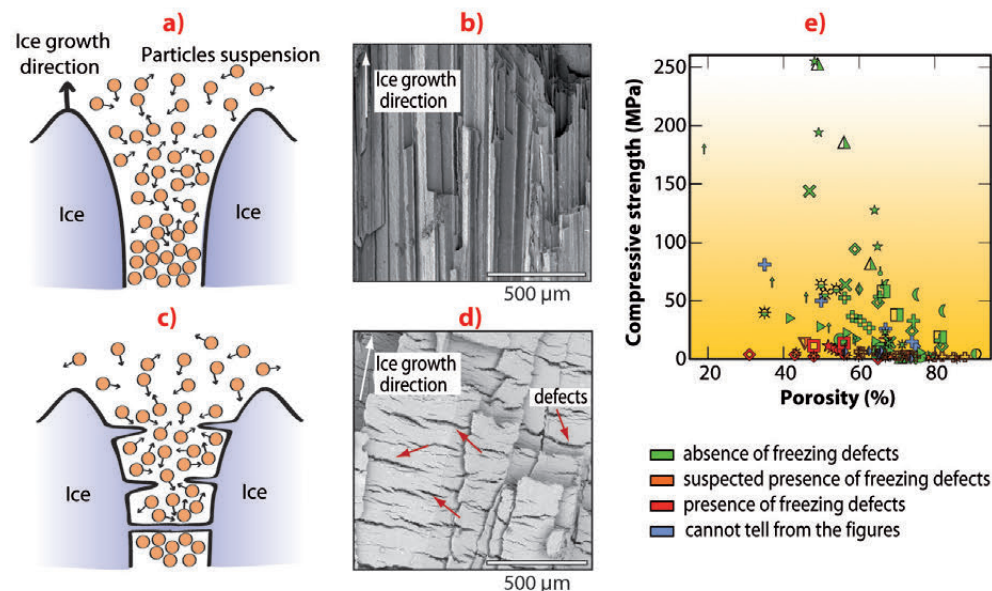
A wide range of compressive strength values is reported in the literature for ice-templated materials (**Figure 62e**). Microstructural observations revealed that many of the weakest samples in the literature had structural defects oriented perpendicular to the ice growth direction (**Figure 62d**). High-strength samples (**Figure 62b**) are systematically free of such defects. The absence of such defects is clearly a necessary but insufficient condition to obtain high compressive strength.

Our current understanding of the solidification of colloidal suspensions is

derived primarily from investigation of the behaviour of single particles relative to a moving interface. Many geological, biological and industrial systems involve concentrated particle systems. In colloidal systems, particle–particle electrostatic interactions can strongly determine the behaviour of the system (**Figure 62a**). Through systematic *in situ* X-ray imaging, we investigated the roles of the suspension composition and the particle–particle electrostatic interactions on defect formation during the freezing of colloidal suspensions. We performed *in situ* observations of crystal growth and particle redistribution during freezing by X-ray radiography and tomography at beamline **ID19**. We show that particle–particle interaction can have a dramatic influence on the mechanisms controlling the formation of the structure.

*In situ* radiography of the advancing freezing front shows a behaviour that is highly dependent on the components added in the initial suspension. 3-D tomographic reconstructions of frozen samples show a range of microstructure, from disoriented ice crystals (**Figure 63c**) to aligned, regular ice crystals (**Figure 63a**) corresponding to stable growth (**Figure 62a**). Defects are observed perpendicular to the freezing direction (**Figure 62d**, **Figure 63b**), forming pores that traverse the dense ceramic walls

**Fig. 62:** Particle redistribution in growing ice crystals for stable (a) and unstable (c) growth modes, and the corresponding microstructures (b, d) and mechanical properties from the literature (e). For unstable growth conditions, transverse ice crystals develop between adjacent crystals, forming crack-like defects in the final material.



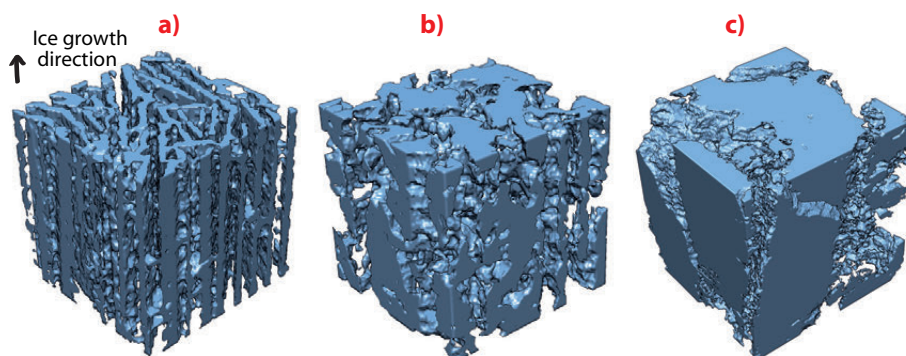


(Figure 62d), significantly affecting the integrity of the structure. The development of defects perpendicular to the main ice growth direction must be avoided to obtain a strong structure. Materials obtained under conditions promoting the development of such defects in the microstructure are practically useless. The perpendicular defects created here in ice-templated materials strongly resembles the ice lenses observed in geophysics. Ice lenses are ice crystals observed in frozen soils or during the directional solidification of colloidal suspension, growing perpendicular to the temperature gradient direction (Figure 62c). Since the porosity found here is a replica

of the ice crystal network obtained after freezing, ice lenses will result in the presence of crack-like pores perpendicular to the main ice growth direction.

The formation of defects was correlated with *in situ* observations revealing the apparition of flocculated and depleted zones in the concentrated suspension during freezing. Our results show that flocculation can be a viable mechanism to facilitate ice lens nucleation and growth in such a system, and are a first step towards incorporating particle–particle electrostatic interactions into our understanding and modelling of the freezing of colloids.

**Fig. 63:** 3-D reconstructions from tomography of the particle-rich regions between the ice crystals, for different formulations of the suspension. The structure can be either lamellar or homogeneous along the ice growth direction (a), or random and heterogeneous (c). The structure in (b) corresponds to the intermediate situation. The desirable structures from a materials science point of view correspond to that observed in (a). Scale is  $140 \times 140 \times 140 \mu\text{m}^3$ .

## ■ Translocation of $\text{TiO}_2$ nanoparticles from root to shoot in cucumber plants

The ever increasing use of nanoparticles has raised concerns about the consequences of their release into the environment.  $\text{TiO}_2$  nanoparticles have been released into the environment by a variety of applications [1]. A few studies have shown that  $\text{TiO}_2$  nanoparticles accumulate in roots and can affect plants in various ways and one report by Larue and coworkers [2] described the presence of  $\text{TiO}_2$  nanoparticles in the leaves of a grass plant. In the latter study, synchrotron micro X-ray fluorescence ( $\mu$ -XRF), combined with X-ray absorption near edge structure (XANES), was used to map the Ti elemental distribution and oxidation states in the roots and leaves of wheat (*Triticum aestivum*) treated with different size  $\text{TiO}_2$  nanoparticles in anatase and rutile forms. The researchers found the Ti species within the roots and leaves was  $\text{TiO}_2$  nanoparticles, with no changes in crystalline structure.

We used  $\mu$ -XRF combined with  $\mu$ -XANES at beamline ID21, to study the distribution

and speciation of Ti in vegetative tissues of cucumber (*Cucumis sativus*). Plant sample spectra were compared to spectra of reference materials  $\text{TiO}_2$  anatase and  $\text{TiO}_2$  rutile nanoparticles. Cucumber plants were hydroponically grown for 15 days in nutrient solution supplemented with  $\text{TiO}_2$  nanoparticles (anatase 82%, rutile 18%) at  $500 \text{ mg L}^{-1}$ .  $\mu$ -XRF images of transverse sections of  $\text{TiO}_2$  NP treated roots showed Ti in the epidermis and vascular tissues. In addition,  $\mu$ -XANES spectra of Ti in the epidermis and xylem resembled the crystalline phase of the anatase  $\text{TiO}_2$  reference material. However, in the root phloem, the  $\mu$ -XANES showed the presence of  $\text{TiO}_2$  mostly in the rutile crystalline phase. As phloem sap plays an important role in fruit formation, the aerial part of cucumber plants was screened for the presence of  $\text{TiO}_2$ . The  $\mu$ -XRF image of a transverse sectioned cucumber leaf showed the presence of Ti in the central vein of the leaf (Figure 64a, red colour).  $\mu$ -XANES spectra of red spots

### Principal publications and authors

A.D. Servin (a,b),  
H. Castillo-Michel (c),  
J.A. Hernandez-Viezcas (a,b),  
B. Corral Diaz (a),  
J.R. Peralta-Videa (a,b) and  
J.L. Gardea-Torresdey (a,b),  
*Environ. Sci. Technol.* **46**, 7637-7643 (2012).  
(a) Chemistry Department, The University of Texas at El Paso (USA)  
(b) University of California Center for Environmental Implications of Nanotechnology (USA)  
(c) ESRF



### References

- [1] L. Windler and B. Nowack, *Environ. Sci. Technol.* **46**, 8181-8188 (2012).  
 [2] C. Larue and M. Carriere, *Sci Total Environ.* **431**, 197-208 (2012).  
 [3] M. Isaure and A. Manceau, *Geochim. Cosmochim. Acta* **74**, 5817-5834 (2010).

from **Figure 64a** showed that most of the Ti in the leaf vein had the same spectral signature as the rutile  $\text{TiO}_2$  nanoparticles reference material (**Figure 64b**).

Trichomes are structures that protect plants from heat and water loss and they are also involved in heavy metal detoxification [3]. Most of the *Cucurbita* plants have trichomes in the aerial parts. We analysed leaf trichomes of cucumber plants treated with  $\text{TiO}_2$  nanoparticles.  $\mu$ -XRF images showed Ti in the base and body of the

trichomes, while the  $\mu$ -XANES spectra showed that Ti was present mostly in the rutile  $\text{TiO}_2$  NP crystalline phase. This suggests that leaf trichomes could be a possible sink or excretory system for Ti in cucumber plants.

In conclusion, the  $\mu$ -XRF and  $\mu$ -XANES analyses of root and leaf transversal sections have shown that the  $\text{TiO}_2$  nanoparticles can be absorbed by the roots and translocated to the aboveground plant parts in cucumber. It is noteworthy that cucumber plants were exposed to anatase/rutile mixture of  $\text{TiO}_2$  nanoparticles, but anatase remained preferentially in the root, while the rutile phase was mainly found in the aerial tissues. This could be a new biological way to separate anatase and rutile. This work also suggests that the  $\text{TiO}_2$  nanoparticles could be stored in cucumber fruits, entering the food chain and the next plant generation.

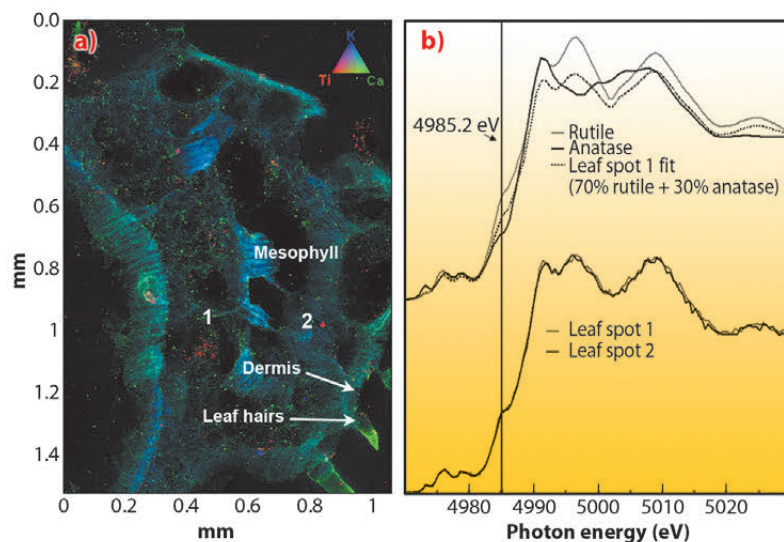


**Fig. 64:** a) Tricolour micro-XRF map of a transverse section of cucumber leaf treated for 15 days with  $500 \text{ mg L}^{-1}$   $\text{TiO}_2$  nanoparticles. Colours: red represents titanium, green for calcium, and blue for potassium. b) Micro-XANES spectra of reference materials and spot 1 and 2 from (a).

### Principal publication and authors

G. Van der Snickt (a),  
 K. Janssens (a), J. Dik (b),  
 W. de Nolf (a), F. Vanmeert (a),  
 J. Jaroszewicz (a), M. Cotte (c,d),  
 G. Falkenberg (e) and L. Van der  
 Loeff (f), *Anal. Chem.* **84**, 10221-  
 10228 (2012).

(a) University of Antwerp  
 (Belgium)

(b) Delft University of Technology  
 (The Netherlands)

(c) Laboratoire d'archéologie  
 moléculaire et structurale, CNRS  
 UMR 8220 (France)

(d) ESRF

(e) DESY (Germany)

(f) Kröller-Müller Museum (The  
 Netherlands)

## ■ The chemical processes behind Van Gogh's discolouring flowers

In the past, we elucidated the chemical process that caused the fading of the bright yellow colour on a painting by James Ensor, a contemporary of Vincent Van Gogh. For this Ensor case, experiments at ESRF beamlines **ID18F** and **ID21** demonstrated that the discolouration was caused by photo-oxidation of the original cadmium yellow pigment ( $\text{CdS}$ ) to colourless cadmium sulphate ( $\text{CdSO}_4$ ). In this work, a similar case was studied: the formation of a disturbing crust on the cadmium yellow paint strokes of a painting by Van Gogh. As **Figure 65** illustrates, a superimposed film of opaque greyish crystals completely obscures the original warm yellow colour of the underlying paint. In addition, the case was rendered more complex due to the presence of a varnish coating that was applied on top of the degraded paint

during a previous conservation treatment, most probably in an attempt to consolidate the affected paint.

Two samples were extracted from this degraded paint and analysed at beamlines **ID21** and **ID18F** and the P06 beamline of PETRA III at DESY. The combination of a number of complementary species-selective analytical techniques (*i.e.*  $\mu$ -XRF/ $\mu$ -XRD,  $\mu$ -XRF/ $\mu$ -XANES and  $\mu$ -FTIR) revealed the presence of a thin ( $< 10 \mu\text{m}$ ) film at the interface between the bulk  $\text{CdS}$  paint and the overlying varnish, containing cadmium oxalate, cadmium carbonate and lead sulphate (**Figure 66**). The identification of these compounds on the micrometre level enabled an explanation of the chemical pathway that led to the discolouration phenomenon observed at the macroscopic level.

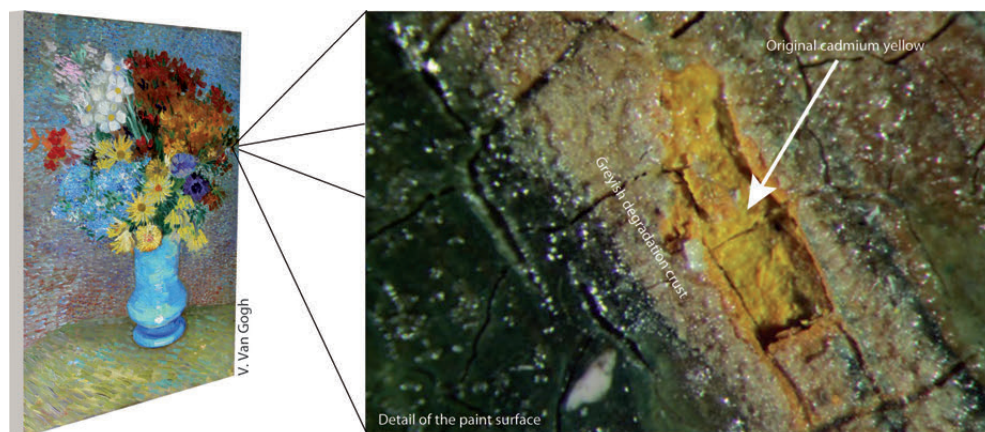


**Fig. 65:** Left: 'Flowers in a blue vase' painted by Vincent Van Gogh in Paris in 1887. Right: Detail of the paint surface: a greyish degradation crust is obscuring the original warm yellow cadmium sulphide paint.

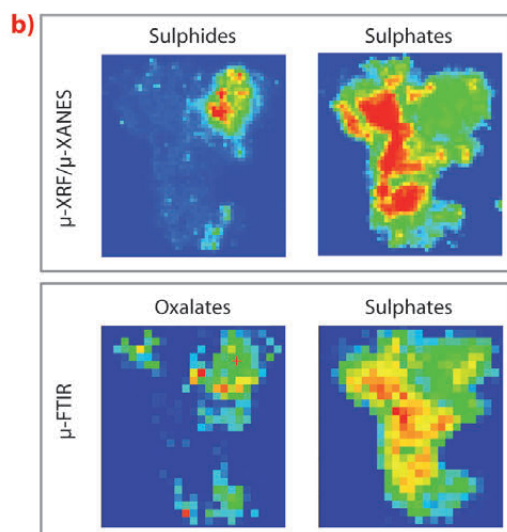
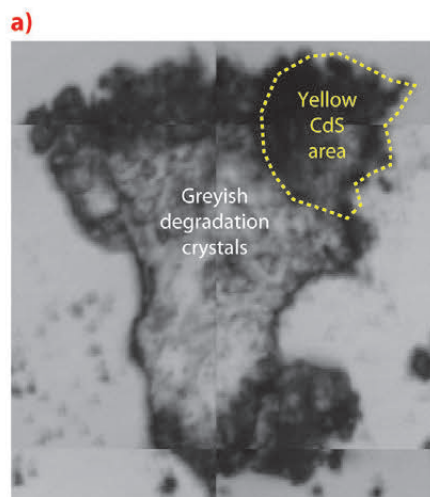
In spite of its divergent morphology, we concluded that the alteration on the Van Gogh still life was initially caused by oxidation of the original CdS pigment, similar to the Ensor case. However, for the Van Gogh case, secondary reactions took place between the primary degradation product ( $\text{CdSO}_4$ ) and lead- and oxalate-ions present in the varnish. Upon its application, the solvent rich varnish would have dissolved the  $\text{CdSO}_4$  and dispersed this degradation product throughout the coating. It appears that the freed  $\text{Cd}^{2+}$  ions reprecipitated out with  $\text{C}_2\text{O}_4^{2-}$  instead of  $\text{SO}_4^{2-}$ . Oxalate ions are commonly observed in cultural heritage materials and are in this case believed to be a degradation product of the varnish/paint medium. The sulphate anions, for their part, found a suitable reaction partner in lead ions which resulted in the formation of anglesite ( $\text{PbSO}_4$ ) crystals. Most probably, the  $\text{Pb}^{2+}$  ions were supplied by a lead-based drier, a hypothesis that was corroborated by the fact that anglesite ( $\text{PbSO}_4$ ) was also identified in the Ensor case [1].

The origin of the encountered cadmium carbonate was less unequivocal. It may

have been formed as a secondary degradation product following the primary photo-degradation of CdS or perhaps by the capture of atmospheric  $\text{CO}_2$ , as suggested by Mass *et al.* [2]. Alternatively, a tertiary process involving the further breakdown of cadmium oxalate into cadmium carbonate cannot be excluded while finally its presence might also be explained as simply a residue of the original raw material used for the industrial production of CdS.

In conclusion, this study showed how the primary degradation process, *i.e.* the oxidation of the original cadmium sulphide to colourless cadmium sulphate, was followed by secondary reactions after the application of a varnish film. Not only did this coating dissolve the highly soluble cadmium sulphate, but it also supplied reaction partners (*i.e.* oxalate and lead ions) for the resulting  $\text{Cd}^{2+}$  and  $\text{SO}_4^{2-}$  ions. In this way, the application of what was once assumed to be a protective coating eventually led to the formation of a disfiguring film at the paint/varnish interface instead.

**Fig. 66:** a) Paint sample pressed between two diamond cells. b)  $\mu$ -XRF/ $\mu$ -XANES chemical state maps (map size  $250 \times 270 \mu\text{m}^2$ , step size  $5 \mu\text{m}$ ) demonstrated that the yellow paint part of the sample contains predominantly sulphides while the area associated with the degradation crystals is rich in sulphates.  $\mu$ -FTIR analysis confirmed the sulphate content and revealed the distribution of oxalates in the proximity of the yellow paint (map size  $250 \times 270 \mu\text{m}^2$ , step size  $10 \mu\text{m}$ ).



#### References

- [1] G. Van der Snickt, J. Dik, M. Cotte, K. Janssens, J. Jaroszewicz, W. De Nolf, J. Groenewegen and L. Van der Loeff, *Anal. Chem.* **81**, 2600-2610 (2009).
- [2] Jennifer Mass, *personal communication*, July 2012.



### Principal publication and authors

G. Martínez-Criado, A. Homs, B. Alén, J.A. Sans, J. Segura-Ruiz, A. Molina-Sánchez, J. Susini, J. Yoo and G.-C. Yi, *Nano Lett.* **12**, 5829-5834 (2012).  
ESRF

## ■ Imaging the geometrical carrier confinement within a single core-multishell nanowire

Nanostructures made from organic and inorganic materials have been extensively characterised using luminescence-related techniques with spectral and temporal resolution. However, obtaining information on individual nanostructures rather than ensembles is a challenge for photoluminescence techniques. X-ray excited optical luminescence (XEOL) is a synchrotron soft X-ray technique that typically suffers from poor spatial resolution and long carrier diffusion length [1]. But recently, this technique has become particularly attractive for imaging certain optical phenomena in nanotechnology by making use of quantum confinement to limit the carrier dynamics. Here, a study of geometrical confinement effects in core-multishell nanowires shows that the hard X-ray approach at the nanoscale can provide new information. This imaging method combines XEOL with simultaneous X-ray fluorescence (XRF) spectroscopy using a nanometre-sized hard X-ray beam.

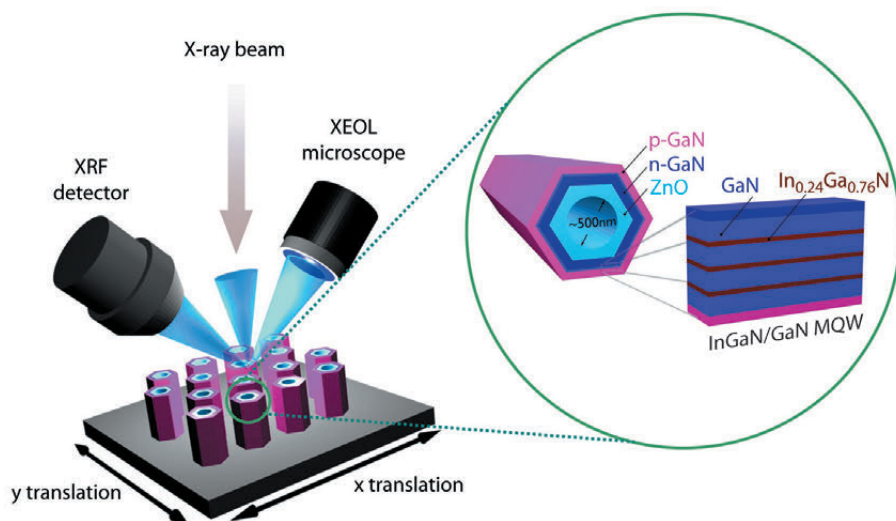
**Figure 67** shows a schematic of the experimental setup at ID22NI [2]. Using a pair of Kirkpatrick-Baez Si mirrors, the X-ray nanobeam ( $60 \times 60 \text{ nm}^2$  with  $10^{12} \text{ ph/s}$  at 29.6 keV) impinges on the sample, which emits luminescence and XRF photons. XEOL and XRF spectra are recorded with a far-field optics system and a silicon drift detector, respectively, for each raster position of the sample. As a proof of concept, we have applied this technique to

p-GaN/In<sub>1-x</sub>Ga<sub>x</sub>N/n-GaN/ZnO nanowires grown by metal-organic vapour phase epitaxy. Recent calculations indicate that the modulation of the radial elemental composition within a nanoscale hexagonal geometry introduces new complexities that create novel confinement effects [3]. **Figure 67** also displays a magnified cross-sectional view of the nanowires, highlighting the GaN/InGaN multi-quantum-well (MQW) structure.

**Figure 68** shows results obtained by scanning the nanowire along the radial direction for nano-XRF and nano-XEOL. The measurements identify the precise spatial location of the nanowire and reveal several points: The three-dimensional representation of the XRF data shows that the major elements exhibit high contrast, indicative of uniform core-multishell encapsulation in the radial chemical composition consistent with the targeted heterostructure. Within the sensitivity of our experimental setup, the sharp elemental images suggest that no significant interdiffusion took place across individual shells. The corresponding XEOL maps reveal three principal emission bands: a shoulder at 2.25 eV attributed to the common yellow band from point defects in GaN (probably Ga vacancies), a dominant green line at 2.45 eV attributed to the transitions from the In<sub>0.24</sub>Ga<sub>0.76</sub>N/GaN MQWs, and a weak blue peak at 2.85 eV attributed to the band-to-acceptor emission of the outmost Mg-doped GaN layer. The 3-D projection of the emissions located at 2.25 and 2.85 eV exhibits a uniform distribution of gallium vacancies and impurities, in good agreement with the XRF results. In contrast, the 3-D illustration of the band emitted at 2.45 eV indicates that the InGaN-related emissions radiate mainly from the six corners of the hexagon. The latter characteristic strongly suggests the existence of additional carrier confinement effects.

Although inhomogeneous distribution of indium and/or small well thickness fluctuations could be the source of the higher intensity of InGaN-related emission at the hexagon corners, the image

**Fig. 67:** Schematic of the hard X-ray nanoprobe experimental setup and magnified cross-sectional view of a GaN/In<sub>1-x</sub>Ga<sub>x</sub>N/GaN/ZnO nanowire heterostructure, highlighting the GaN/InGaN multi-quantum-well.



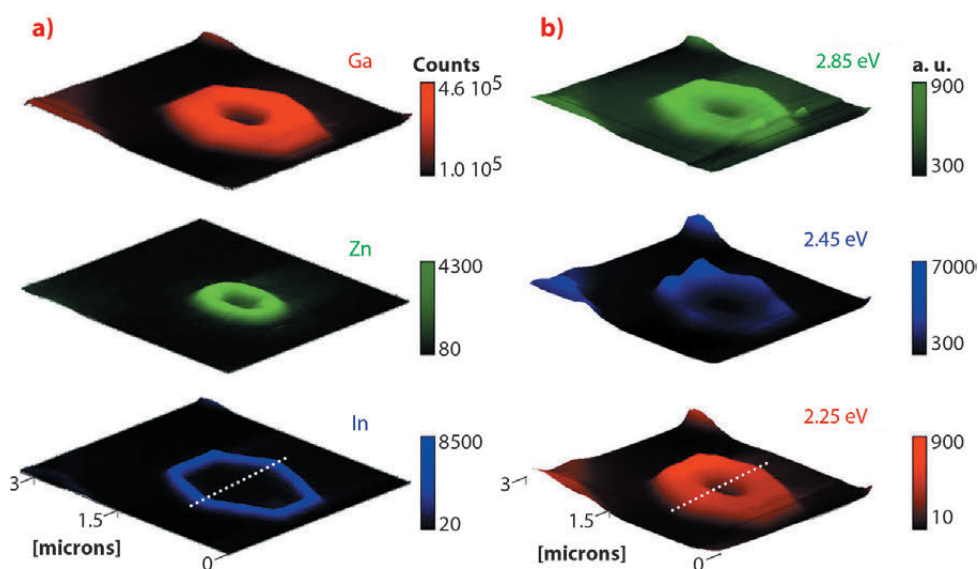


**Fig. 68:** Elemental mappings and luminescence recorded over a  $2 \times 1.4 \mu\text{m}^2$  cross-sectional scan of an individual nanowire with a pixel size of  $50 \times 50 \text{nm}^2$  and 1 s/point counting time. a) Nano X-ray fluorescence; b) Nano X-ray excited optical luminescence.

corresponding to the linewidth (not shown here) actually illustrates a reduction of peak broadening with a small but clear blue energy shift. These findings result from the enhanced carrier confinement within the MQWs merging at the corners, and have been confirmed through a theoretical investigation. A higher confinement of the wave function at the hexagon corners is observed in remarkable consistence with the XEOL results. There is a finite charge separation over the hexagon, which results in an overall greater overlap between the wave functions of electrons and holes at the corners.

In summary, the observation of the carrier confinement effects under hexagonal

cross-section in single core-multishell nanowires presented here gives a glimpse of the new research directions such a hyperspectral imaging method can provide. It represents a step towards the validation of theories of quantum confinement for nanodevices, and also the realisation of nanostructures with spectroscopic properties that could prove advantageous not only in light-emitting diodes but also in biological labelling experiments in life science. Its great potential becomes more valuable when time resolving power is added, as well as when this technique is used in conjunction with other methods, such as X-ray absorption spectroscopy and X-ray diffraction characterisation.

#### References

- [1] A. Rogalev and J. Goulon, X-ray Excited Optical Luminescence Spectroscopies, Chemical Applications of Synchrotron Radiation Part II, World Scientific: Singapore (2002).
- [2] G. Martinez-Criado *et al.*, *J. Synchrotron Rad.* **19**, 10 (2012).
- [3] B.M. Wong *et al.*, *Nano Lett.* **11**, 3074 (2011).

## Phase contrast imaging of lipid membranes in solution

Biomolecules are well known to form large scale supra-molecular aggregates by self-assembly, forming functional units made of non-covalent bonds. Functional properties in biomolecular assemblies depend on the molecular to supra-molecular structure. An excellent example of supra-molecular assembly is the formation of lipid bilayers which represent the basic building block for biological membranes, nature's most important interface.

As in many complex fluids and biomolecular assemblies, functionally

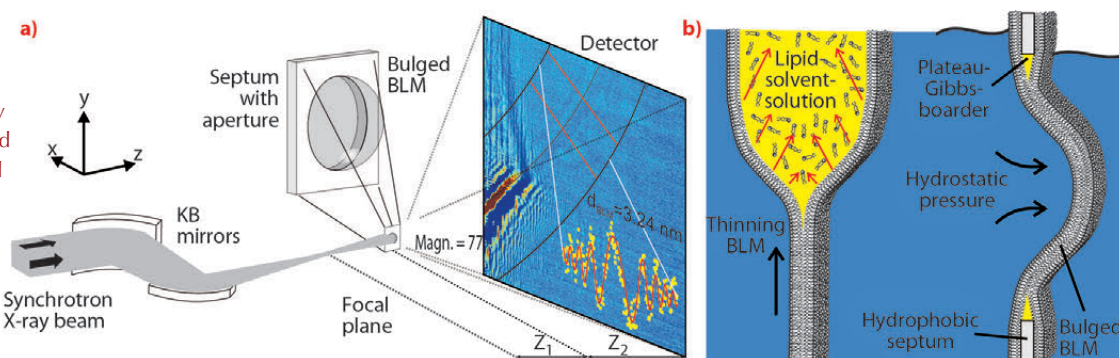
relevant states and properties depend intricately on hydrated environmental conditions, and the parameters of the aqueous solvent, for example pH, ionic strength and molecular concentrations. It is precisely for that reason that X-ray and neutron diffraction, which are compatible with these environmental conditions, have become such invaluable tools to study so-called soft matter or complex fluids samples. This is in sharp contrast to electrons, which would enable similar resolution, but necessitate vacuum conditions.

#### Principal publication and authors

- A. Beerlink (a,b), S. Thutupalli (c), M. Mell (a,d), M. Bartels (a), P. Cloetens (e), S. Herminghaus (c) and T. Salditt (a), *Soft Matter* **8**, 4595-4601 (2012).
- (a) Institut für Röntgenphysik, Georg-August-Universität Göttingen (Germany)
- (b) current address: Deutsches Elektronen-Synchrotron, PETRA III, Hamburg (Germany)
- (c) Max-Planck-Institute for Dynamics and Self-Organization, Göttingen (Germany)
- (d) current address: Mechanics of Biological Membranes and Biorheology, Departamento de Química Física I, Universidad Complutense, Madrid (Spain)
- (e) ESRF



**Fig. 69:** a) Experimental setup: A highly focused X-ray beam coherently illuminates a spherically bulged black lipid membrane (BLM), spanned over a micromachined hole and located downstream of the focal plane of the KB-mirrors system. The image is formed by free propagation of the wave field between the sample and the detector, where the intensity profile is recorded. b) Schematic of the formation and bulging process of a BLM. Application of hydrostatic pressure to one side of the BLM leads to bulging of the interface.

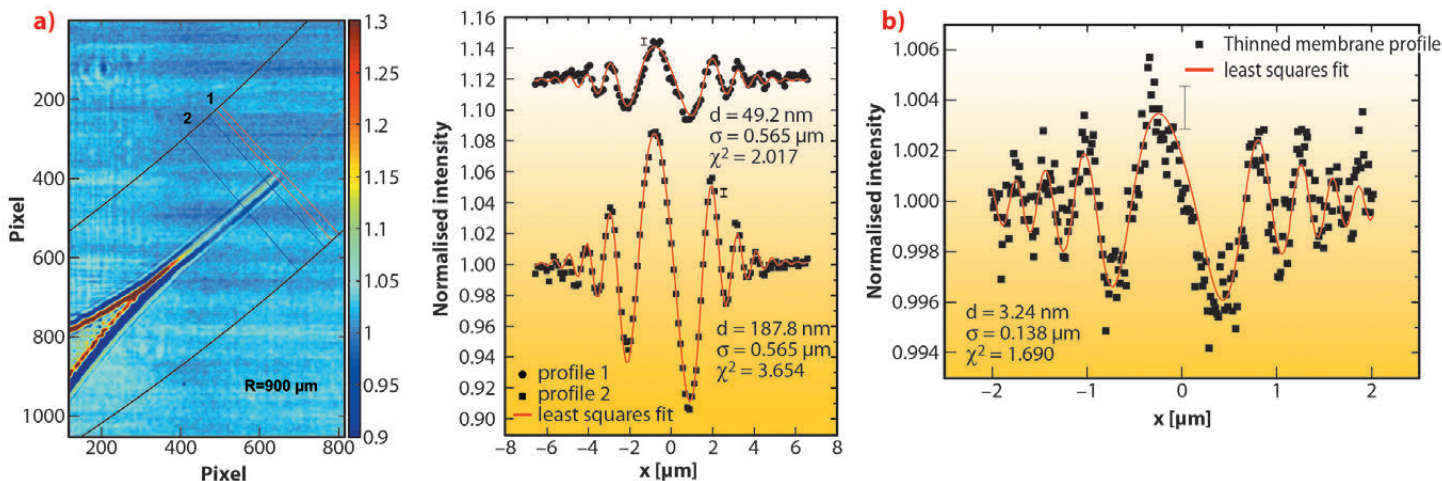


In order to concentrate coherent light onto the sample, it was almost always necessary to work with dry or fixated samples, primarily for dose issues and radiation damage. Therefore one of the strongest advantages of the X-ray probe was lost, and the native and functional structure of most complex fluids samples was again inaccessible.

We now report the first X-ray imaging of a hydrated lipid membrane in solution at its native thickness of several nanometres corresponding to two molecular layers, the so-called lipid bilayer. We were even able to witness the formation of a bilayer from two lipid monolayers in a micro-fluidic device. This has become possible by using a particularly dose efficient approach based on free space X-ray propagation, and an analysis strategy which is a combination of near-field diffraction and imaging. A schematic of the experimental setup at ID22NI is shown in **Figure 69a**. Along the direction perpendicular to the interface, we were able to resolve the thickness and density of the membrane derived from the image of its contour.

We studied a single freely-suspended lipid bilayer using a well-known setup of membrane electrophysiology, the so-called black lipid membranes (BLM), see **Figure 69b**, as an established model system in membrane biophysics. The bilayer was spanned in between two separated, aqueous compartments, allowing studies of functional transport across the bilayer at controlled compositional and environmental parameters, such as protein concentration, ionic strength, pH, and electrical field. The membrane is bulged by hydrostatic pressure, and is placed a few millimetres behind the focal plane of a highly efficient and partially coherent elliptical mirror system developed at ESRF. This quasi-spherical illumination leads to a magnified hologram of the sample which is then recorded a few metres behind the sample by the fast read out low noise detector system (FReLoN) devised at ESRF. The Fresnel oscillations in this hologram, corresponding to the native lipid bilayers with a thickness of less than  $d = 5$  nm, were recorded and analysed with respect to the local structure at molecular length scales, see **Figure 70a** and **b**.

**Fig. 70:** a) Typical dataset showing the BLM contour and Fresnel oscillations, which are fitted to a model of the bilayer profile, yielding the local bilayer structure. b) Analysis of the Fresnel fringes of the thinned native bilayer (data **Figure 69a**) indicating a thickness of around 3 nm.





Straightforward extensions of this approach should enable the extraction of the local interface density profiles of membranes and membrane based materials. More generally, it will allow structure analysis of soft matter interfaces at near-molecular resolution under hydrated conditions, closing the gap between conventional scattering studies on the one hand, carried out over large ensembles and conventional microscopy

studies on the other hand. Combining advantages concerning resolution, interaction volume and complexity of the system studied, the experiment paves the way for the controlled investigation of complex biochemical and physical phenomena, particularly soft interfacial phenomena, such as the formation of bilayers, thinning or bulging, as well as in membrane fusion, down to the length scale of a few nanometres.

## ■ 3-D bone ultrastructure resolved by phase nanotomography

Bone tissue was imaged at the sub-cellular level using synchrotron radiation phase nanotomography. Previously, images at the ultrastructural level have only been available with electron imaging techniques, such as scanning or transmission electron microscopy, thus in 2D. In this study, bone ultrastructure was imaged in 3-D with a 60 nm voxel size. Several ultrastructural properties could be visualised in 3-D for the first time: the collagen fibre orientation, the mineralisation on the nanoscale, and the imprint of the cellular network.

Bone is a hierarchically organised material with remarkable capabilities to maintain and repair itself. However, due to aging or disease, bone becomes fragile, leading to fracture. Understanding the mechanisms determining bone strength and fragility is the prerequisite for advances in bone tissue engineering and disease treatment. For example, the role of the osteocyte, a bone cell embedded in the bone matrix, in sensing damage and converting forces to biological signals has been highlighted. Despite recent advances, a clear picture of the 3-D nano-organisation of bone has not yet been established due to lack of suitable 3-D imaging techniques [1-3].

Magnified X-ray phase nanotomography was performed at the nano-imaging beamline end-station ID22NI (Figure 71). 3-D maps were obtained of the mass density within human cortical bone samples at 60 nm spatial resolution (Figure 72). The images reveal the organisation of the lacunae, which contain the osteocytes in living bone, and the

canaliculi through which they connect in a large region. The cement line, separating bone tissue of different age, could also be studied in 3-D for the first time (Figure 72). In this study we were able to measure the relative electron density directly, and we found that the cement line is hypermineralised. For the first time, the collagen organisation in the compact bone matrix could be directly observed in 3-D.

The information content in the 3-D images is exceptionally high due to the

### Principal publication and authors

M. Langer (a,b),  
A. Pacureanu (a,b,c),  
H. Suhonen (b), Q. Grimal (d),  
P. Cloetens (b) and F. Peyrin (a,b,e),  
*PLoS ONE 7*, e35691 (2012).  
(a) *CREATIS, CNRS 5220, INSERM U1044, INSA Lyon, Université de Lyon (France)*  
(b) *ESRF*  
(c) *Current address: Centre for Image Analysis & SciLifeLab, Uppsala University (Sweden)*  
(d) *UPMC Univ Paris 06, CNRS UMR 7623, LIP, Paris (France)*  
(e) *Labex PRIMES, Université de Lyon (France)*

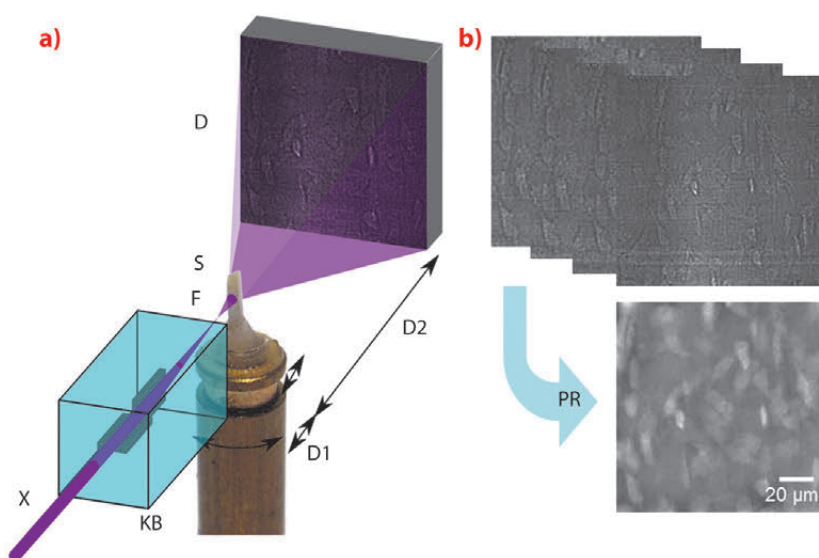


**Fig. 71:** a) Schematic of experimental setup. The X-ray beam (X) is monochromatised and focused into a focal spot (F) by multilayer coated KB optics. The sample (S) is positioned on a translation-rotation stage downstream of the focus and imaged onto a stationary detector. Due to the resulting divergent beam, different spot-sample distances (D1) and different free space propagation distances (D2) imply different magnification factors on the detector. b) Images were recorded at four focus-to-sample distances over a complete turn of the sample at 2999 projection angles. The images were used to reconstruct the phase shift at each angle (phase retrieval, PR), which was used as input to a tomographic reconstruction algorithm to reconstruct the 3-D local mass density.



### References

- [1] L.F. Bonewald, *J. Bone Miner. Res.* **26**, 229-238 (2011).  
 [2] M. Dierolf *et al.*, *Nature* **467**, 436-439 (2010).  
 [3] A. Pacureanu, M. Langer, E. Boller, P. Tafforeau and F. Peyrin, *Med. Phys.* **39**, 2229-2238 (2012).

high spatial resolution and large field of view. Furthermore, the technique requires very little sample preparation, thus avoiding possible unintentional altering of structures. The sensitivity is exceptional and appears to outperform attenuation based full-field X-ray microscopy and ptychography [2,3]. In contrast to

scanning techniques, it is possible to keep acquisition times short (less than two hours per sample) thus facilitating the imaging of series of samples. We believe this method will have a significant impact in osteology since it gives access to information unavailable with other techniques, while being fast and reproducible. Therefore, this work paves the way for new studies to gain a better understanding of bone function, remodelling, and ultimately to new strategies in bone repair and the management of bone related diseases.

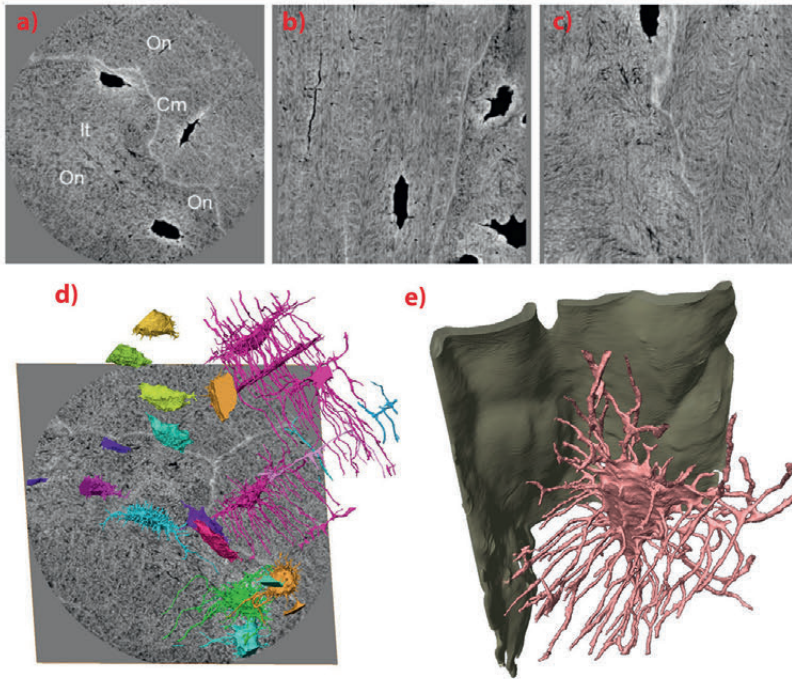


**Fig. 72:** a) Transverse, b) frontal and c) sagittal slices through the images reconstructed from phase data. Grayscale is proportional to local density. Osteocyte lacunae (Lc) and canaliculi (Ca) can clearly be seen. The heterogeneous organisation of the matrix by mineralised collagen fibres can also be distinguished. The cement line (Cm), separating osteonal (On) and interstitial (It) tissue, can clearly be distinguished as more mineralised than the surrounding matrix. Tissue close to osteocyte lacunae is also hypermineralised. d) Rendering of osteocyte lacunae and canaliculi in the whole imaged volume overlaid on the bottom slice shown in grayscale. Colours correspond to connected components and grayscale to mass density. e) Enlargement of a lacuna showing the interaction between the canaliculi (pink) and the cement line (green), and branching of the canaliculi.



# Soft Condensed Matter

As in the previous years, this chapter presents a diverse set of articles related to the Soft Matter field published during the last year. A particular feature of this selection of highlights is the maturity attained by different techniques which now reveal unprecedented details. The first article, by Kim *et al.*, shows the advancement of pump-probe solution scattering that has permitted the reconstruction of three-dimensional molecular envelopes of the microsecond range protein intermediates involved in the photocycle of photoactive yellow protein. The second example, by Bressel *et al.*, demonstrates that the insight gained from time-resolved SAXS experiments could be utilised for the rational design of self-assembled unilamellar vesicles with controllable size and long-term stability. The XPCS technique has reached a new level of sensitivity that allowed Orsi *et al.* to derive even the fourth-order time-correlation function from a two-dimensional gel of a Langmuir monolayer of nanoparticles formed at an air-water interface. Time resolved GISAXS enabled Vegso *et al.* to capture a transient compression phase in a Langmuir film of nanoparticles upon continuous increase of surface pressure.

The article by Liu *et al.* illustrates that the flurry of discoveries of new liquid-crystal phases with T-shaped “bolaamphiphiles” go uninterrupted. Weinhausen *et al.* demonstrate that nanodiffraction with a complex biological specimen does yield results. Finally, new light is shed on crystallisation pathways in globular

proteins (Zhang *et al.*) and polymers (Cavallo *et al.*). Within the space restriction, there are some notable omissions in this chapter, these include two-state rapid assembly mechanism of SV40 virus-like particles [S. Kler *et al.*, *JACS* 134, 8823 (2012)], conformational changes of haemoglobin observed within red blood cells following laser flash photolysis [A. Spilotros *et al.*, *Soft Matter* 8, 6434 (2012)], etc.

Among the technical developments, ID10 has completed a major refurbishment with two end-stations for soft interfaces and coherent scattering coming to successful operation. The preparatory work for UPBL9a (ID02) is progressing well. The existing ID02 beamline will be closed in July and the upgraded beamline is expected to be reopened in May 2014. The technical design report for UPBL9b (ID09 Time Resolved) has been completed. Finally, the formal collaboration contract between ESRF and ILL for the Partnership for Soft Condensed Matter (PSCM) has been signed. The Science Building is nearing completion on schedule and the full scale operation of the PSCM is expected to begin in the second half of 2013. At present, the PSCM is actively seeking collaborative partners from academia and industry. In addition, enhanced services are offered to industrial customers for selected techniques (SAXS/WAXS and microdiffraction) in an effort to promote better use of synchrotron radiation in soft materials industrial R&D.

T. Narayanan

## ■ Unravelling the protein structural dynamics of photoactive yellow protein in solution using pump-probe X-ray solution scattering

Photoreceptor proteins play crucial roles in receiving light stimuli that give rise to biological responses. The detailed time-dependent conformational transitions in their native aqueous environment have been elusive, however, even for a simple prototype photoreceptor, photoactive yellow protein (PYP). PYP is responsible for signal reception of the phototaxis response of the bacterium *Halorhodospira halophila*. It is one of the most studied biophysical systems and has served as a model for understanding the

photoreception and the subsequent signal transduction at a molecular level [1,2]. Various experiments using spectroscopy, crystallography, and NMR have been performed to reveal the kinetic mechanism and the structure of intermediates involved in the photocycle (Figure 73). However, the global structures of intermediates in the solution phase have never been identified due to the lack of structural sensitivity, the restraint by crystal contact, and the limitation of time-resolution of the techniques used so far.

### Principal publication and authors

T.W. Kim (a), J.H. Lee (a), J. Choi (a), K.H. Kim (a), L.J. van Wilderen (b), L. Guerin (c), Y. Kim (a), Y.O. Jung (a), C. Yang (a), J. Kim (a), M. Wulff (c), J.J. van Thor (b) and H. Ihee (a), *J. Am. Chem. Soc.* **134**, 3145–3153 (2012).

(a) Institute for Basic Science, Center for Time-Resolved Diffraction, Department of Chemistry, KAIST (Republic of Korea)

(b) Division of Molecular Biosciences, Imperial College London (UK)

(c) ESRF

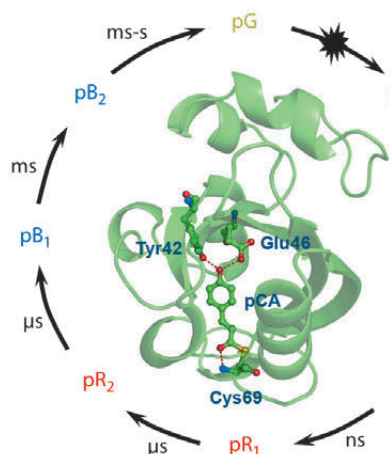


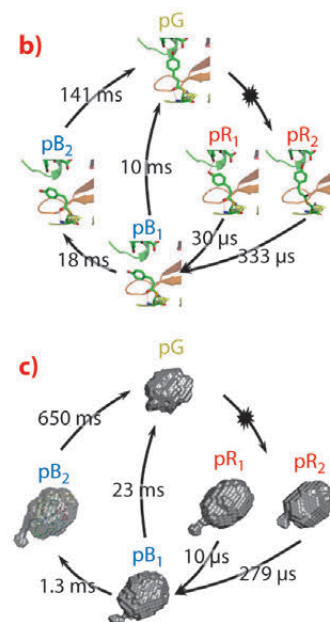
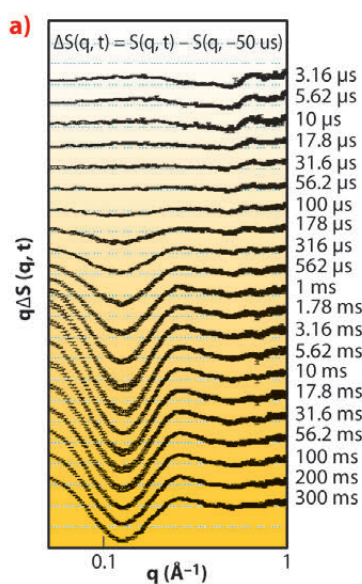
**Fig. 73:** General photocycle of photoactive yellow protein with corresponding time region [1]. On illumination with visible light, the ground state (pG) is set on a photoreaction pathway with the isomerisation of the chromophore region.

We employed the pump-probe X-ray solution scattering method established at beamline **ID09B** to overcome these limitations and unveil the structural dynamics of PYP in a wide time region from 3.16  $\mu$ s to 300 ms (**Figure 74a**). The quantitative kinetic analysis was implemented to determine the number of kinetic components from the scattering curves. The results permit us to suggest the probable kinetic framework during the photocycle of PYP. Four intermediates and five time constants (10  $\mu$ s, 279  $\mu$ s, 1.3 ms, 23 ms, and 650 ms) during the photocycle were identified from the kinetic analysis. These rate-constants and the number of kinetic components are similar to the previous result observed with Laue crystallography [3] (**Figure 74b**). It implies that a common kinetic mechanism (parallel kinetics) can be operated in both the solution and crystalline phases. To describe the structural shape of an intermediate, the structural analysis, based on species-associated scattering curves determined from kinetic analysis, was performed. It permits us to visualise the global molecular shapes of all intermediates (pR<sub>1</sub>, pR<sub>2</sub>, pB<sub>1</sub>, and pB<sub>2</sub>) that show the gradual expansion of protein volume and the protrusion of the N-terminus with the progress of the photocycle (**Figure 74c**). The protrusion of the N-terminus becomes maximal in the pB<sub>2</sub> state, the so-called signalling state.

Our results from pump-probe X-ray solution scattering observations provide several insights into the structural dynamics of PYP. First, the protrusion of N-terminus during the photocycle of PYP is suppressed in the crystalline phase due to the crystal contact [3]. However, in the solution phase, the unrestrained N-terminus is already elongated in the pB<sub>1</sub> intermediate, which is the precursor of the signalling state, and is maximised at the pB<sub>2</sub>. Second, the rate-constant of the intermediate accompanying large conformational change such as the N-terminus protrusion in the solution phase show a dramatic difference from those in the crystalline phase. Third, the movement of the N-terminus in the solution phase is highly correlated with that of the chromophore (*p*-coumaric acid, pCA).

Using pump-probe X-ray solution scattering, we can directly observe a profound effect of the molecular environment on structural dynamics and the reaction rates of the PYP photocycle. This study is the first instance where the three-dimensional molecular envelopes of the protein intermediates are reconstructed with microsecond time resolution and should serve as a cornerstone for further structural studies of protein structural dynamics in solution.

**Fig. 74:** a) Pump-probe X-ray difference scattering curves of the PYP photocycle. The photocycle of the photoactive yellow protein is triggered by blue light excitation ( $\lambda_{\text{max}} = 446\text{nm}$ ). b) The kinetic framework and the rate-constants in the crystalline phase determined by time-resolved Laue crystallography [2]. c) The chromophore motion is visualised with atomic-resolution. Reconstructed molecular shapes of the intermediates and their associated rate-constants in the solution phase determined from pump-probe X-ray solution scattering.



#### References

- [1] K. Hellingwerf, J. Hendriks and T. Gensch, *J. Phys. Chem. A* **107**, 1082 (2003).
- [2] P. Ramachandran, J. Lovett, P. Carl, M. Cammarata, J.H. Lee, Y.O. Jung, H. Ihee, C. Timmel and J. van Thor, *J. Am. Chem. Soc.* **133**, 9395 (2011)
- [3] H. Ihee, S. Rajagopal, V. Srajer, R. Pahl, S. Anderson, M. Schmidt, F. Schotte, P.A. Anfinrud, M. Wulff and K. Moffat, *Proc. Natl. Acad. Sci. USA* **102**, 7145 (2005).

## Shaping vesicles by the presence of amphiphilic copolymer

Vesicles are globular objects of closed amphiphilic bilayers, which are formed spontaneously by phospholipids but also by a large number of surfactants and amphiphilic polymers. With their bilayer structure, unilamellar vesicles resemble natural membranes and they are often used in a number of applications including cosmetics, pharmaceutical formulations and detergents. However, for many reasons, it is very important to have precise control over the vesicle size and their stability, as frequently vesicles are metastable and structurally not so well-defined.

In the past, we have studied the spontaneous formation of vesicles occurring upon rapidly mixing either oppositely charged surfactants or mixtures of anionic and zwitterionic surfactants. Very detailed structural information regarding the formation process could be obtained by stopped-flow SAXS experiments down to a time resolution of 2 ms. These experiments showed that very small disk-like micelles form initially, grow by coalescence and then, once beyond a critical size, close spontaneously to form monodisperse vesicles [1]. This critical size is basically determined by an energetic balance between the unfavourable rim of the disk and the energy required

to bend the bilayer into the curved vesicles [2,3].

A logical idea then is to make this rim more stable, thereby forming correspondingly larger vesicles. This concept has been realised by adding an amphiphilic copolymer, in our case of the PEO-PPO-PEO type (EO: ethylene oxide, PO: propylene oxide), which can be expected to become enriched in the rim of the disk-like micelles and thereby reduce the line tension. Here we have studied the corresponding process of vesicle formation in the presence of the amphiphilic copolymer in order to verify this hypothesis. We obtained detailed structural information about the progression of vesicle formation by time-resolved SAXS performed at beamline ID02. Examples for such sets of SAXS curves, with and without added copolymer, are shown in Figure 75 and demonstrate clearly the growth of the small disks, which formed immediately ( $t < 5$  ms), and the subsequent closure to form vesicles (marked in the SAXS curves by the occurrence of oscillations in the form factor). The progression is basically similar to the case without added copolymer but the growth proceeds for much longer, this prolonged growth being proportional to the amount of

### Principal publication and authors

K. Bressel (a), M. Muthig (a), S. Prévost (a,b), J. Gummel (c), T. Narayanan (c) and M. Gradzielski (a), *ACS Nano* **6**, 5858-5865 (2012).

(a) *Stranski Laboratorium für Physikalische und Theoretische Chemie, Institut für Chemie, Technische Universität Berlin (Germany)*

(b) *Helmholtz-Zentrum Berlin (HZB) für Materialien und Energie GmbH (Germany)*

(c) *ESRF*

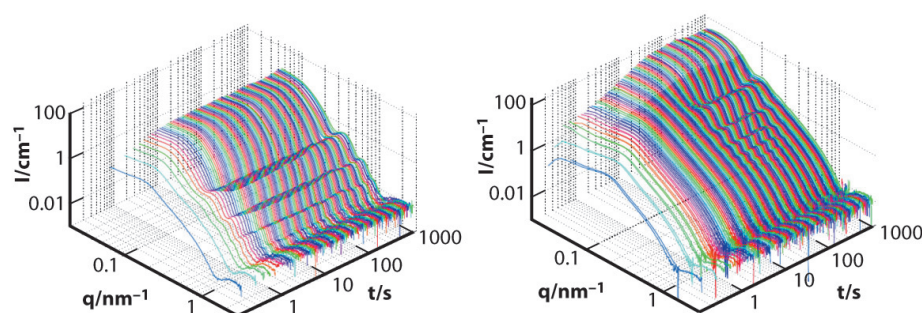
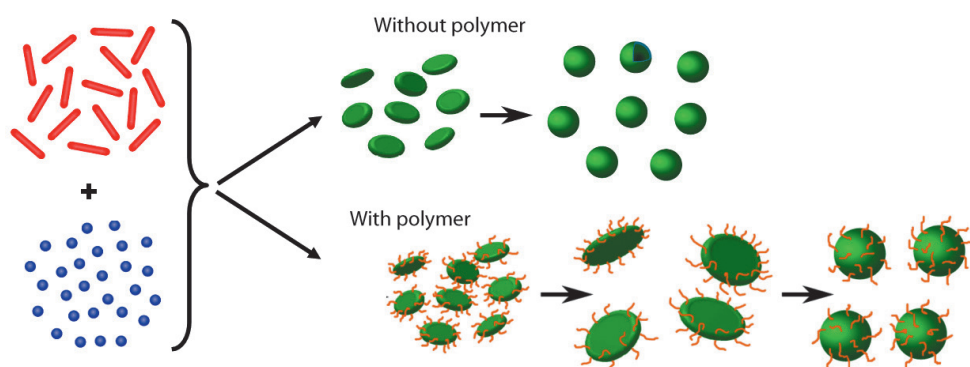


**Fig. 75:** SAXS intensity curves as a function of time for mixtures of 27.5 mM tetradecyl dimethyl amine oxide (TDMAO) and 22.5 mM lithium perfluoro octyl sulphonate (LiPFOS) without added copolymer (left) and for the addition of 0.275 mM Pluronic L35 (EO<sub>11</sub>-PO<sub>16</sub>-EO<sub>11</sub>). Below the structural progression occurring in the solutions as a function of time.



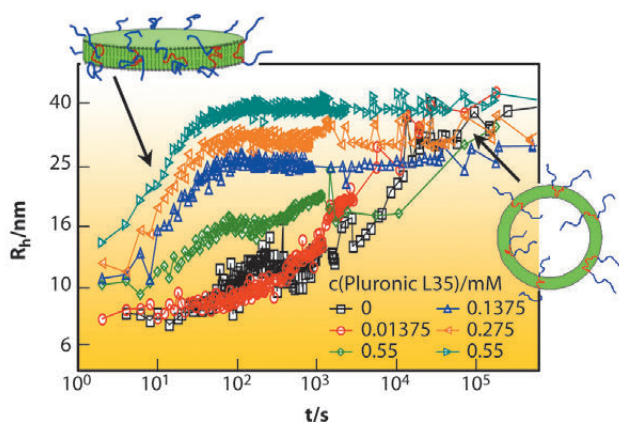


### References

- [1] T.M. Weiss, T. Narayanan and M. Gradzielski, *Langmuir* **24**, 3759-3766 (2008).  
 [2] W. Helfrich, *Phys. Lett.* **50A**, 115-116 (1974).  
 [3] A. Shioi, T.A. Hatton, *Langmuir* **18**, 7341-7348 (2002).

added copolymer. This then leads to larger vesicles (as seen by the much higher scattering intensity), which are highly monodisperse (as seen from the pronounced form factor oscillations).

This kinetic control of the vesicle formation process yields very well-defined vesicles of controlled size and, in addition, these copolymer modified vesicles are much more stable than without copolymer. This is demonstrated in **Figure 76** which shows dynamic light scattering (DLS) results as a function of time. The presence of the copolymer largely suppresses ageing and systems that were stable before for



only a few minutes are now stable for weeks due to the copolymer addition, a point very important for applications.

In summary, it can be stated that, for this model of mixed surfactants, a new way of a rational structural design of self-assembled systems has been employed, based on detailed knowledge of the formation process, which is uniquely accessible by highly time resolved SAXS experiments. In our experiments the self-assembly process was manipulated in a systematic way, in a fashion similar to modifying a chemical reaction by a catalyst, *i.e.* one could call this “colloid catalysis”, which tailors the vesicle shape in our example. In this way, self-assembly of metastable systems leads to well-defined systems, otherwise inaccessible, and with much enhanced stability. This opens access to novel systems, which should also be of great importance for future developments in formulating self-assembled systems.

**Fig. 76:** Hydrodynamic radius  $R_h$  from DLS as a function of time after mixing together 27.5 mM TDMAO and 22.5 mM LiPFO in the presence of different concentrations of Pluronic L35 (at 25°C).

### Principal publication and authors

D. Orsi (a), L. Cristofolini (a), G. Baldi (a,b) and A. Madsen (c,d), *Phys. Rev. Lett.* **108**, 105701 (2012).  
 (a) Physics Department, Parma University (Italy)  
 (b) CNR-IMEM Institute, Parma (Italy)  
 (c) ESRF  
 (d) European X-Ray Free Electron Laser, Hamburg (Germany)

## ■ Dynamical anisotropy and heterogeneity in a bidimensional gel

What do snow tires share with chocolate and plasters for transdermal drug delivery? The notable properties of all these systems are determined by molecular mobility, which is slowed down by the presence of a dynamical arrest transition. As a matter of fact, molecular mobility determines many of the properties of soft matter systems, particularly in interfacial systems which are retrieved in a wide variety of technologies and products, from paints to food science, and from oil recovery to personal care products. Molecular mobility may be slowed down by a transition to dynamical arrest, often happening without any associated structural transition. To date, there is no unifying theory describing these kinds of dynamical transitions, in marked contrast with “classic” phase transitions, *e.g.* crystallisation or evaporation, where

the underlying mechanisms are well understood. However, there is a broad consensus that transition to dynamical arrest is characterised by heterogeneous, non-Gaussian dynamics [1]. This has become evident in numerical simulation work [2], but direct experimental evidence on real systems is scarce.

Dimensionality is known to play a key role in arrested systems: in a well-known example, hard sphere caging occurs in three dimensions at volume fractions of about 60%–64%, while in two dimensions the random close packing is only attained at a much higher area fraction, about 82%. The system we study here is a two-dimensional gel formed by gold nanoparticles at the air-water interface. The XPCS [3] experiments were performed at beamline **ID10A**.

The high brilliance and stability of the coherent X-ray beam at the ESRF was necessary to obtain data with excellent signal-to-noise ratio from a sample consisting of only one single Langmuir monolayer (see **Figure 77**). This allowed the intensity autocorrelation function,  $g^{(2)}$ , to be measured with high accuracy, and the anisotropy of the dynamics to be assessed, which turned out to be completely confined at the air/water interface plane. Moreover, as the interfacial mechanical properties [4] of the same interfacial gel system have been characterised independently, a direct comparison between the rheological properties and the dynamical properties could be made. A model advanced a few years ago by Bouchaud and Pitard [5] proved particularly successful in describing the data. In this model, a relation between the elastic modulus  $G'$  and the characteristic relaxation time of  $g^{(2)}$  in elastic soft solids is postulated. Our findings clearly corroborate this hypothesis, as shown in **Figure 78a**. The good signal-to-noise ratio of the data allowed the four times correlation functions  $g^{(4)}(q, t_1, t_2)$  to be measured for the first time by XPCS, as displayed in **Figure 78b**, where it is compared with the usual second-order time correlation function  $g^{(2)}(q, t)$ . Access to  $g^{(4)}$  allowed a determination of the lifetime and nature of the dynamical heterogeneity (e.g. avalanches, intermittency, etc.) that characterises the dynamics of this 2-D gel. The right panel of **Figure 78c** shows the  $q$ -dependency of the lifetime of dynamical heterogeneity (open symbols) compared with the relaxation time of the dynamics obtained by  $g^{(2)}$ .  $g^{(4)}$  features a broad peak centred at a characteristic time which is one order of magnitude smaller than the relaxation time of  $g^{(2)}$ . Both times follow the same qualitative law  $\tau \approx q^{-1}$  which is an experimental finding that challenges the different theoretical frameworks attempting to describe dynamical arrest transitions.

In summary, the XPCS experiment on a Langmuir monolayer forming a 2-D gel provided detailed insight into the anisotropic dynamics of this system, which is confined at the air-water interface. In particular, the non-Gaussian nature of the dynamical fluctuations was characterised by directly calculating the fourth order temporal correlation

function  $g^{(4)}(q, t_1, t_2)$ , which thereby was experimentally accessed for the first time by XPCS.

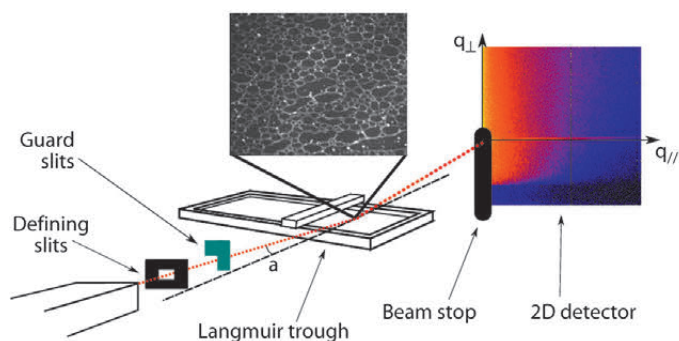
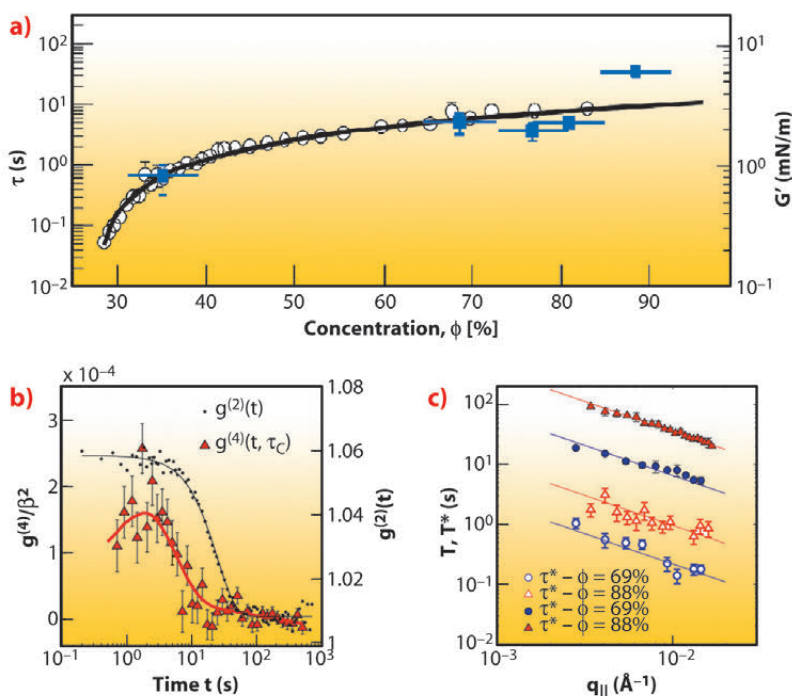


**Fig. 77:** Sketch of the setup used for XPCS experiments on Langmuir monolayers.



#### References

- [1] A. Madsen, R.L. Leheny, H. Guo, M. Sprung and O. Czakkel, *New Journal of Physics* **12**, 055001 (2010).
- [2] L. Berthier, *Physics* **4**, 42 (2011).
- [3] G. Grübel, A. Madsen and A. Robert, in *Soft-Matter Characterization*, edited by R. Borsali and R Pecora (Springer, 2008), pp. 935-995.
- [4] *Interfacial Rheology*, edited by R. Miller, L. Liggieri (V S P International Science Publishers) 2009.
- [5] J.-P. Bouchaud and E. Pitard, *The European Physical Journal E* **6**, 231-236 (2001).



### Principal publication and authors

K. Vegso (a), P. Siffalovic (a),  
E. Majkova (a), M. Jergel (a),  
M. Benkovicova (a), T. Kocsis (a),  
M. Weis (a), P. Siffalovic (a),  
K. Nygård (b) and O. Konovalov  
(b), *Langmuir* **28**, 10409 (2012).  
(a) Institute of Physics, SAS,  
Bratislava (Slovakia)  
(b) ESRF

## ■ New non-equilibrium compression phase in a nanoparticle Langmuir film

Large-area homogenous nanoparticle arrays are attractive for novel applications. They are fabricated by a transfer onto a substrate of self-assembled nanoparticle Langmuir films confined at the air/water interface that are formed by a controlled compression of the nanoparticles spread on the water subphase into close-packed self-assembled layers. We performed a fast-tracking *in situ* grazing-incidence small-angle X-ray scattering (GISAXS) study of the compression process and revealed a new non-equilibrium phase preceding the collapse of the nanoparticle monolayer.

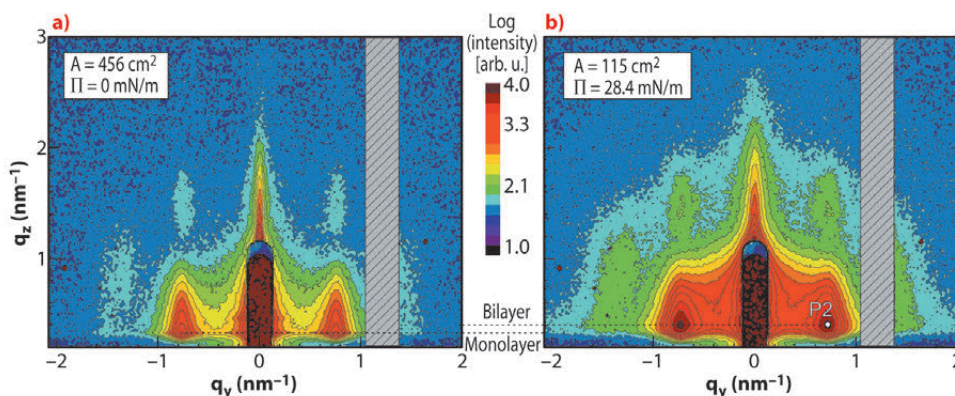
The GISAXS measurements [1] of the silver nanoparticle Langmuir films during compression on the water subphase with a constant speed were performed at beamline ID10B. **Figure 79a** shows the GISAXS pattern of the nanoparticle submonolayer film at the surface pressure of 0 mN/m. The first Bragg rod corresponding to (10) diffraction is an evidence of lateral correlation between the nanoparticles organised into small self-assembled islands on the water surface. The GISAXS pattern of the collapsed nanoparticle monolayer at the surface pressure of 28.4 mN/m is shown in **Figure 79b**. The intensity modulation observed along the first Bragg rod indicates the nanoparticle bilayer formation while the peak marked as P2 suggests the vertical correlation in the nanoparticle bilayer. In order to track the temporal evolution of the nanoparticle monolayer during the continuous compression in real time, a series of fast recorded GISAXS patterns (“snapshots”) was taken and

the first Bragg rod position and intensity distribution were analysed.

The analysis was based on the paracrystal model [2]. In particular, numerical simulations of the GISAXS patterns with systematic variation of the interparticle distance and paracrystal disorder based on the distorted wave Born approximation provided a paracrystal “landscape” in the reciprocal space (**Figure 80**) where the experimental points in terms of the first Bragg rod maximum position ( $q_y$ ) and width (FWHM) could be inserted (open circles). These points for various surface pressures during the film compression show a “pathway” characterising the Langmuir film behaviour within the paracrystal model. Four compression stages could be distinguished in the simultaneously measured surface pressure isotherms that are indicated along the “pathway”.

In stage I of the nanoparticle film compression, we do not observe any increase in the surface pressure. The isolated self-assembled nanoparticle islands coalesce into larger domains, forming a compact percolated network of nanoparticles. Stage II is accompanied by a steady increase of surface pressure. The mechanical stress induced at the boundaries of the coalesced nanoparticle islands leads to a re-ordering and densification of the percolated network and a slight increase in the paracrystal disorder while the interparticle distance remains constant. As a result, a homogenous self-assembled nanoparticle monolayer forms. A further increase in the surface pressure (stage III)

**Fig. 79:** GISAXS pattern of the self-assembled nanoparticle (a) submonolayer and (b) collapsed monolayer.



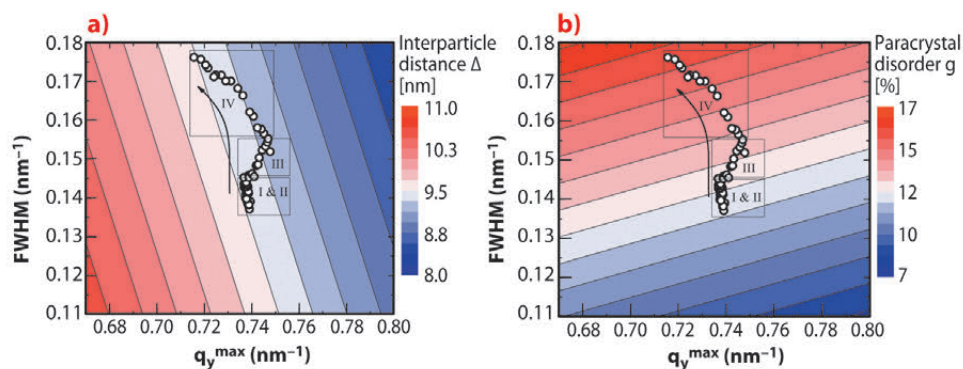


**Fig. 80:** The paracrystal "landscape" decorated with the experimental points (open circles) that mark the "pathway" of the nanoparticle layer during compression. The arrow shows the compression direction.

results in the paracrystal disorder increasing by 1% and the mean interparticle distance decreasing by 0.2 nm. This effect can be attributed to a compression of the organic nanoparticle shell and formation of a previously unobserved transient phase far from equilibrium that could be observed solely due to our fast tracking GISAXS scheme. A further increase in the surface pressure (stage IV) leads to an irreversible 2-D to 3-D transition and the second layer formation that is accompanied by a relief of the stress accumulated in the first layer. Simultaneously, the voids and defects in the first layer are formed that results in a significant increase of the paracrystal

disorder by 2% and relaxation of the interparticle distance back to the initial value.

The *in situ* observation of the non-equilibrium phases in the nanoparticle Langmuir film compression by conventional imaging and scanning probe techniques like SEM, TEM, STM or AFM is principally impossible. The newly-observed non-equilibrium compression phase documents unique potential of the synchrotron-based time-resolved X-ray scattering measurements in tracking fundamental properties of matter at the nanoscale.

#### References

- [1] G. Renaud, R. Lazzari and F. Leroy, *Surf. Sci. Rep.* **64**, 255 (2009).
- [2] R. Hosemann and S.N. Bagchi, *Direct analysis of diffraction by matter* (North-Holland Publ. Comp., Amsterdam, 1962).

## ■ New 2-D and 3-D liquid crystal phases: Segmented cylinders, crossed columns and ribbons between sheets

In recent years a new type of liquid crystal molecules, pioneered by C. Tschierske, gained prominence, having flexible chains attached to the side of the aromatic rods. With sticky hydrogen-bonding groups at the ends of the rod, these T-shaped "bolaamphiphiles" (Figure 81 a,b) were found to assemble in a range of new structures, many of which can be described as honeycombs [1]. The rods form the walls and the side chains fill the channels. In a recent study using grazing-incidence small-angle X-ray scattering (GISAXS) at beamline **BM28** (XMaS) three new types of liquid crystals have been discovered.

By increasing the volume of the side-chain of the T-shaped molecules, the shape of the honeycomb cells can be changed from triangular, via rhombic, square, pentagonal all the way to stretched hexagonal, as more and more rods are required

to encircle the cell – Figure 81 a,b. A further increase in side chain volume, e.g. by attaching two chains instead of one, makes the honeycombs give way to layered structures – Figure 81c. The work highlighted here has gone a step further by replacing the linear side-chains with branched "swallow-tail"

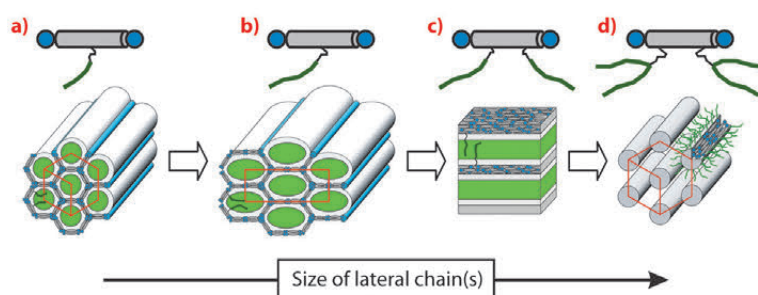


**Fig. 81:** Some representative LC structures in bolaamphiphiles with increasing volume of the side chains. Blue: hydrogen-bonding glycerol groups; grey: aromatic rod-like cores; green: laterally attached chains.

#### Principal publication and authors

F. Liu (a), M. Prehm (b), X. Zeng (a), G. Ungar (a) and C. Tschierske (b), *Angew. Chem. Int. Ed.* **50**, 10599–10602 (2011).  
(a) Department of Materials Science and Engineering, University of Sheffield (UK)  
(b) Institute of Chemistry, Martin-Luther-University Halle-Wittenberg, Halle (Germany)



### References

- [1] G. Ungar, C. Tschierske, V. Abetz, R. Holyst, M.A. Bates, F. Liu, M. Prehm, R. Kieffer, X. Zeng, M. Walker, B. Glettner and A. Zywockinski, *Adv. Funct. Mater.* **21**, 1296-1323 (2011).

### Acknowledgement

This work was supported by the EC 7<sup>th</sup> and 6<sup>th</sup> Framework Programmes, under contracts 2007-2013 (NANOGOLD, grant agreement n°228455), and ERAS-CT-2003-989409. It was also supported by DFG and EPSRC as part of the ESF EUROCORES Programme SONS.

ones (Figures 81d and 82a). Interestingly, such compounds exhibit the hexagonal columnar phase again. However, this time the structure is an inverted honeycomb, in fact it is closer to the classical columnar discotic, with the columns having a hard aromatic centre and a soft aliphatic sheath. But unlike the discotic, the new columnar phase is made up of bundles of around 14 rod-like molecules in cross-section, with the rods aligned *parallel* to the column. The flexible side-chains provide the surrounding continuum (Figure 81d). The axial alignment of the rods is confirmed by the distribution of colours in polarised optical micrographs using an optical compensator (Figure 82b).

The compound used in this work has a lateral chain with two incompatible branches, a fluorinated ( $R_F$ ) and a carbosilane one ( $R_{Si}$ ) (Figure 82a). At high temperatures the rod-like molecules group together forming periodic modulation of the columns, as seen in the electron density map in Figure 82g (red), reconstructed from X-ray diffraction. The weak but distinct Bragg reflection at  $q = 3.5 \text{ nm}^{-1}$  indexed as (001) (Figure 82f) indicates true 3-D-ordered packing of molecular bundles, with  $P6/mmm$  symmetry. Each bundle is centred at a vertex of a simple 3-D hexagonal unit cell (see Figures 82g and 81d).

On cooling, a transition to a lamellar phase takes place (see Figure 82d) via an intermediate orthorhombic LC phase  $Cmmm$  (for the complete SAXS cooling series see Figure 82f and the GISAXS pattern in Figure 82e). The molecular bundles are in fact ribbons, rotating in the hexagonal phase but locked in the orthorhombic  $Cmmm$  (Figure 82h). Figure 82h also shows the presence of undulating  $R_F$ -rich columns running perpendicular to the main aromatic columns. Thus, this crossed column mesophase consists of two orthogonal interpenetrating sets of columns, one segmented and the other undulated. On further cooling, in the  $Lam_{Sm}/p2mm$  phase the ribbons fuse to form infinite sheets. In the lamellar phase the  $R_F$ -rich columns remain, but change from undulated to straight. Thus, the  $Lam_{Sm}$  phase contains fluorinated columns intercalated between aromatic sheets (Figure 82i).

In summary, three new LC phases were discovered with decreasing temperature, each with an intriguing structure: a hexagonal 3-D phase with correlated modulated columns, a 3-D phase with crossed columns, and a phase with columns between layers. This work illustrates the fact that there is much more yet to be discovered in liquid crystals. There has been a flurry of discoveries of new and ever more complex structures with great promise of new nanomaterials for optics and molecular electronics, photovoltaics, LEDs, ceramics templating and other applications.

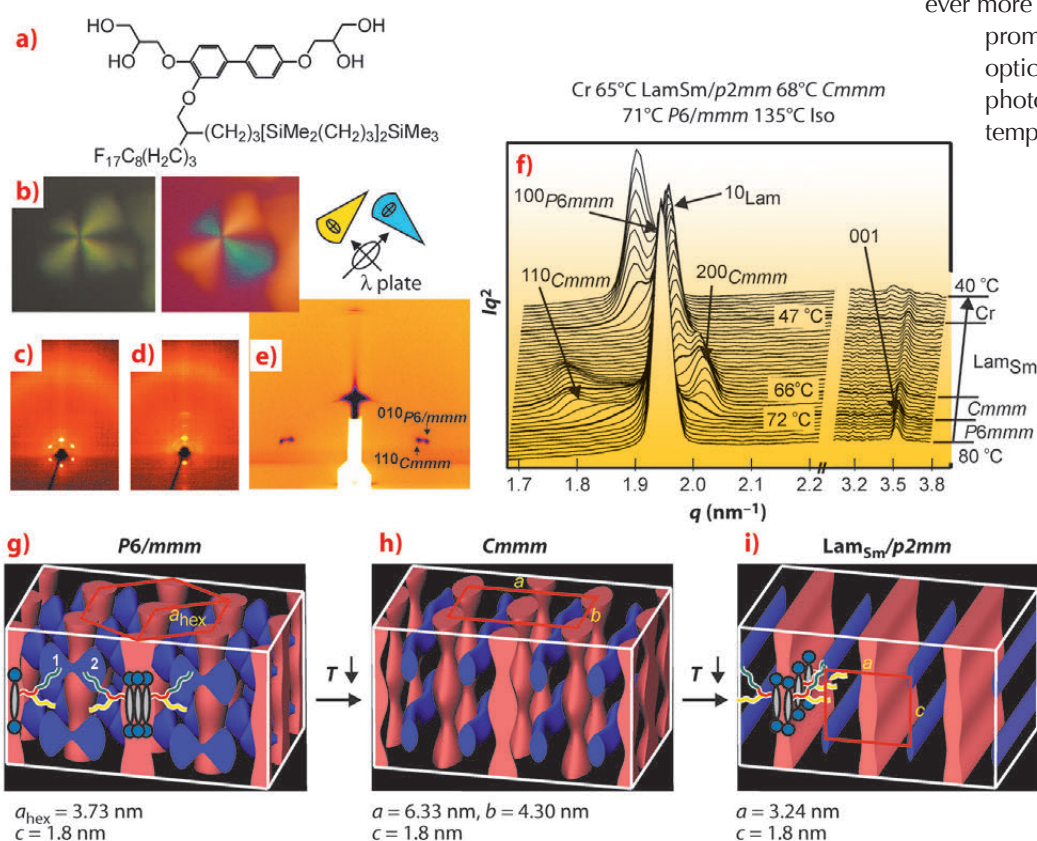


**Fig. 82:** a) The compound used in this work. b) Single spherulite of the  $P6/mmm$  phase between crossed polarisers (left), with a retarder plate (middle), and indicatrix orientation of the retarder (right). c) XRD pattern (surface-aligned sample) at  $T = 125^\circ C$  ( $P6/mmm$ ) and d) at  $T = 59^\circ C$  ( $Lam_{Sm}/p2mm$  phase). e) GISAXS pattern at  $T = 71^\circ C$  showing the coexistence of  $P6/mmm$  and  $Cmmm$  phases. f) Powder SAXS during continuous cooling, covering the three LC phases and the crystal. Electron density maps obtained from synchrotron powder patterns at g)  $T = 80^\circ C$ , h)  $T = 60^\circ C$  and i)  $T = 52^\circ C$ . Red = low density (bolaamphiphilic moieties); blue = high density (richest in  $R_F$  chains); molecules are sketched.



## ■ Anisotropic dynamics of the tenuous gel in a liquid crystal–nanoparticle composite

Liquid crystals are a particular liquid state of matter that can undergo phase transition depending on external conditions such as temperature, concentration and composition. They are abundant in living systems but are most likely known for their technological applications in electronic displays. One of the directions to tune or tailor liquid crystal properties is by introducing colloidal particles. Particles perturb the organisation of the molecules and generate defects. It was shown that a high concentration of particles immersed in a liquid crystal can produce a new class of soft solids [1].

Gelation in particle-liquid crystal mixture originates from the direct interactions between particles and the distortion to the ordering of the host solvent. The latter results in effective interactions between the particles which have been well studied in the nematic phase [1,2] and more recently explored in the cholesteric phase [3]. The consequences of the particles for the liquid crystalline ordering and associated phase transitions have been explored in some detail but the static and dynamics behaviour of the particles has received far less attention. Investigations of the structural and dynamics properties of fumed hydrophilic silica in 8CB composites using XPCS show that, at low silica concentration, the composites are able to restructure themselves in time [4] by expansion of the network structure, which was confirmed by SAXS. For higher silica concentrations the network structure remains constant. The studies [4] suggest that there may be coupling between the dynamics of the particle-gel and the the dynamics of the nematic host. Here we build on these ideas by using silica particles with controlled surface chemistry to modify the direct interactions.

We investigated the structure, ageing and dynamics of 4'-pentyl-4-biphenylcarbonitrile (5CB)-nanoparticle gels using SAXS and XPCS. The strength of the hydrogen bonding was tuned by silanisation of the fumed silica nanoparticles. **Figure 83** presents the freeze-fracture electron microscopy of the composite. SAXS results show that the silica adopts a fractal structure in 5CB with only modest changes to the fractal dimension  $d_f$  between 1.98 and 2.26. It was confirmed that the composite samples were gels by rheology. Because the samples were opaque to visible light the dynamics was probed using XPCS with a CCD camera. We were able to quantify nonequilibrium dynamic properties and characterise the dynamics in two orthogonal directions. The dynamics of the composites show time-dependent behaviour and anisotropy evidenced by the different relaxation times in the vertical and horizontal directions. This anisotropy is not a result of sedimentation or the shape of the cell but reflects the local arrangement of nematic domains. In the same  $q$  range, the structure of the composite was isotropic. The decay of the intensity correlation functions can be described by compressed exponential functions. Quantitatively, we find that relaxation rate  $1/\tau_c$  varies linearly with scattering vector  $q$  for both directions. This indicated that the relaxation mechanism is not of diffusive origin (for which  $1/\tau_c \sim q^2$ ). Such behaviour has also been observed in other soft glassy systems and has been attributed to randomly distributed internal stress relaxations within the sample. The ageing observed in our liquid crystal-nanoparticle composite is consistent with slow reorganisation and has anisotropic character. We interpret ageing as being due to the slow relaxation of the

### Principal publication and authors

D.D. van't Zand (a), Y. Chushkin (b), L. Belkoura (c), C.V. Lobo (a), R. Strey (c), K. Lyakhova (d) and P.S. Clegg (a), *Soft Matter*, **8**, 4062 (2012).

(a) *School of Physics and Astronomy, University of Edinburgh (UK)*

(b) *ESRF*

(c) *Institute of Physical Chemistry, University of Cologne (Germany)*

(d) *Eindhoven University of Technology (The Netherlands)*

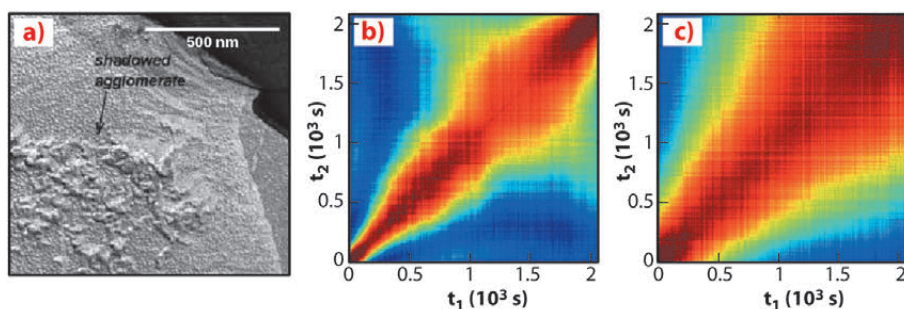


**Fig. 83:** a) Freeze-fracture electron microscopy of a silica agglomerate in 5CB; two-time correlation functions in the horizontal (b) and vertical direction (c), measured at  $q = 0.005 \text{ \AA}^{-1}$ , show slowing down with ageing time and dynamical anisotropy.



### References

- [1] T.A. Wood *et al.*, *Science* **334**, 79 (2001).  
 [2] H. Stark, *Phys. Rep.* **351**, 387 (2001).  
 [3] N. Hijnen, T.A. Wood, D. Wilson and P.S. Clegg, *Langmuir* **26**, 13502 (2010).  
 [4] A. Roshi, S. Barjami, G.S. Iannacchione, D. Paterson and I. McNully, *Phys. Rev. E* **74**, 031404 (2006).

composite. The longevity of these stresses is associated with the particles' ability to form hydrogen bonds and 5CBs' tendency to align.

Because the fumed silica induces homeotropic anchoring of the 5CB molecules at its surface, disorder is induced locally in 5CB near the particles as well. Local attempts to relax can result in a further large scale build up of stresses within the sample. After sufficient build

up of internal stress the gel 'yields' which means that rearrangements take place which gives rise to the slow pronounced ageing that we have observed. This is not a new phenomenon as such, however, it has not previously been found to have marked anisotropy.

### Principal publication and authors

D. Mishra (a), M.J. Benitez (a,b), O. Petracic (a,c), G.A. Badini Confalonieri (a,d), P. Szary (a), F. Brüßing (a), K. Theis-Bröhl (e), A Vorobiev (f), O. Konovalov (f), B.P. Toperverg (a,g) and H. Zabel (a), *Nanotechnology* **23**, 055707 (2012).

(a) Ruhr-University Bochum (Germany)

(b) Max-Planck Institut für Kohlenforschung, Mülheim (Germany)

(c) JCNS-2 and PGI-4, Forschungszentrum Jülich GmbH (Germany)

(d) Instituto de Ciencia de Materiales, CSIC Madrid (Spain)

(e) University of Applied Sciences Bremerhaven (Germany)

(f) ESRF

(g) Petersburg Nuclear Physics Institute RAS, Gatchina, St Petersburg (Russia)

## ■ Structural correlations in iron oxide nanoparticle monolayers and multilayers

Chemically synthesised magnetic nanoparticles (NPs) can be self-assembled as a 2-dimensional (2-D) or three-dimensional (3-D) monolayer or multilayer, respectively. Their magnetic and electrical properties can be tuned depending on *intra*-particle structure and *inter*-particle ordering within the film. Therefore, it is important to understand their ordering in self-assembled monolayers and multilayers. The present report highlights the inter-particle ordering investigated by grazing-incidence small-angle X-ray scattering (GISAXS) at beamline **ID10B**.

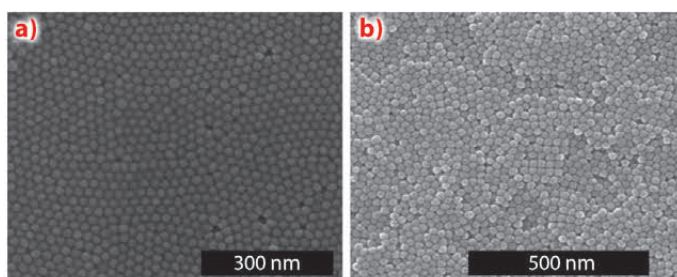
Self-assembly is a process in which smaller building blocks, such as NPs, are spontaneously organised to form an ordered pattern [1]. These self-assembled monolayers and multilayers may show collective physical properties that are completely different from their constituting individual building blocks. The ordering of the NPs plays an important role in defining these properties. Therefore, a considerable effort is devoted to the understanding of their structure (chemical and magnetic) using synchrotron and neutron radiation.

Iron oxide NPs of mean diameter 20 nm ( $\pm 1.4$  nm) were spin-coated on a silicon substrate. The NPs are dispersed in a toluene solvent and remain separated due to oleic acid surfactants. They form monolayers and multilayers depending on the concentration of toluene. **Figure 84a** and **Figure 84b** show scanning electron microscope images of a monolayer and a multilayer, respectively. The NP films show a relatively long-range hexagonal close-packed order, interrupted by vacancies and disclinations.

In NP films one encounters two different periodicities at the mesoscopic scale. One is the out-of-plane periodicity, which can be probed by specular reflectivity scans. The second one is the in-plane hexagonal order, which can be probed by GISAXS measurements and reveals the in-plane electron density variation. The GISAXS patterns were measured with a photon energy of 7.96 keV ( $\lambda = 0.127$  nm). A MAR CCD camera captured the diffuse scattering at an incident angle of  $0.15^\circ$ .

**Figure 85a** and **Figure 85b** show the GISAXS patterns from a monolayer and a multilayer, respectively. The patterns can be understood by the convolution of two factors. The first one is a ring-like intensity distribution, which represents the form factor of the NP shape and corresponds to the Fourier transform of the radial electron density of a spherical particle. On top of these rings, high intensity Bragg peaks are visible

**Fig. 84:** SEM image of (a) monolayer and (b) multilayer iron oxide NP film. The hexagonal ordering can be recognised from the images. Originating from the principal publication.





that originate from the 2-D long range hexagonal ordering, corresponding to the Fourier transform of the in-plane pair-correlation function.

The GISAXS patterns are indexed to a 2-D hexagonal lattice of 26.31 nm. The mismatch between the value of the lattice parameter and the mean diameter arises from the oleic acid shell surrounding the NPs. The Bragg peak widths were calculated from a Lorentzian fit yielding a mean value for the in-plane correlation length, which is 133 nm and 55 nm for the monolayer and the multilayer, respectively. The ordering in the normal direction was also investigated with X-ray reflectivity measurements and the multilayer shows a Bragg peak, which indicates that a well ordered NP multilayer can be prepared by the simple spin-coating method.

The in- and out-of-plane structural ordering has been correlated to the magnetic ordering. In fact polarised neutron reflectivity (PNR) reveals an enhanced magnetic correlation due to strong dipolar interaction amongst the superparamagnetic NPs. However, the contrary is expected as the NPs should fluctuate thermally at room temperature being in single domain states. But the long-range in-plane hexagonal order as

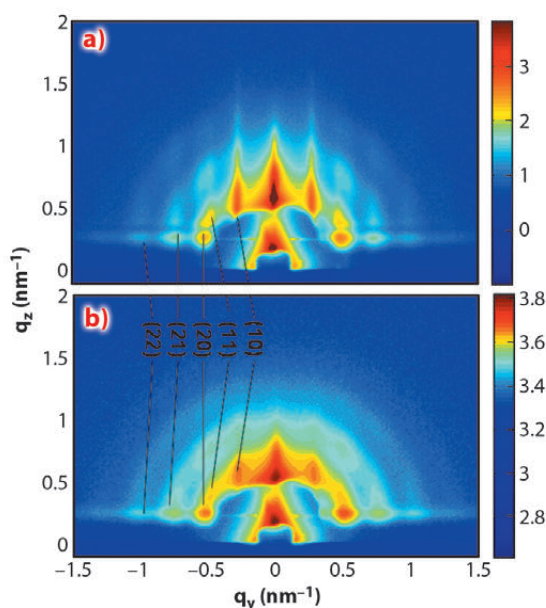


**Fig. 85:** GISAXS pattern measured for (a) monolayer and (b) multilayer. The colour codes show the intensity distributions, which are different for two images. Originating from the principal publication.

seen by GISAXS induces a long-range magnetic order in the films, suppressing thermal fluctuations.

In summary, we have studied by GISAXS the in-plane structural ordering of iron-oxide nanoparticles of 20 nm in diameter, which are self-assembled in monolayers and multilayers. The in-plane correlation length is larger in monolayers and decreases with the number of layers within a multilayer. This is an important finding for the understanding of their intriguing magnetic properties.

#### References

- [1] C.T. Black, C.B. Murray, R.L. Sandstrom and S. Sun, *Science* **290**, 1131 (2000).

## ■ Cytoskeletal network structure studied by X-ray nanodiffraction

The cytoskeleton of eukaryotic cells is a complex network of different filamentous biopolymers that gives cells their versatile shapes and specific mechanical properties, and consequently enables cells to perform particular functions. The main constituents of the cytoskeleton are three different classes of fibrous proteins: actin filaments, microtubules and intermediate filaments. These proteins are organised in distinct superstructures such as bundles, networks or networks of bundles. One example of intermediate filaments are cytokeratins, which are expressed in various epithelial cells and provide these cells with the necessary mechanical properties to withstand external stress [1,2]. Cytokeratins assemble via a complex process into filaments with a diameter of about 10 nm and these filaments can

further form bundles with diameters up to a few hundreds of nanometres, that are organised in a superstructure.

To study the structure of keratin bundles, we performed scanning X-ray diffraction experiments on freeze-dried cells using a nanofocused X-ray beam at beamline **ID13**. On the one hand, this method allows us to calculate, e.g., the total scattered intensity at each scan point and arrange these values in a two-dimensional array to obtain a so-called X-ray dark-field image of the sample in real-space as shown in **Figure 86**. On the other hand, we were able to analyse the scattering signal from a small sample volume with dimensions on the order of the beam size and obtain information about the local sample structure as shown in **Figure 87**.

#### Principal publication and authors

- B. Weinhausen (a), J.-F. Nolting (a), C. Olendrowitz (a), J. Langfahl-Klabes (a), M. Reynolds (b), T. Salditt (a) and S. Köster (a), *New J. Phys.* **14**, 085013 (2012).  
(a) Institute for X-Ray Physics and Courant Research Centre 'Nano-Spectroscopy and X-Ray Imaging', Georg-August-Universität Göttingen (Germany)  
(b) ESRF

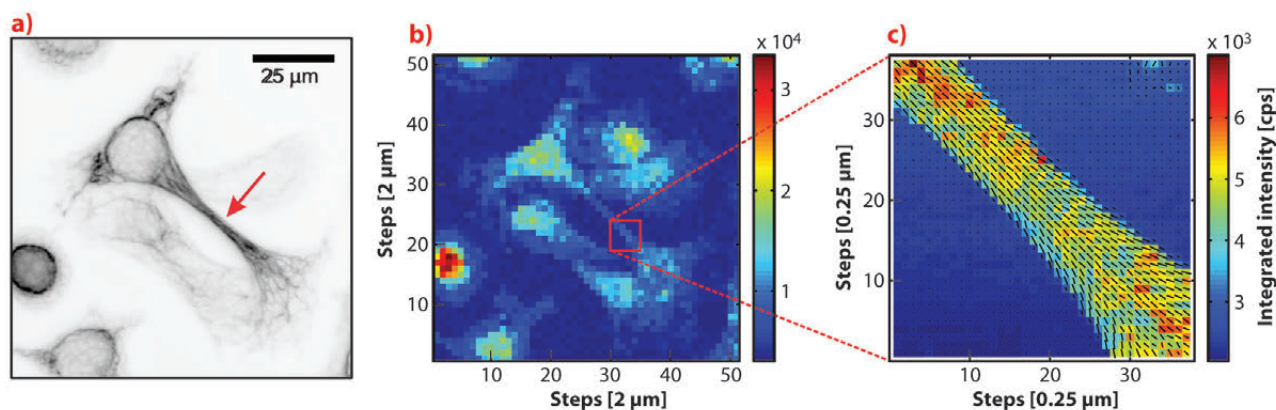


**Fig. 86:** a) Inverted fluorescence microscopy image of the keratin network in hydrated, paraformaldehyde-fixed SK8/18-2 cells. b) X-ray dark-field image from a coarse mesh scan on the same sample area as shown in panel (a) after freeze-drying. c) Overlay of the calculated structure orientation, indicated by black lines, with the corresponding X-ray dark-field image obtained from a region of interest scan recorded on the keratin-rich extension of one cell as highlighted in panels (a) and (b).

**Figure 86a** shows a visible-light fluorescence microscopy image of the keratin network of a group of cells and **Figure 86b** shows the corresponding X-ray dark-field image of the same sample region. Note that some cells, which are visible in the X-ray dark-field image, do not have a keratin network and are therefore not visible in the fluorescence microscopy image. From the fluorescence microscopy images we selected cells with a pronounced network morphology, like the cell in the centre of **Figures 86a and b** exhibiting a keratin-rich extension, and performed fine scans with a longer exposure time on smaller sample regions, see **Figure 86c**. For the fine measurements we not only calculated X-ray dark-field images, but also determined the degree and direction of local sample structure orientation from the anisotropy of the scattering signal in each scattering pattern. In **Figure 86c** the local structure orientation is indicated by black lines

and is depicted as an overlay with the dark-field image. The calculated structure orientation agrees very well with visible structures in the fluorescence microscopy image.

Single scattering patterns were further analysed to determine the local structure in the sample. Here, we integrated the scattered intensity in the azimuthal direction for eight angular segments, as marked by the white lines in **Figure 87a**. The resulting radial intensity profiles, shown in **Figure 87b**, exhibit scattering maxima and minima indicating distinct structure in the sample. The employed method therefore allows imaging of the sample in real-space as well as probing the local sample structure using scattering patterns in reciprocal-space, yielding structural information on two different length scales. Furthermore, this technique can be applied to a variety of samples or materials.

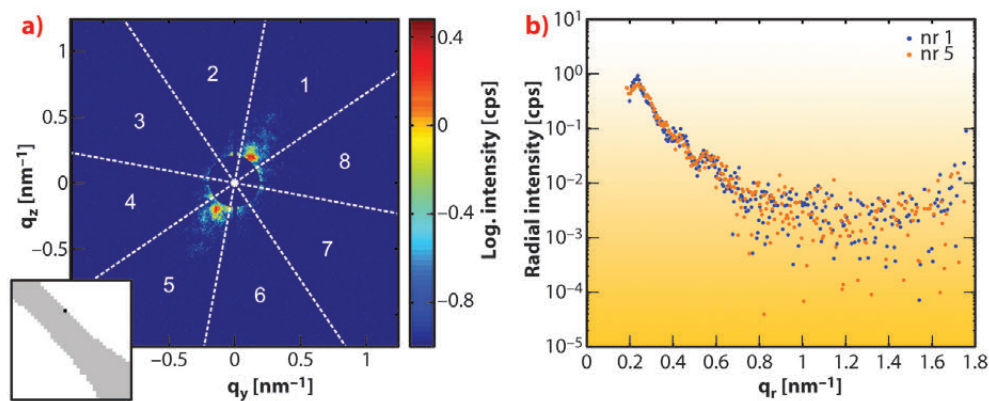


**Fig. 87:** a) The intensity of a single scattering patterns taken on the edge of the cellular extension (position is indicated in inset) is integrated in eight angular regions as indicated by white lines. The segments are oriented such that the first and fifth segment are centred around the direction of highest scattering intensity. b) Radial intensity profiles obtained from azimuthal integration in the first and fifth segment of the scattering pattern in (a).

#### References

- [1] H. Herrmann, H. Bär, L. Kreplak, S.V. Strelkov and U. Aebi, *Nature Rev. Mol. Cell Biol.* **8**, 562-573 (2007).
- [2] E. Fuchs and D.W. Cleveland, *Science* **279**, 514-519 (1998).



## How $\text{YCl}_3$ helps proteins crystallise

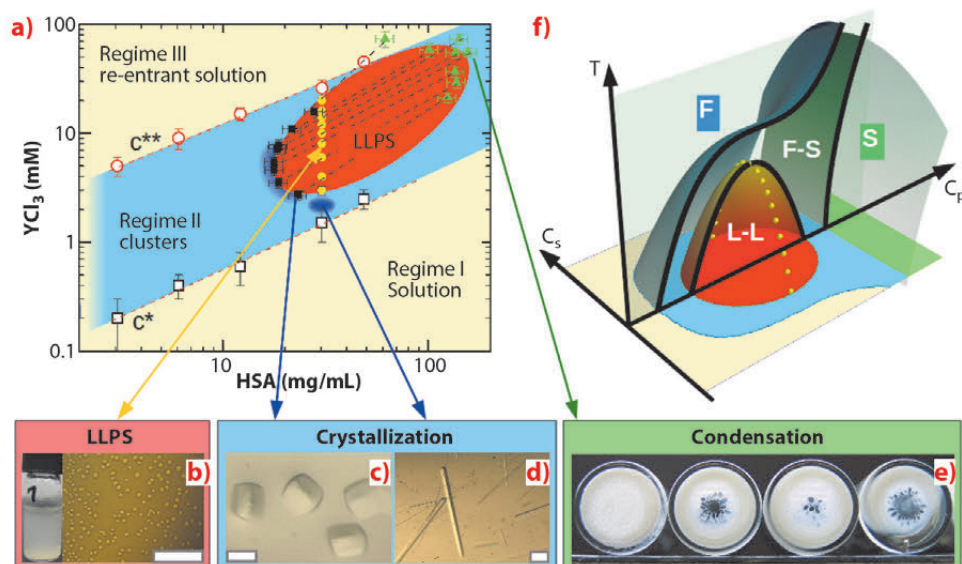
Metastable liquid-liquid phase separation (LLPS) in protein solutions is a fundamental biophysical phenomenon and provides a pathway for biological structure formation [1]. Proteins in solution, like colloids, often interact *via* effective interactions caused by other components of the solution, *i.e.* the solvent, salt, *etc.* Usually the range of the effective attraction for proteins in solution is shorter than their diameter, which leads to a metastable LLPS (corresponding to the gas-liquid phase separation in one-component systems). Close to the LLPS, density fluctuations can significantly reduce the energy barrier of protein crystallisation. In addition to the classical nucleation mechanism, a two-step nucleation mechanism has been proposed [2].

Here we show that trivalent salts can be used to optimise crystallisation conditions for globular proteins and also present some general physical insights. Human serum albumin (HSA) is a medium size globular protein abundant in the blood with a molecular weight of 67 kDa. In **Figure 88a**, we present the HSA phase diagram as a function of the protein concentration,  $c_p$ , and the concentration of the trivalent salt  $\text{YCl}_3$ ,  $c_s$ , at 20°C. Trivalent cations tune protein interactions by binding to acidic surface residues, causing a charge-inversion [3,4]. The phase diagram is divided into three regimes. Regime I and III correspond to a transparent single-phase solution and

regime II to a turbid two-phase state (**Figure 88a**). Closer examination of regime II by optical microscopy (**Figure 88b**) reveals tiny droplets of the protein-rich phase suspended in solution. They merge and grow, indicating a LLPS. A similar LLPS induced by  $\text{YCl}_3$  is also observed in bovine serum albumin and  $\beta$ -lactoglobulin solutions, suggesting LLPS to be a universal phenomenon for negatively charged proteins (46% of the protein family) in the presence of trivalent cations. The partitioning of both protein and salt into two coexisting phases has been determined by X-ray and ultra-violet light absorption. The pairs of coexisting phases connected by tie-lines in **Figure 88a** define the LLPS coexistence region (in red).

The effective protein-protein interaction upon LLPS has been characterised by SAXS (**Figure 89**) with a sticky hard sphere structure factor with stickiness  $\tau$ . The related second virial coefficient  $B_2$  indicates a variation in interaction strength throughout the two-phase region as expected for different protein-cation complexes. Approaching the phase boundary,  $B_2$  fulfills the thermodynamic criterion for the LLPS critical point as well as lying in the crystallisation regime.

The phase behaviour shown in **Figure 88a** can now be understood along the usual phase diagram for colloids with short-range attraction. The growth of high quality protein single crystals (**Figures 88c and d**)



### Principal publication and authors

F. Zhang (a), R. Roth (b), M. Wolf (a), F. Roosen-Runge (a), M.W.A. Skoda (c), R.M.J. Jacobs (d), M. Sztucki (e) and F. Schreiber (a), *Soft Matter* **8**, 1313-6 (2012).  
(a) Universität Tübingen (Germany)  
(b) Universität Erlangen-Nürnberg (Germany)  
(c) ISIS, Rutherford Appleton Laboratory (UK)  
(d) University of Oxford (UK)  
(e) ESRF

**Fig. 88:** Tuning interactions in protein solutions towards controlled protein crystallisation (scale bars correspond to 0.1 mm): (a) Phase diagram of HSA with  $\text{YCl}_3$  at 20°C. (b) LLPS observed under a microscope. (c-d) Crystals grown from different conditions. (e) Amorphous aggregation in the protein-rich coexisting phase. (f) Sketch of a phase diagram with three control parameters: temperature,  $T$ , protein and salt concentration,  $c_p$  and  $c_s$ .

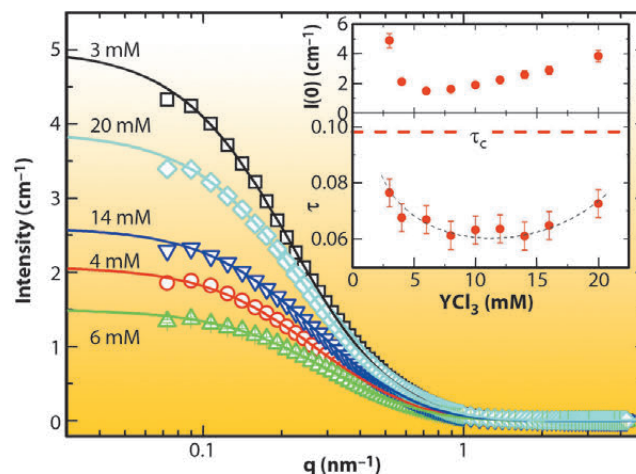


### References

- [1] J.D. Gunton, A. Shiryayev and D.L. Pagan, *Protein Condensation-kinetic pathways to crystallization and disease*, Cambridge University Press, New York (2007).
- [2] P. Rein ten Wolde and D. Frenkel, *Science* **277**, 1975-1978 (1997).
- [3] F. Zhang, M.W.A. Skoda, R.M.J. Jacobs, S. Zorn, R.A. Martin, C.M. Martin, G.F. Clark, S. Weggler, A. Hildebrandt, O. Kohlbacher and F. Schreiber, *Phys. Rev. Lett.* **101**, 148101 (2008).
- [4] F. Zhang, G. Zocher, A. Sauter, T. Stehle and F. Schreiber, *J. Appl. Cryst.* **44**, 755-762 (2011).
- [5] F. Zhang, F. Roosen-Runge, A. Sauter, R. Roth, M.W.A. Skoda, R.M.J. Jacobs, M. Sztucki and F. Schreiber, *Faraday Discuss.* **159**, 313 (2012).

supports these theoretical predictions. Importantly, by using multivalent ions, both two-step nucleation (**Figure 88c**) and classical nucleation close to the LLPS critical point (**Figure 88d**) can be realised at the same temperature [4,5]. By varying temperature, crystallisation conditions can be further optimised. Several proteins have been previously crystallised using  $\text{YCl}_3$  as a crucial additive without clarifying its exact role.

**Fig. 89:** SAXS data with model fitting for the protein-poor phases from sample solutions with initial  $c_p$  of  $31.0 \text{ mg mL}^{-1}$  after LLPS. Only every second data point is plotted for clarity. The insets show  $\tau$  and the forward intensity  $I(0)$  as a function of  $c_s$ .



The presented phase diagram with  $T$ ,  $c_p$  and  $c_s$  as control parameters (**Figure 88f**) provides a physical understanding of the salt-induced phase behaviour as a pathway towards crystallisation.

### Principal publication and authors

D. Cavallo (a), D. Mileva (b), G. Portale (c), L. Zhang (d), L. Balzano (a), G.C. Alfonso (d) and R. Androsch (b), *ACS Macro Lett.* **1**, 1051-1055 (2012).

(a) Polymer Technology Group, Eindhoven University of Technology (The Netherlands)

(b) Center of Engineering Sciences, Martin-Luther University Halle-Wittenberg, Halle/Saale (Germany)

(c) DUBBLE CRG, ESRF, Grenoble (France)

(d) Department of Chemistry and Industrial Chemistry, University of Genova (Italy)

## Dual crystallisation pathway in a semi-crystalline aromatic polyester

The understanding of the melt-crystallisation process in synthetic polymers represents a fundamental challenge, both from the scientific and technological points of view. Indeed, most of the polymers used in everyday products, from the fibres of our clothes to the shopping bags at the supermarkets, are crystallisable. However, the solidification conditions commonly applied during the production of plastic goods are largely different from those typically achieved in a laboratory. For instance, the cooling rates attained in actual processing span from few to hundreds  $\text{K s}^{-1}$ , while they seldom reach  $1 \text{ K s}^{-1}$  in “classical” polymer crystallisation studies. Recently developed experimental techniques, such as nano-calorimetry or ultra-fast X-ray diffraction are now allowing us to fill this gap [1].

Even under isothermal or mild cooling conditions, polymer crystallisation suffers from kinetics limitations: the highly entangled melt of macromolecular chains is unable to form a completely ordered structure. As a result, crystallites always

coexist with disordered amorphous regions, *i.e.*, the material is semi-crystalline. Moreover, crystallisation at large undercoolings/high cooling rates might bring further complications, since structures with an intermediate degree of order between that of the amorphous phase and crystal, generally named “mesophases”, can develop [1,2].

The exact role of mesophases in polymer melt-crystallisation is debated. In many cases they can appear as intermediate states on the route to the ultimately stable crystalline structure, according to the well-known Ostwald’s rule of stages [3,4]. The controversy lies in the interpretation of these observations: whether the multi-stage process via metastable states is a general prerequisite of polymer crystallisation [3], or whether it is the manifestation of a kinetic effect such as mesophase formation being faster than crystal development [4].

In this work we have shown that the same semi-crystalline material can either “obey” or “defy” Ostwald’s rule of

stages, depending on the crystallisation conditions. The material elected for the investigation is PBN, poly(butylene-2,6-naphthalate), an aromatic polyester with important applications as a high performance fibre. By coupling a custom-built quenching device with a state-of-the-art X-ray detector (Pilatus 300K-W) at beamline **BM26** (DUBBLE-Dutch Belgian Beamline) [1], the crystallisation process can be monitored at industrially relevant cooling rates, up to about  $200 \text{ K s}^{-1}$ .

Representative examples of time-resolved WAXD experiments during cooling from the melt are presented in **Figure 90**.

A dual crystallisation behaviour can be appreciated. For the lowest cooling rate, the triclinic crystalline structure ( $\alpha$ -phase) develops directly from the isotropic melt. In contrast, when the cooling rate is high enough, crystallisation of the  $\alpha$ -phase is preceded by mesophase formation. This step can be recognised by a distinct enhancement of the scattering in the central region of the WAXD pattern with respect to the melt, indicating an increased lateral correlation of molecular segments.

PBN offers the interesting possibility of probing the formation of crystals both from the melt and the pre-ordered mesomorphic phase. This can conveniently be done with conventional and chip-based differential scanning calorimetry. As shown in **Figure 91 (inset)**, the formation of mesophase and its transformation to crystals at large undercooling are both detected as separated exothermic events in the calorimetric trace. The rates of the three transitions, namely melt to crystal, melt to mesophase and mesophase to crystal, can be compared in **Figure 91**.

In conclusion, combining the results of fast scanning chip-calorimetry with time-resolved X-ray diffraction experiments, the reason behind the dual ordering behaviour of PBN can be unravelled. Crystallisation occurs directly from the melt at low undercooling, above the limit of stability of the mesophase or when its rate of formation is too sluggish. On increasing undercooling/cooling rate, mesophase formation from the melt becomes kinetically favoured in comparison to the melt-crystallisation process. In the latter case

the material behaves accordingly to Ostwald's rule of stages, exhibiting a two-step crystallisation mechanism.

#### References

- [1] D. Cavallo, G. Portale, L. Balzano, F. Azzurri, W. Bras, G.W. Peters and G.C. Alfonso, *Macromolecules* **43**, 10208-10212 (2010).
- [2] F. Auriemma, C. De Rosa and P. Corradini *Adv. Polym. Sci.* **181**, 1-74 (2005).
- [3] G. Strobl, *Rev. Mod. Phys.* **81**, 1287-1300 (2009).
- [4] S.Z.D. Cheng, *Phase transitions in polymers: the role of metastable states* Elsevier, Amsterdam (2008).

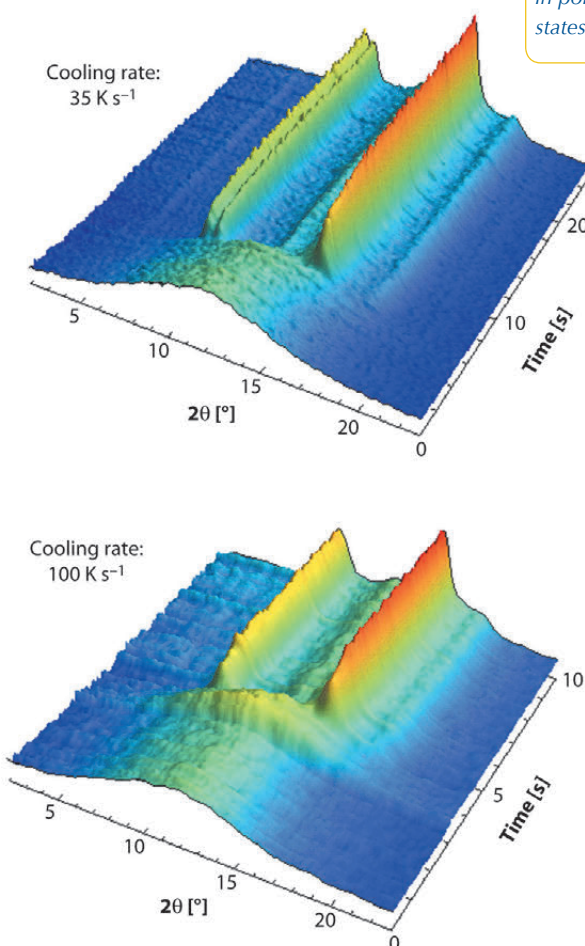


**Fig. 90:** Time-resolved WAXD patterns during cooling PBN samples at the indicated cooling rates.

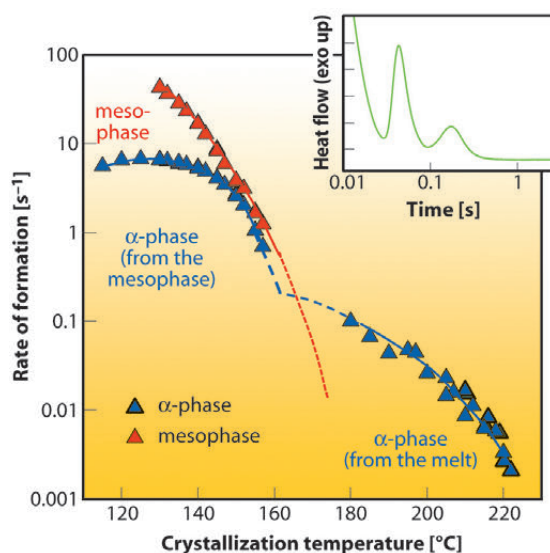


**Fig. 91:** Rate of mesophase and crystal formation as a function of temperature and example of calorimetric signal (inset).



### Principal publication and authors

P. Horcajada (a), F. Salles (b), S. Wuttke (a,c), T. Devic (a), D. Heurtaux (a), G. Maurin (b), A. Vimont (c), M. Daturi (c), O. David (a), E. Magnier (a), N. Stock(d), Y. Filinchuk (e,f), D. Popov (g), C. Riekel (h), G. Férey (a) and C. Serre (a), *J. Am. Chem. Soc.* **133**, 17839 (2011).  
 (a) Institut Lavoisier, (UMR CNRS 8180), Université de Versailles (France)  
 (b) Institut C. Gerhardt Montpellier, UMR CNRS 5253, ENSCM, Montpellier (France)  
 (c) Laboratoire Catalyse et Spectrochimie LCS, UMR CNRS 6506, ENSICAEN, Caen (France)  
 (d) Institute of Inorganic Chemistry, Christian-Albrechts-Universität, Kiel (Germany)  
 (e) SNBL at ESRF, Grenoble (France)  
 (f) Institute of Condensed Matter and Nanosciences, Université Catholique de Louvain, Louvain-la-Neuve (Belgium)  
 (g) HPCAT, Geophysical Laboratory, Carnegie Institution of Washington, Argonne (USA)  
 (h) ESRF

### References

[1] G. Férey and C. Serre, *Chem. Soc. Rev.* **38**, 1380 (2009).  
 [2] C. Serre, C. Mellot-Draznieks, S. Surblé N. Audebrand, Y. Filinchuk and G. Férey, *Science* **315**, 1828 (2007).

## Functionalisation of highly flexible metal organic framework materials

Crystalline porous hybrid solids or metal organic frameworks (MOFs) are of interest due to their potential applications in domains such as separation, gas storage, catalysis or biomedicine. While MOFs are usually rigid structures with large unit cells, some of them exhibit a very large and reversible swelling under external stimuli including pressure, temperature, light, gas or solvent adsorption. The overall performance of the flexible MOF depends on the structure type and the nature of the constitutive metal and linker [1]. MOFs are usually only available as powders. Nonetheless, high resolution structural data can be obtained using microdiffraction techniques. In this work single-crystal microdiffraction was performed at beamline **ID13** with about a 1  $\mu\text{m}$  beam.

We have previously shown [2] that these solids possess a giant and reversible increase in their cell volumes (~85-220%) upon solvent sorption and also possess a selective sorption capacity while retaining their crystal structure. Replacement of one or several aromatic proton(s) by functional groups strongly affects the flexible character of these phases. We report here

how the swelling of a series of iron(III) dicarboxylates, denoted MIL-88B or D, built from a hexagonal array of trimeric iron(III) building units and dicarboxylate moieties, can be tuned by changing the functional groups grafted onto the organic spacer.

The effect of the modifications was dependent on the nature, size and number of functional groups grafted onto the organic spacer (Figure 92) [2]. The initial degree of pore opening of the dried solid can be varied. This allows the amplitude of the swelling to be varied and can lead to either dried solids being non porous or possessing a permanent porosity to nitrogen (at -196°C). As a consequence, the increase in pore opening is associated with a lower degree of interactions between the aromatic spacer units from the dried structure, and the adsorption of solvents becomes much easier. In addition, the presence of polar or apolar functional groups allows the sorption selectivity of the porous solid to be tuned. This paves the way for the use of functionalised flexible MOFs for separation or drug delivery applications.

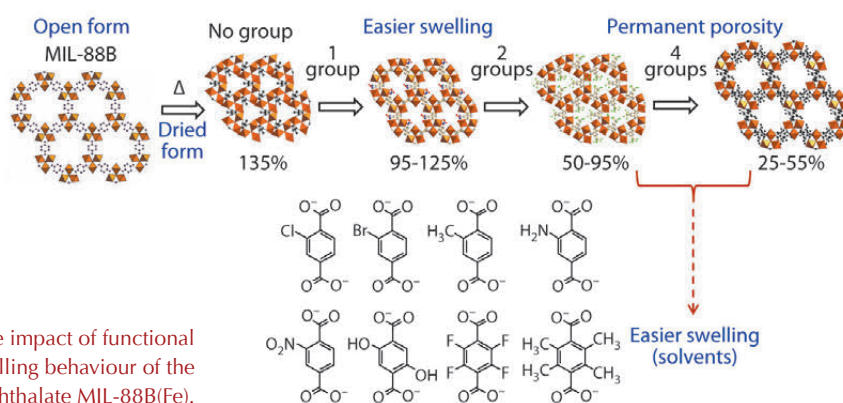


**Fig. 92:** Schematic representation of the impact of functional groups over the porosity and the swelling behaviour of the iron(III) terephthalate MIL-88B(Fe).



# Electronic Structure and Magnetism

One year ago the ESRF was in the midst of a long shutdown to carry out major construction work for Phase I of the Upgrade Programme. Although work continues, operation restarted back in May 2012 and many new experiments have been successfully performed since then. In the Electronic Structure and Magnetism Group, the first upgrade beamlines on BM23 and ID24 have gone into user operation enhancing our portfolio of beamlines. The upgrade continues for the group's beamlines with the closure of the soft X-ray beamline ID08 in July 2013. It will be replaced by the new soft X-ray beamline being built on ID32. The construction has already started.

Amongst all this construction activity, the main business of producing scientific results has continued. The articles chosen for this year's Highlights show the timely, topical and exciting work being done. They represent typical examples of the cutting-edge research being carried out and address a diverse range of important scientific questions. These range from heavy Fermions, topological insulators to dilute magnetic semiconductors, arsenic in soils and catalysts. A short introduction to the topics follows.

Studies of heavy Fermion materials have attracted interest for many decades. Below a characteristic temperature, the conduction electrons behave as if they have an effective mass several orders of magnitude larger than the free-electron mass (hence heavy). Typically compounds of Ce, U, Yb with localised f-electrons fall into this class of materials. Due to competing effects there are many possible ground states. Understanding the electronic properties of such materials is of basic interest and essential to explain their extraordinary properties, such as their low temperature resistivity. The highlight by Willers *et al.* shows how X-rays can help in understanding such properties, using the example of  $\text{YbInNi}_4$ .

Topological insulators are fascinating materials in which the bulk of the material is insulating but the surface is metallic. Conducting surface states can arise due to special symmetry properties. For example, in the case of  $\text{Bi}_2\text{Se}_3$ ,

which is studied in the article by Honolka *et al.*, spin-orbit coupling and time reversal lead to a surface conducting state in which the spin and the momentum of the electron are coupled. Two electrons moving in opposite directions will have reversed spins. This opens up interesting possibilities for spin electronic applications, as the topological surface state allows a spin current to move with little resistance.

Even before the discovery of topological insulators extensive efforts were employed to find suitable materials for spintronic applications. One area of investigation has been that of dilute magnetic semiconductors. The hope is that a material combining magnetic and semiconductor properties could be integrated in future semiconductor devices using the spin of the electron as an extra degree of freedom. However, it is often difficult to separate intrinsic properties from spurious sources of magnetism, e.g. magnetic impurities or clusters of magnetic atoms. X-ray studies using magnetic dichroism (XMCD) techniques allow both structural and magnetic properties to be measured. Importantly, X-ray dichroism studies are element specific giving vital additional information. A study of this type is described in the Highlight by Ney *et al.*

XMCD is also a highly sensitive method and this combined with its element specificity and access to high magnetic fields and low sample temperature allows for unique experiments. One such example is the study of Rh clusters by Narthem *et al.* where exchange enhanced Pauli paramagnetic properties are revealed.

Single walled carbon nanotubes, which are essentially like a graphene sheet folded into a cylinder, also have many novel properties. They are highly flexible and have a high tensile strength together with interesting electronic properties. There are many potential uses including nanotube transistors, solar cell applications, etc. By doping with halogens, the electronic properties can be modified, and that is the subject of the article by Chorro *et al.*

In a totally different vein, the article by Langner *et al.* addresses the environmental problem



of arsenic contamination in the environment, where it is a threat to some of the world's water resources. This is an important issue affecting millions of people in dozens of countries. To address this problem, an understanding of the biogeochemical cycle is needed and spectroscopic studies of soils can help in this respect, as is shown in the article.

The final two articles deal with chemical problems; one concerns the meso-sphere of complexes in solution and the other the study of catalytic materials under reaction conditions. Both combine results from several different techniques. The former combines neutron, X-ray results and Monte Carlo simulations; the latter X-ray diffraction, infrared and EXAFS results.

The meso-shell describes the solvation molecules, often water but not only, that surround a molecule in solution and influence

its reactivity. Having a better understanding of this structure is important for synthesis and is addressed in the article by Bowron *et al.*

The Highlight by Kubacka *et al.* emphasises the importance of studying *in situ* and as close as possible to real catalytic systems using a multitechnique approach. The results are significant in the context of pollutant elimination in three-way conversion materials (TWC) used in car catalytic converters.

In order to continue to produce scientific results at the forefront of research, we need to further develop our capabilities. This is happening through Phase I of the Upgrade Programme and will hopefully continue in a Phase II, which is currently under discussion.

N.B. Brookes

#### Principal publication and authors

T. Willers (a), J.C. Cezar (b), N.B. Brookes (b), Z. Hu (c), F. Strigari (a), P. Körner (a), N. Hollmann (c), D. Schmitz (d), A. Bianchi (e), Z. Fisk (f), A. Tanaka (g), L.H. Tjeng (c) and A. Severing (a), *Phys. Rev. Lett.* **107**, 236402 (2011).  
 (a) Institute of Physics II, University of Cologne (Germany)  
 (b) ESRF  
 (c) MPI for Chemical Physics of Solids, Dresden (Germany)  
 (d) Helmholtz-Center Berlin for Materials and Energy (Germany)  
 (e) Département de Physique, Université de Montréal (Canada)  
 (f) University of California, Irvine (USA)  
 (g) Department of Quantum Matter, ADSM Hiroshima University (Japan)

## Magnetic field induced orbital polarisation in cubic YbInNi<sub>4</sub>

In many cerium and ytterbium based heavy fermion materials the localised 4f electrons interact with conduction electrons giving rise to extraordinary low energy properties. Therefore, for a deeper understanding of these properties, the knowledge of the 4f ground-state wave functions is crucial.

In a crystalline environment the 4f electrons experience a crystal field which lifts the degeneracy of the Hund's rule ground state and the resulting states are highly anisotropic. We used linear polarised soft X-ray absorption spectroscopy (XAS) at the rare earth M edges as a complementary tool to neutron scattering to determine crystal field ground-state wave functions in some tetragonal and orthorhombic cerium compounds [1-3]. Here the selection rules of the linear polarised light give the sensitivity to the initial state symmetry. However, XAS is a dipole technique, so that anisotropies in an environment with a higher than twofold rotational axis appear isotropic although they are not. Hence

linear polarised XAS seemingly cannot be applied for cubic systems. Using the example of YbInNi<sub>4</sub> where the crystal field ground state had been disputed in the past, we demonstrated that XAS with the application of a magnetic field induces linear dichroism even in cubic compounds, so that key information about the ground-state wave function can be obtained.

In the cubic symmetry of YbInNi<sub>4</sub> the eightfold degenerate Hund's rule ground state of Yb<sup>3+</sup> with J = 7/2 splits into two doublets  $\Gamma_6$  and  $\Gamma_7$ , and one quartet  $\Gamma_8$ . These wave functions can be written in the basis of  $J_z$

$$\begin{aligned}
 |\Gamma_6\rangle &= \begin{pmatrix} c|-7/2\rangle + d'|+1/2\rangle \\ c|+7/2\rangle + d'|-1/2\rangle \end{pmatrix} \\
 |\Gamma_7\rangle &= \begin{pmatrix} a'|-5/2\rangle - b'|+3/2\rangle \\ a|+5/2\rangle - b|-3/2\rangle \end{pmatrix} \\
 |\Gamma_8\rangle &= \begin{cases} |\tilde{\Gamma}_6\rangle = \begin{pmatrix} d'|-7/2\rangle - c'|+1/2\rangle \\ d|+7/2\rangle - c|-1/2\rangle \end{pmatrix} \\ |\tilde{\Gamma}_7\rangle = \begin{pmatrix} b'|-5/2\rangle + a'|+3/2\rangle \\ b|+5/2\rangle + a|-3/2\rangle \end{pmatrix} \end{cases}
 \end{aligned}$$

with  $a^2+b^2 = a'^2+b'^2 = c^2+d^2 = c'^2+d'^2 = 1$ .

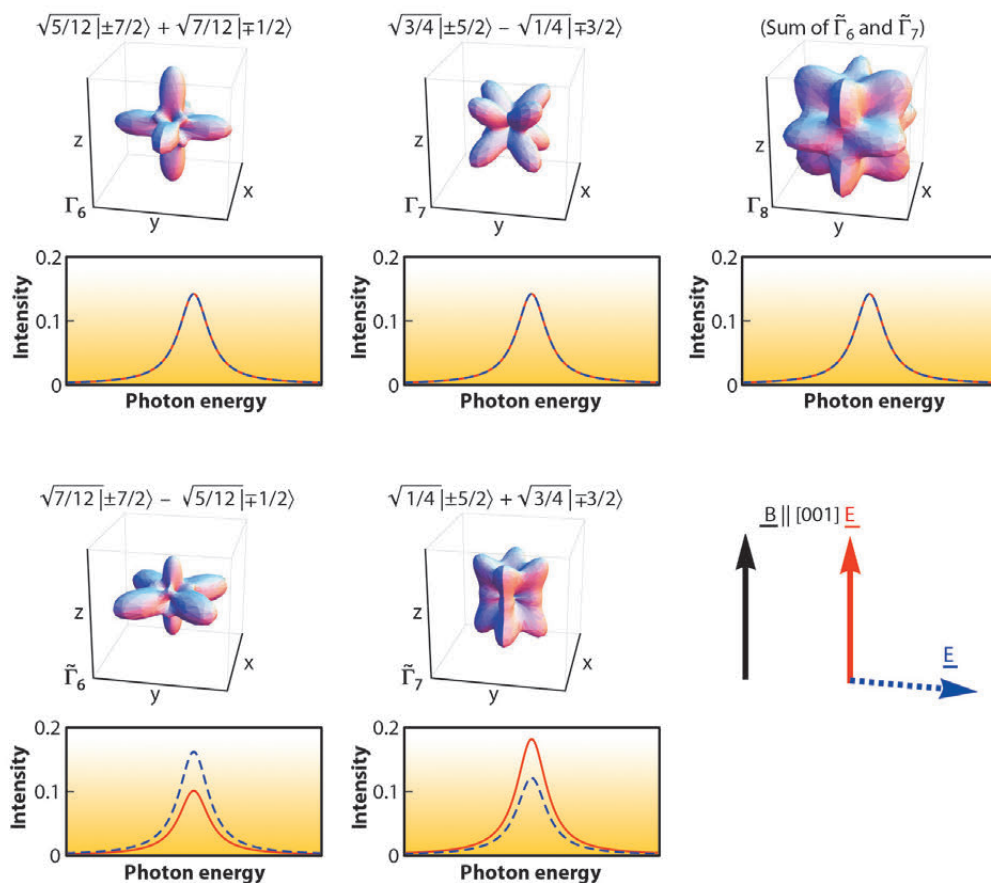


**Fig. 93:**  $4f$  angular hole-distributions and their corresponding polarisation dependent XAS spectra without (top) and with (bottom) applied field. The orientation of the applied magnetic field  $\mathbf{B}$  and electric field  $\mathbf{E}$  of the linear polarised light relative to the [001] axis is also depicted.

The upper panel of **Figure 93** shows the corresponding angular hole-distributions. Despite the strong asymmetry, they would not show any linear dichroism in an XAS experiment because of the dipole limitations. This is also demonstrated in **Figure 93** where the  $3d \rightarrow 4f$  XAS spectra for the  $\Gamma_6$ ,  $\Gamma_7$  and  $\Gamma_8$  states have been calculated in a full multiplet routine [4] for the electric field vector  $\mathbf{E}$  parallel (red) or perpendicular (blue dashed) to the [001] crystallographic axis. However, when lifting the remaining degeneracy with a magnetic field this changes considerably for some of the states: While the linear dichroism of the two Zeeman states of the  $\Gamma_6$  and  $\Gamma_7$  remains zero because they are Kramer's doublets, this is not the case for the  $\Gamma_8$ . The  $\Gamma_8$  quartet splits into two Zeeman-split  $\tilde{\Gamma}_6$  and  $\tilde{\Gamma}_7$  doublets and each of these two couples exhibits linear dichroism. The dichroism will only cancel out in the degenerate case. This can be understood when looking at the spatial hole-distribution of the  $\tilde{\Gamma}_6$  and  $\tilde{\Gamma}_7$  and Kramer's doublets, which make up the  $\Gamma_8$  state (bottom panel of **Figure 93**). They do not have a fourfold rotational symmetry and consequently their anisotropy is observable in a dipole limited experiment. We call this effect magnetic field induced linear dichroism (MILD).

Yet, if the crystal field splittings are of the order of the Zeeman splitting, the magnetic field will cause  $J_z$  intermixing of the  $\Gamma_6$  and  $\tilde{\Gamma}_6$  and the  $\Gamma_7$  and  $\tilde{\Gamma}_7$  states, so that all states give rise to dichroism and a quantitative analysis taking into account the exact thermal population of each state becomes indispensable. Low and well-controlled temperatures are a prerequisite for such an experiment. Experimentally, this MILD idea could be realised at **ID08**, where a magnetic field can be applied perpendicular to the pointing vector of

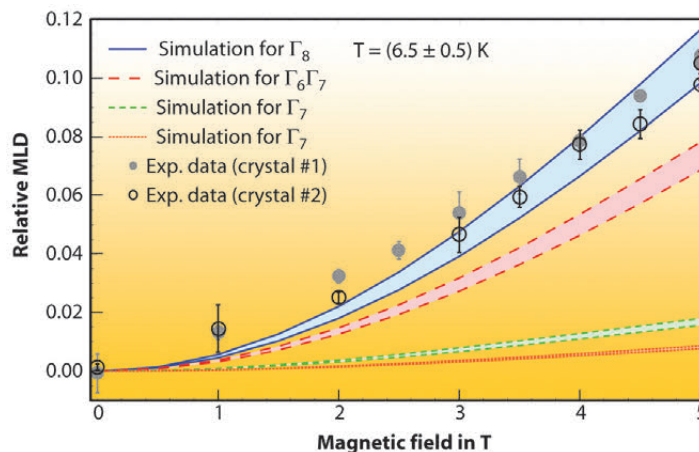


**Fig. 94:** MILD as function of field. The four different colours represent simulations corresponding to four different proposed crystal field scenarios. Open and closed circles are the measured MILD of  $\text{YbInNi}_4$ .



**References**

- [1] P. Hansmann *et al.*, *Phys. Rev. Lett.* **100**, 066405 (2008).
- [2] T. Willers *et al.*, *PRB* **80**, 115106 (2009).
- [3] F. Strigari *et al.*, *PRB* **86**, 081105 (2012).
- [4] A. Tanaka and T. Jo, *J. Phys. Soc. Jpn.* **63**, 2788 (1994).

the light and an accurately calibrated temperature of  $6.5 \pm 0.5$  K at the sample was provided.

The four coloured regions in **Figure 94** display the calculated MILD for four different proposed crystal field scenarios of  $\text{YbInNi}_4$ . The upper limit of each region corresponds to 6 K and the lower one to 7 K. At large fields the MILD of the respective scenarios is well separated.

These calculations can now be compared with the experimental MILD at  $6.5 \pm 0.5$  K shown as open and full circles in

**Figure 94**, referring to measurements of two different crystals. Only the  $\Gamma_8$  quartet scenario fits well to the experimental data thereby unambiguously answering the question about the crystal field ground state.

**Principal publication and authors**

J. Honolka (a),  
 A.A. Khajetoorians (b),  
 V. Sessi (c), T.O. Wehling (b,d),  
 S. Stepanow (a), J.-L. Mi (e),  
 B.B. Iversen (e), T. Schlenk (b),  
 J. Wiebe (b), N.B. Brookes (c),  
 A.I. Lichtenstein (b),  
 Ph. Hofmann (e), K. Kern (a) and  
 R. Wiesendanger (b), *Phys. Rev. Lett.* **108**, 256811 (2012).  
 (a) Max-Planck-Institute for Solid State Research, Stuttgart (Germany)  
 (b) University of Hamburg, Hamburg (Germany)  
 (c) ESRF  
 (d) Bremen University, Bremen (Germany)  
 (e) Aarhus University, Aarhus (Denmark)

**Iron magnetic moments in-plane on the topological insulator  $\text{Bi}_2\text{Se}_3(111)$  surface**

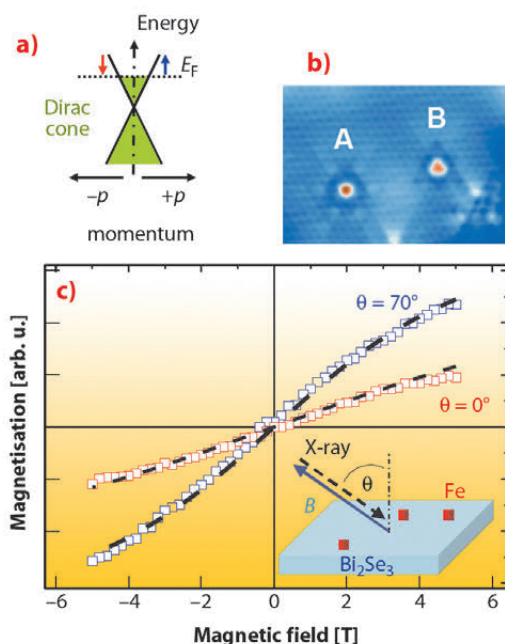
Topological insulators have gained interest from the scientific community as a new class of materials illuminating fascinating yet exotic physics and offering large potential for applications in the field of spintronics [1]. Bulk topological insulators host a 2-dimensional gapless topological surface state with very special properties. An hour-glass shaped dispersion is observed, the so-called Dirac cone, where the energy of the topological surface state increases linearly with the electron momentum  $p$  in the  $(p_x, p_y)$  surface plane (see **Figure 95a**). In contrast to graphene, where such Dirac cones are also observed, in the topological surface state spin-orbit coupling and time reversal symmetry leads to a locking of both spin and momentum degrees of freedom: two electrons moving in opposite directions ( $\pm p$ ) must have

reversed spins (symbolised as red and blue spins in **Figure 95a**). One consequence is the suppression of  $180^\circ$  elastic back-scattering electrons in the absence of spin-flip processes, which in principle allows for a high mobility of electrons within the surface plane. An interesting question is the robustness of these “topologically protected” processes against perturbations. It has been suggested that the interaction with magnetic impurities opens a gap at the Dirac point of the topological surface state, provided that the magnetic order is oriented normal to the surface plane and thus breaks the time-reversal symmetry [2]. This mechanism is of critical importance for spin-based transport in such materials.

Magnetic properties of iron impurities on a  $\text{Bi}_2\text{Se}_3$  surface, a prototypical topological insulator, were studied at **ID08** using X-ray magnetic circular dichroism (XMCD) techniques. **Figure 95b** shows a low-temperature scanning tunnelling microscopy image of isolated iron atoms on the selenium-terminated surface of  $\text{Bi}_2\text{Se}_3$ . The iron atoms are located on surface fcc and hcp hollow site positions ('A' and 'B'). The iron atoms are deposited on the surface at low temperatures  $T = 10$  K in order to prevent migration of atoms on the surface and cluster formation. A multiplet structure visible in X-ray absorption spectra reflects the high-spin state of single Fe atoms which are influenced by the resultant trigonal crystal fields due to the absorption site.

**Figure 95c** shows magnetisation curves  $M$  versus magnetic field  $B$  extracted from XMCD data at the iron  $L_{3,2}$  absorption

**Fig. 95:** a) Linear dispersion relation around the Dirac-cone of a topological insulator. b) Low-temperature scanning tunnelling microscopy image of iron atoms on the  $\text{Bi}_2\text{Se}_3$  surface. c) XMCD magnetisation curves of iron along two directions  $\theta = 0^\circ$  and  $70^\circ$  with respect to the surface normal.





edges. The magnetisation clearly differs for the two different angles  $\theta = 0^\circ$  and  $70^\circ$  between the  $\text{Bi}_2\text{Se}_3$  surface normal and the X-ray beam direction. Magnetic fields were applied collinear to the X-ray beam as shown in the inset of **Figure 95c**. The magnetisation curves  $M(B)$  show smaller values along  $\theta=0^\circ$  demonstrating a preferential orientation in the surface plane. A fit of the experimental magnetisation curves in **Figure 95c**, using a thermodynamic model which includes the Zeeman term and a magnetic

anisotropy term, leads to a significant in-plane magnetic anisotropy energy of 1.9 meV per atom. The observed in-plane anisotropy is supported by DFT calculations if both crystal fields and dynamic hybridisation processes between iron 3d states and the topological insulator are taken into account. As a consequence it is expected that iron tends to leave the topological surface state unperturbed, since the in-plane magnetisation states, which obey time-reversal symmetry, are preferred.

#### References

- [1] M.Z. Hasan and C.L. Kane, *Rev. Mod. Phys.* **82**, 3045 (2010).  
 [2] L.A. Wray *et al.*, *Nature* **7**, 32 (2011).

## Quantification of magnetic exchange in Co:ZnO via high-field XMCD magnetometry

Dilute magnetic semiconductors (DMS) are envisioned as sources of spin-polarised carriers for future semiconductor devices which simultaneously utilise spin and charge degrees of freedom.  $\text{Zn}_{1-x}\text{Co}_x\text{O}$  (Co:ZnO) has been thought to be a promising DMS material. Paramagnetic  $\text{Co}^{2+}$  impurities in ZnO single crystals have been studied already fifty years ago and a model Hamiltonian for the  $3d^7$  (*i.e.*  $S = 3/2$ ) impurity is well-established including a single ion anisotropy  $DS_z^2$  to account for the anisotropy of the wurtzite host crystal [1]. Most DMS Co:ZnO samples contain Co concentrations at or above 5% so that the next-cation-neighbour exchange  $J$  of Co-O-Co pairs comes into play as well. It has already been indirectly inferred that  $J$  is antiferromagnetic [2], however direct evidence and quantification of its strength was lacking so far. To reach both goals, the magnetisation steps associated with a spin-flop transition were measured up to high magnetic fields to overcome the antiferromagnetic coupling.

Co:ZnO epitaxial films with 5% to 15% of Co grown by reactive magnetron sputtering onto c-plane sapphire [3] were studied with synchrotron radiation. X-ray absorption near-edge spectra (XANES) were recorded at beamline ID12 in total fluorescence yield using circularly polarised light under  $10^\circ$  grazing and normal incidence. The X-ray magnetic circular dichroism (XMCD) was recorded at the Co K-edge while reversing the polarisation as well as the magnetic field direction. Element selective

XMCD(H) curves were measured up to high magnetic fields of 17 T for both principal orientations.

**Figure 96a** shows the XANES and respective XMCD spectra recorded at the Co K-edge of 15% Co:ZnO at 5 K under grazing and normal incidence, *i.e.* probing the Co-specific electronic and magnetic properties either perpendicular ( $H \perp c$ ) or parallel ( $H \parallel c$ ) to the  $c$ -axis. The XANES is anisotropic, reflecting the uniaxial symmetry of the wurtzite lattice

#### Principal publication and authors

A. Ney (a), V. Ney (a), F. Wilhelm (b), A. Rogalev (b) and K. Usadel (a), *Phys. Rev. B* **85**, 245202 (2012).  
 (a) *Experimentalphysik, Universität Duisburg-Essen, Duisburg (Germany)*  
 (b) *ESRF*

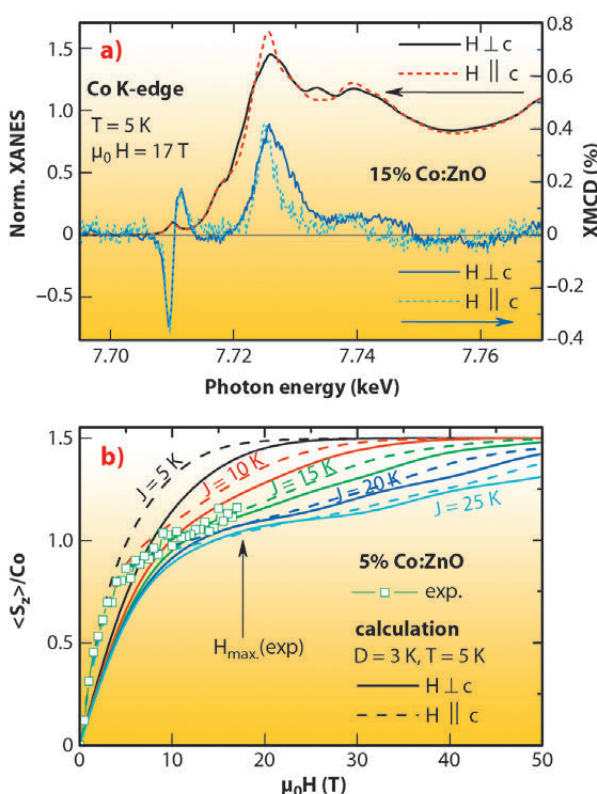


**Fig. 96:** a) XANES spectra at the Co K-edge of 15% Co:ZnO recorded with circular polarisation under grazing and normal incidence at 5 K, and the respective XMCD spectra. b) XMCD(H) curve for 5% Co:ZnO under grazing incidence in comparison with model calculations (lines) for various coupling strengths  $J$  (see text).



### References

- [1] T.L. Estle and M. de Wit, *Bull. Am. Phys. Soc.* **6**, 445 (1961); P. Koidl, *Phys. Rev. B* **15**, 2493 (1977).  
 [2] A. Ney, K. Ollefs, S. Ye, T. Kammermeier, V. Ney, T.C. Kaspar, S.A. Chambers, F. Wilhelm, and A. Rogalev, *Phys. Rev. Lett.* **100**, 157201 (2008).  
 [3] A. Ney, T. Kammermeier, K. Ollefs, S. Ye, V. Ney, T.C. Kaspar, S.A. Chambers, F. Wilhelm and A. Rogalev, *Phys. Rev. B* **81**, 054420 (2010).

of Co:ZnO. The size of the resulting XLD can be associated with a substitutional incorporation of the Co into the ZnO host lattice [2]. The XMCD at 17 T is virtually isotropic, in particular at the pre-edge feature, where 4p-3d hybridised  $\text{Co}^{2+}$  states are probed. At the photon energy of the maximum XMCD, Co-specific magnetisation curves were measured. **Figure 96b** displays an XMCD(H) curve for 5% Co:ZnO for  $\text{H}||\text{c}$ . To quantify  $J$ , the following procedure was used: The  $M(H)$  curves for  $\text{H}\perp\text{c}$  and  $\text{H}||\text{c}$  were calculated for isolated Co ions (singles), pairs (two  $S = 3/2$  spins coupled by  $J$ ) and triples separately using the effective spin Hamiltonian [1] and an isotropic, Heisenberg-like antiferromagnetic coupling strength  $J$ . The resulting  $M(H)$  curves were weighted by the relative abundances of singles, pairs and triples, assuming a statistical dopant distribution [2]. **Figure 96b** displays this calculation for various values of  $J/k_B$  from 5 K to 25 K and a fixed value of  $D/k_B = 3$  K [3]. The best

agreement between experiment and simulation is reached for  $J/k_B = 15$  K for the 5% Co:ZnO sample. **Figure 97** shows the respective analysis of the XMCD(H) curves for  $\text{H}\perp\text{c}$  and  $\text{H}||\text{c}$  of the 10% Co:ZnO sample yielding  $J/k_B = 15$  K. In this case,  $D/k_B$  was also varied from 2 K to 4 K (not shown) with  $D/k_B = 3$  K as best fit, which is in agreement with the SQUID analysis in [3]. The quantitative analysis of SQUID data from [2] also fits the XMCD(H) curve well (cross in **Figure 97**). An identical analysis for the 15% Co:ZnO sample yields a reduced  $J/k_B = 10$  K and  $D/k_B = 2$  K (not shown). The reduction of  $J$  and  $D$  at higher Co concentrations may be understood by an increasing contribution from larger dopant configurations.

In conclusion, we could determine the antiferromagnetic coupling strength  $J$  and the single ion anisotropy  $D$  in Co:ZnO by element selective, high-field XMCD-magnetometry to be  $J/k_B = 15$  K and  $D/k_B = 3$  K for 5% and 10% of Co which are both reduced for 15% Co doping to  $J/k_B = 10$  K and  $D/k_B = 2$  K. These findings allow direct quantification of magnetic interaction parameters of DMS materials and open up the possibility of estimating the success of changes of the magnetic interactions in DMS systems upon co-doping or external parameters like electrical field, current or stress.

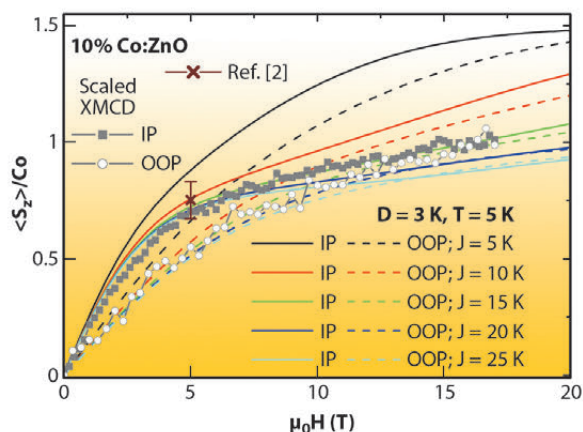


**Fig. 97:** XMCD(H)-curves of 10% Co:ZnO for  $\text{H}\perp\text{c}$  (IP) and  $\text{H}||\text{c}$  (OOP) at 5 K in comparison with model calculations to determine the coupling strength  $J$ .

### Principal publication and authors

V.M.T.S. Barthem (a), A. Rogalev (b), F. Wilhelm (b), M. M. Sant'Anna (a), S.L.A. Mello (a), Y. Zhang (c), P. Bayle-Guillemaud (d) and D. Givord (a,c), *Phys. Rev. Lett.* **109**, 197204, (2012).  
 (a) Instituto de Física, Universidade Federal do Rio de Janeiro (Brazil)  
 (b) ESRF  
 (c) Institut Néel, CNRS/UJF, Grenoble (France)  
 (d) CEA-INAC/UJF, SP2M, LEMMA, Minatec Grenoble (France)

## ■ XMCD reveals the magnetism of Rh clusters

The source of magnetism in solids is the electrostatic repulsion between electrons. Due to the Pauli principle, the repulsion is reduced when their spins are parallel. However, for a parallel coupling between spins to happen, the electrons need to become more localised and this leads to an unwanted increase in their kinetic energy. In Fe, Co and Ni, elements belonging to the 3d transition series of the periodic table, the lower energy state is magnetic, whereas, for heavier elements belonging to the 4d or 5d

transition series, the lowest energy state is non magnetic. The 4d metals Ru, Pd or Rh, exhibit Pauli paramagnetism, which means that the d-band becomes polarised under an applied magnetic field.

In very small clusters, electron bands tend to be narrower in energy than in bulk materials, a property inherently associated with the reduced number of neighbours. Consequently, the kinetic energy lost is less when displacing

electrons from one sub-band with a given spin state to another with an opposite spin. This tends to favour magnetism for small clusters over bulk. Very small Rh clusters, containing up to 35 atoms, were shown to exhibit ferromagnetism as early as 1993 [1]. Subsequent theoretical and experimental studies indicated that stable ferromagnetism could persist up to around 100 atoms or more [2].

Physical systems characterised by the existence of two states of almost equal energy present an opportunity to learn by studying the competition between these states. Earlier descriptions of the properties of Rh made us realise that Rh clusters containing about 150 atoms could constitute a model system to study paramagnetism close to the onset of stable magnetism. Classically, clusters can be prepared by evaporating atoms from a target and letting them agglomerate “in-flight”. Under such conditions, the cluster size is typically below 50 atoms. One can deposit these clusters on a substrate, but they tend to agglomerate to sizes of about 1000 atoms. We used a different approach based on the implantation of Rh atoms in an insulating layer of alumina by using an ion accelerator at the Federal University of Rio de Janeiro (UFRJ). The clusters we obtained showed a diameter around 1.5 nm by transmission electron microscopy (Figure 98) and comprised about 150 atoms, as desired.

Magnetic characterisation using the most sensitive bulk magnetometry available (superconducting quantum interference device, SQUID) was not a success as the magnetic signal was systematically dominated by undesired signals from the substrate on which the alumina had been deposited and into which the Rh clusters were implanted. This led us to undertake an experiment using X-ray Magnetic Circular Dichroism (XMCD), a technique that combines element selectivity (allowing the measurement of the Rh signal alone) with extreme sensitivity. The XMCD signals measured at beamline ID12 for a variety of different experimental parameters are shown in Figure 99. At 2 K, the XMCD signal increases linearly with the field as expected for a paramagnetic system. However, the deduced magnetic susceptibility appears to be 20 times higher than the one due to the known Pauli paramagnetism of bulk Rh. Furthermore,

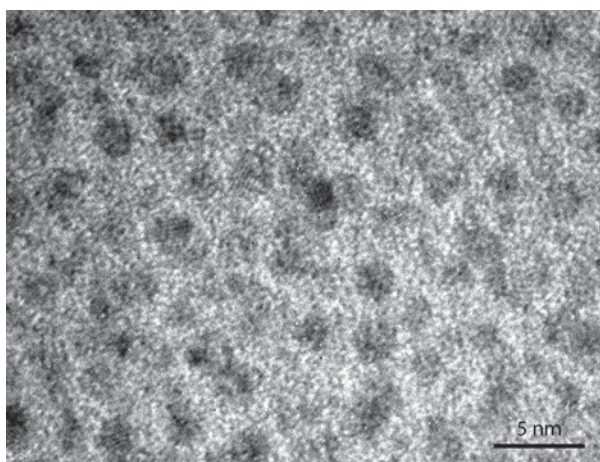


**Fig. 98:** TEM image of Rh clusters implanted in an alumina matrix.

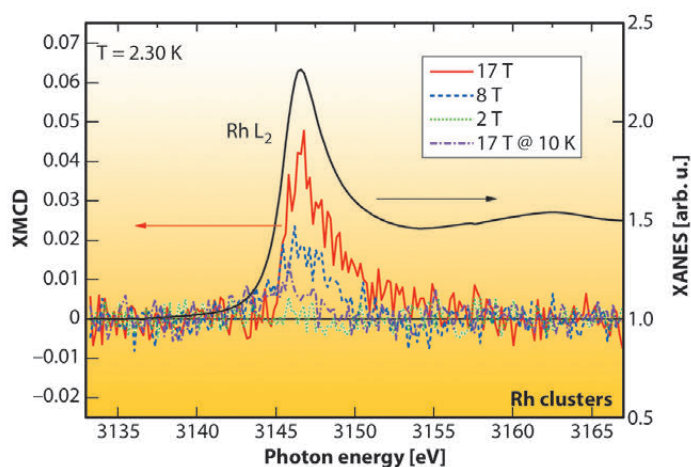


**Fig. 99:** XMCD signal at the Rh L2 edge at 2 K, under a magnetic field of 2 T, 8 T and 17 T respectively and at 10 K under a magnetic field of 17 T.

the paramagnetic signal decreases very rapidly with temperature (the XMCD signal at 10 K under 17 T is much weaker than the one at 2 K) following an approximate  $1/T$  law, instead of being almost temperature independent, as expected for Pauli paramagnetism.

These results appear to confirm theoretical predictions made independently by Murata and Doniach [3] and by Moriya and Kawabata [4] in the 1970's. They predicted a strong enhancement of the susceptibility close to the onset of stable magnetism due to correlations between electrons. With increasing temperature, spin-fluctuations (excitations of the moments having a certain collective character) become excited and the susceptibility consequently decreases. These predictions were awaiting confirmation due to the lack of systems to test them as well as to experimental difficulties. The unique combination of element selectivity of XMCD and low temperature and high magnetic field available at ID12 has been essential for the success of our experiment.

#### References

- [1] A.J. Cox, J.G. Louderback and L.A. Bloomfield, *Phys. Rev. Lett.* **71**, 923-926 (1993); A.J. Cox, J.G. Louderback, S.E. Apsel and L.A. Bloomfield, *Phys. Rev. B* **49**, 12295-12298 (1994).
- [2] C. Barreteau, R. Guirado-Lopez, D. Spanjaard, M.C. Desjonqueres and A.M. Oles, *Phys. Rev. B* **61**, 7781-7794 (2000).
- [3] K.K. Murata and S. Doniach, *Phys. Rev. Lett.* **29**, 285-288 (1972).
- [4] T. Moriya and A. Kawabata, *J. Phys. Soc. Jpn.* **34**, 639-651 (1973).



### Principal publication and authors

P. Langner, C. Mikutta and R. Kretzschmar, *Nat. Geosci.* **5**, 66-73 (2012).

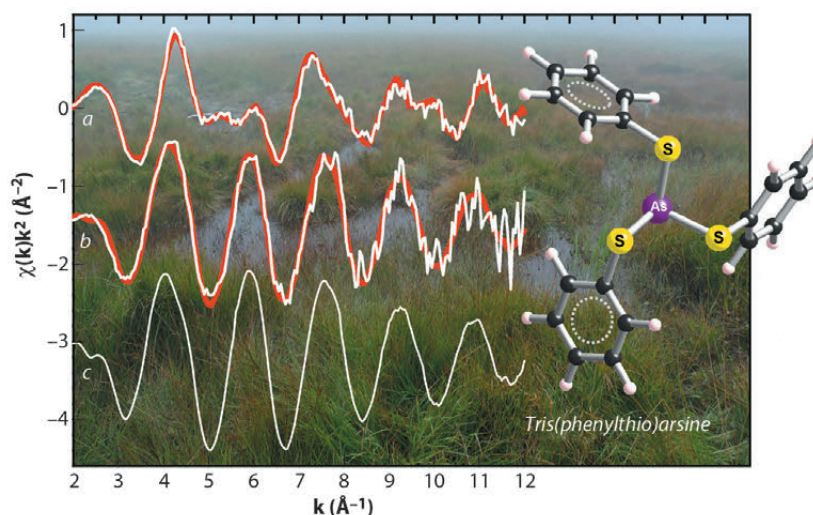
Soil Chemistry Group, Institute of Biogeochemistry and Pollutant Dynamics, ETH Zurich (Switzerland)

## X-ray absorption spectroscopy reveals natural organic matter as major sorbent for arsenic in peat

Approximately 6% of the global ice-free land area is covered by wetlands, which play an important role in the storage, transformation, and mobilisation of trace elements like arsenic originating from natural and anthropogenic sources. In wetland soils and peaty sediments, natural organic matter (NOM) is thought to control the mobility and bioavailability of As by promoting its release from As-bearing metal-oxyhydroxides or, conversely, by triggering the formation of As-sequestering sulphides under strongly reducing conditions. Numerous wetland systems as well as peaty sediments, however, show enrichments of As not obviously related to the presence of As-bearing minerals, suggesting a direct immobilisation of As by NOM. Although several modes of As-NOM interactions, for example, ternary As complex formation or covalent binding of As by functional groups of NOM, have been proposed in the literature, spectroscopic evidence was missing so far. Here, we analysed the solid-phase speciation of As and Fe in a naturally As-enriched (<1,800 mg As/kg), slightly acidic minerotrophic (groundwater-fed) peatland located in southern Switzerland by X-ray absorption spectroscopy (XAS). Our main objectives were to (i) provide spectroscopic evidence for As binding to NOM, (ii) identify the governing binding mechanism(s), and (iii) quantify the extent of As binding to NOM. Peat samples collected at the field site were immediately shock-frozen in liquid N<sub>2</sub> to preserve

the speciation of As, transported on dry ice to the laboratory, freeze-dried, and processed in an anoxic glove box. Based on mineralogy and elemental composition, selected peat samples were prepared for XAS analyses by sieving the material to a particle size <500 μm. The samples were then placed in Plexiglas sample holders, sealed with Kapton<sup>®</sup> tape, and kept anoxic until the final XAS measurements. Arsenic K-edge (11,867 eV) XAS spectra were collected at beamline **BM29** in fluorescence-yield mode at approximately 80 K using a N<sub>2</sub> Oxford cryostream. The XAS spectra were analysed by means of principal component analysis and target transformation testing followed by linear combination fitting as well as shell fitting. Linear combination fit analyses showed that close to the peat surface, As was present as As-NOM complexes (As<sup>III</sup>), realgar-type sulphide minerals (As<sub>4</sub>S<sub>4</sub>, As<sup>II</sup>), and As sorbed to Fe(III)-oxyhydroxides (As<sup>III/V</sup>). In contrast, samples of deep peat layers were entirely dominated by As-NOM complexes (**Figure 100**), despite the presence of potentially As-sequestering Fe(III)-oxyhydroxides and pyrite (FeS<sub>2</sub>). Shell-fit analysis of the extended X-ray absorption fine structure (EXAFS) spectra of these samples revealed that As<sup>III</sup> was coordinated to 2-3 S atoms with an average interatomic As-S distance of 2.26 ± 0.01 Å (**Figure 101**). This distance is identical to interatomic As-S distances of thioarsine model compounds (**Figure 101**) and thus implies that trivalent As in the

**Fig. 100:** Arsenic K-edge EXAFS spectra of two representative peat samples (a, b) and the organic As reference compound tris(phenylthio)arsine (c). The peat samples were collected from a depth of 0-10 cm (a) and 190-200 cm (b). Experimental data is shown as white lines and linear combination fits of the peat samples as red lines.





peat was bound to 2-3 sulphhydryl groups of NOM. These findings demonstrate for the first time that in anoxic NOM- and S-rich environments, NOM can be a quantitatively important sorbent for As, capable of successfully rivalling mineral phases known to have a high affinity towards As – a result which highlights the need to account for NOM in geochemical speciation models used to assess the toxicity and mobility of As in anoxic NOM-rich environments. Overall, our findings suggest that the binding of As to sulphhydryl groups of NOM represents the major As-NOM interaction mode in anoxic NOM-rich environments subject to moderately sulphate-reducing conditions. The spectroscopic analyses conducted at the ESRF have thus greatly improved our understanding of the biogeochemical As cycle and are key to interpreting As-NOM associations observed in other European peatlands, as well as in peats and peaty sediments of Southeast Asia.

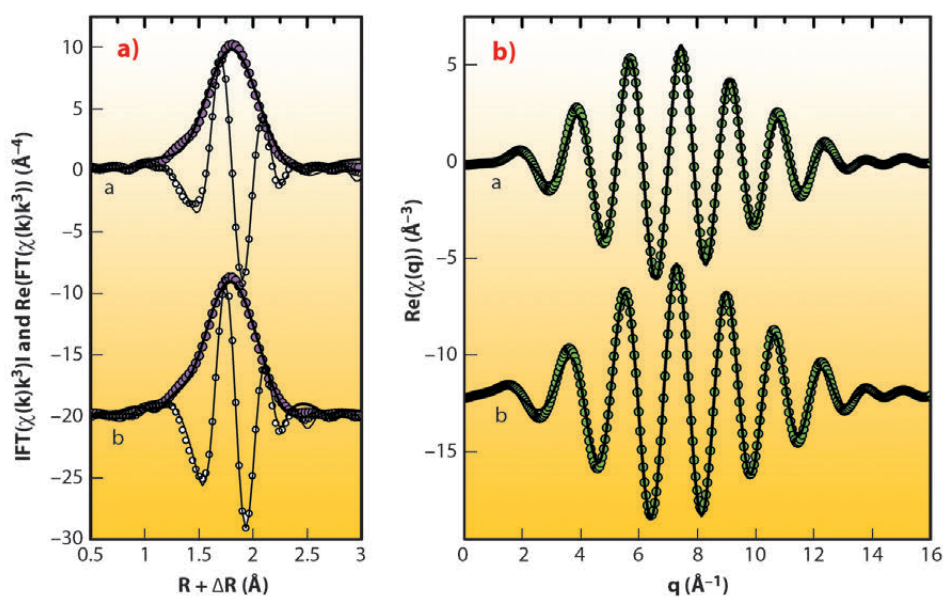
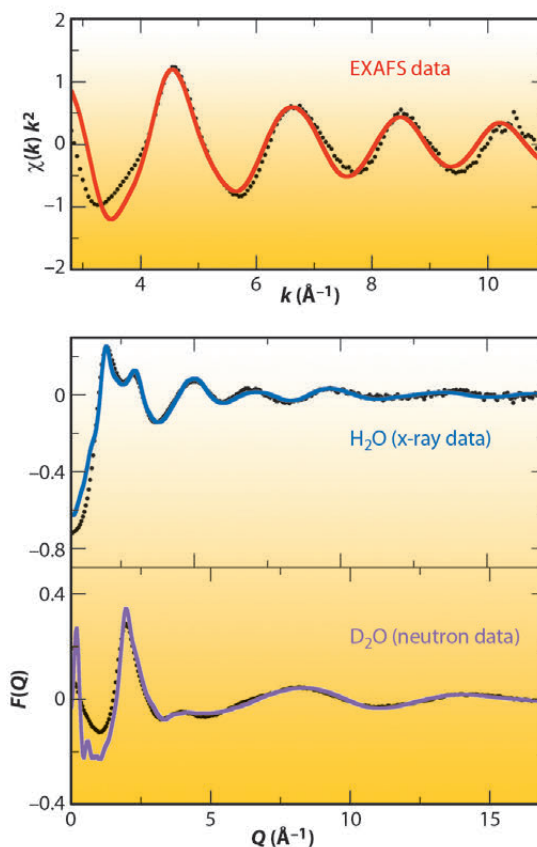


**Fig. 101:** a) Magnitude and real part of the Fourier transform of As K-edge EXAFS spectra of a peat sample retrieved from 175-185 cm depth (a) and tris(phenylthio)arsine (b). b) Real part of the back Fourier transform of the respective samples calculated over  $R + \Delta R = 1.2-2.3 \text{ \AA}$ . In both graphs experimental data is shown as solid and model fits as dotted lines.

## ■ Characterising the elusive axial hydration shell of the Pd(II) aqua ion

Chemical behaviour and characterisation of Pd(II) and Pt(II) complexes in solution is a very active area of study because of the large number of their applications in fields such as catalysis, intermediate reaction synthesis and antitumoural treatments. The structure of these metal complexes in solution is characterised by a well defined square-planar arrangement that contrasts with a rather diffuse axial environment. A theoretical proposal for a characteristic hydration shell in this axial region, called the meso-shell [1], stimulated further experimental and theoretical studies which have led to various different pictures.

The present report addresses the question of the experimental detection of this structure by undertaking a recently proposed multitechnique approach which is particularly appropriate for this demanding problem [2]. A set of neutron and X-ray diffraction measurements have been performed; they were combined with a modified reverse Monte Carlo



### Principal publications and authors

D.T. Bowron (a), E.C. Beret (b), E. Martín-Zamora (c), A.K. Soper (a) and E. Sánchez Marcos (b), *J. Am. Chem. Soc.* **134**, 962 (2012).  
(a) ISIS Facility, Rutherford Appleton Laboratory, Harwell Science and Innovation Campus, Didcot (UK)  
(b) Departamento de Química Física. Universidad de Sevilla (Spain)  
(c) Departamento de Química Orgánica. Universidad de Sevilla (Spain)

**Fig. 102:** Experimental (black points), fitted neutron diffraction (magenta line), X-ray diffraction (blue line) and simulated EXAFS (red line) spectrum of various Pd(II) aqueous solutions.



### References

- [1] J. M. Martínez, F. Torrico, R.R. Pappalardo and E. Sánchez Marcos, *J. Phys. Chem. B Soc.* **108**, 15851 (2004).  
 [2] D.T. Bowron and S. Díaz-Moreno, *J. Phys. Chem. B Soc.* **113**, 11858 (2009).  
 [3] A.K. Soper, *Phys. Rev. B* **72**, 104204 (2005).  
 [4] D.T. Bowron, *Pure Appl. Chem.* **80**, 1211 (2008).

method, empirical potential structure refinement (EPSR) [3], which applies constraints to the local order around the metal cation by means of information derived from the corresponding EXAFS spectrum [4]. These techniques are able to provide structural information on different regions around the central cation with different weightings.

**Figure 102** shows the neutron (bottom) and X-ray data (middle) together with the fitted data obtained by the EPSR model. It must be noted that a common atomistic representation provided by the Monte Carlo simulation using the final refined intermolecular potentials is able to simultaneously match the structure of the different diffractograms. The top of **Figure 102** shows the comparison of the experimental and simulated  $k^2$ -weighted Pd K-edge EXAFS spectrum of the Pd(II) aqueous solution obtained at beamline BM29. The simulated EXAFS spectrum was obtained by averaging the individual spectra that result from selecting 10000 local structures from the same MC simulation.

**Figure 103** presents the most relevant pair distribution functions (RDF) of the EPSR model that fits the experimental data. The Pd-O<sub>w</sub> RDF (bottom) shows a first sharp

peak centred at 2.04 Å that integrates to 4 oxygen atoms which belongs to the Pd aqua ion, and a second less intense but well defined peak centred at 2.85 Å that integrates to 2 oxygen atoms. This peak confirms the axial hydration, which encloses a distance range distribution of 2.7-3.5 Å. The second plotted RDF corresponds to the Pd-O<sub>ClO<sub>4</sub></sub> distribution of the perchlorate anions around Pd(II). It is noticeable that the first Pd-O<sub>ClO<sub>4</sub></sub> peak is centred at the same position as the second Pd-O<sub>w</sub> peak, and their widths are also similar. Both peaks present the same topology, except for their heights. This is expected due to the preferential attractive character that metal cation aqua ion induces in its closest environment for anions, as well as their relative concentration with respect to water. In fact the running coordination number is 0.5 oxygen atoms for the ClO<sub>4</sub><sup>-</sup> case. This close similarity indicates that the regions above and below the molecular plane of the aqua ion can be envisaged as a hydration shell and also as a coordination region.

Due to the molecular plane defined by the Pd(II) aqua ion, a decomposition of the total RDF into partial RDFs could be performed, with each partial RDF corresponding to different regions of the space. The partial Pd-O<sub>w</sub> and Pd-O<sub>ClO<sub>4</sub></sub> RDFs corresponding to the axial region (0-45° range of the azimuthal angle) for the Pd-O<sub>w</sub> and Pd-O<sub>ClO<sub>4</sub></sub> pairs have been included in **Figure 103** (top). These plots support the structural analysis carried out previously. The Pd-O<sub>w</sub> peak at 2.85 Å appears in its axial partial RDF, whereas in the axial Pd-O<sub>ClO<sub>4</sub></sub> partial RDF a peak at 2.85 Å is seen for the perchlorate oxygen coordinating the Pd and a second peak at 5 Å belonging to the rest of oxygens of the axial perchlorate anion.

The results confirm the existence of the meso-shell [1] and structurally characterise the water molecules within it. An important finding not previously reported is that the counter ion of the metal cation, the perchlorate anion, competes with water molecules for the meso-shell occupancy. The important role played by the axial region in many ligand substitution reactions is therefore intimately connected to the presence of the counterion and not just hydration water. This highlights the non-secondary role the counterions may play in synthesis.

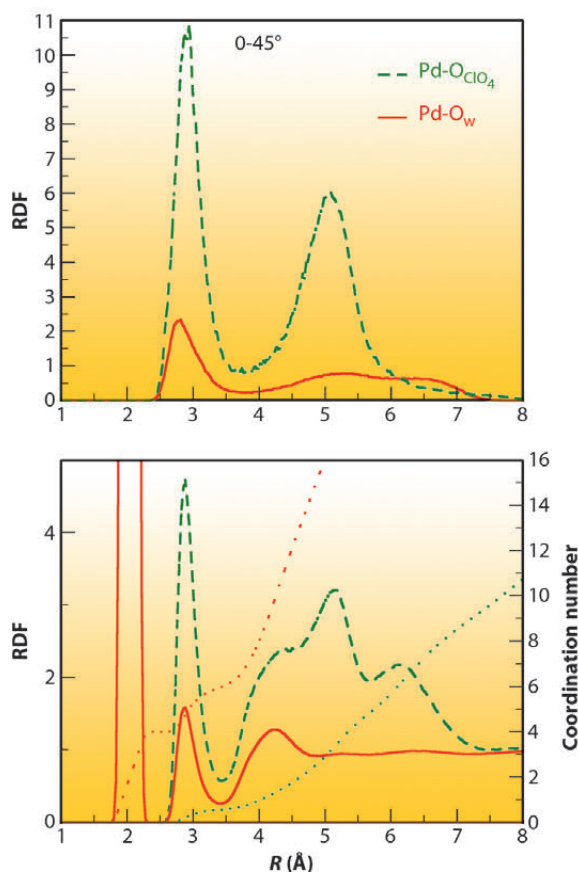


**Fig. 103:** Pd-O<sub>water</sub> (red line) and Pd-O<sub>perchlorate</sub> (green line) RDF and running coordination number corresponding to the whole solution (bottom) and the axial region (0-45°) above and below the Pd aquaion molecular plane.



## ■ Surface and bulk approach to time-resolved characterisation of heterogeneous catalysis

Chemical phenomena of both fundamental and technological importance are often very complex in nature. Catalysis is a discipline in which such complexity is paradigmatic. Typically, heterogeneous catalytic processes involve the contact of gases or liquids with nanosized active components. To shed light on these complex systems, multi-technique approaches, often having high time-resolution as well the capability to address surface and bulk properties, appear as optimal tools for unravelling the elusive details of catalysts function. Surface and bulk sensitivity is generally achieved by a combination of at least two techniques such as X-ray and vibrational spectroscopies. Here we highlight work carried out in two fields: the preparation and the evolution under reaction conditions of catalytic materials.

As a first representative example we focus on the morphological control of the anatase polymorph of titanium oxide. **Figure 104** displays the structural differences observed using total scattering (PDF-XRD; atom pair density function) among a series of initial, amorphous precursors of titania samples prepared by microemulsion. The figure also includes the corresponding XRD observation of the nucleation and growth process during thermal treatment. The latter is based upon the analysis of the intensity of Bragg diffraction peaks that eventually appear when sufficient crystallinity arises. The initial precursors can pertain to two different groups; initial precursors T, Tw, and TwB (differing in initial synthesis conditions) display rather similar patterns and appear to show significant differences (**Figure 104a**) with samples TA and TB. Such differences are directly linked to the temperature of nucleation, which divides the materials in the two groups mentioned in relation to their initial precursor structure. This observation provides strong evidence of a thermodynamic control of the anatase nucleation process. Primary particle size is obviously affected by both nucleation and growth, but additional studies demonstrated the key importance of the nucleation. Therefore, an inherently thermodynamic factor was shown to control the size of the (crystalline) anatase

phase. This fundamental understanding opens up the possibility for tuning the morphology of nano-anatase by manipulating the initial structure of the precursor materials. More importantly, by a joint analysis of XRD-PDF and infrared spectroscopy, the physical basis for controlling the size and shape of the oxide can be unravelled.

### Principal publications and authors

A. Kubacka (a),  
A. Iglesias-Juez (a),  
M. Fernández-García (a),  
M. Di Michiel (b) and  
M.A. Newton (b), *ChemCatChem*  
**4**, 725-737 (2012).  
(a) Instituto de Catálisis y  
Petroquímica, CSIC, C/Marie  
Curie 2, Madrid (Spain)  
(b) ESRF

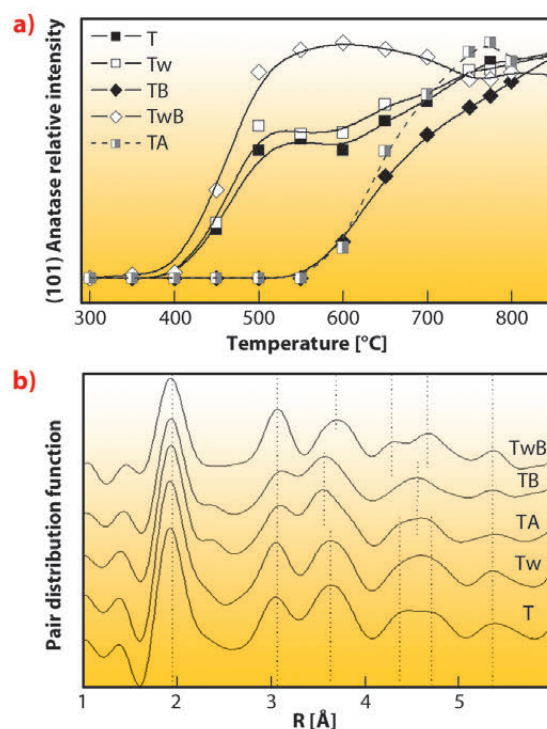


**Fig. 104:** Room temperature PDF-XRD and XRD peak intensity during a calcination ramp of a series of anatase solid precursors.

As a second example, **Figure 105** summarises the rich chemistry displayed by Pd nanoparticles observed using a CO-NO gas mixture. **Figure 105a** display the Pd metal phase behaviour through the Pd-Pd EXAFS coordination number (C.N.) and dispersion of the metal phases for a series of catalysts with increasing quantity of palladium. The first result is that the metal responds actively to the gas mixture nature in all cases, showing that the apparent C.N. increases under CO and diminishes -in a fully reversibly manner- to the initial value under NO. This behaviour is quantified in the dispersion plot assuming spherical particles and an exclusive size effect. In **Figure 105** we can also observe that we detected a slowly varying region in the C.N. behaviour toward the middle-end part of the CO



treatment. This region can be understood with the help of high energy XRD which clearly reveals this transient phenomenon as a saw-tooth variation in the d spacing of the Bragg reflection from Pd nanoparticles (**Figure 105a**); this in turn is related to the somewhat unexpected formation of a palladium carbide phase, not previously detected under stoichiometric CO-NO mixtures. The synchronous infrared panels

of **Figure 105b** indicate that such PdC<sub>x</sub> phase is formed from dissociated CO and leads to storage of carbon species at the metal; concomitantly the partitioning of the adsorbed CO between linear and bridged sites is changed with a promotion of the linear bound CO over the bridged. Moreover, the carbide phase is completely removed under NO and a large amount of NCO is formed simultaneously. The

reversible chemistry summarised in **Figure 105** is connected to two key steps, in turn related to, firstly, surface CO coverage and dissociation at the surface of the Pd and, secondly, the subsequent stripping of C from the metal bulk. Such steps are synchronised with (reversible) size/shape changes of Pd with profound implications in CO/NO elimination reactions. The uncovering of such physical/chemical phenomena, with significance in practical use of pollutant elimination using Pd-TWC systems, is only possible with the combined *in situ* use of XRD-XAS-IR spectroscopies.

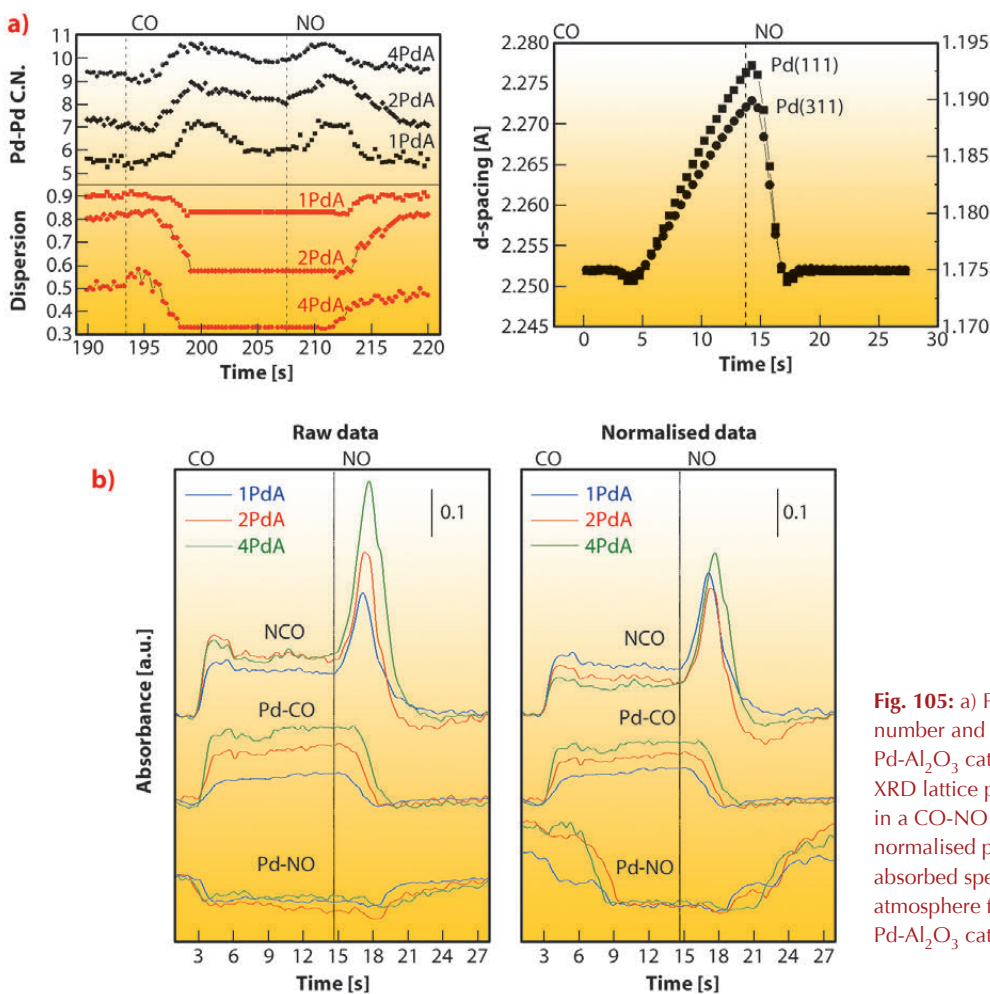


**Fig. 105:** a) Pd-Pd EXAFS 1st shell coordination number and dispersion for several (1, 2, 4 wt.%) Pd-Al<sub>2</sub>O<sub>3</sub> catalysts and variation of two Pd metal XRD lattice planes for a 2 wt.% Pd-Al<sub>2</sub>O<sub>3</sub> catalyst in a CO-NO atmosphere. b) IR intensity (raw and normalised per Pd surface atom) of characteristic absorbed species behaviour in a CO-NO atmosphere for several (1, 2, 4 wt.%) Pd-Al<sub>2</sub>O<sub>3</sub> catalysts.

## ■ Confinement effect controls the hole doping of carbon nanotubes

Single-walled carbon nanotubes (SWCNT) represent ideal nano-confinement systems owing to their one dimensional hollow core with diameters varying between 0.7 and 2 nm and up to a few millimetres in length. The insertion of foreign species into these 1-D nano-cavities leads to novel hybrid system with new and original physical properties.

Inserting iodine into the nanotubes leads to formation of atomic wires *i.e.* linear chains of iodine atoms. The number of chains inside the nanotube is dependent on the nanotube diameter [1]. As iodine is a typical p-dopant, charge transfer occurs from the nanotube to the iodine, leading to a hole doping of the tubes [2]. Transport properties of nanotubes can thus

be modified. Moreover, iodine wires are fragmented in several units of polyiodides  $I_n^-$ . The hole doping of the tube is therefore closely linked to the wire fragmentation.

By means of X-ray absorption spectroscopy (XAS) we have studied the local atomic arrangement of the iodine in hybrid iodine@SWCNT of various diameters. Complementary to this, we studied the dependence of the hole doping with the diameter of the tubes using Raman spectroscopy.

The XAS experiments were carried out at iodine K-edge (32169 eV) on the **BM29** beamline. Selected nanotube samples exhibit average diameter around 0.9, 1.1 and 1.42 nm. Synthesis of hybrid iodine@SWCNT was done by mixing nanotubes powders with molten iodine as described elsewhere [3].

**Figure 106a** displays the tangential modes (G-band, around  $1600\text{ cm}^{-1}$ ) of the Raman spectra of the nanotube samples. Both positions and profiles of the G-band are particularly sensitive to environmental effects and/or charge transfer, enabling the interactions between nanotubes and host polyiodides to be probed. A significant upshift of  $2\text{ cm}^{-1}$  upon iodine insertion is observed for the large diameter tubes (1.1 nm and 1.4 nm), consistent with the charge transfer between the nanotubes and the polyiodides. By contrast, no shift is shown for the small diameter tube (0.9 nm), suggesting a much weaker charge transfer in the latter case.

R-space (**Figure 106b**) XAS spectra are very similar for the three samples. All spectra are dominated by the iodine-iodine first coordination shell while a significant contribution is also observed around  $5.6\text{ \AA}$ . This second shell peak is governed by the multiple scattering paths of the photoelectron (**Figure 106**). As its amplitude is extremely sensitive to disorder, the presence of this peak reflects the nearly perfect 1D structure of the chains in the system. Average long range 1D ordering was also evidenced thanks to complementary X-ray and electron diffraction experiments.

Analysis of XAS spectra was performed using the Landweber iterations method adapted for EXAFS defined in [4]. By analysing the variation of the structural

parameters (bond lengths and coordination numbers), we showed that average lengths of the  $I_n^-$  vary with confinement. In thin nanotubes where confinement effect is strong,  $I_n^-$  are long ( $I_{21}^-$ ) and the doping of the tubes is by consequence weak. In larger nanotubes,  $I_n^-$  are shorter, more charges are thus transferred from the tubes, increasing the hole doping.

In conclusion, X-ray spectroscopy experiments allow the dependence of the length and charge of the confined polyanions with the tube diameter to be assessed. A critical diameter  $\Phi_C$  around 1 nm was identified. Below  $\Phi_C$ , long polyanions with subsequent weak charge transfer are obtained. For diameters above  $\Phi_C$ , significant shortening of the polyanions leads to a more important charge transfer.

We have shown that confinement effect plays a crucial role in the charge transfer between the confined polyiodide species and the host nanotube.

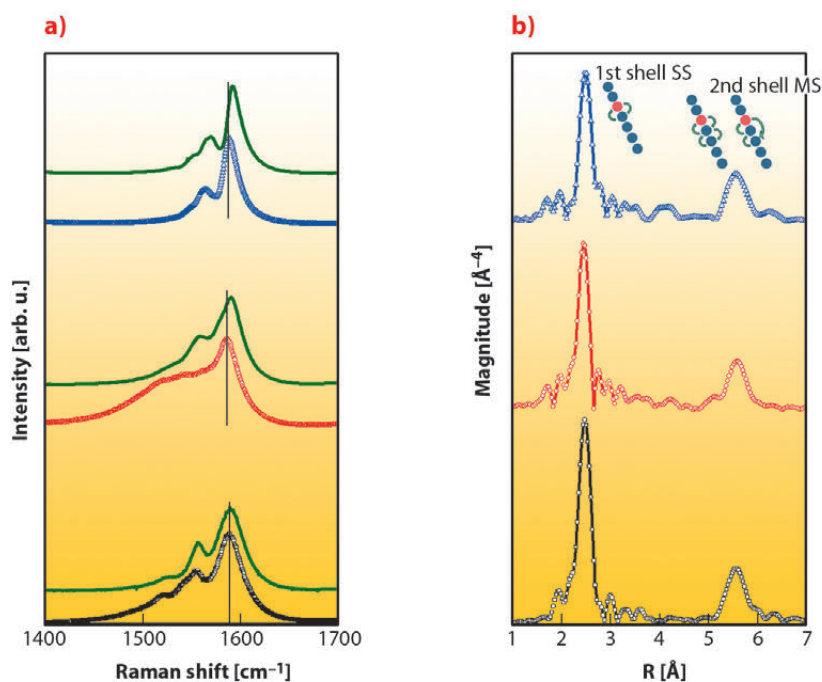


**Fig. 106:** a) Comparison of Raman spectra before and after doping (green solid line). b) EXAFS Fourier Transform and sketch of the scattering paths Single Scattering (SS) and Multiple Scattering (MS). From bottom to top, nanotubes of average diameter 0.9 nm (black), 1.1 nm (red) and 1.4 nm (blue).

#### Principal publication and authors

M. Chorro (a), G. Kane (b, c), L. Alvarez (b,c), J. Cambedouzo (d), E. Paineau (d), A. Rossberg (e), M. Kociak (d), R. Aznar (b,c), S. Pascarelli (a), P. Launois (d) and J.L. Bantignies (b, c), *Carbon* **52**, 100-108 (2013).  
 (a) ESRF  
 (b) Laboratoire Charles Coulomb UMR 5221, Université Montpellier 2 (France)  
 (c) Laboratoire Charles Coulomb, UMR 5221, CNRS, Montpellier (France)  
 (d) Laboratoire de Physique des Solides, UMR CNRS 8502, Université Paris Sud 11, Orsay (France)  
 (e) Helmholtz-Zentrum Dresden-Rossendorf, Institute of Radiochemistry, Dresden (Germany)

#### References

- [1] L. Guan, *et al.*, *Nanoletters* **7**, 1532-5 (2007).
- [2] L. Grigorian *et al.*, *Phys. Rev. Lett.* **80**, 5560-3 (1998).
- [3] T. Michel, *et al.*, *Phys. Rev. B* **73**, 195419-5 (2006).
- [4] A. Rossberg, *et al.*, *Jour. of Synch. Rad.* **17**, 280-8 (2010).



## Structure of Materials

The development of existing technologies and the creation of new ones with reduced environmental impact strongly depends on the fabrication of new materials with specifically tailored and controlled properties. In this respect, the comprehension of the structure of materials plays a fundamental role in providing the crucial piece of knowledge necessary for understanding their properties and, in the case of artificially engineered materials, the experimental confirmation of theoretical predictions. Complementary to static structure determination is the study of the structure and morphology of materials during their synthesis or under realistic working conditions. These *in situ* studies make it possible to study all of the steps necessary for the production of a particular material and to determine the intermediate compounds which are formed. They aid also in the optimisation of productivity and to reduce degradation. The ESRF has always been at the forefront in this field thanks to its beamlines, which take advantage of the high quality X-ray beams, and to the development of new methodologies and to the continuous improvement of the available sample environments.

In this chapter we present several highlights from ESRF and CRG beamlines. They deal with different scientific cases ranging from the structural characterisation of nanomaterials, either natural as in the case of sea-shells or artificial such as SiGe quantum dots, to the correlation between crystallographic structure and electronic or magnetic properties. Several contributions are about *in situ* and real-time studies of different kinds of reactions, mainly catalysis studies. They provide, via X-ray diffraction, information revealing the formation of intermediate phases which turn out to be crucial for the reaction mechanisms. Similar results are presented in the case of electrochemically-controlled deposition, highlighting the role of the applied potential which results in different growth modes.

The year 2012 has been an important one for the beamlines of the Structure of Materials Group. The designs for UPBL1, the upgrade of ID01, UPBL2, the upgrade of ID15, and the upgrade of ID31 have been completed and construction will start during 2013. All the beamlines have expanded the scope of the sample environments and ancillary tools that can be installed on their instruments so as to increase the possibilities for controlling the sample conditions.

In addition, ID03 has installed a new diffractometer, which makes it capable of carrying larger and heavier sample environment setups. ID11 has further strengthened and standardised its methodologies for high-energy nanocharacterisation providing direct mapping with a resolution better than 100 nm or the possibility of studying samples with volumes smaller than 1  $\mu\text{m}^3$ . X-ray diffraction computed tomography has been a major breakthrough at the high energy beamline ID15. In experiments where a time resolution of several minutes is acceptable, this technique may provide much more physical and chemical information than the conventional tomography technique. Furthermore X-ray diffraction and conventional computed tomography can be combined since they are installed on the same instrument. Last July ID32 was definitively closed for operation and dismantled during the summer. Its high energy X-ray photoemission spectrometer will eventually be installed at a new beamline. The electrochemistry laboratory has been temporarily relocated to ID03, waiting for a location in the new building. In 2013 UPBL1 will begin its construction phase while the new powder diffraction beamline will be constructed at the ID22 location. All the personnel of the different beamlines will continue working to improve the instruments and to develop new methodologies to promote science and better serve our user community.

R. Felici



## ■ Three-dimensional microscopy of extended crystals through X-ray Bragg ptychography

Understanding the growth mechanisms of bio-mineralised sea-shells or improving the performances of optical, mechanical or electronic devices requires a detailed knowledge of crystalline properties at the nanoscale. This motivates the development of powerful characterisation techniques for strain determination. Today, X-ray lensless microscopy, exploiting the coherence properties of third-generation synchrotron sources, is gaining a larger place among the classical imaging techniques. This technique is quantitative, non-invasive, and provides a resolving power meeting the requirements of nanoscience. In this approach, the lenses are advantageously replaced by inversion algorithms: all the information about the inside structure of the sample can be reconstructed from the coherently scattered intensity, without specific sample preparation. By means of this imaging approach, the details about shape and chemical composition of crystalline nanostructures are obtained. The high sensitivity to the displacement field in the crystal is provided by the Bragg geometry, which allows additional strain information [1].

One main limit is defined by the size of the field of view, which is of the order of a few micrometres. The use of ptychography [2] has been proposed to extend the field of view without degrading the image resolution. Ptychography (from the Greek for “fold”) is a technique originally developed for electron microscopes and recently expanded to X-rays in the forward scattering direction to image the morphology of extended samples [2]. It is based on the redundancy of the information taken from partially-overlapping illumination areas on an extended sample. A set of far-field coherent intensity patterns is recorded while the sample is moved through the finite-sized beam spot. The redundancy, resulting from the overlapping condition, is the key of the iterative process convergence and, consequently, of a successful reconstruction of the sample.

The extension of this method to the Bragg case is a development successfully exploited in this work. In this case, the full 3D Bragg diffraction pattern is recorded at

each position of the beam on the sample. The whole set of data is fed into a Bragg-adapted algorithm which allows the retrieval of the sample image.

**Figure 107** shows the schematic layout of the experimental setup. The coherent finite-sized beam spot needed for the ptychography scan is obtained by a Fresnel zone plate (FZP) illuminated in an area that matches the beam transverse coherence lengths. As the FZP central part is occluded by a beam stop to avoid direct beam contribution, the aperture is shifted laterally. The sample, patterned from a silicon-on-insulator wafer is composed of two Si <110> lines of about 40 nm height and of 520 and 260 nm width, respectively (**Figure 108**). The separation between the lines results in an edge-to-edge distance of 1.7  $\mu\text{m}$ . The line length is about 30  $\mu\text{m}$ , much larger than the beam footprint. The areas delimited by the white ellipses correspond to the first positions of the beam during the scan.

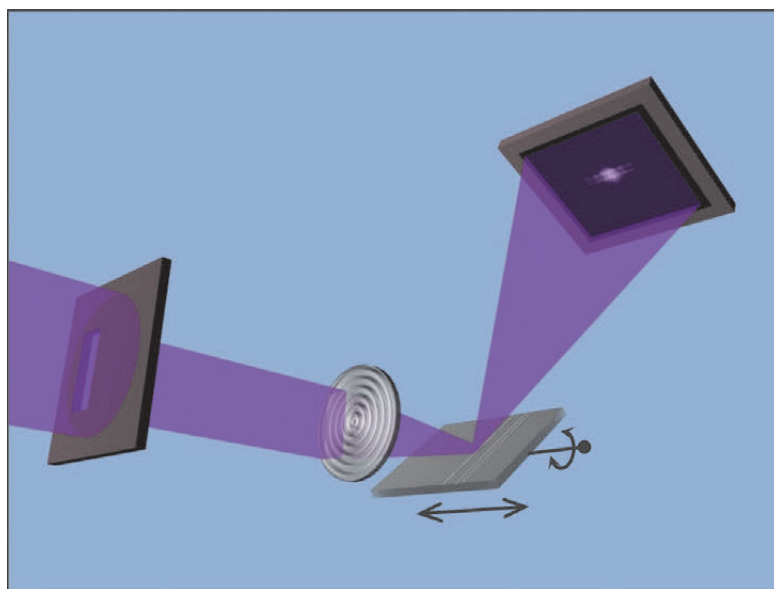


**Fig. 107:** Schematics of the Bragg ptychography experiment: the focused X-ray beam illuminates several overlapping areas in an extended sample. Each 3D diffraction patterns presents the information from one part of the sample.

The 3D intensity frames recorded in each point of the ptychographical scan are fed into the inversion algorithms. Together with the morphology of the sample, the displacement field is also imaged in radian units.

Bragg ptychography makes the three-dimensional imaging of crystals by X-ray

### Principal publication and authors

P. Godard (a), G. Carbone (b), M. Allain (a), F. Mastropietro (b,c), G. Chen (d), L. Capello (e), A. Diaz (b), T.H. Metzger (b), J. Stangl (d) and V. Chamard (a), *Nature Communications* **2**, 568 (2011).

(a) Institut Fresnel, Aix-Marseille University, CNRS, Marseille (France)

(b) ESRF

(c) CEA/Grenoble SP2M/Nanostructures et Rayonnement Synchrotron, Grenoble (France)

(d) Institute of Semiconductor and Solid State Physics, Johannes Kepler Universität, Linz (Austria)

(e) Soitec S.A., Parc Technologique des Fontaines, Bernin (France)



microscopy possible by overcoming the size constraint for samples. That is in addition to providing crystal-specific information such as strain fields or the presence of defects in the crystalline

structure. This first demonstration paves the way for the exploration of a wide range of crystalline materials, belonging to such diverse fields as life sciences and microelectronics.

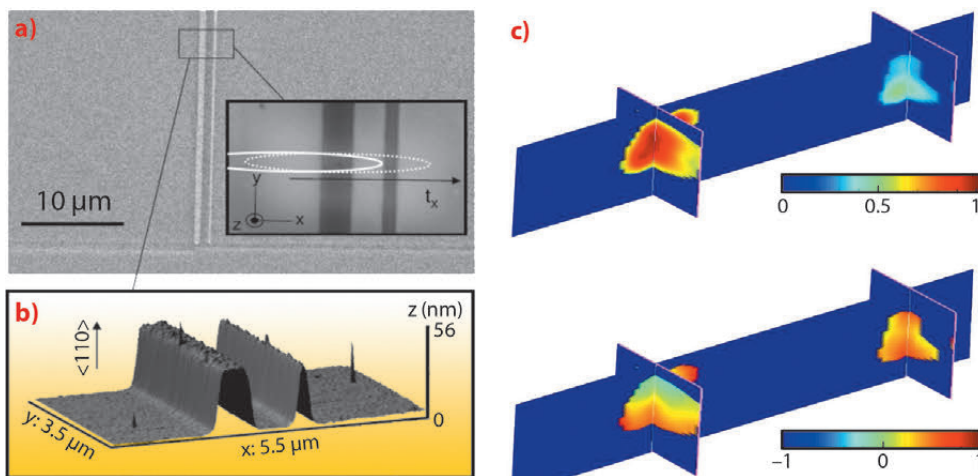


**Fig. 108:** a) Scanning electron micrograph of the lines patterned on the silicon-on-insulator substrate. The enlarged region indicates the area investigated during the ptychography scan. The translation direction  $t_x$  is shown together with the two first illumination areas (white ellipses). b) The same region as seen by atomic force microscopy. c) 2D cross-sectional views of the reconstructed density (upper image) and phase (lower image) of the sample.

#### References

- [1] M.C. Newton, S.J. Leake, R. Harder and I.K. Robinson, *Nature Mater.* **9**, 120 (2010).  
 [2] M. Dierolf, A. Menzel, P. Thibault, P. Schneider, C.M. Kewish, R. Wepf, O. Bunk and F. Pfeiffer, *Nature* **467**, 436 (2010).

#### Principal publication and authors

P.G. Evans (a,b), D.E. Savage (a), C.B. Simmons (a), M.G. Lagally (a), S.N. Coppersmith (a), M.A. Eriksson (a) and T.U. Schulli (b), *Adv. Mater.* **24**, 5217 (2012).  
 (a) University of Wisconsin, Madison (USA)  
 (b) ESRF

## ■ Nanoscale structural distortion in SiGe quantum-electronic heterostructures

Semiconductor quantum electronic devices provide the opportunity to manipulate individual quantum states of electrons, and thus promise to extend microelectronics into an entirely new regime. One promising route to forming these quantum structures using the ubiquitous and highly developed processing technology associated with silicon-based microelectronics is to create coupled quantum dots in which electrons are trapped in a thin silicon quantum well layer within a stack of layers of an alloy of silicon and germanium. As in conventional semiconductor devices, the properties of quantum mechanical devices based on the two-dimensional electron gas within the silicon quantum wells depend very strongly on the local atomic-scale structure, and on the changes in the structure induced by the creation of the devices. The role of specific structural defects, including atomic steps and other local sources of distortion, has been predicted theoretically and observed by electrical measurements [1,2], but has been difficult to probe in structural studies.

It has been particularly challenging to understand the shape and distortion of the silicon quantum well layer at length scales similar to the size of the confined electron wavefunction.

X-ray nanodiffraction allows structural information to be obtained at the length scale relevant to devices within the silicon quantum well. Nanodiffraction studies at beamline **ID01** demonstrate that the relevant structural parameters of these layers can be probed using the tightly-focused X-ray beam produced by a Fresnel zone plate. The diffraction experiments (see **Figure 109**) probe the buried silicon quantum well layer within integrated quantum dots without destructive sample preparation. The nanodiffraction results show that the structure of the silicon quantum well is influenced both by the fundamental processes of epitaxial growth in the silicon/silicon germanium materials systems and by the subsequent lithographic processing required to produce quantum dots.



A key feature of the design of the silicon quantum well is the introduction of a large biaxial tensile strain to modify the band structure within the well. In nanodiffraction studies, this strain allows X-ray reflections from the silicon quantum well to be easily distinguished from the reflections arising from the silicon substrate. In addition, the silicon quantum well has smooth interfaces, which lead to rods of intensity in reciprocal space. Maps of the intensity and angular location of these rods as a function of the position of the X-ray nanobeam provide local information about the thickness and orientation of the silicon quantum well layer. The intensity of the rod extending from the 004 X-ray reflection of the Si quantum well (inset in **Figure 109**) exhibits variations at the 100 nm length scale that result from local differences in the thickness of the quantum well layer. The intensity exhibits local variations of several percent, a magnitude that is consistent with what would be expected due to unit-cell-scale variations in the thickness of the quantum well. In addition to these local differences in thickness, the local orientation of the atomic planes within the quantum well varies due to the randomness associated with the underpinning silicon-germanium layers of the heterostructure. These orientation variations lead to a lateral variation of the strain in the quantum well over distances of hundreds of nanometres to 1  $\mu\text{m}$ , modifying the potential well confining electrons. Precise structural information allows theoretical studies of the effects of

structural features on quantum electronic properties to be tested and will enable the creation of optimised devices.

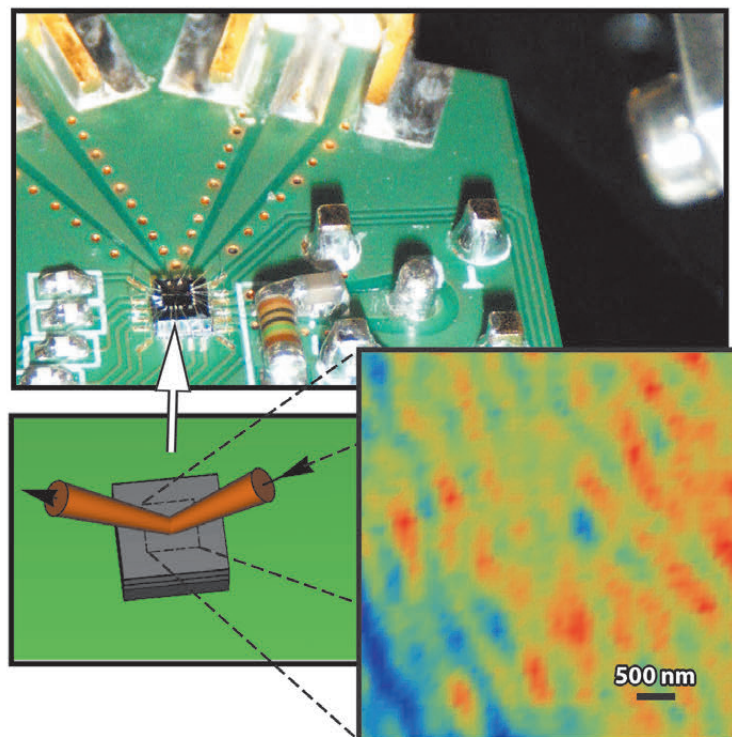


**Fig. 109:** X-ray nanodiffraction map of the waviness in a 10 nm-thick buried Si quantum well. Si quantum wells in a Si/SiGe heterostructure are characterised using a tightly-focused X-ray beam, without destructive sample preparation. Structural effects at the 100-nm length scale arising from local variations in the quantum well thickness are apparent in the total intensity of the 004 X-ray reflection of the quantum well.

#### References

- [1] M. Friesen, S. Chutia, C. Tahan and S.N. Coppersmith, *Phys. Rev. B* **75**, 115318 (2007).
- [2] L.M. McGuire, M. Friesen, K.A. Slinker, S.N. Coppersmith and M.A. Eriksson, *New J. Phys.* **12**, 033039 (2010).

## ■ BaTiO<sub>3</sub> (001) (2x1): Relation between structure and magnetism

BaTiO<sub>3</sub> (BTO) is an archetype ferroelectric whose physical properties have been well known for decades and have been thoroughly documented in solid state physics textbooks. Bulk BTO is a perovskite type ferroelectric (transition temperature  $T_C = 408$  K) insulator (bulk band gap = 3.2 eV). It is used in technological applications as a piezoceramic capacitor and in nonlinear optics. In contrast, nothing is known about the structure and physical properties of the surface of a BTO crystal, which has become

a focus for research owing to possible applications in nanoscale oxide spintronic devices [1]. Although the (001) surfaces of STO and BTO are known to reconstruct to form a (2x1) and a (2x2) superstructure [2], a structure model exists only for STO [3]. We have carried out a combined surface X-ray diffraction (SXR) and theoretical study of the atomic structure and the corresponding physical properties for BTO.

The SXR experiments were carried out at beamline **ID03** using a bulk crystal, which

#### Principal publication and authors

H.L. Meyerheim (a), A. Ernst (a), K. Mohseni (a), I.V. Maznichenko (b), S. Ostanin (a), F. Klimenta (a), N. Jedrecy (c), W. Feng (a), I. Mertig (a,b), R. Felici (d) and J. Kirschner (a,b), *Phys. Rev. Lett.* **108**, 215502 (2012).  
 (a) Max-Planck-Institut f. Mikrostrukturphysik, Halle (Germany)  
 (b) Institut für Physik, Martin-Luther-Universität Halle-Wittenberg, Halle (Germany)  
 (c) Institut des NanoSciences de Paris, UPMC-Sorbonne Univ. CNRS-UMR7588, Paris (France)  
 (d) ESRF



after mild Ar<sup>+</sup> sputtering and annealing up to about 1000°C exhibits a (2x1) reconstruction with no traces of a (2x2) reconstruction.

**Fig. 110:** Model of the BaTiO<sub>3</sub>(001)-(2x1) structure in perspective side view. Two TiO<sub>2</sub> layers (atoms #1-8) are located above the bulk-like BaO layer (primed labels correspond to symmetrically equivalent atoms).

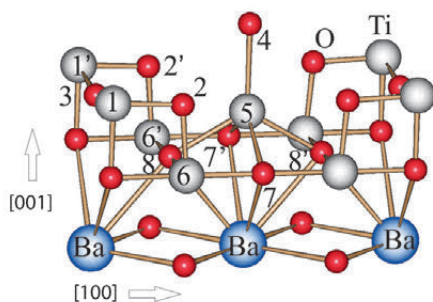
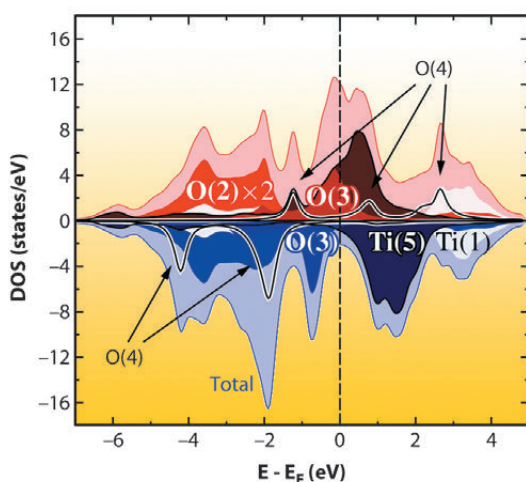


**Fig. 111:** Spin resolved DOS of BTO(001)-(2x1). The contributions of the different atoms are indicated. Dark colour (red, blue) corresponds to Ti (5). The light (red) and blue profiles correspond to the total DOS.



The structure model is shown in **Figure 110** in perspective side view. The BTO crystal is terminated by two stoichiometric TiO<sub>2</sub> layers, similar to the STO(001) surface [3], but significant differences exist with respect to the position of the top layer structure. Here, the most important characteristic is that one titanium atom (5) resides in a fivefold coordination to oxygen atoms (7, 7', 8, 8' and 4) in the centre of a pyramid. In this way, the titanium atom (5) shifts inward thereby binding to oxygen atom (4) and to the second layer oxygen atoms at a distance of 2.30 ± 0.15 Å.

Based on this structure model the electronic and magnetic properties of the (2x1) BTO surface were calculated within the density functional theory (DFT) in the local density approximation using a Korringa-Kohn-Rostoker Green-function method, which is specially designed for semi-infinite layered systems. According to the DFT calculations, the BTO(001)-(2x1) surface is metallic and magnetic. **Figure 111** shows the density of states (DOS) for spin up (↑) in red which is different from the spin down DOS (↓) shown in blue.

The DOS is large at the Fermi level (E<sub>F</sub>), this is related to the (↑) contribution of titanium atom (5) and oxygen atom (3). The filling of the titanium 3d states is mainly a consequence of the charge transfer from oxygen to titanium. Moreover, due to the low coordination and reduced symmetry, the different DOS contributions are narrow and involve partially unsaturated 2p states in the case the oxygen atoms (3) and (4). In turn this leads to high local magnetic moments up to 1.3 μ<sub>B</sub> and -2.0 μ<sub>B</sub> for the titanium atom (5) and oxygen atom (4), respectively.

In summary, our X-ray diffraction analysis of the BTO(001)-(2x1) reconstruction has identified an atomic arrangement that had not been considered before for (001) oriented perovskite surfaces. The most remarkable unit is a titanium atom in the centre of a tetragonal pyramid. This unique motif causes symmetry breaking, localisation of the electronic states, and charge transfer to the central titanium atom from surrounding oxygen atoms. This leads to metallisation and magnetisation which is now identified as an intrinsic property of the surface. We infer that this metallisation might also contribute to the stabilisation of the reconstruction related to the depolarisation of the surface.

**References**  
 [1] E.Y. Tsymlal and H. Kohlstedt, *Science* **313**, 181 (2006).  
 [2] R. Courths, *Phys. Stat. Solidi B* **100**, 135 (1980).  
 [3] R. Heger, P.R. Willmott, O. Bunk, C.M. Schlepütz, B.D. Patterson and B. Delley, *Phys. Rev. Lett.* **98**, 076102 (2007).

## ■ Reversible formation of a PdC<sub>x</sub> phase in Pd nanoparticles upon CO and O<sub>2</sub> exposure

Palladium nanoparticles are usually assumed to be in a purely metallic state during a CO oxidation reaction when CO is in excess. In this work, we tested this hypothesis studying the behaviour of Pd

nanoparticles under reaction conditions. A combination of X-ray diffraction and X-ray photoelectron spectroscopy was used for pressures ranging from UHV to 10 mbar and from room temperature to a



few hundred degrees Celsius. Under CO exposure, above a certain temperature, carbon dissolves into the particles forming a carbide phase. Upon exposure to CO and O<sub>2</sub> mixtures, the carbide phase forms and disappears reversibly, switching at the stoichiometric ratio for CO oxidation.

We have characterised the reversible formation of PdC<sub>x</sub> *in situ* by monitoring the position of the Pd(111) powder ring using a 2D detector, while mixtures of CO and O<sub>2</sub> were flown through the reactor. The size-monodisperse Pd nanoparticles (15 and 35 nm) deposited on SiO<sub>x</sub> and alumina samples were synthesised in Lund. The experiment was performed at 550 K and at a constant CO pressure of 7 mbar while varying the O<sub>2</sub> pressure from 0 to 10, 5, 2, 15, 0 and 30 mbar. The total pressure was kept constant at 1000 mbar by adding argon. **Figure 112a** shows the angular position of the intensity maximum in the Pd(111) region against time. Depending on the gas composition, the angular position of the Pd(111) ring changes between 17.6 degrees and 17.0 degrees (energy: 18 keV),

corresponding to an expansion of the lattice constant from 3.90 Å to 4.03 Å (**Figure 112b**). **Figure 112c** shows the evolution of the gas composition in the UHV chamber. The lattice expansion is consistent with the formation of PdC<sub>x</sub>. In **Figure 112b** the lattice parameter of the Pd nanoparticles, extracted from the angular position of maximum intensity in the Pd(111) ring, is plotted against time. A jump can be seen in the lattice parameter evolution between 3.92 Å and 3.98 Å, which is a signature of a phase transition. The measurements demonstrate that two different carbon containing Pd phases exists depending on the gas surroundings, one with a C concentration of 1-2% and one with C concentration in the range 11-16%.

Ambient pressure XPS studies, carried out at the ALS (Beamlines 11.0.2 and 9.3.2) revealed that the Pd 3d<sub>5/2</sub> peak shifted up, from the metallic Pd energy by 1.6 eV upon exposure of the nanoparticles to 1 mbar oxygen at 550 K, indicating the formation of an oxide shell of at least 1 nm thick. By introducing 1 mbar of CO,

#### Principal publication and authors

O. Balme (a), A. Resta (a), D. Wermeille (a), R. Felici (a), M.E. Messing (b), K. Deppert (b), Z. Liu (c), M.E. Grass (c), H. Bluhm (d), R. van Rijn (e), J.W.M. Frenken (e), R. Westerström (f), S. Blomberg (g), J. Gustafson (g) and E. Lundgren (g), *Phys. Chem. Chem. Phys.* **14**, 4796-4801 (2012).

(a) ESRF

(b) Solid State Physics, Lund University (Sweden)

(c) ALS, Lawrence Berkeley National Laboratory, Berkeley (USA)

(d) Chemical Sciences Division, Lawrence Berkeley National Laboratory, Berkeley (USA)

(e) Kammerlingh Onnes Laboratory, Leiden University (The Netherlands)

(f) Surface Physics Group, University of Zürich (Switzerland)

(g) Division of Synchrotron Radiation Research, Department of Physics, Lund University (Sweden)

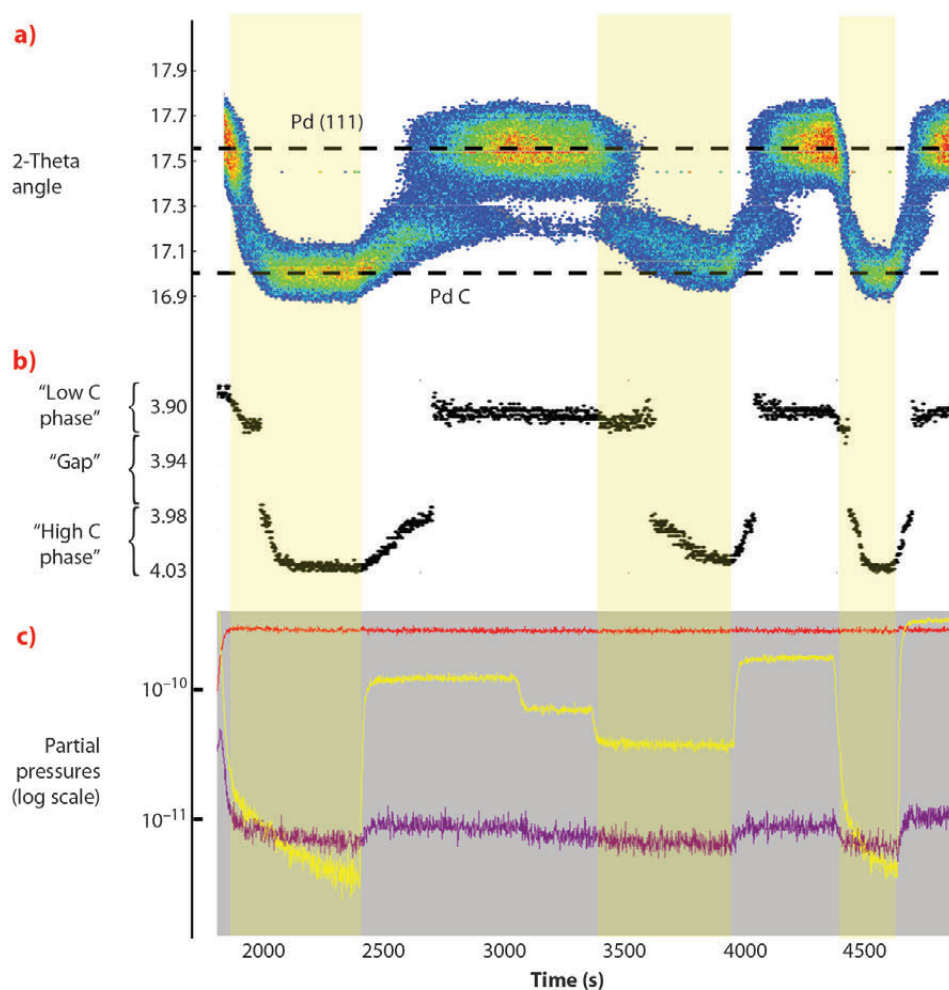


**Fig. 112:** a) Position of the the Pd(111) ring over time (red-strong diffraction signal, blue-weak diffraction signal). b) The Pd(111) lattice parameter (in angstrom) taken as the position of maximum intensity from graph A, as a function of time. The light yellow regions indicate a below-stoichiometric mix for O<sub>2</sub>, allowing the Boudouard reaction. Note the correspondence between the expansion and contraction of the Pd lattice and the partial O<sub>2</sub> pressure. c) Partial pressure of O<sub>2</sub> (yellow), CO (red) and CO<sub>2</sub> (magenta) as seen by the residual gas analyser.



PdO is reduced. While a weak Pd bulk component at 335 eV appears, a new intense component can be observed at 335.6 eV (Figure 113). At these excitation energies, at most 40% of the total intensity

**Fig. 113:** Pd  $3d_{5/2}$  core level spectrum from a clean Pd(100) reference (bottom), after oxidation of 15 nm Pd particles at 1 mbar  $O_2$  exposure at 550 K (centre) and after 1 mbar CO exposure at 550 K (top).

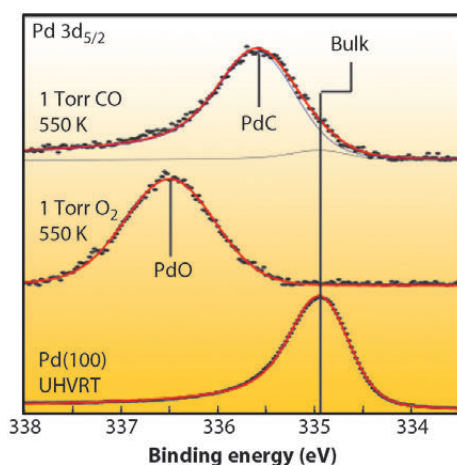
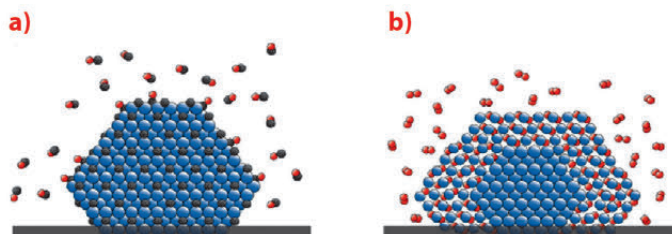


**Fig. 114:** Schematic model of a) a  $PdC_x$  particle in CO pressures in the mbar range with  $pCO/pO_2 > 2$ , and elevated temperatures, and b) a PdO particle with a metallic core in  $O_2$  pressures in the mbar range,  $pCO/pO_2 < 2$ , and elevated temperatures (Pd in blue, C in Black, O in red).



of the peak derives from the particle surface, confirming the formation of a  $PdC_x$  phase in the particle.

In conclusion, Pd particles will transform into  $PdC_x$  (Figure 114a) in pure CO or a mixed  $O_2/CO$  atmosphere with excess CO at temperatures of around 550 K, while a PdO shell forms (Figure 114b) in excess oxygen. The formation of  $PdC_x$  is easier than expected, and might play an important role for palladium catalysts whenever CO is present. Our study indicates that compound formation between the active catalyst and the gas phase may be a general phenomenon.

#### Principal publication and authors

A.A. Eliseev (a),  
N.A. Sapoletova (a),  
I. Snigireva (b), A. Snigirev (b) and  
K.S. Napolskii (a,c), *Angewandte  
Chemie International Edition* **51**,  
11602–11605 (2012).  
(a) Department of Materials  
Science, Lomonosov Moscow State  
University (Russia)  
(b) ESRF  
(c) Department of Chemistry,  
Lomonosov Moscow State  
University (Russia)

## Photoelectrons add versatility to electrochemical processing and enable electrochemical X-ray photolithography

Today lithography techniques are among the most rapidly developing areas in both science and engineering. In the last two decades, well-known and widespread methods of photo- and e-beam lithography have been complemented by a number of novel approaches that include direct writing processes, mask-based techniques, and unconventional wet lithographies [1]. Further improvements in this method can be introduced by the integration of lithography with chemical or electrochemical processes. Electrochemical processing possesses a number of important advantages, including room-temperature synthesis, the ability to control deposit morphology, and enhanced versatility. The idea of combining electrochemistry with X-ray photolithography originated from experimental observation of the variation in

electrochemical deposition/etching rates at the working electrode under illumination.

Generally, absorption of a high-energy photon by the electrode surface leads to numerous secondary events with an avalanche-type creation of low-energy excited electrons. In some cases, the energy of the electron exceeds the Volta potential difference, permitting it to escape from the surface to the electrolyte volume. In the case of cathodic polarisation, low-energy electrons emitted from the electrode surface can further reduce cations in the Helmholtz layer, while high-energy electrons pass through the electric double layer to the electrolyte volume (Figure 115). Thus, emitted photoelectrons generally produce an additional electric current at the electrode-electrolyte

interface that involves electrochemical transformation. Unlike the radiolysis products, these electrons have no oxidising pairs, which obviously shifts the electrochemical equilibrium and enhances deposition rates on the illuminated areas of the electrode. The holes on core levels generated by X-rays move away from the electrode surface under the applied potential and annihilate effectively in the electrode volume. The circuit completes through electrochemical reactions on the anode.

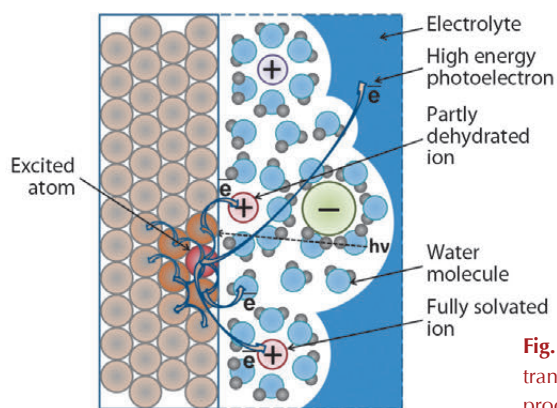


**Fig. 115:** Illustration of the charge transfer during electrochemical X-ray processing.

Indeed, in nickel electrochemical deposition experiments, the thickness of the deposited metal film was found to increase substantially on the illuminated area of the electrode as compared to the non-irradiated surface. Moreover, an extensive increase in current was observed on switching on X-ray illumination.

As X-rays provide opportunities for optical imaging, the X-ray assisted electrochemical approach can be successfully utilised for a direct pattern transfer to a liquid–solid interface by coherent X-ray irradiation. Moreover, the small ( $\ll 10$  nm) inelastic mean free path of low-energy secondary electrons brings hope to proceed with lithographic imaging with the resolution of X-ray optics. Proof-of-concept pattern transfer experiments were carried out through electrochemical deposition of nickel under coherent X-ray illumination guided through a lithographic mask with 4 micrometre pitch at the micro-optics test bench of beamline **ID06**. A silicon grating illuminated with collimated coherent light (12 keV, total flux  $2 \times 10^{13}$  photons/s) was used to produce a pattern in the transmitted light. To create a periodic intensity distribution on the substrate, the mask-to-working electrode distance was adjusted to half of the Talbot length. Electrodeposition was carried out from a Watts nickel plating bath in potentiostatic mode at room temperature.

**Figure 116** shows a SEM image of nickel electrodeposited onto an X-ray-illuminated Au/Si electrode. The resulting structure corresponds well to the image of the diffraction grating; the periodicity of the fabricated Ni pattern ( $4 \mu\text{m}$ ) is identical to that of the mask. The height of the islands in the resulting structure (inset in **Figure 116**) is clearly dependent on the contrast provided by the self-image

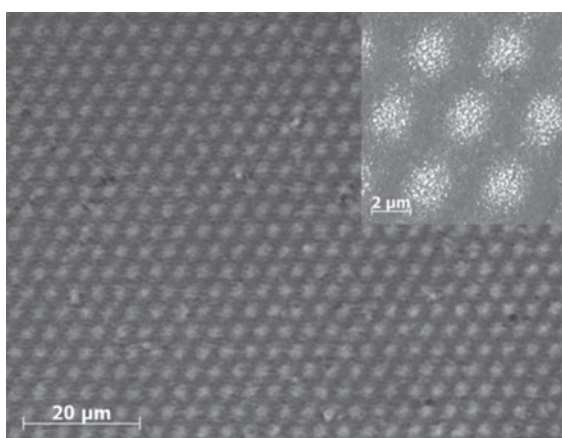


**Fig. 116:** Top-view SEM image of the nickel electrodeposited onto an Au/Si electrode under periodic X-ray illumination.

of the grating. The EDX mapping of the resulting structure indicates a metal electrodeposition enhancement of up to 150% in the illuminated areas compared to the unilluminated regions.

The proposed electrochemical X-ray photolithography method thus results in a direct non-contact pattern transfer onto an electrodeposited metal film. The rather short lifetime of radiolysis products, in combination with a small spur radii and electron inelastic mean free paths in condensed matter, provide a possible means to rapidly improve the ultimate resolution of the proposed method to tens of nanometres with further development of the X-ray optics. Moreover, regulation of the working electrode potential represents an effective pathway to control deposition rates through variation of ion concentration in the Helmholtz layer. We believe that this electrochemical X-ray photolithography technique presents no limitations for electrochemical processing and can be further expanded to various technical applications including electrodeposition of metals, semiconductors, and complex structures, and X-ray assisted anisotropic electrochemical etching.

#### References

- [1] F.C. Simeone, C. Albonetti and M. Cavallini, *J. Phys. Chem. C* **113**, 18987-18994 (2009).



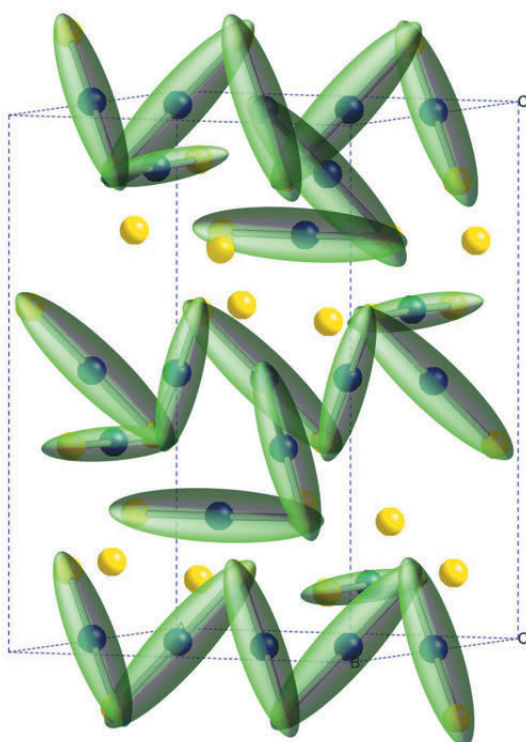
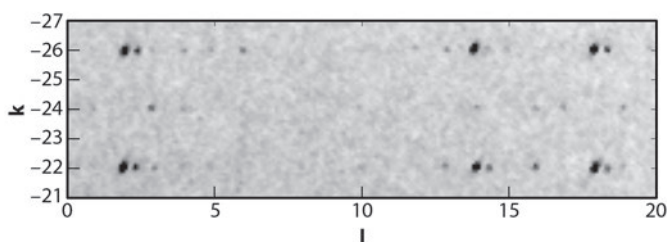
### Principal publication and authors

M.S. Senn (a), J.P. Wright (b) and J.P. Attfield (a), *Nature* **481**, 173-6 (2012).

(a) *Centre for Science at Extreme Conditions and School of Chemistry, University of Edinburgh (UK)*

(b) *ESRF*

**Fig. 117:** X-ray diffraction intensities from a 40  $\mu\text{m}$  magnetite grain at 90 K, shown for the  $h = 50$  ( $hkl$ ) plane. The microcrystal is almost single domain; faint spots to the right of the main intensities reveal the secondary twin.



transition temperature it was not possible to confirm the electronic order.

The low temperature structure of magnetite proved to be remarkably complex. The presence of many small shifts of the atomic positions, of technical problems with crystallographic twinning, and of extinction and multiple scattering effects, have prevented the full structural details from emerging until now. By using a tiny (40  $\mu\text{m}$ ) crystal and a focused beam of high energy (74 keV) X-rays at beamline **ID11**, we were finally able to solve and refine the structure. Cooling the crystal in a magnetic field produced a sample which had a dominant single domain, as shown by the data image in **Figure 117**. An abundance of diffraction peaks down to a 0.3  $\text{\AA}$  d-spacing were measured, allowing us to refine a full and accurate structure.

The low temperature distorted structure is very complex, with 24 different iron sites present. Eight of these have tetrahedral  $\text{FeO}_4$  co-ordination and remain as  $\text{Fe}^{3+}$  both above and below the transition. The other 16 sites have octahedral  $\text{FeO}_6$  co-ordination and have an average valence state of 2.5+ in the high symmetry structure. Our results showed that these split into two groups approximately corresponding to the expected  $\text{Fe}^{2+}$  and  $\text{Fe}^{3+}$  states. However, we discovered an additional and unexpected interaction. The  $\text{Fe}^{2+}$  sites form weak bonds to two of their neighbours so their electron density is spread over all three iron atoms. We describe this unit and the accompanying local distortion as a 'trimeron'. The low temperature structure of magnetite is thus described by an ordered arrangement of trimerons, as shown on **Figure 118**. Dynamic motion of trimerons may be important in magnetite above the Verwey transition and to the electronic properties of other transition metal oxides.

**Fig. 118:** Charge order in the low temperature structure of magnetite, with  $\text{Fe}^{2+}/\text{Fe}^{3+}$  states shown as blue/yellow spheres and the three site trimeron units represented as green ellipsoids.

### References

- [1] E.J.W. Verwey, *Nature* **144**, 327–328 (1939).
- [2] F. Walz, *J. Phys.: Condens. Mat.* **14** R285 (2002).

## ■ Crystallisation during bending of a metallic glass

Atoms in metallic glasses are arranged in no particular long-range order and instead form a rather random packing of compact clusters [1], without the availability of slip systems and dislocation glide for plastic deformation as in crystalline materials which have long-range lattice order. Their disorder endows metallic glasses with high resilience up to elastic strains of 2% or more before undergoing heterogeneous plastic deformation via the formation of shear bands.

Shear bands are thin (20-50 nm), nearly planar zones of intense plastic deformation where dissipation of mechanical work generates free volume [2] and results in local heating estimated to be anywhere from negligible to reaching above the melting temperature  $T_f$  [3]. Crystallite formation after plastic deformation has been detected by transmission electron microscopy (TEM) but only after specimen thinning followed by electron-beam focusing on regions of shear bands, and many experimental artifacts must be excluded.

We performed non-destructive diffraction on a bent 35  $\mu\text{m}$  thick glassy  $\text{Pd}_{40}\text{Cu}_{30}\text{Ni}_{10}\text{P}_{20}$  ribbon in transmission geometry using a monochromatic beam at beamline ID11. The incident beam was focused to 2  $\mu\text{m}$  in diameter for microprofiling across the bent specimen width every few micrometres along the thickness. Figure 119 shows the resulting X-ray microscopy images together with a scanning electron microscope (SEM) image of the bend in the ribbon. Crystalline Bragg peaks are seen to appear on the compressive fibre side of the bend but not on the tension side.

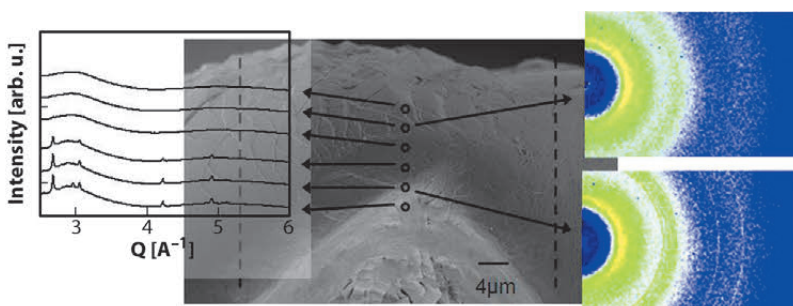


**Fig. 119:** X-ray microscopy images during microprofiling along the thickness through the width of bent glassy  $\text{Pd}_{40}\text{Cu}_{30}\text{Ni}_{10}\text{P}_{20}$  ribbon.

**Figure 120** is a close-up SEM image of the inner (compressive) side of the bend in the ribbon showing shear steps with viscous shapes and meniscus formation [3].

What remained to be explained was why crystallisation occurs on the compression side and not on the tension side of the bend. Homogeneous nucleation frequency per volume per time  $I_v^{\text{hom}}(T)$  in the so-called steady-state regime is formulated as:

$$I_v^{\text{hom}}(T) = \frac{D_n N_v}{a_0^2} \times e^{-\frac{16\pi}{3kT} \times \frac{\sigma^3}{\Delta G_v^2}} \quad (1)$$

where  $D_n$ ,  $N_v$  and  $a_0$  are respectively an atomic diffusivity, number of atoms per unit volume and an average inter-atomic distance.  $\sigma$  is the crystal-liquid

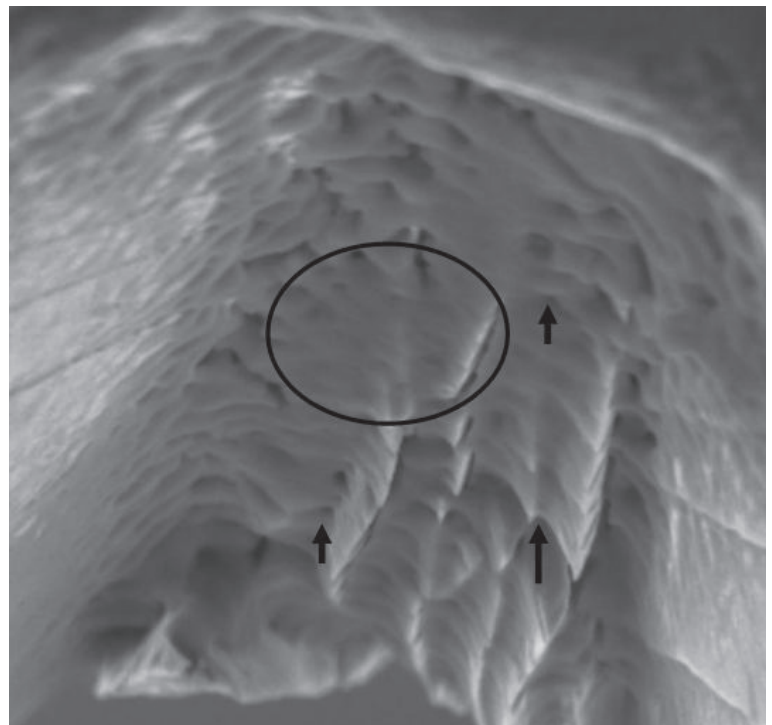


**Fig. 120:** SEM image of the inner surface of bent glassy  $\text{Pd}_{40}\text{Cu}_{30}\text{Ni}_{10}\text{P}_{20}$  ribbon showing shear steps with viscous shapes and meniscus formation.

### Principal publication and authors

A.R. Yavari (a,b),  
 K. Georgarakis (a,b),  
 J. Antonowicz (c), M. Stoica (d),  
 N. Nishiyama (b), G. Vaughan (e),  
 M. Chen (b) and M. Pons (a), *Phys. Rev. Lett.* **109**, 085501 (2012).  
 (a) Euronano SIMaP-CNRS, Institut Polytechnique de Grenoble INPG (France)  
 (b) WPI AIMR Tohoku University (Japan)  
 (c) Faculty of Physics, Warsaw University of Technology (Poland)  
 (d) Institute for Complex Materials, IFW Dresden (Germany)  
 (e) ESRF



### References

- [1] A.R. Yavari, *Nature* **439**, 405 (2006).  
 [2] A.R. Yavari, A. Le Moulec, A. Inoue, N. Nishiyama, N. Lupu, E. Matsubara, W.J. Botta, G. Vaughan, M. Di Michiel and Å. Kvick, *Acta Materialia* **53**, 1611 (2005).  
 [3] K. Georgarakis, M. Aljerf, Y. Li, A. LeMoulec, F. Charlot, A.R. Yavari, K. Chornokhvostenko, E. Tabachnikova, G.A. Evangelakis, D.B. Miracle, A.L. Greer and T. Zhang, *Appl. Phys. Lett.* **93**, 031907 (2008).  
 [4] L.D. Landau and E.M. Lifshitz, "Statistical Physics", Addison-Wesley Publishing, p. 261 (1974).  
 [5] K. Hajlaoui, A.R. Yavari, B. Doisneau, W.J. Botta, W. Zhang, G. Vaughan, A. Kvick, A. Inoue and A.L. Greer, *Mater. Sci. Eng. A* **105**, 449–451 (2007).

interfacial energy,  $\Delta G_v$  the driving free energy for crystallisation per unit volume,  $T$  the temperature and  $k$  the Boltzmann constant. **Eq. (1)** can be modified for crystallisation under external hydrostatic compressive pressure  $P$  as:

$$I_v^{\text{hom}}(T) = \frac{D_n N_v}{a_0^2} \times e^{-\frac{16\pi}{3kT} \times \frac{\sigma^3}{(\Delta G_v + P\Delta V_x/V)^2}} \quad (2)$$

where  $\Delta V_x/V$  is the usually negative reduced volume-change on crystallisation and the term  $P\Delta V_x/V$  comes as a modification of  $\Delta G_v$  due to a pressure-induced increase in the melting temperature  $T_m$  (or an increase in undercooling) as formulated in the Clapeyron-Clausius formula [4].

A glassy ribbon reaches plastic yield resulting in the formation of shear bands under an applied stress  $\tau \approx \tau_y$ . For the PdCuNiP family of metallic glasses  $\tau_y \geq 1.5$  GPa. When temperature  $T$  reaches that of crystallisation  $T_x \approx 700$  K as determined by calorimetry, we can write:

(3)

$$I_v(T_x, P \approx \tau_y) / I_v(T_x, P = 0) \approx \exp \left\{ - (16\pi\sigma^3/3k \cdot T_x) \cdot [(1/(\Delta G_v)^2) - (1/(\Delta G_v + \tau_y \cdot \Delta V_x/V)^2)] \right\}$$

Using the materials parameters listed in the principal publication, we obtain  $I_v(T_x, \tau_y) / I_v(T_x) \approx 10^{55}$  as compared to  $I_v^{\text{hom}}(700\text{K}) \approx 10^{-5}/\text{m}^3 \cdot \text{s}$  without any external stress. Thus, in the compression side of the bend, the value could reach  $10^{50}/\text{m}^3 \cdot \text{s}$ .

The above numbers show high nucleation frequencies because a large volume change  $\Delta V_x/V \approx -2\%$  on crystallisation at  $T_x \approx 700$  K as compared with a much smaller volume change of below 1% at room temperature. The larger volume change  $\Delta V_x/V$  is due to the large thermal expansion coefficient of the liquid state and an extended supercooled liquid region  $\Delta T$  stretching about 100 K between  $T_g$  and  $T_x$ .

The analysis suggests that a wide supercooled liquid region is required for stress-crystallisation of a metallic glass deformed in compression. This confirms previous suggestions that shear band crystallisation contributes to a more extended strain which causes the fracture of metallic glasses under compressive load by shear delocalisation [5], a mechanism that does not intervene under tension.

### Principal publication and authors

D.S. Wragg (a), M.G. O'Brien (b), F.L. Bleken (a), M. Di Michiel (c), U. Olsbye (a) and H. Fjellvåg (a), *Angew. Chem. Int. Ed.* **51**, 7956–7959 (2012).  
 (a) *inGAP Centre for Research Based Innovation, University of Oslo (Norway)*  
 (b) *Utrecht University Debye Institute for Nanomaterials Science (Netherlands)*  
 (c) *ESRF*

## Looking inside a working chemical reactor with time and space resolved X-ray diffraction

As we move away from oil as a source of petrochemicals, the methanol-to-olefin (MTO) process is becoming a key step in the route from inexpensive, plentiful and even renewable feeds like gas, coal and biomass, to the chemical building blocks we depend on every day. Olefins are a particularly useful group of chemicals which can be transformed into polymers used in anything from plastic bottles to thermal underwear. At present, they are produced mainly by distilling crude oil, however, the MTO route is becoming economically viable. Several plants are under construction in China.

The catalyst in the MTO process is the porous zeotype framework SAPO-34, which suffers from deactivation caused by the build-up of coke in its zeolite cavities. Understanding the progress of this reaction and coke formation in a large, industrial-like reactor is very important

in the quest to optimise the process. For example, extending the lifetime of the catalyst before coking could allow fixed bed reactors to replace the current breed of complex and expensive recirculating fluidised bed MTO reactors, leading to a major cost saving. Our earlier research at the beamline BM01A (Swiss-Norwegian CRG beamline) revealed that the MTO process causes significant expansion of SAPO-34 due to the build-up of hydrocarbon intermediates in the catalyst cavities [1]. The catalyst expands as the content of the cavities changes from relatively small reaction intermediates to large, inactive coke molecules. We collected time- and space-resolved data at the high-energy beamline **ID15B** and used the expansion of the catalyst as an indication of the progress of the reaction in a 4 mm diameter tube reactor. Diffraction patterns were collected every second as the reactor and heaters were moved down

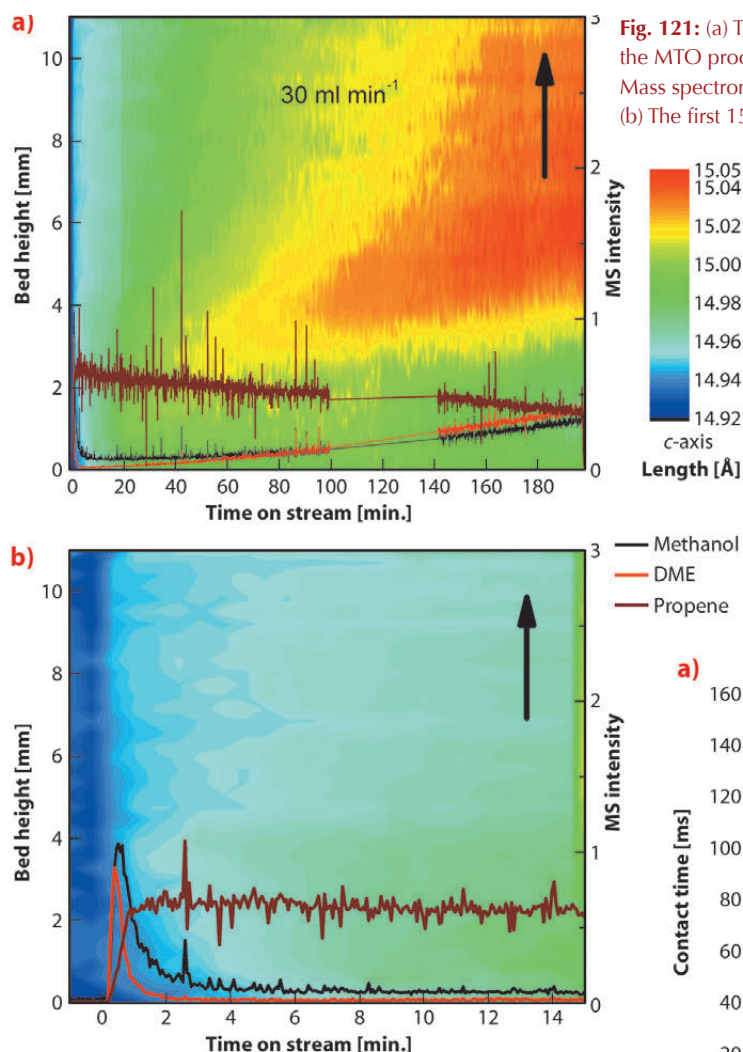
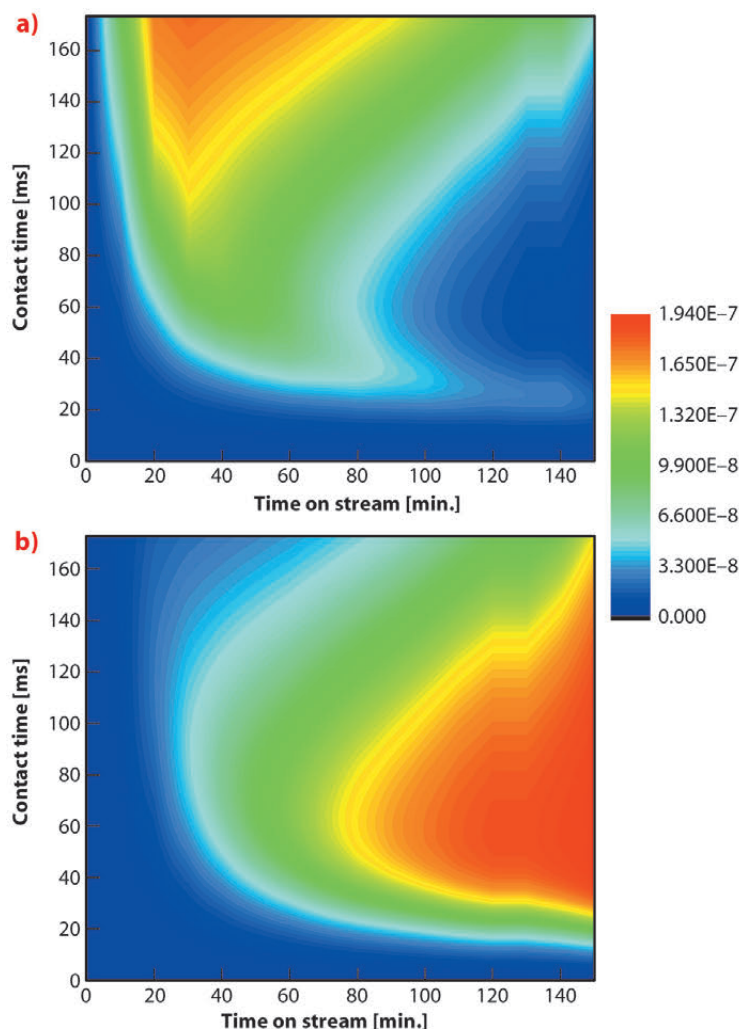


**Fig. 121:** (a) Time- and space-resolved HEXRD data for the MTO process at 350°C and a flow rate of 30 ml min<sup>-1</sup>. Mass spectrometry activity data are shown as line plots. (b) The first 15 minutes of the reaction in more detail.

**Fig. 122:** Simulated bed profiles from the kinetic model with contact time as for a flow rate of 30 ml min<sup>-1</sup>. Profile (a) shows the development of the intermediates which cause the initial expansion of the catalyst; (b) shows the development of the heavy coke responsible for the final expansion.



through the beam, giving a series of scans along the vertical axis of the reactor. The output from the reactor was analysed with a mass spectrometer. Each pattern was processed using parametric Rietveld methods (up to 500 datasets at a time) and c-axis expansion was plotted against time and position in the reactor. The resulting contour plots are shown in **Figure 121**.

Early in the reaction we see that the initial expansion of the catalyst corresponds to an increase in the production of olefins, while the later deactivation of the reactor bed is correlated to the appearance of highly expanded regions of catalyst in the top section of the bed, caused by inactive coke. The point at which the expansion first appears is determined by the flow rate of methanol and the number of catalytic active sites.

Kinetic modelling reproduces the observed behaviour very well (**Figure 122**), with the initial expansion observed in the experiment following a similar pattern to the modelled behaviour of the hydrocarbon intermediates and the

larger expansion in the later stages of the reaction corresponding to the spread of large coke molecules in the model. This model is the first to include the link between methanol feed and increasing coke levels. The results of this work will help to improve the efficiency of the MTO process at an industrial scale.

#### References

- [1] D.S. Wragg, R.E. Johnsen, M. Balasundaram, P. Norby, H. Fjellvåg, A. Grønbold, T. Fuglerud, J. Hafizovic, Ø.B. Vistad and D. Akporiaye, *J. Catal.* **268**, 290-296 (2009).



### Principal publication and authors

T. Friščić (a,b), I. Halasz (c,d),  
P.J. Beldon (b), A.M. Belenguer (b),  
F. Adams (d), S.A.J. Kimber (e),  
V. Honkimäki (e) and  
R.E. Dinnebier (d), *Nature  
Chemistry* **5**, 66–73 (2013).  
(a) McGill University (Canada)  
(b) University of Cambridge (UK)  
(c) Faculty of Science, University of  
Zagreb (Croatia)  
(d) Max-Planck-Institute for Solid  
State Research (Germany)  
(e) ESRF

## ■ The first real-time study of a mechanochemical reaction

Reactions induced by mechanical force, also known as mechanochemical reactions [1], have been known and used for millennia. According to recent accounts, the first written record of metal extraction from an ore was performed by grinding cinnabarite (HgS) in a copper mortar in the presence of vinegar [2] – an ancient analogy to the highly efficient liquid-assisted grinding (LAG) methodology used by the modern pharmaceutical industry to discover new solid forms, polymorphs, salts and cocrystals of pharmaceuticals [3]. Despite continuous use from extractive

metallurgy to pharmaceuticals, the understanding of mechanochemical reactions remains to a large extent mysterious. This is not surprising, considering the difficulty of directly measuring a chemical reaction taking place in a rapidly moving milling vessel and under intense impact of stainless steel milling balls.

The solution to this long-standing problem was recently devised at beamline ID15B where the excellent penetrating ability of short wavelength X-rays (0.1427 Å)

**Fig. 123:**  
Experimental setup  
for mechanochemical  
synthesis developed at  
ID15B.

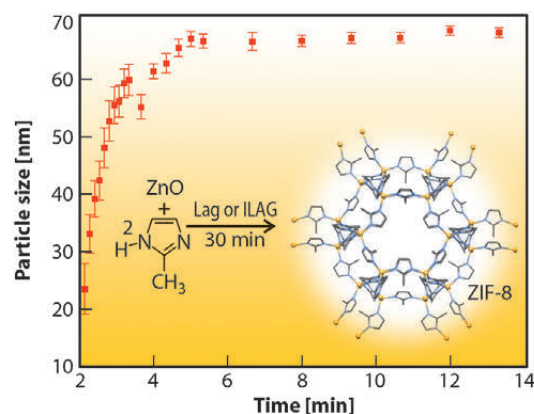
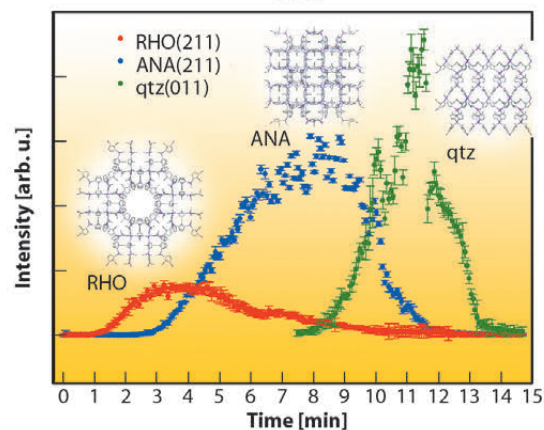
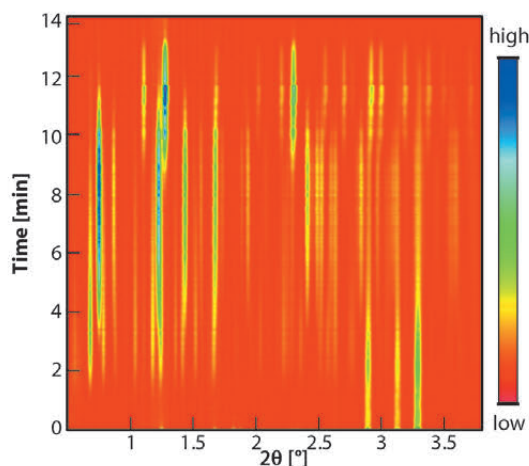
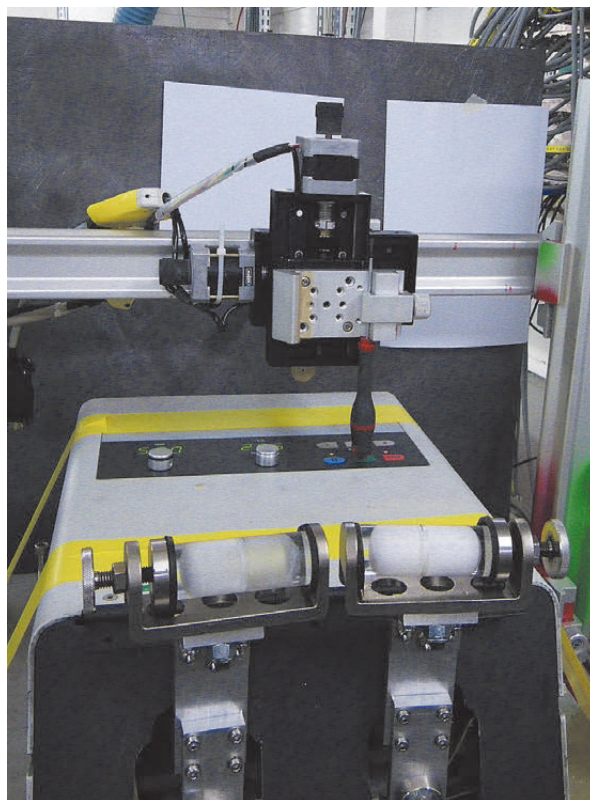


**Fig. 124:** Top panel: Example time-resolved powder X-ray diffractograms from the mechanochemical synthesis of porous zeolitic imidazolate frameworks. Middle panel: By monitoring the variation in time of the intensity of a characteristic X-ray reflection for each intermediate (RHO and ANA frameworks) and product (qtz framework), it is now possible to monitor the appearance and disappearance of different porous and non-porous crystalline phases in a mechanochemical reaction. Bottom panel: Measurement of diffraction peak widths allows *in situ* measurement of particle size evolution in a mechanochemical reaction; Inset: Reaction for the synthesis of ZIF-8.



enabled the direct, real-time recording of diffractograms of reaction mixtures being ball milled within the milling vessel operating at a rapid 30 Hz (**Figure 123**). As the first entry into real-time observation of mechanochemical reactions, we investigated the assembly of porous metal-organic frameworks directly from the simplest metal oxide precursor and using the latest mechanochemical techniques of LAG and ion- and liquid-assisted grinding (ILAG) [4].

The *in situ* studies provided a direct insight into the kinetics of mechanochemical formation of the porous structure, *in situ* observation of particle growth, as well as into how changes in catalytic additives and reaction conditions can control and direct the formation of different reaction intermediates. One of the most surprising results coming from this work was the observation of reaction intermediates lasting minutes or less, which would not

be monitored or even detectable using conventional stop-and-see approaches.

The methodology that was demonstrated at **ID15B** provides unprecedented insight into the mechanisms of mechanochemical reactions, both in terms of monitoring reaction kinetics, observing previously unknown intermediate phases and monitoring particle size development (**Figure 124**). Porous metal-organic frameworks have been proposed as versatile materials in gas storage, catalysis and even light harvesting, and mechanochemical reactions are becoming increasingly important in the context of sustainable chemical synthesis and manufacturing. Consequently, potential applications of the described *in situ* monitoring methodology await in materials science, but also in mineral extraction, metallurgy, pharmaceutical and cement industry, as well as nanoparticle synthesis.

#### References

- [1] S.L. James, P. Collier, I. Parkin, G. Hyatt, D. Braga, L. Maini, W. Jones, C. Bölm, A. Krebs, J. Mack, D. Waddell, W. Shearouse, A.G. Orpen, C.J. Adams, T. Friščić, J.W. Steed and K.D.M. Harris, *Chem. Soc. Rev.* **41**, 413-447 (2012).
- [2] L. Takacs, *JOM* **52**, 12-13 (2000).
- [3] A. Delori, T. Friščić and W. Jones, *CrystEngComm* **14**, 2350-2362 (2012).
- [4] P.J. Beldon, L. Fábrián, R.S. Stein, A. Thirumurugan, A.K. Cheetham and T. Friščić, *Angew. Chem. Int. Ed.* **49**, 9640-9643 (2010).

## ■ Oxygen storage and release at work in catalysis for pollution abatement: illuminating synergies between noble metal and oxide promoter

Many modern functional materials are made of multi-phase, nanoscale entities wherein cooperative behaviour between different components is required to obtain optimal performance. Prototypical of such situations are modern three-way catalysts which are utilised in vehicle exhausts to reduce exhaust gas emissions. They convert the three main pollutants in vehicle exhaust, carbon monoxide (CO), unburnt hydrocarbons (HC) and oxides of nitrogen (NO<sub>x</sub>), to H<sub>2</sub>O, CO<sub>2</sub> and nitrogen. Three-way catalysts comprise a support (Al<sub>2</sub>O<sub>3</sub>) upon which both noble metal nanoparticles (Pd, Pt, Rh) and promoting oxides (e.g. CeZrO<sub>4</sub>) are deposited. Key to the desired catalytic conversions is the structure-reactivity interplay between the promoting oxide and the noble metals, in particular regarding the storage/release of oxygen under process conditions.

We have addressed these interactions at beamline **ID15B** by combining techniques to achieve bulk, surface and catalytic sensitivity. The techniques used were high-

energy X-ray diffraction (HEXRD), infrared spectroscopy (IR) and mass spectrometry (MS). This combination aims to render complete information concerning all solid and gas phases as well as solid-gas interface relevant phenomena. The behaviour of three-way catalysts was thus analysed in dynamic conditions where the gas phase in contact with the catalyst changes from reducing (CO) to oxidising (NO) conditions. The use of HEXRD [1,2] provides kinetic assessment of the above mentioned interactions as well as delineation of how they come together to yield superior catalysts.

**Figure 125** shows time-resolved HEXRD data for two samples with approximately equal Pd particle size in the absence or presence of the CeZrO<sub>4</sub> promoter (ZC). The Pd/Al<sub>2</sub>O<sub>3</sub> case (ZC free, **Figure 125a**) shows the dynamical response of the supported Pd nanoparticles to the change of environment: during CO exposure the Pd lattice parameter expands monotonically (Bragg peaks shift to lower Q).

#### Principal publication and authors

M.A. Newton (a), M. Di Michiel (a), A. Kubacka (b), A. Iglesias-Juez (b) and M. Fernández-García (b), *Angew. Chem. Int. Ed.* **5**, 2363-7 (2012).  
(a) ESRF  
(b) CSIC, Madrid (Spain)



### References

- [1] M.A. Newton, M. Di Michiel, A. Kubacka and M. Fernández-García, *J. Am. Chem. Soc.* **132**, 4540 (2010).  
 [2] A. Iglesias-Juez, A. Kubacka, M. Fernández-García, M. Di Michiel and M.A. Newton, *J. Am. Chem. Soc.* **133**, 4481 (2011).

This behaviour is rapidly reversed under NO resulting in a “sawtooth” variation of the lattice parameter. This is due to the sequential storage and removal of atomic carbon by the Pd nanoparticles [1,2].

The influence of the ZC promoter in Pd chemistry, particularly in its interaction with CO, becomes evident from **Figure 125b**. The response of the Pd phase to CO/NO gas in the presence of ZC is minimal, but big variations in the ZC lattice parameter as a function of the reducing or oxidising environment can be detected.

In **Figure 126** we present the changes in the ZC lattice parameter and the corresponding redox states, related to  $\text{Ce}^{3+}$  formation/annihilation during the same CO/NO dynamical cycle. The Pd-based three-way catalyst system ( $\text{Pd} + \text{ZC} + \text{Al}_2\text{O}_3$ ) is compared with the support consisting of the ZC promoter deposited onto the alumina carrier. The plot quantifies the oxygen dynamically stored and released and establishes the

kinetic dependence of both phenomena. The presence and magnitude of the synergy between Pd and the  $\text{CeZrO}_4$  are evident. Without noble metal,  $\text{CeZrO}_4$  donates or stores a limited amount of oxygen. The presence of Pd significantly promotes the process of oxygen transfer in both directions (uptake and release), leading to greatly enhanced catalytic operation.

From the XRD measurements we also observe precisely when the oxygen donating capacity of the  $\text{CeZrO}_4$  is exhausted and from MS and IR (not shown) the ramifications this has on the speciation present at the surface of the catalyst. The occurrence of oxygen transfer arising from the  $\text{CeZrO}_4$  radically changes the behaviour of the Pd nanoparticles toward CO and NO molecular and dissociative adsorption, and indeed the formation or not of  $\text{PdC}_x$  phases and or adsorbed CN and NCO molecules during the catalysis. All of these species have fundamental roles to play in the successful removal of pollutant species in the applied process.

**Fig. 125:** Variation in HEXRD (colour map) observed during CO/NO cycling at 673 K over two Pd-containing samples. The experiment shows three cycles comprising a CO/NO treatment of  $2 \times 13.86$  s.

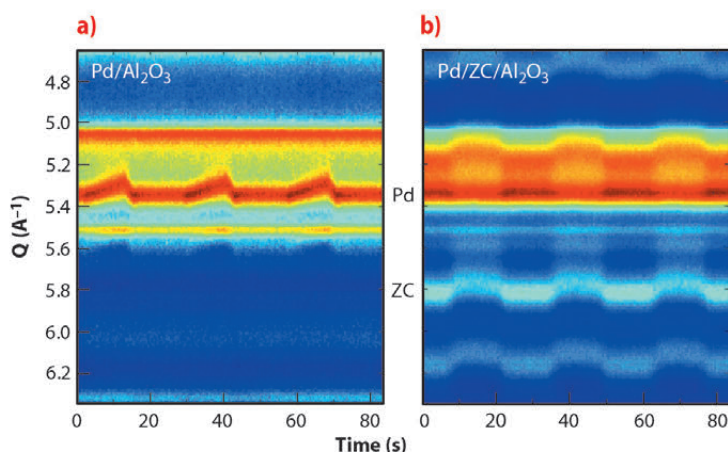
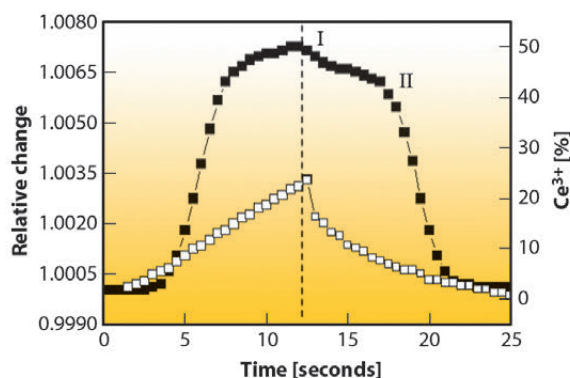


**Fig. 126:** Relative change of the ZC lattice constant and corresponding  $\text{Ce}^{3+}$  content during a CO/NO single cycle at 673 K for the  $\text{Pd/ZC/Al}_2\text{O}_3$  catalyst (full symbol) and  $\text{ZC/Al}_2\text{O}_3$  support (open symbol).

## ■ Charge order at the frontier between the molecular and solid states in $\text{Ba}_3\text{NaRu}_2\text{O}_9$

Strong many body correlations between electrons in solids result in extremely diverse properties including insulating antiferromagnetism, charge order and superconductivity. This is especially true in

organic based materials like fullerides or the  $\text{K}-(\text{BEDT-TTF})_2\text{X}$  or  $(\text{Pd}[\text{dmit}])_2$  salts, due to the narrow electronic bandwidth resulting from the overlap of molecular orbitals [1]. Our recent investigation



of  $\text{Ba}_3\text{NaRu}_2\text{O}_9$  shows that similar competition between ground states can also be observed in simple metal oxides which have quasi-molecular structures.

We synthesised powder samples of  $\text{Ba}_3\text{NaRu}_2\text{O}_9$  which were characterised by high resolution synchrotron X-ray diffraction measurements using ID31. The 6H hexagonal perovskite structure is found at room temperature (Figure 127a), with isolated  $\text{Ru}^{5.5+}_2\text{O}_9$  dimers of face-sharing octahedra packed into triangular layers. Previous reports indicate that a metal-insulator transition [2] and structural distortion occur below 210 K.

Below 210 K, we detected a monoclinic distortion and solved the structure in  $P2/c$ . The key feature of our structure is a splitting of the  $\text{Ru}^{5.5+}_2\text{O}_9$  dimers into two symmetry inequivalent units, implying charge ordering. Our refinements allowed us to examine distortions on the single-ion and molecular levels, and compare them to other members of the  $\text{Ba}_3\text{ARu}_2\text{O}_9$  family of known oxidation states. The valences of the two Ru sites are reflected [2] by a linearly varying  $\langle\text{Ru-O}\rangle$  distance (Figure 127b), and the refined values for the  $P2/c$  structure are in agreement with ‘integer’ separation into  $5^+$  and  $6^+$  oxidation states. The inter dimer Ru-Ru distances also vary linearly with oxidation state (Figure 127c). This implies a well defined ‘bond order’ determined by the occupation of molecular orbital states and allows a precise estimate of the charge separation into  $4.86(16)^+$  and  $6.11(16)^+$  states.

Although the  $P2/c$  phase of  $\text{Ba}_3\text{NaRu}_2\text{O}_9$  has large ( $\sim 0.1$  Å) atomic displacements, the charge order is unusually sensitive to external perturbations. We discovered that an X-ray induced melting of charge order is found below  $\sim 40$  K. By cooling the sample to 10 K without the X-ray beam, then continuously measuring diffraction profiles, we found that the  $P2/c$  charge ordered structure transforms continuously to a higher symmetry  $C2/c$  structure in which only one Ru site is present (Figure 128). This phase was found

to be stable for periods of hours at 10 K, and was not observed by neutron powder diffraction.

Our LDA+U calculations, and analysis using an extended Hubbard model, show that it is the combination of local and molecular distortions with long-range Coulomb interactions that stabilise charge order in  $\text{Ba}_3\text{NaRu}_2\text{O}_9$ . The low temperature X-ray induced melting of the charge order is possibly related to frustration of these degrees of freedom on the triangular lattice of dimers. We speculate that other strongly correlated phenomena await discovery in the broader class of hexagonal perovskite materials.

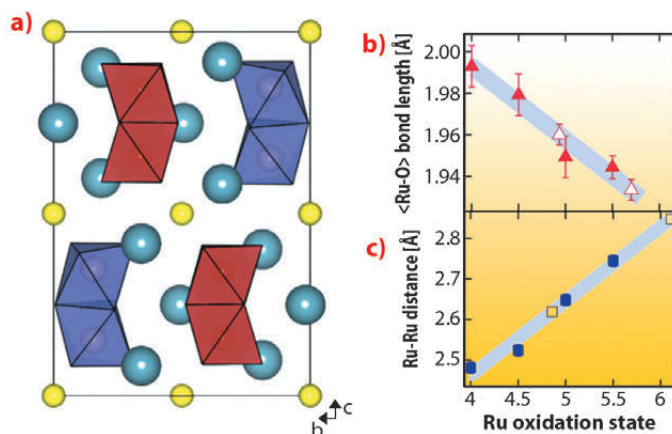


**Fig. 127:** a) Charge ordered  $P2/c$  structure of  $\text{Ba}_3\text{NaRu}_2\text{O}_9$  as determined from synchrotron powder X-ray diffraction projected down  $[100]$ , sodium atoms are yellow spheres, barium atoms are blue. The symmetry inequivalent  $\text{Ru}_2\text{O}_9$  dimers are shown in red ( $5^+$ ) and in purple ( $6^+$ ). b) The average Ru-O bond distance has a linear dependence on oxidation state in the  $\text{Ba}_3\text{ARu}_2\text{O}_9$  family of compounds with  $A = \text{Na}^+, \text{Ca}^{2+}, \text{Nd}^{3+}$  and  $\text{Ce}^{4+}$ , which have similar ionic radii. The formal ruthenium oxidation states are  $5.5^+, 5^+, 4.5^+$  and  $4^+$ , open symbols are from the  $P2/c$  phase. The shaded region shows the standard deviation of the calibration fit. c) A similar linear dependence upon formal oxidation state is found for the Ru-Ru distance. The symbols are as above.

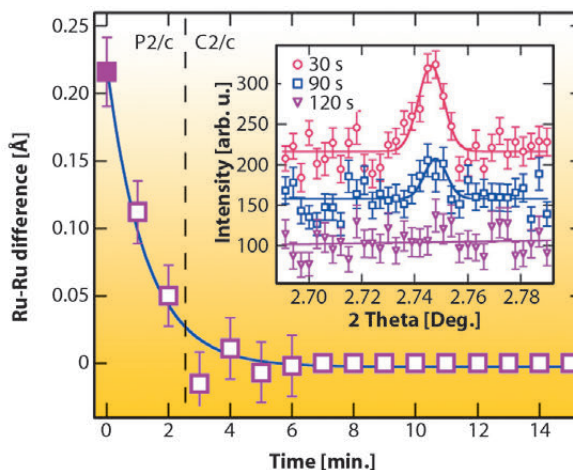


**Fig. 128:** Difference between the refined Ru-Ru distance for the two dimer types in  $\text{Ba}_3\text{NaRu}_2\text{O}_9$  as a function of irradiation time at 10 K. The  $(h+k) = \text{odd}$  superstructure reflections (inset) also disappear, showing that the CO melts.

#### Principal publication and authors

S.A.J. Kimber (a,b), M. Senn (c), S. Fratini (d), H. Wu (e), A.H. Hill (a), P. Manuel (f), J.P. Attfield (c), D.N. Argyriou (a,g) and P.F. Henry (a,g), *Phys. Rev. Lett.* **108**, 217205 (2012).

(a) ESRF

(b) Helmholtz-Zentrum Berlin für Materialien und Energie (Germany)

(c) Centre for Science at Extreme Conditions and School of Chemistry, University of Edinburgh (UK)

(d) Institut Néel-CNRS and Université Joseph Fourier, Grenoble (France)

(e) Laboratory for Computational Physical Sciences, Surface Physics Laboratory and Department of Physics, Fudan University (China)

(f) ISIS Science and Technology Facilities Council, Rutherford Appleton Laboratory (UK)

(g) European Spallation Source ESS AB, Lund (Sweden)

#### References

[1] B.J. Powell and R.H. McKenzie, *J. Phys. Cond. Matt.* **18**, R827 (2006).

[2] K.E. Stitzer et al., *J. Am. Chem. Soc.* **124**, 13877 (2002).



### Principal publication and authors

R.M.P. Colodrero (a), P. Olivera-Pastor (a), E.R. Losilla (a), D. Hernández-Alonso (a), M.A.G. Aranda (a), L. Leon-Reina (b), J. Rius (c), K.D. Demadis (d), B. Moreau (e), D. Villemin (e), M. Palomino (f), F. Rey (f) and A. Cabeza (a), *Inorg. Chem.* **51**, 7689-7698 (2012).  
 (a) Departamento de Química Inorgánica, Universidad de Málaga (Spain)  
 (b) Servicios Centrales de Apoyo a la Investigación, Universidad de Málaga (Spain)  
 (c) Institut de Ciència de Materials de Barcelona, Catalunya (Spain)  
 (d) Crystal Engineering, Growth and Design Laboratory, Department of Chemistry, University of Crete (Greece)  
 (e) Laboratoire de Chimie Moléculaire et Thioorganique, ENSICAEN & Université de Caen (France)  
 (f) Instituto de Tecnología Química (UPV-CSIC), Valencia (Spain)

## High proton conductivity in a flexible, cross-linked, ultramicroporous magnesium tetrakisphosphate hybrid framework

Multifunctional metal phosphonates are thermally and chemically stable hybrid materials (metal-organic frameworks, MOFs) possessing a great diversity of architectures and properties [1]. Their unique structural architectures, framework flexibility and their Brønsted acidity (mainly derived from POH groups), make them attractive materials for proton conductors and sensors, as well as for many other possible applications such as gas storage, catalysis, photochemistry, etc.

We focused our attention on diaminetetrakisphosphonic acids, in particular hexamethylenediamine-*N,N,N',N'*-tetrakis(methylenephosphonic acid),  $H_8$ HDTMP and octamethylenediamine-*N,N,N',N'*-tetrakis(methylenephosphonic acid),  $H_8$ ODTMP, as suitable organic ligands. These tetrakisphosphonic acids are versatile organic linkers which show different coordination modes to the cations, as well as different arrangements of the alkyl chains. These features are evident in new adsorbate-responsive materials [2], and/or 3D-ultramicroporous materials with high proton conductivity [3]. The systematic study of synthesis conditions, using a high-throughput methodology, has permitted the optimum conditions for crystallisation to be determined for a new magnesium hybrid material,

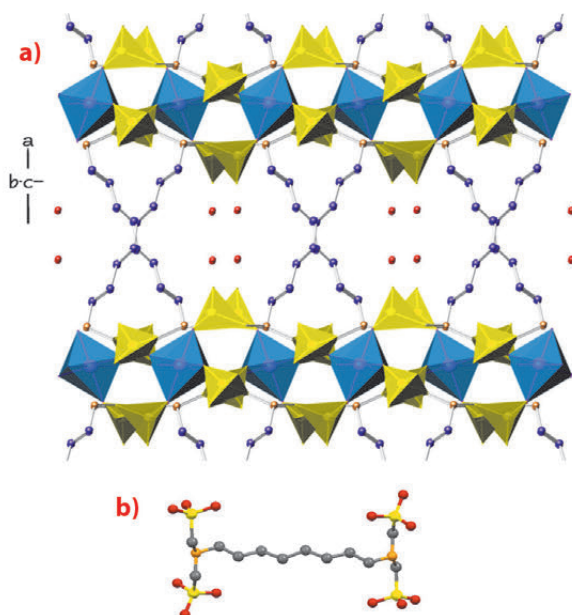
$MgH_6$ ODTMP·2H<sub>2</sub>O(DMF)<sub>0.5</sub> (DMF stands for dimethylformamide). Its crystal structure was solved by the recently-developed Patterson-function direct methods from high-resolution synchrotron powder X-ray diffraction data collected at beamline ID31 [4]. This type of direct method can accurately resolve clusters of overlapped reflections, so that the effective resolution of the extracted intensity data is extended.

$MgH_6$ ODTMP·2H<sub>2</sub>O(DMF)<sub>0.5</sub> shows a novel open-framework 3D pillared structure, see Figure 129. The inorganic layers are built by MgO<sub>6</sub> octahedra and O<sub>3</sub>PC tetrahedra. Neighbouring layers are connected along the *a* axis by the organic groups (CH<sub>2</sub>)<sub>2</sub>-NH-(CH<sub>2</sub>)<sub>8</sub>-NH-(CH<sub>2</sub>)<sub>2</sub> in cross-diagonal fashion. This linkage results in an open-framework, with two types of 1D channel filled by water and remnant DMF molecules.

The aliphatic -(CH<sub>2</sub>)<sub>8</sub>- chain of the ligand provides substantial framework flexibility, with the cavities adapting to the guest molecules (water). Thus, after dehydration (thermal or under vacuum) and rehydration cycles, new crystalline phases can be obtained, with the highest hydrated phase having the composition  $MgH_6$ ODTMP·6H<sub>2</sub>O. X-ray powder diffraction using a laboratory source indicated that a crystalline-quasi-amorphous-crystalline transformation takes place for a complete cycle of dehydration/rehydration, while the integrity of the framework is maintained. Moreover, depending on temperature and water partial pressure, intermediate phases with different hydration states were identified, from the anhydrous phase,  $MgH_6$ ODTMP, to the most hydrated state,  $MgH_6$ ODTMP·6H<sub>2</sub>O. Therefore, the compound is more appropriately formulated as  $MgH_6$ ODTMP·*n*H<sub>2</sub>O, with 0 ≤ *n* ≤ 6.

The gas adsorption/separation features of the anhydrous phase correspond to an ultramicroporous material with a maximum CO<sub>2</sub> uptake of 1.2 mmol/g, at 900 kPa and a relatively high selectivity

**Fig. 129:** a) View of the 3D pillared open-framework ( $MgO_6$  octahedra blue;  $CO_3$  tetrahedra yellow; C cyan; O red; N orange). b) Schematic representation of the tetrakisphosphate ligand,  $H_8$ ODTMP.

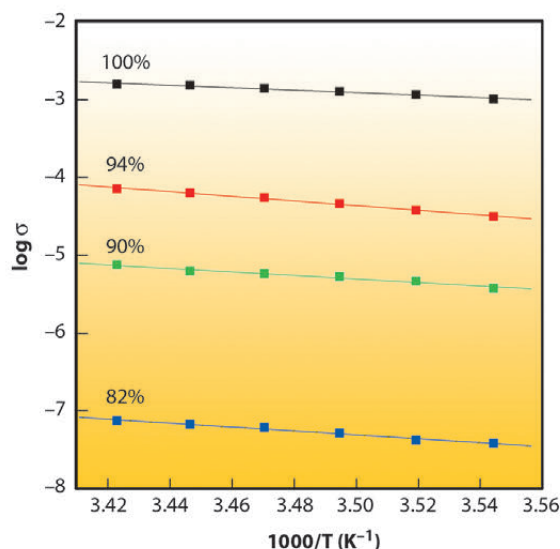




towards CO<sub>2</sub> adsorption in CO<sub>2</sub>/CH<sub>4</sub> mixtures. This separation ability could be useful for natural gas upgrading.

On the basis of these structural features, a preliminary study to characterise the proton conductivity features of the magnesium tetrakisphosphate hybrid material has been carried out. A small temperature range (282–292 K) was selected to ensure constant water content at a given water partial pressure. High proton conductivity, up to a maximum value of  $\sigma = 1.6 \cdot 10^{-3} \text{ S}\cdot\text{cm}^{-1}$  ( $T = 292 \text{ K}$ ), was observed for the fully-hydrated phase, *i.e.* MgH<sub>6</sub>ODTMP·6H<sub>2</sub>O, at a relative humidity of ~ 99%. The relatively low activation energy values, between 0.1 – 0.5 eV, are consistent with a Grotthuss transfer mechanism, *via* water molecules (Figure 130). It must be underlined, however, that small changes in water partial pressure (from ~ 1.8 to ~ 2.2 kPa) modify the proton conductivity by up to four

orders of magnitude very likely due to a change in the water content of the solid. Other hybrid materials based on tetrakisphosphate ligands, with different topologies and structural features, are currently being investigated in order to establish structure-property correlations.



#### References

- [1] *Metal phosphonate chemistry: From synthesis to applications*, A. Clearfield, K.D. Demadis, Eds. The Royal Society of Chemistry: London (2012).
- [2] R.M.P. Colodrero, A. Cabeza, P. Olivera-Pastor, A. Infantes-Molina, E. Barouda, K.D. Demadis and M.A.G. Aranda, *Chem. Eur. J.* **15**, 6612-6618 (2009).
- [3] R.M.P. Colodrero, P. Olivera-Pastor, E.R. Losilla, M.A.G. Aranda, L. León-Reina, M. Papadaki, A.C. McKinlay, R.E. Morris, K.D. Demadis and A. Cabeza, *Dalton Trans.* **41**, 4045-4051 (2012).
- [4] J. Rius, *Acta Cryst* **A67**, 63-67 (2011).

Fig. 130: Arrhenius plots of  $\log \sigma_T$  for MgH<sub>6</sub>ODTMP·6H<sub>2</sub>O at four different levels of relative humidity.

## ■ Physisorption vs. chemisorption: adsorption of copper-phthalocyanine on noble metal surfaces

The growth of large  $\pi$ -conjugated molecules on noble metal surfaces has recently attracted much interest in the surface science community. Most studies concentrate on metal-organic interfaces and their geometric and electronic properties since they strongly influence the electronic transport in electronic devices. A very delicate parameter is the interaction strength between the molecules and the substrate because this determines the charge exchange at the metal-organic interface. The normal incidence X-ray standing wave (NIXSW) technique, which could be performed at beamline ID32 until recently, allows the adsorption strength to be quantified by measuring the adsorption height of individual atomic species with an otherwise unreachable precision of < 0.05 Å.

Using low-energy electron diffraction (LEED), ultraviolet photoelectron spectroscopy (UPS), and NIXSW, we have investigated the adsorption of copper-

phthalocyanine (CuPc) for different coverages on three substrates: Au(111), Ag(111) and Cu(111) [1-3]. At very low coverages, disordered layers were found in all cases. On increasing coverage or cooling to low temperature (LN<sub>2</sub>), the disordered layers transform to long-range ordered films. On Au(111) these ordered structures show merely point-on-line registry with the substrate (or are even incommensurate) [1]. UPS data indicate that no charge transfer across the metal-organic interface takes place. On Cu(111) the behaviour is very different [1]. Already above 0.76 monolayers (ML) the molecules are arranged in a commensurate superstructure with one molecule per unit cell, which indicates a favourable adsorption site for the molecules. In UPS a spectral feature just below the Fermi energy is visible and proves charge transfer from the Cu(111) electronic states into the lowest unoccupied molecular orbital (LUMO). CuPc on Ag(111) [2] represents an intermediate case: It forms both point-

#### Principle publication and authors

- I. Kröger (a), B. Stadtmüller (a), C. Kleimann (a), P. Rajput (b) and C. Kumpf (a), *Phys. Rev. B* **83**, 195414 (2011).  
(a) Peter Grünberg Institut (PGI-3), Forschungszentrum Jülich, and Jülich-Aachen Research Alliance (JARA) – Fundamentals of Future Information Technology (Germany)  
(b) ESRF

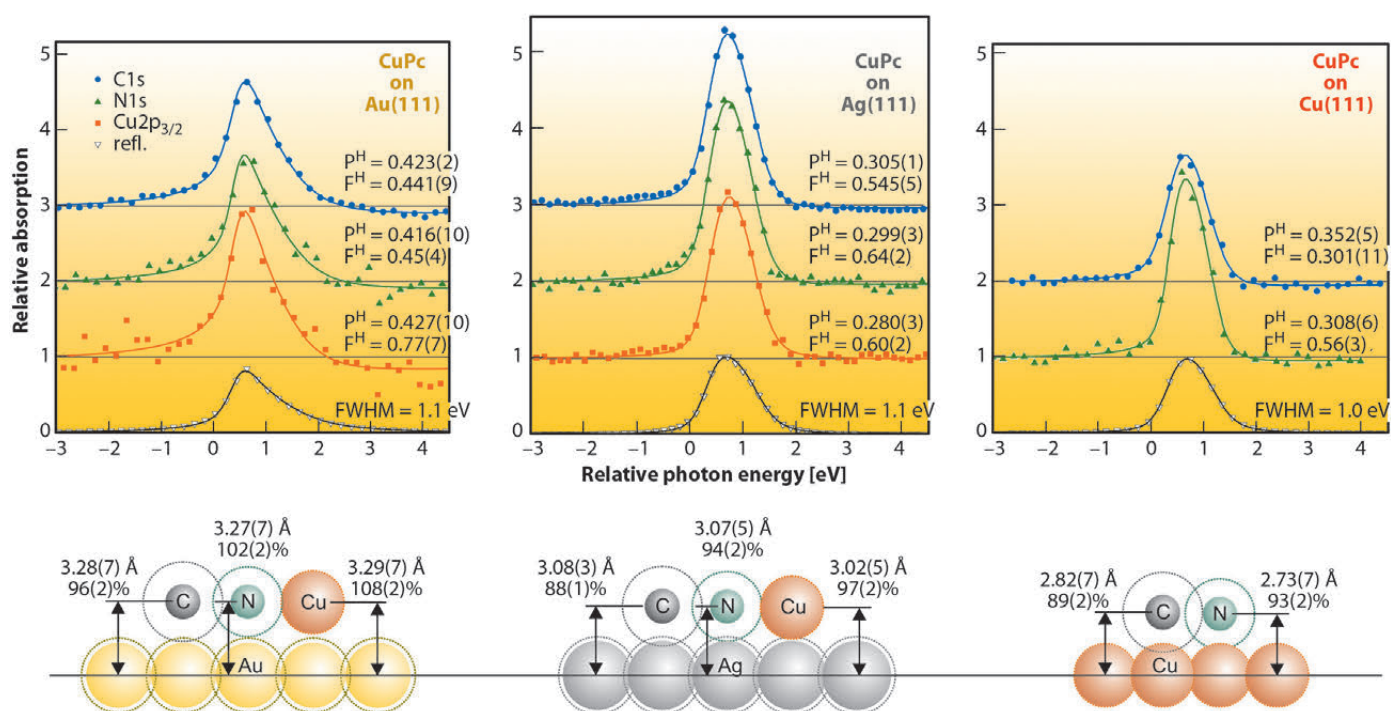


**Fig. 131:** XSW data (symbols) and fit results (lines) for a closed layer of CuPc on Au(111), Ag(111) and Cu(111) at LN<sub>2</sub> temperature. Schematics show the size of all species on scale. Ball diameters represent covalent bonding radii, larger dashed circles correspond to van der Waals radii. Measured bonding distances are given in angstrom and in % of the corresponding van der Waals bonding distances. The height of Cu on Cu(111) could not be obtained due to the bulk-dominated PE signal.

on-line (at coverages > 0.89 ML) and commensurate superstructures (at low temperature between 0.75 and 0.89 ML), and UPS revealed a half filled LUMO located directly at the Fermi-level. Our XSW study on these three systems aimed at linking these findings with the vertical geometric structure of the interfaces.

In **Figure 131** NIXSW data and some on-scale schematics of the adsorption heights are shown for all three systems. In an NIXSW scan the photon energy is scanned through a Bragg reflection while the reflected X-ray intensity (grey triangles) and the partial photoelectron yields of all atomic species (coloured symbols) are recorded. Fitting the yield curves results in structural parameters P<sup>H</sup> (coherent position) and F<sup>H</sup> (coherent fraction). The first corresponds to the mean adsorption height; the latter reflects the quality of vertical order (F<sup>H</sup> = 0 corresponds to complete disorder, F<sup>H</sup> = 1.0 to perfect order).

The differences in the adsorption heights for the three systems ( $\approx 3.3$  Å,  $\approx 3.05$  Å and  $\approx 2.8$  Å for CuPc/Au(111), Ag(111) and Cu(111), respectively) clearly indicate an increasing interaction strength for this row. However, when comparing these absolute numbers, one neglects the differences in the size of the individual atomic species. Since Cu is significantly smaller than Au and Ag, one should rather consider bonding distances normalised

by van der Waals radii. These “relative bonding distances” indicate physisorption of the molecules on Au(111) (values around 100%), but chemisorption on Ag(111) and Cu(111) (88–94% for C and N). The schematics in **Figure 131** illustrate the situation: Van der Waals radii of all species (dotted circles) overlap in the case of CuPc on Cu(111) or Ag(111), but not on Au(111).

These findings are in excellent agreement with UPS results. Chemisorptive interaction for CuPc on Ag(111) and Cu(111) and physisorption for CuPc on Au(111) are both compatible with the charge transfer found in electron spectroscopy. It also explains the differences in the lateral structure formation for the adsorbate layers: In the case of a strong molecule-substrate interaction (chemisorption), the substrate dictates the structure formation in the organic layer and enforces a commensurate registry. In the case of weaker, physisorptive interaction, the overlayer structure is dominated by the intermolecular interaction and hardly influenced by the substrate [3]. Point-on-line or incommensurate structures are the consequence. In summary, we could reveal this delicate interplay of (vertical) molecule-substrate and (horizontal) intermolecular interactions and identify the driving force for the lateral structure formation.

#### References

- [1] B. Stadtmüller, I. Kröger, F. Reinert and C. Kumpf, *Phys. Rev. B* **83**, 085416 (2011).
- [2] I. Kröger, B. Stadtmüller, C. Stadler, J. Ziroff, M. Kochler, A. Stahl, F. Pollinger, T.L. Lee, J. Zegenhagen, F. Reinert and C. Kumpf, *New. J. Phys.* **12**, 083038 (2010).
- [3] I. Kröger, B. Stadtmüller, C. Wagner, C. Weiss, R. Temirov, F.S. Tautz and C. Kumpf, *J. Chem. Phys.* **135**, 234703 (2011).

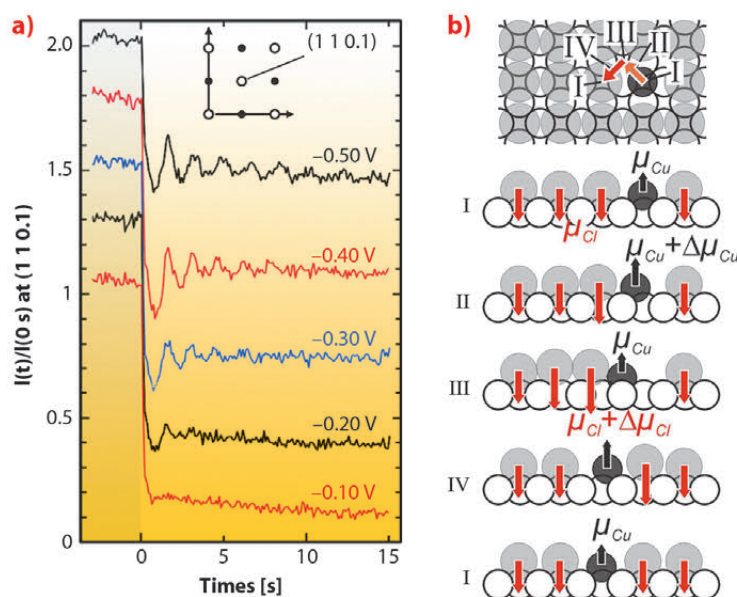
## Smooth plating: Surface diffraction studies detect anomalous growth of copper

Copper galvanic plating is a widely used industrial process with numerous applications. Because of the nanoscale dimensions of current copper interconnects, precise control of the electrochemical deposition processes, and hence an improved fundamental understanding of the underlying elementary steps, is required. In contrast to Cu homoepitaxy under UHV conditions, fundamental understanding of the electrodeposition of Cu is largely lacking. Specifically, the precise influence of the solid-liquid interface structure and the applied electrode potential on the elementary surface processes involved in electrodeposition is unclear.

The presence of small amounts of chloride in the acidic plating bath is known to be vital to obtain optimal growth behaviour and deposition properties in almost any industrial plating process. However, how this simple inorganic species influences the Cu growth on the atomic scale is surprisingly still unresolved. To obtain deeper insight into these processes, homoepitaxial electrochemical growth of Cu(001) in a chloride-containing acidic solution was studied *in operando* by surface X-ray diffraction at beamline ID32 ( $E_\gamma = 22.5$  keV).

The experiments were performed using an electrochemical three-electrode cell (“hanging meniscus” cell), where the electrode is contacted by a droplet of the electrolyte. The high-speed surface scattering setup allowed the Cu growth to be studied at rates of several monolayers per second by recording the time-dependent intensity of the crystal truncation rod close to the anti-Bragg position. The Cu-sample potential was first kept at  $-0.6$  V<sub>Ag/AgCl</sub>, where the high Cu deposition rate and very high surface mobility result in a rapid smoothing even of rough surfaces. Then the potential was gradually increased. Analogous to MBE growth studies, different kinetic growth modes result in characteristic intensity transients at various constant deposition rates (Figure 132a). Characteristic intensity oscillations indicate layer-by-layer growth in an intermediate potential regime, whereas crossover to 3D growth is observed at the most positive potentials.

Thus, the Cu surface mobility is reduced at positive electrode potential. This is in stark contrast to the potential dependence commonly found for metal self-diffusion on electrode surfaces. Usually, higher mobility is found at more positive potentials as demonstrated by our previous results on the homoepitaxial electrodeposition on Au(001) in Cl-containing electrolyte [1] and is also predicted by the current theory of surface transport at electrochemical interfaces [2]. It is explained by an electrostatic energy contribution, resulting from the interaction of the metal adatom’s dipole moment with the strong electric field of the electrochemical double layer.



### Principal publications and authors

F. Golks (a,b), J. Stettner (a),  
Y. Gründer (a), K. Krug (a),  
J. Zegenhagen (b) and  
O.M. Magnussen (a), *Phys. Rev. Lett.* **108**, 256101-1-256101-5 (2012).

(a) Institut für Experimentelle und Angewandte Physik, Universität Kiel (Germany)

(b) ESRF

The surprising, anomalous behaviour of Cu(001) can be explained by including the presence of the co-adsorbed  $c(2 \times 2)$  chloride adlayer into this theory. Apparently, it strongly modifies and actually inverts the effective change in the dipole moment during the metal adatom hopping. As schematically illustrated in Figure 132b, the metal adatoms have to move through this rather close-packed adlayer, displacing neighbouring Cl from their preferred fourfold-hollow adsorption sites. The resulting additional dipole contribution of those rather anionic species is opposite in sign to that of the metal adatom itself and can dominate the potential-dependent term of the

**Fig. 132:** a) Scattered intensity  $I(t)$  at  $(1\ 1\ 0.1)$  during Cu electrodeposition from  $0.1$  M  $\text{HClO}_4 + 1$  mM  $\text{HCl} + 5$  mM  $\text{Cu}(\text{ClO}_4)_2$  on  $\text{Cu}(001)$  at different potentials. b) Illustration of Cu adatom diffusion on  $\text{Cu}(001) / c(2 \times 2)$  Cl, arrows in I to IV indicate surface dipole moments of Cu ( $\mu_{Cu}$ ) and Cl ( $\mu_{Cl}$ ) adsorbates.



surface diffusion barrier. In other words, Cu atoms moving across the surface have to push through the Cl layer and become more mobile at more negative electrode potentials, where the chloride is more weakly bound. On Au(001) this coadsorbate contribution is smaller, probably due to differences in the adlayer structure and charge state of the Cl adsorbates.

ubiquitously present in technological electrodeposition processes. Knowledge on whether the electrode surface transport is normal or anomalous will allow an assessment of whether a lower roughness of the deposit may be expected at low or at high deposition overpotentials, respectively. The novel concept of an effective diffusion dipole moment provides a simple conceptual framework that allows microscopic physical growth theories to be extended to liquid phase deposition processes. Since these dipole moments can be obtained by *ab initio* calculations, our results open the way for predicting and quantifying the growth behaviour in these complex systems.

#### References

[1] K. Krug, J. Stettner and O.M. Magnussen, *Phys. Rev. Lett.* **96**, 246101 (2006).

[2] M. Giesen *et al.*, *Surf. Sci.* **595**, 127 (2005).

Our findings not only aid substantially the fundamental understanding of growth and surface transport in electrochemical environments, but also have significant practical implications. Strongly chemisorbing anions such as halides are

#### Principal publication and authors

G. Bellussi (a), E. Montanari (a), E. Di Paola (a), R. Millini (a), A. Carati (a), C. Rizzo (a), W. O. Parker Jr. (a), M. Gemmi (b), E. Mugnaioli (c), U. Kolb (c) and S. Zanardi (a), *Angew. Chem. Int. Ed.* **51**, 666-669 (2012).

(a) *eni s.p.a. – Refining & Marketing Division (Italy)*

(b) *Center for nanotechnology innovation@NEST Istituto Italiano di Tecnologia (Italy)*

(c) *Institut für Physikalische Chemie, Johannes Gutenberg-Universität Mainz (Germany)*

## ■ Towards hybrid organic-inorganic aluminosilicate zeolites

In recent years, X-ray powder diffraction has become a powerful tool for crystal structure determination. Significant advances over the last 10 years were made with the advent of new methods and algorithms, along with the availability of third generation synchrotron radiation sources. Nowadays, *ab initio* structure solution by powder diffraction data is almost a routine procedure. However, in the case of very complex structures and multiphase samples, it remains a

challenging task. In order to overcome this problem, an approach based on the combined use of high-resolution X-ray powder diffraction and precession electron diffraction has been developed. Though very powerful, this approach cannot be applied to beam-sensitive samples. Therefore, a new technique called automated diffraction tomography (ADT) has recently been developed for the acquisition of electron diffraction data from submicrometric beam-

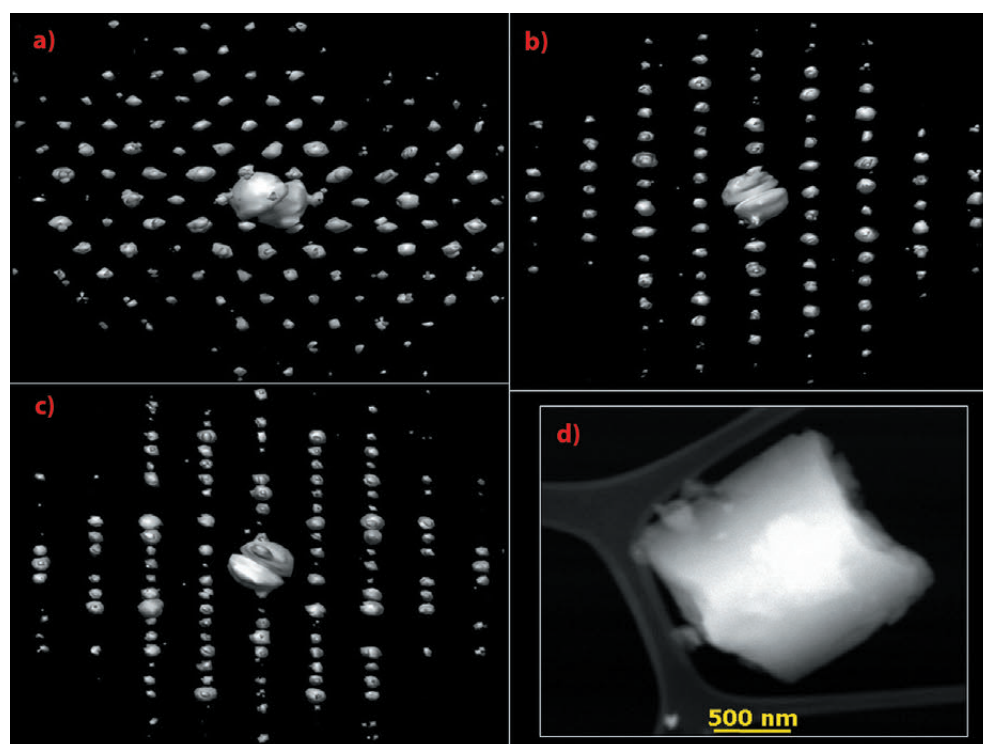


**Fig. 133:** a), b), and c) three-dimensional ADT diffraction volume reconstruction. d) ECS-3 crystallite used for the ADT data collection.



sensitive crystals. Because of the very low electron dose striking the sample, ADT allows complete electron diffraction data collection, even on beam-sensitive materials.

ECS-3 is an interesting material belonging to the new family of crystalline hybrid organic-inorganic aluminosilicate referred to as eni carbon silicates. ECS-3 attracted our attention because of the  $N_2$  adsorption/desorption Type I isotherm, typical of microporous materials (specific surface area =  $296 \text{ m}^2 \text{ g}^{-1}$ , specific pore volume =  $0.13 \text{ cm}^3 \text{ g}^{-1}$ ). Unfortunately, the X-ray powder diffraction pattern of ECS-3, collected at the high-resolution beamline **BM01** ( $0.80175(2) \text{ \AA}$ ), showed extremely high complexity that prevented a correct unit cell determination.

ECS-3 was then submitted to ADT data collection (Figure 133). Through symmetry information obtained by electron diffraction, the correct unit cell parameter as well as a possible space-group symmetry were derived. The search for the unit cell converged to a monoclinic symmetry with parameters:  $a = 19.7$ ,  $b = 27.7$ ,  $c = 9.5 \text{ \AA}$ ,  $\beta = 102.7^\circ$  and possible space-groups  $C2/c$  or  $Cc$ . Using the ADT data and the non centrosymmetric space group, a preliminary structural model for the ECS-3 scaffolding was achieved by direct methods and completed by model building. The ECS-3 scaffolding involves 62 crystallographically-independent non-hydrogen atoms in the asymmetric unit, making it intriguing as the most complex zeolite structures.

The ECS-3 scaffolding structure can be described by the stacking of aluminosilicate layers held together by phenylene groups (Figure 134). This structural model confirms that ECS-3 is a microporous organic-inorganic aluminosilicate. Its microporosity results from the union of the organic and inorganic parts of the structure which produces a sinusoidal channel. In addition, large lateral side pockets shaped by the phenylene rings alternating on both sides of the sinusoidal channel are also present.

However, the low resolution of electron diffraction data collected on ECS-3 did not allow the completion and the refinement of the structural model. In fact,

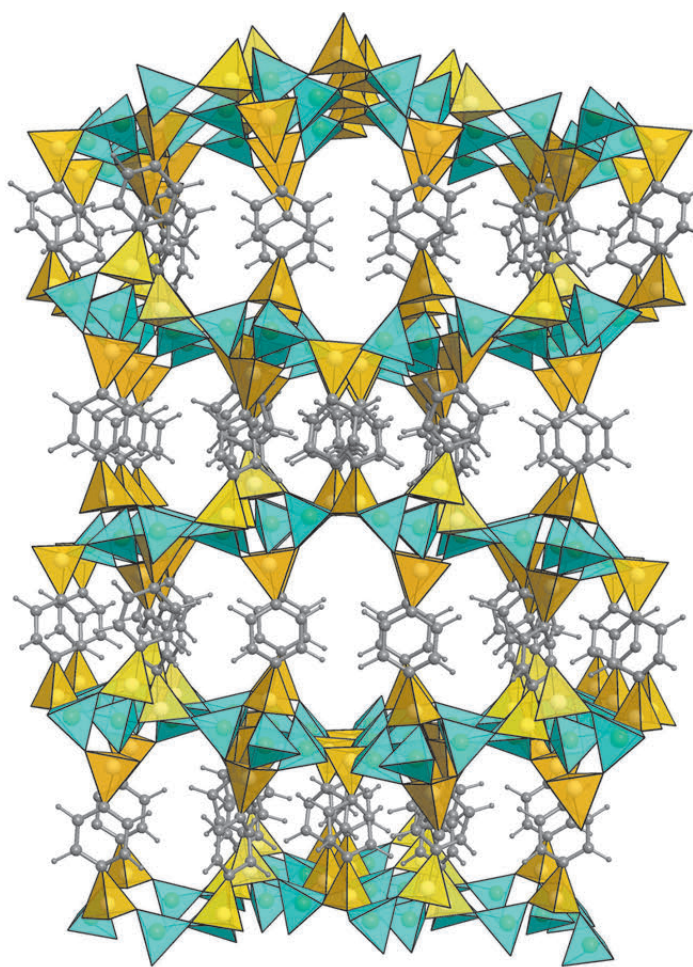


**Fig. 134:** Representation of the ECS-3 scaffolding.  $AlO_4$  tetrahedra are in light blue whereas  $SiO_3C$  are yellow. Extra-framework cations and water molecules are not shown.

the extra-framework cations (sodium and potassium), necessary to counterbalance the framework charge imposed by aluminium, were still missing. The ADT model was then used as a trial structure for the Rietveld refinement of high resolution X-ray powder diffraction data. During the Rietveld refinement, 12 extra-framework positions were localised by Fourier maps (4 were attributed to cations) and it converged to rather good discrepancy factors, confirming the correctness of the initial structural model.

In conclusion, the fruitful synergy of ADT and high-resolution X-ray powder diffraction data allowed determination of the ECS-3 structure, which is one of the most complex structures solved so far using electron diffraction data. However, the low resolution ADT data did not permit structural validation (*i.e.* refinement). High-resolution X-ray powder diffraction data were of paramount importance for demonstrating that it is possible to synthesise a crystalline hydride organic-inorganic aluminosilicate with open porosity.



#### Principal publication and authors

C. Kirchlechner (a,b), C. Motz (b), P.J. Imrich (a), W. Liegl (b), J. Keckes (b), O. Thomas (c), S. Labat (c), J.S. Micha (d,e), O. Ulrich (d,e) and G. Dehm (a,b), *Acta Materialia* **60**, 1252–1258 (2012).

(a) Department of Materials Physics, Montanuniversität Leoben (Austria)

(b) Erich Schmid Institute of Materials Science, Austrian Academy of Sciences (Austria)

(c) Aix-Marseille Université, CNRS, IM2NP UMR 7334 (France)

(d) CEA-Grenoble/Institut Nanosciences et Cryogénie (France)

(e) CRG-IF BM32 at ESRF (France)

**Fig. 135:** SEM image of a micrometre sized single crystalline copper pillar deformed at BM32 with slip steps only on one {111} crystallographic plane.

## An alternative pathway for understanding plasticity at the micrometre scale

The flow stress of a material, being the stress where a permanent change in sample shape occurs, inherently depends on the chemical composition and the microstructure of the material, including also the density and type of lattice defects. From a classical point of view, the flow stress should not depend on the geometrical sample dimensions. This assumption, believed valid for centuries and used as a fundamental basis of design in mechanical engineering, was proven to be incorrect less than a decade ago. Uchic and co-workers [1] have reported on the tremendous increase of the flow stress when sample sizes are reduced and reach micrometre or even submicrometre dimensions. This size effect is not only interesting from a scientific point of view, but also a challenge for future developments. The ongoing trend in miniaturisation – for instance in microelectronics – requires a thorough understanding of the material properties at this length scale.



The reason for the unexpected increase in flow stress is, however, not fully understood. Advanced techniques in materials science, like *in situ* scanning electron microscopy (SEM, see **Figure 135**) or transmission electron microscopy (TEM) have been applied to small scale samples

but have not completely shed light on the fundamental mechanisms increasing the strength. Thus, alternative pathways like *in situ*  $\mu$ Laue diffraction are needed and have been applied successfully at beamline **BM32** (CRG-IF).

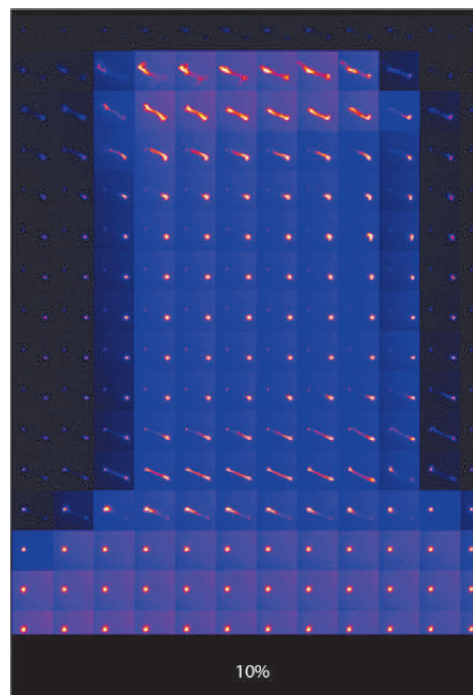


**Fig. 136:** Corresponding map of the (111) Laue spot across the entire sample. In the sample base (bottom) and in the sample centre the Laue spot appears circular (no excess dislocations), whereas at the top and the end of the gauge section the spot is streaked, indicating the storage of excess dislocations on the primary slip system.

Compression, bending, and tensile samples ranging from 3 to 10  $\mu$ m in diameter were produced from macroscopic single crystalline copper using focused ion beam milling (FIB). Subsequently, the samples were loaded in displacement controlled mode with a force resolution of typically 10  $\mu$ N. During loading, a 1  $\mu$ m sized polychromatic X-ray beam was focussed on the sample allowing for an *in situ* characterisation of microstructural changes like crystal rotations, formation of deviatoric strains and dislocation structures. The site specific investigations of the dislocation densities were used to link the defect structure to the mechanical response of the material. Furthermore, raster scanning as presented in **Figure 136** leads to a global image

#### References

- [1] M.D. Uchic, D.M. Dimiduk, J.N. Florando and W.D. Nix, *Science* **305**, 986 (2004).
- [2] C. Kirchlechner, J. Keckes, C. Motz, W. Grosinger, M.W. Kapp, J.S. Micha, O. Ulrich and G. Dehm, *Acta Materialia* **59**, 5618 (2011).
- [3] C. Kirchlechner, P.J. Imrich, W. Grosinger, M.W. Kapp, J. Keckes, J.S. Micha, O. Ulrich, O. Thomas, S. Labat, C. Motz and G. Dehm, *Acta Materialia* **60**, 1252 (2012).
- [4] C. Kirchlechner, W. Grosinger, M.W. Kapp, P.J. Imrich, J.S. Micha, O. Ulrich, J. Keckes, G. Dehm and C. Motz, *Philosophical Magazine* **92**, 3231 (2012).

of dislocation storage across the entire sample. In regions with a high density of excess dislocations the diffraction spot is elongated (*i.e.* “streaked”), whereas in regions with low excess dislocation content the peak appears circular.

In the underlying studies, we demonstrated the severe impact of sample misalignments

on the storage of excess dislocations in micrometre sized compression pillars [2], the critical influence of the initial dislocation source size statistics onto the deformation behaviour at the micrometre scale during tensile testing [3] and, finally, the reversibility of dislocation movement in bending beams due to internal stress fields [4].

## ■ A surface science approach in aqueous phase used to rationalise the preparation of heterogeneous catalysts

The rational design of heterogeneous catalysts involves the implementation of model approaches, “surface science” being the best known. This approach aims to model a complex industrial catalyst using simple chemical systems most often presented in the form of plane monocrystalline supports capable of reproducing, at least in part, the physicochemical behaviour of a metal particle or a pulverulent metal oxide with a large specific surface area.

This study focused on catalysts using Ni on alumina ( $\text{Ni}/\text{Al}_2\text{O}_3$ ), which can be found in many applications such as steam reforming (hydrogen production from hydrocarbons), hydrogenation and hydrotreating (removal of S, N, O and metals from petroleum fractions). To model the industrial  $\gamma$ -alumina oxide support (poorly crystalline and exhibiting many different crystallographic faces) we decided to use single crystal wafers of  $\alpha$ -alumina in different crystallographic orientations to model the different surface groups (hydroxyl) of the industrial support.

The originality of this study lies in how the catalyst was synthesised. This was carried out in the aqueous phase (as done industrially) and the characterisation was carried out under ambient conditions. This is in contrast to more traditional surface science approaches, where the model catalyst is synthesised under ultra-high vacuum, industrially far less realistic.

The use of oriented single crystals required a characterisation technique

capable of providing molecular information for very low concentrations of active phase (Ni(II) in this case) deposited on the oxide surface. Grazing incidence EXAFS spectroscopy (grazing-incidence XAS or GI-XAS) turned out to be an ideal technique for such a study. This technique has been implemented on several complementary beamlines during this study: **BM30B** (FAME) and **BM08** (GILDA) at the ESRF and DIFFABS and SAMBA at SOLEIL.

The use of oriented monocrystals coupled with the polarisation of the synchrotron beam yielded new information about the orientation of the supported active phase and showed that the crystalline orientation of the oxide support strongly governed speciation (chemical distribution) of the active phase. When Ni(II) was adsorbed in the aqueous phase, Ni K-edge EXAFS revealed an oriented precipitation of nickel hydroxide ( $\text{Ni}(\text{OH})_2$ ) on the ( $1\bar{1}02$ ) surface of  $\alpha$ -alumina. For example, **Figure 137** shows the effect of polarisation

### Principal publication and authors

A. Tougeri (a), I. Llorens (b,e), F. D’Acapito (c), E. Fonda (d), J.-L. Hazemann (e,f), Y. Joly (f), D. Thiaudière (d), M. Che (a) and X. Carrier (a), *Angewandte Chemie, International Edition* **51**, 7697-7701 (2012).

(a) UPMC-Université Pierre et Marie Curie, Laboratoire de Réactivité de Surface, Paris (France)

(b) CEA/DSM/INAC/CNRS, Grenoble (France)

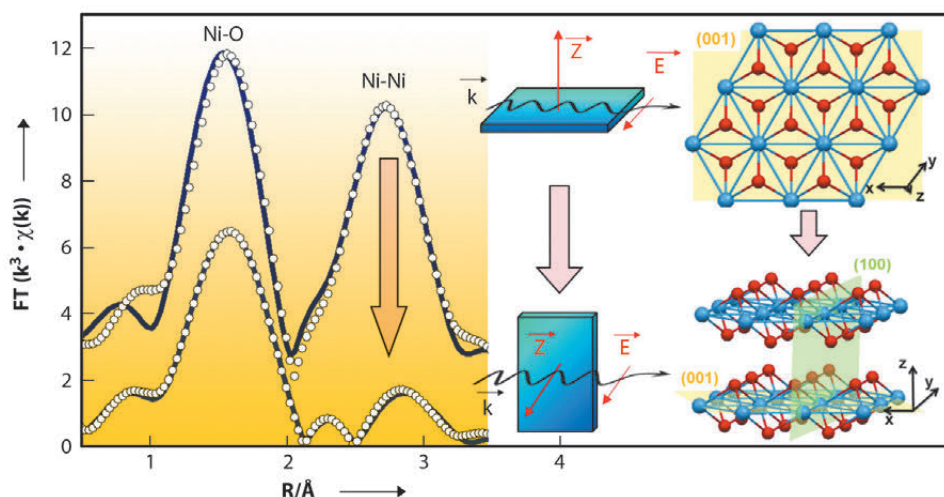
(c) ESRF-GILDA, Grenoble (France)

(d) Synchrotron Soleil, Gif-sur-Yvette (France)

(e) ESRF-FAME, Grenoble (France)

(f) Institut Néel, CNRS-Université J. Fourier Grenoble (France)

**Fig. 137:** Fourier transforms of the Ni K-edge EXAFS signal ( $k^3$ -weighted) for parallel and perpendicular polarisation of the sample obtained by depositing Ni(II) on the ( $1\bar{1}02$ ) surface of  $\alpha$ -alumina. The solid blue line shows the experimental spectrum and the circle, refinement of the signal. The structure of the nickel hydroxide ( $\text{Ni}(\text{OH})_2$ ) is shown on the right as seen from the top or on the side with respect to the (001) basal plane.





on the second peak in the Fourier transform of the EXAFS signal (Ni-Ni distances): this peak is very pronounced for a single crystal orientation parallel to the electric field vector,  $\vec{E}$ , whereas the intensity of the same Ni-Ni peak decreases sharply when the sample is oriented perpendicular to the electric field vector  $\vec{E}$ . In contrast, for the (0001) surface of  $\alpha$ -alumina, no Ni deposit was observed, which shows the importance of the type of surface group exposed by the oxide for controlling the adsorption of the active phase.

These results demonstrate at the molecular level that the oxide support does not merely act as a physical container of the active phase and that the nature of specific surface sites plays a key role in the formation and orientation of the

nickel hydroxide precipitate. The fact that  $\text{Ni}(\text{OH})_2$  precipitated only on the (1102) face can be explained by the minimisation of surface energy between the alumina and the nickel hydroxide.

The use of a model system shows that the Ni dispersion on individual oxide particles is highly heterogeneous for an industrial catalyst as it will depend on the type of face exposed and therefore on the morphology of the oxide support. These findings also highlight the fact that each face of the alumina has a specific reactivity depending on which OH groups are exposed. Controlling the morphology of  $\gamma$ -alumina is therefore a key factor at the industrial scale in order to be able to control the deposition and dispersion of the active phase.

#### Principal publication and authors

E. Verheyen (a), L. Joos (b), K. Van Havenbergh (c), E. Breynaert (a), N. Kasian (a,d), E. Gobechiya (a), K. Houthoofd (a), C. Martineau (e), M. Hinterstein (f), F. Taulelle (e), V. Van Speybroeck (b), M. Waroquier (b), S. Bals (c), G. Van Tendeloo (c), C.E.A. Kirschhock (a) and J.A. Martens (a), *Nat. Mater.* **11**, 1059–1064 (2012).

(a) Center for Surface Chemistry and Catalysis, KU Leuven (Belgium)

(b) Center for Molecular Modeling, Ghent University (Belgium)

(c) Electron Microscopy for Materials Science, University of Antwerp (Belgium)

(d) L.V. Pisarzhevsky Institute of Physical Chemistry, National Academy of Sciences of Ukraine, Kyiv (Ukraine)

(e) Tectospin, Institut Lavoisier, UMR 8180 Université de Versailles (France)

(f) Institut für Werkstoffwissenschaft, Technische Universität Dresden (Germany)

## ■ Design of zeolite by inverse sigma transformation: Cut and paste zeolites

Zeolites are crystalline microporous aluminosilicates which consist of corner-sharing  $\text{TO}_4$  tetrahedra. They are workhorses in industry for adsorption, separation and catalysis. Heteroelements are often inserted to enhance desired properties such as catalytic activity and selectivity. The introduction of germanium however results in stability problems.

Germanosilicate IM-12 zeolite (UTL topology) consists of dense silicate layers connected by double-four rings (D4Rs), the preferential location of germanium (**Figure 138**). The systematic instability of the UTL zeolite can be used to harvest building units that can be rearranged to transform UTL zeolite into a new and stable zeolite. Acid leaching removes the germanium from the UTL framework while preserving the dense silicate layers and reconnects these layers to form new zeolite topologies –COK-14 or COK-14. –COK-14 is a new all-silica interrupted framework topology with a two-dimensional channel system and interconnecting 8-, 10- and 12-membered rings (**Figure 138**). Upon drying in the absence of water, silanol condensation takes place and COK-14 is formed (**Figure 138**). The transformation from UTL zeolite to COK-14 involves the systematic removal of one layer of T-atoms and as

such is the first experimentally observed inverse sigma transformation.

To verify if a true inverse sigma transformation occurred, an intermediate state was captured named Ge-COK-14. This sample was synthesised by reducing transformation time.  $^{29}\text{Si}$ -NMR and  $^1\text{H}$ -NMR indicated this sample contained  $\text{Q}^3$  silicon environments, associated with silanol groups, while still having Si-O-Ge bonds. Approximately 50 wt% of the original germanium content was still present in Ge-COK-14. High-resolution powder X-ray diffraction data and X-ray absorption spectra for Ge-COK-14 were collected at room temperature at beamline BM01B (the Swiss Norwegian Beamline SNBL) in collaboration with beamline BM26 (DUBBLE) (**Figure 139**). Indexing of the powder pattern of Ge-COK-14 resulted in a unit cell of  $a = 24.43 \text{ \AA}$ ,  $b = 13.90 \text{ \AA}$ ,  $c = 12.28 \text{ \AA}$  and a monoclinic angle of  $108.97^\circ$  compared to  $a = 24.64 \text{ \AA}$ ,  $b = 13.92 \text{ \AA}$ ,  $c = 12.26 \text{ \AA}$  and  $\beta = 109.20^\circ$  for –COK-14 and  $a = 29.00 \text{ \AA}$ ,  $b = 13.98 \text{ \AA}$ ,  $c = 12.45 \text{ \AA}$  and  $\beta = 104.91^\circ$  for the parent UTL zeolite. This indicated that Ge-COK-14 already had the interlayer spacing of –COK-14 but still contained germanium. Ge K-edge EXAFS spectra revealed the local environment

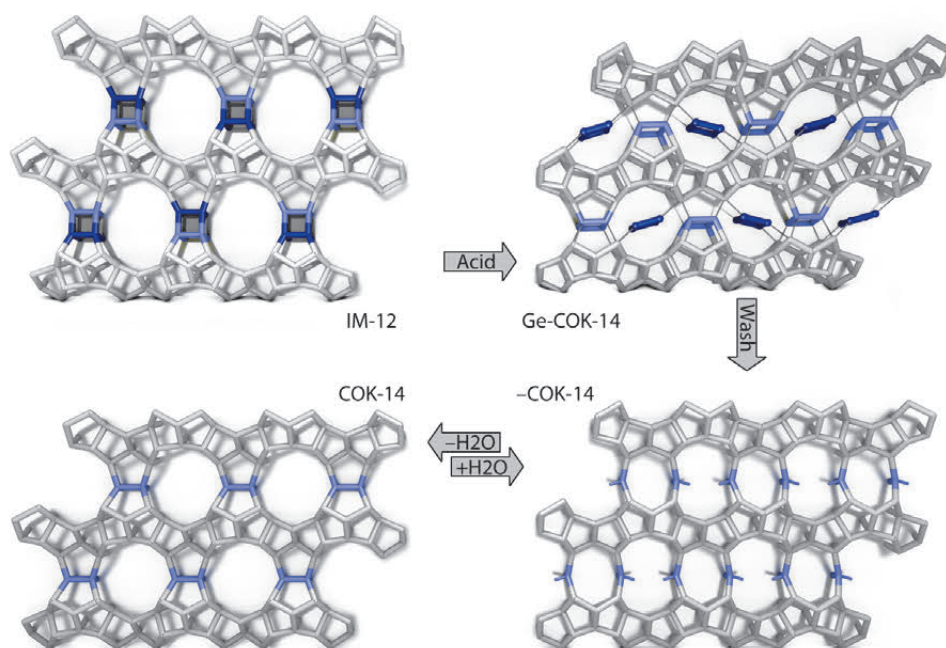


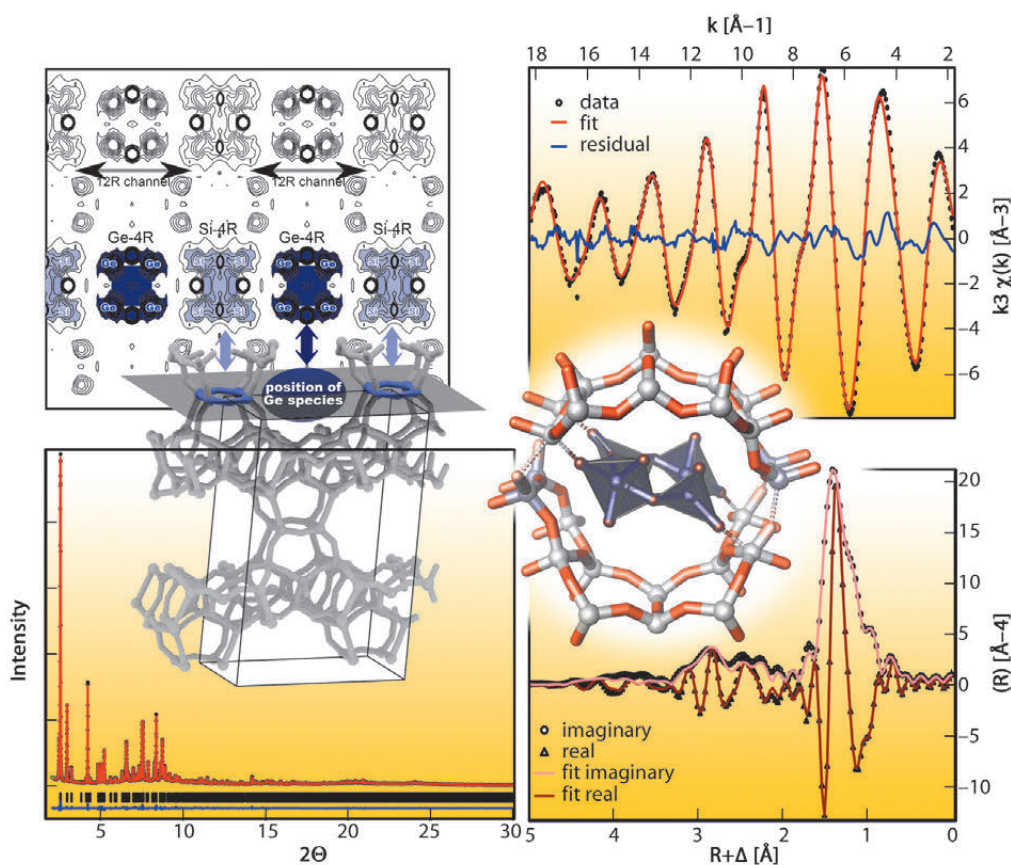
**Fig. 138:** Acid leaching of IM-12 zeolite can dislodge the germanate four-ring (dark blue) and shift it into the channels of the contracted framework of Ge-COK-14. Further acid leaching fully eliminates the germanate four-ring resulting in the interrupted (-COK-14) or fully condensed framework (COK-14) depending on the conditions.

and coordination of Ge in Ge-COK-14 (Figure 139). Each Ge atom had two Ge neighbours at 3.2 Å. A combination of HRXRD and Ge-K-edge EXAFS measurements allowed the structure of Ge-COK-14 to be unravelled (Figure 138, Figure 139). In this sample, germanium was present as a germanate four-ring in the position that would later become the 12-membered ring of COK-14. Ge-K-edge EXAFS measurements of the parent UTL zeolite revealed this germanate four-ring was already present (Figure 138).

Acid leaching removes the germanate four-ring from the UTL zeolite and shifts it into the channels of Ge-COK-14. Prolonging the

transformation and washing leads to full elimination of germanium and results in the new zeolite frameworks -COK-14 and COK-14 (Figure 138). The COK-14 zeolite family is a valuable addition to the all-silica large-pore zeolite types. More new zeolites with attractive pore architectures may be obtained by this inverse sigma transformation approach.

**Fig. 139:** Rietveld refinement (bottom left), observed electron density (upper left) and fitted EXAFS data (right) of Ge-COK-14. EXAFS analysis was based on the inserted fragment from Rietveld refinement. Inset on the left indicates the shown plane of observed electron density.





# Enabling Technologies

The instrumentation and enabling technology-related activities aim to provide state-of-the-art instruments and infrastructure to support the ESRF's forefront science programme. When designing a beamline, one of the primary objectives is to preserve the photon beam properties along the beamline and in particular, to ensure that the full brightness of the source reaches the sample. However, following a more holistic approach, one should aim to achieve an optimum conversion of brightness into high-quality data and ultimately extract the most significant scientific output from the recorded data. In this context, the design specifications should span from optical design to online data analysis. Most synchrotron beamline projects worldwide show two different trends in the way beamlines are designed. On one hand, there are beamlines that perform challenging but routine measurements. This class of beamlines targets high throughput, reliability and standardisation and requires an increasing level of automation, intelligent decision algorithms and state-of-the-art data acquisition chains. On the other hand, the second class of beamlines performs experiments that require instrumentation with a high level of flexibility and versatility, where the scientist is constantly involved in the decision process. In this case, the use of tailored tools to support the decision process helps to minimise the dead-time and maximises the use of beam time.

Both classes of beamlines rely increasingly on modelling tools and on an optimised acquisition system from the high-throughput detectors down to the strategy for data transfer, processing and storage. In 2012, many new projects were launched while others were consolidated. Most of them concerned the hardware (optics, mechanics, detection and control systems, etc.). The long shutdown offered a unique opportunity to update several beamline control software applications and to strengthen our initial efforts in developing a comprehensive strategy for data processing and online data processing. By definition, computing infrastructure strives for invisibility. Our users are understandably interested in the applications that perform useful services for their scientific endeavour, rather than in the layers of system abstractions or the physical components that make these services

possible. Whether it takes place at the level of operating systems, data centres, communication protocols, file formats, standardisation, or policy work, the design, planning, and operation of the computing infrastructure are major professional activities which are in constant evolution. In 2012, the invisibility of the computing infrastructure has been challenged by the needs to transfer massive amounts of data while simultaneously analysing the data. With finite financial resources at our disposal, delicate trade-offs had to be made and we decided to put emphasis on the enhancement of the data communication network and disk-based data storage.

This year, the chapter on enabling technologies reflects this effort and thus comprises a collection of four articles, focussing on software and computing infrastructure issues.

The first article illustrates the importance of optical simulations when dealing with coherent beams. Indeed, the dramatic improvement of synchrotron source properties has driven the development of new simulation tools, no longer using a purely ray-tracing approach but rather based on an accurate wave-propagation model that takes into account all physical properties of both the incident radiation and the optical system involved in the propagation of the beam. Among many such projects developed worldwide, the article selected treats the particular case of focusing X-ray multilayers for nanofocusing applications.

The second article exemplifies the efforts of the ESRF in developing on-line data analysis packages to optimise the coupling of feedback from data analysis to the experimental control system for macromolecular crystallography experiments. The article reports on a new intuitive graphical user interface (GUI) called the Data Analysis WorkbeNch (DAWN), which provides a flexible framework to build complex process workflows, used in macromolecular crystallography and other domains.

The third article deals with high-resolution diffraction experiments using multi-million-pixel area detectors producing huge volumes of complex data. For this class of experiments, data processing increasingly requires innovative

computing approaches to reduce the volume of collected diffraction data into exploitable diffraction patterns in a way that does not slow down the overall acquisition process. This article is an introduction to a new algorithm, PyFAI, which has been designed to reduce SAXS and WAXS patterns by azimuthal integration using a new approach.

The final article discusses the current state-of-the-art in disk-based data storage, describing the trade-offs required to find the right balance between performance, functionality, compatibility with client operating systems, ease of operation, reliability and, last but not least, cost.

R. Dimper and J. Susini

## Application of wave optical simulations to focusing X-ray multilayers

Many experimental stations at modern synchrotron or FEL sources use X-ray focusing devices that produce spots below 100 nm using a variety of optical elements. A very popular optical scheme is the Kirkpatrick-Baez (KB) setup [1] where two perpendicularly oriented curved mirrors focus the beam independently in the vertical and the horizontal direction, respectively. To increase their numerical aperture, that is, to obtain smaller focal spots, the traditional total reflection mirrors can be replaced by graded multilayers, allowing for steeper grazing angles. While wave optical models for curved total reflection mirrors have been developed in the past, an equivalent description for curved graded multilayers was missing.

Recently, a new software tool was developed at the ESRF that can perform wave optical simulations on curved multilayer optics [2]. It is based on a Takagi-Taupin approach in the two-beam approximation. Outside the multilayer structure the beam is propagated by phase ray tracing and by solving the Kirchhoff integral. Extended sources can

be modelled by superposition of point sources. The spatial coherence can be varied by the degree of random averaging of amplitude and phase of the point sources and by their distribution in space.

The wave-optical simulations show that diffraction limited focal spots of less than 8 nm full width at half maximum (FWHM) can be expected using realistic curved multilayer structures with d-spacings of the order of 2 nm and reflectivities of more than 70%. This is in good agreement with the best available experimental data [3].

Figure 140 shows the simulated intensity distribution near the image plane at  $q = 100$  mm from a 50 mm long curved  $W/B_4C$  multilayer positioned at  $p = 100$  m from a point source. The resulting spot size of 7.5 nm FWHM agrees with the diffraction limit estimated from a straight aperture (thin lens approach).

The surface figure error of the underlying mirror substrates is a performance limiting factor that can be taken into account by the simulation programme. Applying frequently measured height error spectra with spatial frequencies in the millimetre

### Principal publication and authors

M. Osterhoff (a,b) and  
Ch. Morawe (b), *Proc. SPIE*  
**8502**, 850208 (2012); doi:  
10.1117.12.928938  
(a) Georg-August University,  
Göttingen (Germany)  
(b) ESRF

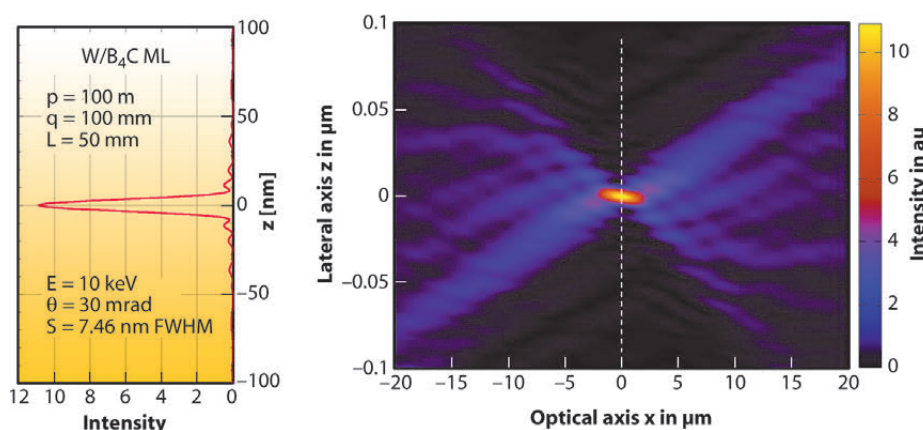


Fig. 140: Simulated intensity distribution near the focal spot at  $q = 100$  mm from a 50 mm long curved  $W/B_4C$  multilayer positioned at  $p = 100$  m from a point source. Further parameters are indicated in the vertical cross section reported on the left.



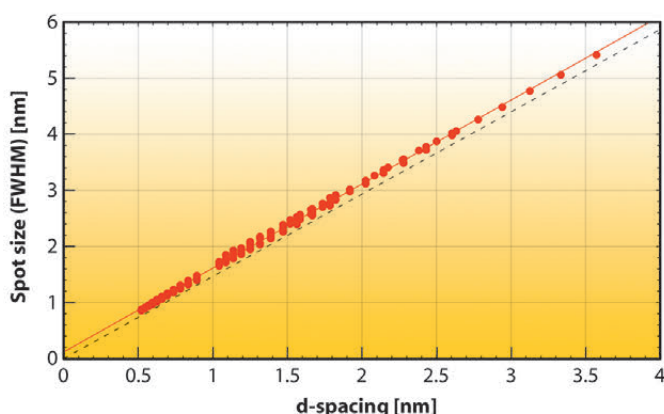
### References

- [1] P. Kirkpatrick and A.V. Baez, *Journal of the Optical Society of America* **38**, 766 (1948).  
 [2] M. Osterhoff, Ch. Morawe, C. Ferrero and J-P. Guigay, *Optics Letters* **37**, 3705 (2012).  
 [3] H. Mimura *et al.*, *Nature Physics* **6**, 122 - 125 (2010).  
 [4] L.G. Parratt, *Phys. Rev.* **45**, 359 (1954).  
 [5] Ch. Morawe and M. Osterhoff, *X-Ray Optics and Instrumentation*, 479631 (2010).

range indicates an intensity transfer from the main peak into the side lobes while its width remains constant.

The simulation of finite and incoherent storage ring X-ray sources returns focal spots that are blurred from their original diffraction limited size to the de-magnified image of the source, as expected from geometrical optics.

In order to explore fundamental multilayer focusing limits, a large number of different curved multilayers with d-spacings as low as 0.5 nm were simulated, approaching the ultimate limit of layered structures made of alternating materials (two atomic layers). **Figure 141** shows that all data



points follow a linear slope converging only 0.1 nm above the expected zero crossing. There is no evidence of a major deviation from the diffraction limit down to spot sizes below 1 nm.

The simulations confirm that the modified Bragg equation, corrected for refraction in the stack, but derived for flat multilayers is a very good approximation for the design of curved multilayer mirrors. They also suggest that curved multilayers can be considered as achromatic optical elements with respect to the focal spot size and that their local reflectivity spectra can be approximated using Parratt's formalism [4] for flat multilayers.

These results are of fundamental importance for the fabrication of curved graded multilayers for third-generation synchrotron beamlines since they validate the present design approach [5] on a wave-optical level.

**Fig. 141:** Simulated focal spot size (circles) as a function of the multilayer d-spacing at various energies from 12.4 keV to 49.6 keV and for 50 to 300 bi-layers. The solid line is a linear fit to all data points. The broken line corresponds to the diffraction limit of a straight aperture.

### Principal publication and authors

S. Brockhauser (a), O. Svensson (b), M.W. Bowler, (a,b), M. Nanao (a), E. Gordon (b), R.M.F. Leal (b), A. Popov (b), M. Gerring (c), A.A. McCarthy (a) and A. Götz (b), *Acta Cryst.* **D68**, 975-984 (2012).  
 (a) EMBL, Grenoble (France)  
 (b) ESRF  
 (c) Diamond Light Source (UK)

## ■ Enabling complex experiments using a workflow tool

A general trend at synchrotron radiation facilities is the increased demand for automated on-line data analysis. Increases in flux, improved optics and fast read-out detectors now enable complex experiments to be performed routinely, where data acquisition and data analysis must not only be linked, but also take place almost simultaneously. The need to automate these processes has become more urgent with the ESRF upgrade programme, in particular for the new MASSIF beamlines for high-throughput macromolecular crystallography (MX). These experiments pose a challenge for both hardware (sample changers, sample centring, etc.) and software (data acquisition and data analysis). In order to automate such experiments, a high level software environment is required to coordinate data acquisition and data analysis. The development of this software

requires care as it needs to be robust and highly flexible in order to be able to respond rapidly to the constantly evolving scientific needs and instrumentation developments.

To meet this challenge we have developed a data analysis workbench (DAWN) in collaboration with the Diamond Light Source, EMBL Grenoble and other institutes [1]. This software package/environment contains tools for data visualisation, data analysis and most importantly a workflow tool called Passerelle (developed by the Belgian company iSencia and based on Ptolemy II). Workflow tools have been used extensively for scientific applications [2], however, these tools have not been widely used at synchrotron radiation facilities. Reported here is the first use of



a workflow tool to link data analysis and data acquisition. The DAWN workflow tool provides a framework and structure onto which complex on-line data analysis workflows can be built. Workflows can be implemented in traditional programming languages (e.g. Fortran, C/C++, Java, Python, etc.), but the DAWN workflow tool allows beamline scientists (non-programmers) to be highly involved in the developments: with a minimum of training, they can modify and adapt the workflows to meet new scientific requirements without the intervention of a programmer. The DAWN workflow tool helps to bridge the gap between beamline scientists, who have the scientific expertise, and programmers, responsible for implementing the on-line data analysis software components. The role of the programmer is to provide robust workflow 'actors', i.e. plugins that perform specific tasks, which can be intuitively used by the beamline scientists. The visual approach of describing the workflows facilitates the communication of the experimental protocols to other scientists by hierarchically structuring and highlighting the main logic (Figure 142).

We have implemented a host of on-line data analysis workflows that are now available at the MX beamlines:

- **Sample re-orientation using Kappa goniometers:** Data collected from macromolecular crystals can be improved and optimised by re-orientating the sample prior to data collection. The workflow for sample re-orientation consists of collecting reference images, analysing the images, controlling the Kappa goniostat and calculating optimised data collection strategies.
- **Automatic crystal centring using X-rays:** This workflow scans the largest face of a loop using a 2D mesh scan and then performs a 1D scan 90 degrees away on the best area of diffraction, as determined from the first scan. The optimum crystal volume is then automatically centred with respect to the beam, ready for final characterisation and data collection.
- **Automatic control of a dehydration device:** The dehydration of macromolecular crystals has long been known for having the potential to increase their diffraction quality. We have developed a workflow which automates the cycle of dehydration, equilibration,

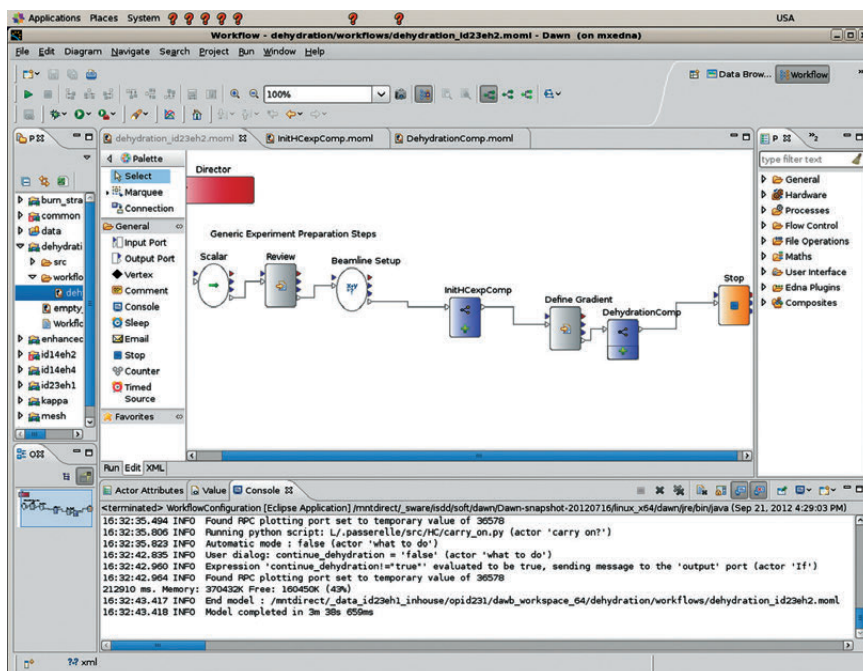


**Fig. 142:** The DAWN workflow tool. The screenshot shows a workflow in development. The workflow is represented graphically with actors shown as individual elements.

acquisition of reference images, data analysis and production of graphs which describe the crystal diffraction quality as a function of the humidity level.

- **Enhanced EDNA [3] crystal characterisation workflow:** When characterising crystals, the diffraction quality is unknown. The program BEST [4] can calculate not only the optimal data collection strategy but also the theoretical maximum resolution for a complete data set. This workflow automatically recollects the reference images at the maximum resolution if the crystal diffracts better than the resolution obtained with the initial reference images.
- **Crystal radiation-sensitivity measurement workflow:** Radiation damage severely limits the data that can be obtained from single crystals. By sacrificing a crystal, the degree of radiation-sensitivity of similar crystals can be accurately estimated and optimal data collection strategies calculated taking into account this sensitivity.

The workflows described above have already been used successfully on ESRF MX beamlines. Most of them make use of existing EDNA plugins, therefore the workflow tool should not be seen as a replacement but as an enhancement of workflows implemented in EDNA. Users interact with the workflows through the standard beamline control interface MXCuBE (Figure 143) [5]. We are now in the process of preparing new workflows



which will enable even more complex experiments, for example:

- Optimisation of data collections from multiple crystals by re-orienting samples and taking into account data already collected

- Automatic crystal ranking by characterising a large number of samples and selecting those with the best diffraction qualities
- High-throughput automatic MAD data collection
- Fully-automatic data collection pipelines for drug discovery

The successful use of workflows for MX experiments implies that other types of experiment could profit from this approach, too.

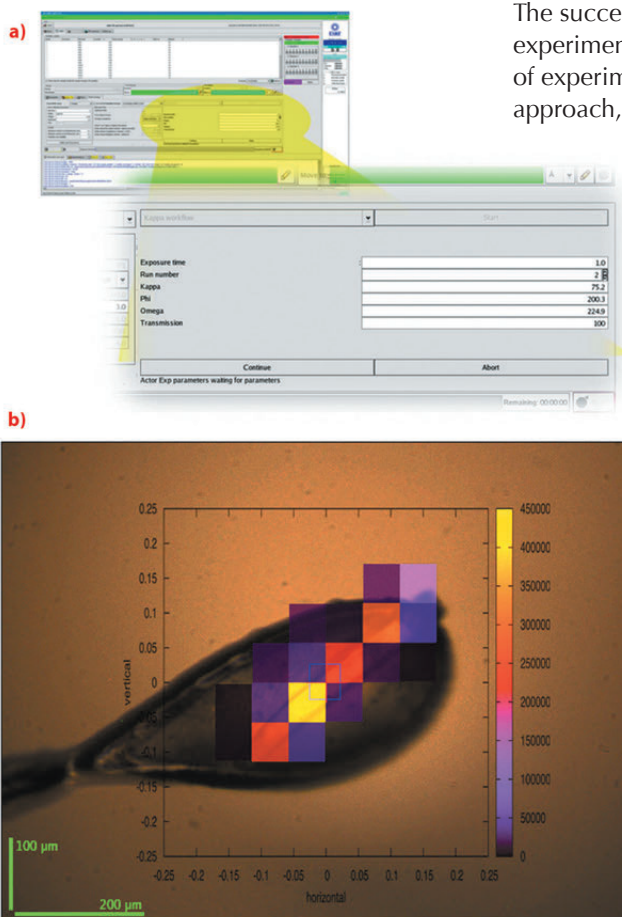


**Fig. 143:** a) The workflow GUI component in the beamline user interface MXCuBE. The GUI component displays dynamic content from the workflows and can therefore adapt to the needs of a particular experiment, in this case Kappa reorientation angles. b) The output from an auto-centring workflow. A diffraction quality map is shown overlaid with the sample.

#### References

- [1] <http://www.dawnsci.org>. DAWN is a collaboration between the ESRF, the Diamond Light Source (Didcot, UK), EMBL Grenoble, iSencia (Gent, Belgium) and Global Phasing (Cambridge, UK).
- [2] I.J. Taylor, E. Deelman, D.B. Gannon and M. Shields, (Eds.), *Workflows for e-Science*, Springer, London, (2007).
- [3] M.-F. Incardona *et al.*, *J. Sync. Rad.* **16**, 872-879 (2009).
- [4] A. Popov *et al.*, *Acta Cryst. D* **59**, 1145-1153 (2003).
- [5] J. Gabadinho, *et al.*, *J. Sync. Rad.* **17**, 700-707 (2010).

#### Authors

J. Kieffer, D. Karkoulis and  
J.P. Wright  
ESRF

## PyFAI, a python tool for fast azimuthal integration

PyFAI [1,2] is a software package designed to reduce SAXS, WAXS and XRPD images recorded by area detectors to 1D plots (azimuthal integration), or 2D patterns (a polar transformation called “caking” or “azimuthal regrouping”). PyFAI is also a software library that can be integrated into other tools like PyMca and EDNA. It also provides a clean python-based interface to enable interactive use from the console, as shown in **Figure 144**. PyFAI features tools for batch processing and calibration facilities for optimising the geometry of the experiment by

using the Debye-Scherrer rings of a reference sample.

The geometry used in pyFAI is compatible with any flat area detector at any orientation, even significantly tilted. Moreover geometry configurations can be imported from other tools like FIT2D or SPD. Fast integration is obtained by combining the data processing algorithm, which ensures that each pixel from the detector provides a direct contribution to the final diffraction pattern, with a



parallelisation algorithm optimised for modern hardware.

The Python programming language, which is already used in many scientific applications, was chosen for data analysis because it permits rapid testing of new algorithms thanks to the NumPy toolbox and the iPython interface (a free alternative to Matlab). Python allows programs to scale from small scripts to large applications, and can be used with graphical interfaces such as PyMca or MxCube.

Building blocks for X-ray science have been developed at the ESRF such as FabIO [3] for image data access, pyHST for tomographic reconstructions and pyFAI (presented here) for azimuthal regrouping.

Azimuthal integration is a transformation from Cartesian to polar space where the radial dimension can either be the distance (radius), the momentum transfer ( $q$ ) or the scattering angle ( $2\theta$ ). Throughout this geometrical transformation, total intensities must be conserved in order to obtain quantitatively accurate results (unlike interpolation). Integration is performed via a histogram-like algorithm:

- Each pixel of the image is associated with its polar coordinates, then a pair of histograms versus the radial dimension are built, one unweighted for measuring the number of pixels falling into each bin and another weighted by the pixel intensities.
- Intensities are taken after dark-current subtraction, corrections for flat-field as well as for solid-angle and polarisation effects.
- The diffraction pattern is obtained by dividing the weighted histogram by the number of pixels per bin.
- 2D regrouping is obtained in the same way using two-dimensional histograms over radial and azimuthal dimensions.
- In order to avoid high frequency noise where pixel statistics are low, pixels are split over multiple bins according to their spatial extent.

While the histogram build-up technique is efficient on a single processor, it faces write-access conflicts when run in parallel [2] and requires costly locking. This issue was addressed by pre-calculating (and storing) the full correspondence table (or look-up table) between all the image pixels and the histogram bins. Thanks to

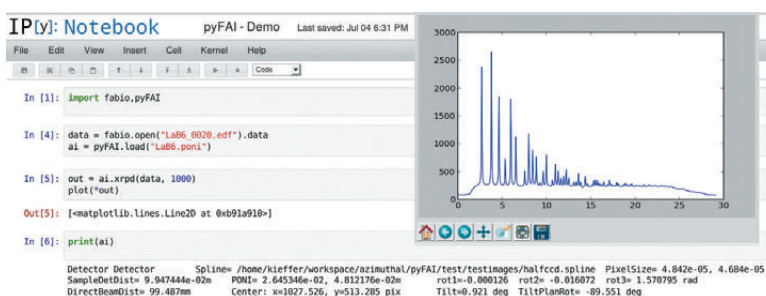


Fig. 144: Example of interactive use of FabIO and pyFAI in the notebook edition of IPython.

the look-up table, different output bins can then be processed in parallel making azimuthal integration computationally effective on multi-core systems and on graphics cards. Figure 145 shows the number of frames processed per second versus image size on a typical beamline workstation.

Parallel implementations are much faster than their serial equivalents but have a drawback in their larger memory footprint due to the look-up table. The graphics card is used because it is as fast as the processor for this kind of task, and it is a relatively cheaper resource.

The maximum attainable data throughput is in the order of 200 Mpixels/second (800 MBytes/second of float data; much more than the speed of current hard disks), and therefore depends on a computer having a sustained supply of data to be able to continue working at this speed. For a typical image of 2048 x 2048 pixels, and after loading and setting up, pyFAI takes about 20 milliseconds per new frame to compute the 1D integrated profile. However, the sustained rate for integrating large datasets (thousands of images) is only around 100 milliseconds per image due to reading bottlenecks.

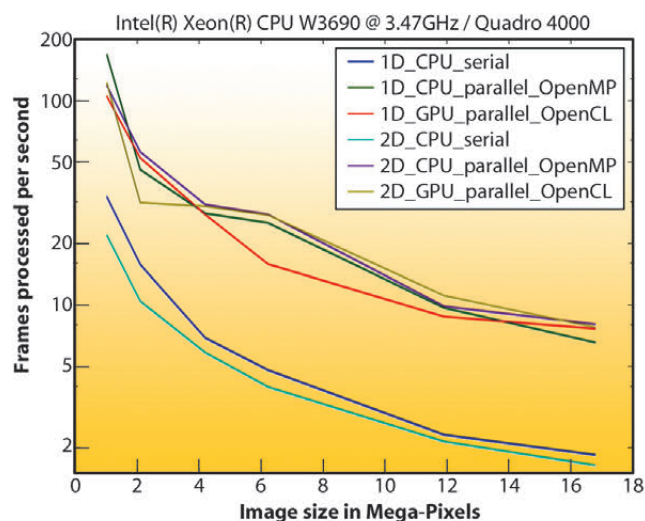


Fig. 145: Performances of pyFAI on a beamline workstation (ID13): frames processed per second versus image size (in mega-pixel).



### References

- [1] J. Kieffer and D. Karkoulis, PyFAI, a versatile library for azimuthal regrouping, *Journal of Physics: Conference Series* (2013), Accepted (volume: SRI2012).
- [2] J. Kieffer and J.P. Wright, PyFAI: a Python library for high performance azimuthal integration on GPU, Powder Diffraction (Proceedings of EPDIC13), *Submitted*.
- [3] E.B. Knudsen, H.O. Sørensen, J.P. Wright, G. Goret and J. Kieffer, FabIO: easy access to 2D X-ray detector images in Python, *Journal of Applied Crystallography* (2013), Accepted.

PyFAI has been used online on two SAXS beamlines at the ESRF (BM26 – Dubble and BM29 – BioSaxs) since Spring 2012. It is also integrated into Python servers (like EDNA), where it processes images at speeds of up to 1 fps, being mainly limited by the network and disk latencies. To overcome this limitation, pyFAI is currently being integrated into the image acquisition server LImA, providing integrated images directly as output frames from the detector, reaching 30 fps in test conditions. Thanks to the FabIO library [3], pyFAI is compatible with at least 20 detectors formats from 12 different manufacturers.

Several ESRF beamlines are interested in this development including ID02, ID11, ID13 and ID22. Other institutes have also shown interest: CEA Grenoble, CEA Saclay and Synchrotron Soleil.

The source code is open source under the GPL license conditions and is available at <http://github.com/kif/pyFAI>. PyFAI is packaged and available in common Linux distributions like Debian 7.0 and Ubuntu 12.04. Installer packages for Windows and MacOSX can be downloaded from <https://forge.epn-campus.eu/projects/azimuthal/files>.

### Authors

B. Lebayle, D. Gervaise, C. Mary and R. Dimper  
ESRF

## ■ Disk based data storage at the ESRF – Striking the ideal balance between performance and functionality

In 1994, the Networked Interactive Computing Environment (NICE) was set up for use by experiments at the beamlines, which routinely store and process large volumes of data, ranging from theoretical simulations to sophisticated image processing. Visitors arriving at the ESRF are given a NICE account and their experimental data is stored in a large shared area offering a massive 1 PetaByte of disk space and for a duration of fifty days after the end of the experiment. ESRF staff scientists use other dedicated areas offering a further 500 TeraBytes of disk space. Visitors' raw and processed data can be exported to the home laboratory either via the Internet or by using removable storage devices such as USB disks.

The ESRF is equipped with two state-of-the-art data centres allowing the physical separation of disk-based storage and tape-based backups. NICE, in addition to disk storage, also has incremental tape backups which are made overnight on a daily basis as a protection against accidental deletion of data. A full back up is made prior to the removal of data from the disks after the fifty-day period following the actual experiment and is kept for another six months. Experimental data is processed using high performance computers – the so-called compute clusters. A data communication network provides multiple high-speed links between the data producers, the central disk storage, the compute clusters, and the data analysis workstations. For the last few years, single connections for computers have run increasingly on 10 Gbit/second fibre-optic links.

Disk array.



The main cloud on the horizon is the central disk storage which recently became a frequent bottleneck in this topology. This is due to the large number of powerful computers in the compute clusters draining disk bandwidth during data analysis and, therefore potentially disrupting the writing of data from the beamlines. Overcoming this hurdle entails having an optimal vision of all the constraints inherent to a central disk storage facility, from the ever increasing quantity of large-sized detector images,



the need for fast simultaneous access from multiple data producers, ease of operation, compatibility with many different client operating system and an extreme resilience to guarantee a non-stop 24/7 operation. In 2011, after an unsuccessful attempt to find a 1 PetaByte high-performance system, the ESRF had to lower its sights and adopted a somewhat slower but highly-reliable solution of 500 TeraBytes. This was in order to attain compatibility with in-house resources and a high level of reliability to minimise the risk of exposing the facility to a major failure (potentially provoking severe consequences on operation, with a worst case scenario of down time for up to several days before restoring normal operation). This storage system is based on the NFS protocol guaranteeing compatibility with the large variety of client operating systems at the ESRF.

This strategic choice allows individual data streams of up to 500 MBytes/sec and an aggregated performance of 2 GBytes/sec. During the first run of 2012, a massive 350 TB of data were produced in less than three months. Single experiments in excess of 10 TB are now commonplace. Positive feedback from users on the ease of use and the flexibility of the shared space has encouraged us to increase its capacity. A further 500 TB were added at the end of 2012.

As part of the ESFRI (European Strategy Forum on Research Infrastructure) roadmap, ESRF is involved in the CRISP project [1]. The ESRF's participation in this project includes work on high-speed data transfers based on a local buffer storage system inserted between the detector and the central disk systems to absorb peaks in data acquisition. It is expected that this will offload the central disk system while providing guaranteed performance levels in the GByte/sec range.

In parallel with this upgrade, it is necessary to replace the older central disk systems used for ESRF in-house research and general purpose storage. Given that only three beamlines occupy most of the space, it was decided to evaluate another tactic and set up small dedicated private storage servers (40-50 TB capacity per server) for these demanding beamlines. In addition to cost considerations, this solution affords several advantages, notably:



Visitors enjoying a guided tour of the data centres during SRI 2012.

- high flexibility in terms of disk space, when more space is required additional storage servers can simply be added
- dedicated bandwidth to access storage resources for the beamlines
- higher aggregated performance: every private storage server adds its own high speed link to the overall available bandwidth

However this scenario has some potential stumbling blocks as private storage servers are less reliable and, in case of failure, a manual operation has to be performed to store data on a standby system. Beamlines will have to manage their own disk space and be vigilant to ensure that “disk full” status is not reached as this might stop on-going experiments or interrupt data analysis. Also daily incremental backup to tape will no longer be technically feasible.

The three most demanding beamlines in terms of data storage –ID19, ID15 and ID22– have recognised the potential of this approach and agreed to take it on board. Tests will start on ID19 which will be equipped with two private storage servers at the beginning of 2013. Should tests prove conclusive, then a number of such dedicated servers will be rolled out in the course of 2013 to replace the ageing central disk systems holding the in-house research data.

To conclude, the ESRF has taken a prudent approach by opting for solutions that combine reliability, flexibility and performance to satisfy increasingly challenging storage demands. Keeping abreast of market trends through a constant exploration and analysis of available solutions should enable the ESRF to secure future storage requirements, to the mutual satisfaction of scientists and the IT engineers who guarantee the smooth running of the system.

#### References

- [1] Crisp: <http://www.crisp-fp7.eu/about-crisp/esfri/>



# Accelerator and X-ray Source

In 2012 the Accelerator complex was stopped for a period of five months due to the extensive building works in progress for Phase I of the ESRF Upgrade Programme. The Accelerator and Source Division put to profit this long shutdown to continue its efforts to ensure reliable operation by upgrading a number of systems. The major developments of 2012 are described hereafter.

## ■ Beam parameters of the storage ring

A summary of the characteristics of the storage ring electron beam, the main optic functions, electron beam sizes and divergences at various source points are presented in **Table 1** and **Table 2**. For insertion device source points, the beta functions, dispersion, sizes and divergences are calculated in the middle of the straight section. For bending magnets two representative source points have been selected for each type (even or odd cell number) of magnet, corresponding to magnetic fields of 0.4 T and 0.85 T. These points differ by the observation angles, of respectively 3 and 9 mrad from the entrance of the magnet.

Electron beam profiles are Gaussian and the size and divergence are presented in terms of rms values. The associated

full width at half maximum sizes and divergences are 2.35 times higher. Horizontal electron beam sizes and divergences are given for the multibunch filling modes and apply to almost all filling patterns except when the current per bunch is larger than 4.5 mA, for which a slightly larger size and divergence are attained because of the increased energy spread of the electron beam.

Vertical electron beam sizes and divergences are given for a vertical emittance of 4 pm, which is now the standard for 2 x 1/3 and 7/8+1 filling modes. The vertical sizes and divergences are about 1.4 times larger in uniform filling mode (due to ion effects, which are partially corrected by the use of a vertical bunch by bunch feedback). To increase the lifetime of the stored beam, the vertical beam sizes and divergences are deliberately increased by about a factor of 4 in the 16-bunch, 4-bunch and hybrid filling patterns.

The lifetime, bunch length and energy spread mainly depend on the filling pattern. These are given in **Table 3** for a few representative patterns. Note that in both 16-bunch and 4-bunch filling

**Table 1:** Principal characteristics of the electron beam.

Energy	[GeV]	6.04
Maximum current	[mA]	200
Horizontal emittance	[nm]	4
Vertical emittance	[pm]	4
Revolution frequency	[kHz]	355
Number of bunches		1 to 992
Time between bunches	[ns]	2.82 to 2816

		Even ID (ID2, ID6...)	Odd ID (ID1, ID3...)	Even BM (ID2, ID6...) 3 mrad	Even BM (ID2, ID6...) 9 mrad	Odd BM (ID1, ID3...) 3 mrad	Odd BM (ID1, ID3...) 9 mrad
Magnetic field	[T]	Variable	Variable	0.4	0.85	0.4	0.85
Horiz. Beta function	[m]	37.6	0.35	1.33	1.06	2.12	1.61
Horiz. Dispersion	[m]	0.134	0.031	0.062	0.051	0.089	0.075
Horiz. rms e- beam size	[µm]	413	50	99	85	132	113
Horiz. rms e- divergence	[µrad]	10	107	116	114	104	99
Vert. Beta function	[m]	2.95	2.97	41.7	42.0	32.1	32.2
Vert. rms e- beam size	[µm]	3.4	3.4	12.9	13.0	11.3	11.4
Vert. rms e- divergence	[µrad]	1.17	1.16	0.50	0.50	0.36	0.36

**Table 2:** Beta functions, dispersion, rms beam size and divergence at the various source points.



patterns, the energy spread and bunch length decay with the current (the value indicated in the table corresponds to the maximum current). The bunch lengths are given for the usual radio-frequency accelerating voltage of 9 MV (8 MV for 16-bunch and 4-bunch).

Filling pattern		Uniform	7/8 + 1	Hybrid	16-bunch	4-bunch
Number of bunches		992	870+1	24x8+1	16	4
Maximum current	[mA]	200	200	200	90	40
Lifetime	[h]	50	45	30	16	9
Rms energy spread	[%]	0.11	0.11	0.11	0.12	0.16
Rms bunch length	[ps]	20	20	25	48	55

**Table 3:** Current, lifetime, bunch length and energy spread for a selection of filling modes.

## Summary of accelerator operation

Due to the exceptionally long shutdown, from 5<sup>th</sup> December 2011 to 3<sup>rd</sup> May 2012, user runs in 2012 were different in distribution and duration compared to a normal year of operation. Three runs were scheduled in 2012 instead of the usual five. An overview is presented in **Table 4**.

During the long shutdown, numerous modifications and improvements were implemented on several parts of the accelerator as well as on the facility networks such as fluids and electricity. The accelerator alignment was disturbed by substantial ground movement linked to earth removal and important building works underway on site. To troubleshoot and anticipate possible difficulties for the May restart, one week was dedicated to an intermediate restart of the accelerator complex in March 2012. This proved extremely fruitful since it helped to solve several unforeseen problems, facilitating the user mode restart in May.

At the beginning of the May restart, several days were devoted to extensive radiation

and personnel safety system checks for all the beamlines. Several problems were also found and solved in the front-ends when the X-ray beam was delivered to the users.

In 2012, 442.5 shifts (3540 hours) of beam time had been initially scheduled for the users. Of these 3540 hours, 3459 were effectively delivered (including 31.2 hours of refill). This represents a beam availability of 98.58%, which is slightly lower than for 2011 (98.91%). Indeed, over the three runs several beam interruptions clocked beam downtime in the region of 2-3 hours (PSS beamline trips, water leak on a crotch, failure of one regulation rack on a power supply of one sextupole family, lightning strike on site, etc.). The mean time between failures (MTBF) for this year reached 60 hours, which is also lower compared to 2011 (107.8 hours). The origin of this reduced MTBF is mainly due to commissioning of new hardware and software implemented during the long shutdown. In particular the RF system had to be reconditioned and the fast orbit feedback debugged. Due to

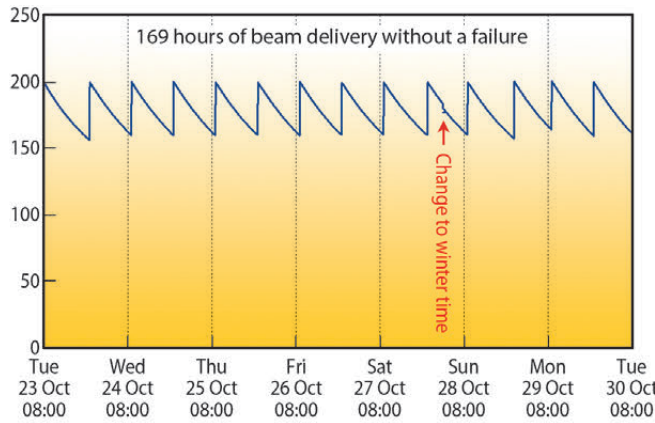
RUN NUMBER	TOTAL 2011	2012-01	2012-02	2012-03	TOTAL 2012
Start		03/05/2012	04/09/2012	23/10/2012	
End		01/08/2012	10/10/2012	12/12/2012	
Total number of shifts	<b>804</b>	270	108	150	<b>528</b>
Number of USM shifts	<b>646.6</b>	216	95.3	131.3	<b>442.5</b>
Beam available for users (h)	<b>5077.2</b>	1685.4	746.1	1027.1	<b>3458.6</b>
<b>Availability</b>	<b>98.91%</b>	<b>98.34%</b>	<b>98.88%</b>	<b>98.76%</b>	<b>98.58%</b>
Dead time for failures	<b>1.1%</b>	1.7%	1.1%	1.2%	<b>1.42%</b>
Dead time for refills	<b>0.8%</b>	0.8%	1%	0.9%	<b>0.88%</b>
Average intensity (mA)	<b>150.3</b>	134	101	172	<b>138.2</b>
Number of failures	<b>48</b>	34	11	14	<b>59</b>
<b>Mean time between failures (h)</b>	<b>107.8</b>	50.8	69.3	75	<b>60</b>
Mean duration of a failure (h)	<b>1.18</b>	0.8	0.8	0.9	<b>0.85</b>

**Table 4:** Overview of storage ring operation in 2012.



the variety and complexity of installations carried out during the shutdown, some

failures resulted from the run-in. These were discovered and fixed over the three runs.



Despite statistics that are worse than in 2011, there were several periods when the beam was delivered for several days without a single interruption. In particular, during week 43 which counted 7 days of delivery instead of the usual 6, when the beam was delivered for 169 hours with 1 additional hour due to the changeover to winter time (see **Figure 146**).

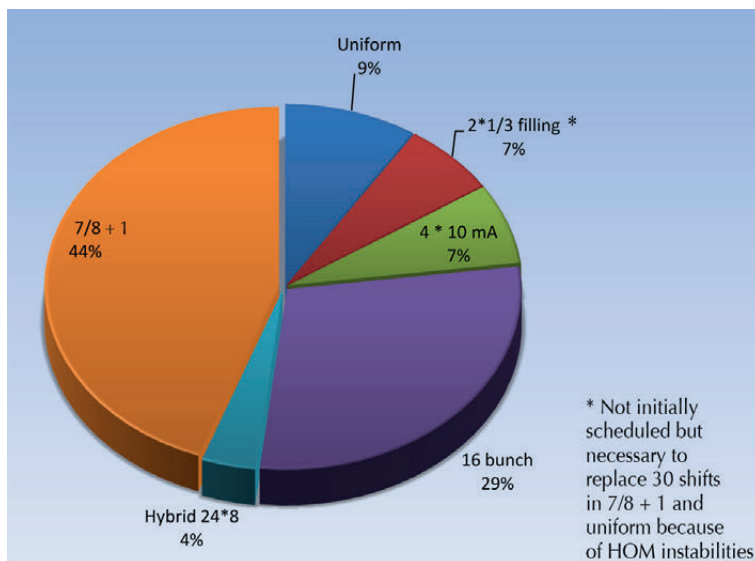
**Fig. 146:** Uninterrupted beam delivery for 169 hours in 7/8 + 1 filling mode during week 43 (RUN 2012- 03).

## ■ Filling patterns

**Fig. 147:** Distribution of the various filling modes in 2012.

**Figure 147** presents the distribution of filling modes delivered in 2012. Due to the long shutdown, only 3672 hours of USM were scheduled in 2012 instead of 5600 hours scheduled in a usual year of

operation. Uniform filling mode remains limited to specific user requirements whilst the preferred standard mode continues to be “7/8 +1” filling mode. This mode undoubtedly offers the best compromise satisfying the majority of the different user communities.



During the 6<sup>th</sup> week of operation, the beam was delivered in uniform filling mode as expected for the first two days. Unfortunately, strong Higher Order Mode (HOM) instabilities appeared during the decays and could not be eliminated through equipment tuning. At the same time, the medical beamline had scheduled its first patients making it essential to deliver a stable and reliable beam. It was therefore decided to switch to 2/3 filling mode to obtain the best conditions of beam quality. Not a single failure occurred over the next days when the patients were being treated.

## ■ Fast orbit correction system

One of the defining features of a third generation light source is an electron beam with an extremely low emittance. Experiments can only take advantage of the resulting small spot size on the sample if the orbit of the electrons in the storage ring is stable within a fraction

of the photon beam size. To achieve the required stability, beam position monitors (BPMs) located around the storage ring take data and calculate an orbit correction which is then applied by way of a set of corrector magnets. The present version of the ESRF’s beam orbit correction system,



implemented in 2009, uses 224 BPMs equipped with new *Libera Brilliance* electronics and 96 corrector magnets. This set-up provides a position resolution of a fraction of a micrometre compared to several micrometres using the electronics implemented in 1992. However, today's experiments demand even higher beam stability. In particular, a major cause of orbit distortion is the frequent modification of insertion device parameters, such as gap and phase changes due to increasingly creative ways of operating the beamlines.

In May 2012, the ESRF orbit correction system was restarted with the implementation of the following new items:

- A new set of wide-band power supplies enabling the 96 corrector magnets to be driven with a bandwidth of 500 Hz.
- A fast data network able to broadcast the position data measured by the Libera modules (and the corresponding correction kick data) over the full system at a rate of 10 kHz via a network of optical fibres that link the Libera crates and all the power-supply controllers. The protocol managing this data flow, the “communication controller”, was developed at the Diamond Light Source and the 10 KHz position data generation is a standard feature of the new Libera Brilliance electronics.
- Eight power-supply controllers connected to the communication controller and to the data ports of the power supplies. These units are equipped with powerful FPGA digital signal processors that compute, every 100  $\mu$ s, a new set of correction kicks derived from the position data.

Due to this upgrade, the storage ring orbit distortion is now damped with a bandwidth

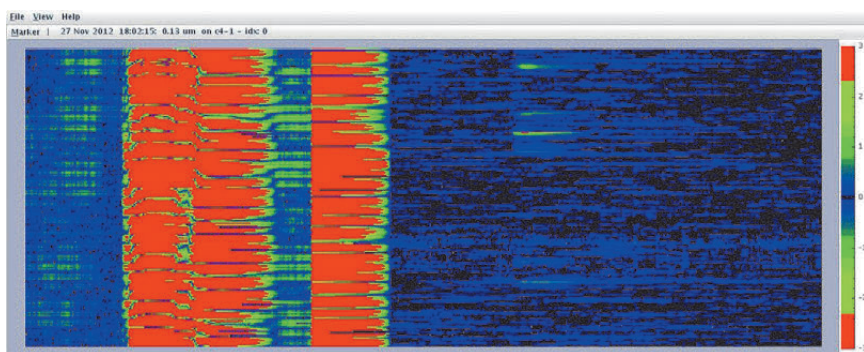


**Fig. 148:** ESRF electron beam stability measured with the 224 BPMs of the orbit correction system over the whole storage ring while closing the ID gaps following injection. The horizontal axis shows time – a total of 15 minutes. The vertical axis shows the readings of the 224 BPMs. On the left, beam movements with a correction every 10 seconds, as was the case until May 2012; On the right, beam movements during the same sequence of ID gap changes, using the fast orbit correction system commissioned in May 2012. The orbit corrections are now applied in a bandwidth ranging from 0 Hz to 150 Hz.

going from DC up to 150 Hz, as before, but with the addition of an accurate fast correction at the location of every BPM.

**Figure 148** shows the gain in stability from using the new system while closing the ID gaps following injection.

For the users, the crucial difference will be to render unnoticeable the effect of the transient parasitic kicks that occur during the change of parameters of some insertion devices. These transient parasitic kicks have been one of the biggest sources of instability in the source over the last few years. Before the beam orbit correction upgrade, vertical steps of more than 5  $\mu$ m could be observed over the two cells surrounding some badly corrected insertion devices. Now, recent tests have demonstrated stability of the beam position in the vertical plane better than 200 nm over the 0.1 to 100 Hz frequency range at all points around the storage ring.

In addition, this new system is expected to provide a powerful diagnostics tool. It will allow us to measure and correct imperfections of the ring lattice and to tune the storage ring optics in order to deliver beam with record low emittance in the near future.

## ■ 7-metre straight section

The ID23 straight section is being lengthened from 5 m to 7 m. This work was distributed throughout 2012 and will continue in 2013 with no effect on the operation of the ID23 beamline. The magnets at both ends of the straight section will be replaced by shorter and stronger ones. The two undulators presently in operation will be moved to either end of the straight section, while the

centre will be equipped with 3 new single-cell RF accelerating cavities (**Figure 149**). Generalising this configuration of RF cavities would allow the creation of new beamlines on sectors presently fully occupied by RF cavities.

In addition to the new magnets and corresponding power supplies installed in the straight section, the modification



requires a change of magnet coils and new power supplies that will provide individual control of the quadrupoles over a full cell. These modifications started during the

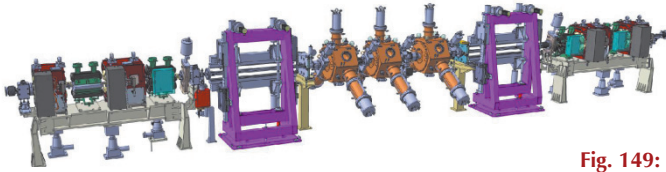
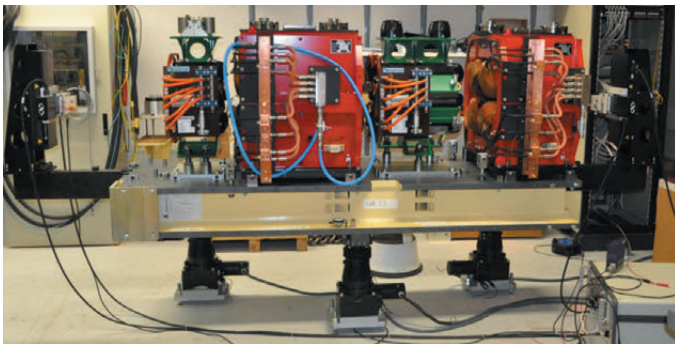


Fig. 149: Layout of the lengthened ID23 straight section.

2011-2012 winter shutdown and will be completed with the installation of the new straight section girders and new magnets during the 2012-2013 winter shutdown. The final step of the operation will see the installation of the three prototypes of HOM-damped RF cavities, scheduled during the summer 2013 shutdown.

## ■ New equipment

Fig. 150: New fully-assembled girder on the magnetic measurement bench.



New quadrupoles have been designed to reach a maximum field gradient of 25 T/m. Magnetic measurements performed on these quadrupoles at the ESRF include the innovation of measuring a fully assembled girder consisting of 2 quadrupoles and 2 sextupoles (Figure 150) with a stretched wire. This process provides information on the final magnet alignment and the reciprocal influence of magnet yokes on their neighbours.

## ■ New optics

Until now the storage ring lattice had 16 identical superperiods. The modifications underway will break the symmetry of the lattice for the first time. This may enhance the sensitivity of the machine to magnet imperfections, however, studies using the flexibility

power supplies on ID6 and ID11 showed that the lifetime should not be affected. The optical functions in ID23 will be close to the present values, with a vertical  $\beta$  increased from 3 m to 3.5 m to better match the new length of the straight section.

## ■ Test of a mini- $\beta$ configuration

Before the RF cavities are installed during the summer 2013 shutdown, the space they will eventually occupy will be free for the first six months of the year. During that time, an additional quadrupole will be installed and powered during machine dedicated studies only. The aim is to test the possibility of splitting a long straight section into two halves with a small vertical  $\beta$  of 1.5 m in the middle of each half. This configuration could allow a

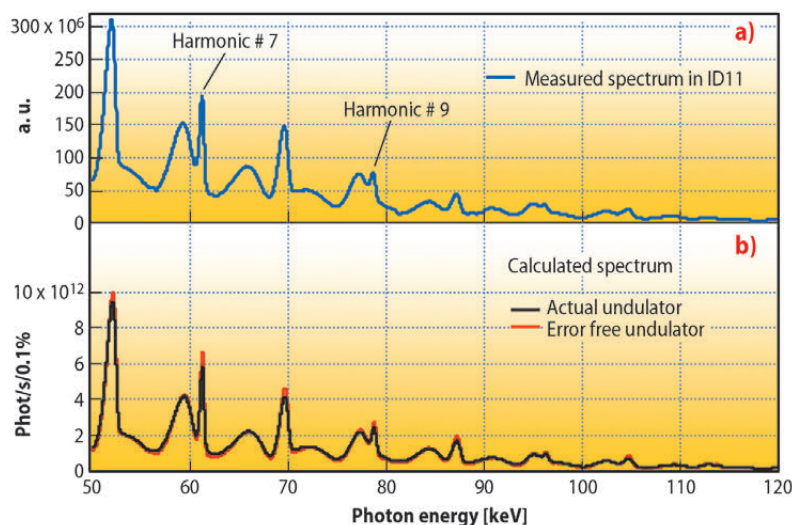
further reduction of the undulator gaps, possibly down to 4 mm. Although such undulators are not currently available, the tests will provide the opportunity to check the impact on the machine performance of such a significant modification of the optics, in particular on injection efficiency and lifetime.



## ■ Cryogenic permanent magnet undulators

Over the last five years, the Insertion Devices Group has played a major role in the development of cryogenic permanent magnet undulators (CPMUs). From the conventional technology of in-vacuum undulators (IVUs) the step toward CPMUs is a straightforward evolution. Due to the cryogenic cooling of the permanent magnet arrays, very high remanence NdFeB or PrFeB permanent magnet materials can be used to increase the undulator peak field. For a similar period and gap, the peak field of a CPMU is typically 40% higher than that of an IVU based on  $\text{Sm}_2\text{Co}_{17}$  material. One key feature of CPMUs is the large resistance to radiation induced demagnetisation reached by the permanent magnet material at cryogenic temperature (80 K to 140 K), an essential aspect for further reduction of the magnetic gap (5 mm or less).

The first use of a CPMU on a storage ring was achieved at the ESRF in 2008 [1]. Installed in the ID06 straight section, this device has provided essential feedback on many technological aspects and also on the compatibility of CPMUs with the operation of a large-scale facility like the ESRF. Based on the experience of this first prototype, a second device was built and has been recently installed on the ID11 straight section. This undulator has a period of 18 mm and a total magnetic length of 2 m. The selected NdFeB material has a magnetic remanence of 1.55 T at 145 K resulting in a peak field of 1 T for the undulator at a gap of 6 mm ( $K = 1.68$ ). The measured X-ray spectrum from the CPMU on ID11 reveals a remarkable agreement with the expected spectrum. **Figure 151a** shows the recorded spectrum on high harmonics ( $\geq 6$ ) in an aperture of  $600 \mu\text{m} \times 600 \mu\text{m}$  at 30 m from the source. The undulator gap was 6.4 mm in this case. **Figure 151b** presents the



calculated spectrum in the same conditions for an error free undulator (red) and the actual undulator using the magnetic measurements performed at 145 K (black). It confirms the methods used for the magnetic measurements which need to be performed under vacuum with the undulator at cryogenic temperature. As expected, the recorded photon flux at photon energy above 70 keV is up to three times higher than that of the neighbouring ID11 IVU (period 22 mm,  $K = 1.74$  at a gap of 6 mm).

Since the restart of the accelerator in May 2012, the operation of the new CPMU has been smooth and without any specific difficulty. A survey of undulator temperature shows a stable working point evolving from 140 K in 4 bunch mode up to 146 K in 16 bunch mode with the undulator gap closed to below 7 mm. In the ESRF context, the use of CPMUs is primarily efficient for improving the brilliance at photon energies above 50 keV. A further development, combining a smaller magnetic gap and better permanent magnet materials is presently under study. This is a very short period device (14 mm) with a  $K$  value of 1.65 at a gap of 4 mm.

**Fig. 151:** a) Recorded spectrum from the new CPMU in ID11; b) Calculated spectra for an error-free undulator (red) and actual undulator (black).

### References

- [1] First Operational Experience with a Cryogenic Permanent Magnet Undulator at the ESRF, J. Chavanne, G. Lebec, C. Penel and F. Revol, *Proc. PAC09*, p. 21414, 2416, Vancouver, 2009.

## ■ Permanent magnet steerers for canted beamlines

Phase I of the ESRF upgrade includes a number of canted beamlines (ID16, ID30 and ID23). In a canted scheme, the

radiation axes from two sets of insertion devices are angularly separated by means of small static steerers that deflect the



**References**

[1] Permanent Magnet Steerers for Canted Undulators at the ESRF, G. Le Bec and J. Chavanne, *NIM A: Accelerators, Spectrometers, Detectors and Associated Equipment*, Volume 664, Issue 1, February 2012, p. 214-222.

electron beam accordingly. A typical steerer layout consists of three magnets: one installed in the middle of the straight section and the two others, each with half the opposite magnetic strength of the middle one, installed at either end of the straight section. This configuration is generally achieved with conventional electromagnet structures. An interesting alternative based on permanent magnets has been designed by the ID group. The new design aims to minimise the space occupancy and to control the magnetic fringe field along the beam path in order to eliminate any impact on the spectrum quality of the neighbouring undulators [1].

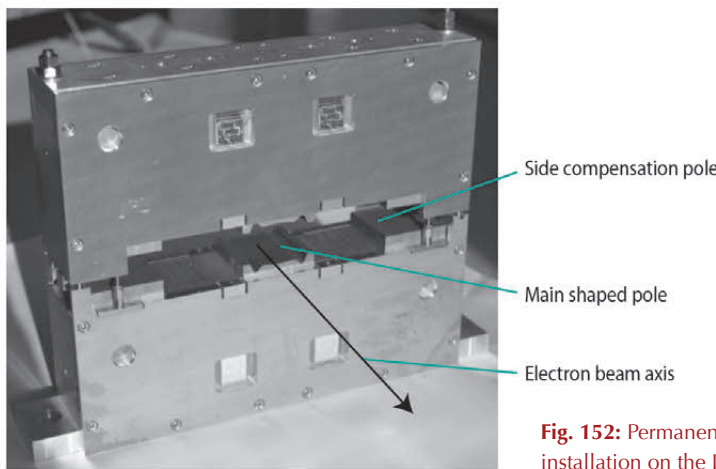


**Fig. 152:** Permanent magnet steerer before installation on the ID16 straight section.

**Figure 152** shows a permanent magnet steerer (PMS) before installation in ID16, at the end of a straight section. The shape of the central main pole is optimised for a flat-top transverse field and ensures negligible impact on the beam dynamics. The residual field outside the structure is controlled through the implementation of side openings (side compensation poles). The magnetic measurements carried out on different PMS are in excellent agreement with expectations. In particular, the distance between the last and first magnets of two undulators separated by the middle PMS could be reduced to 350 mm without impacting the phase error of either undulator. The first set of PMS was installed on ID16 in summer 2012 and provides a canting angle of 5.4 mrad between the two future branches of ID16 (NINA). No specific impact on the electron beam dynamics has been observed so far. Further interesting results are anticipated and will be communicated once ID16 comes into operation.

■ **Powering the ESRF booster cavities with four 150 kW RF solid state amplifiers**

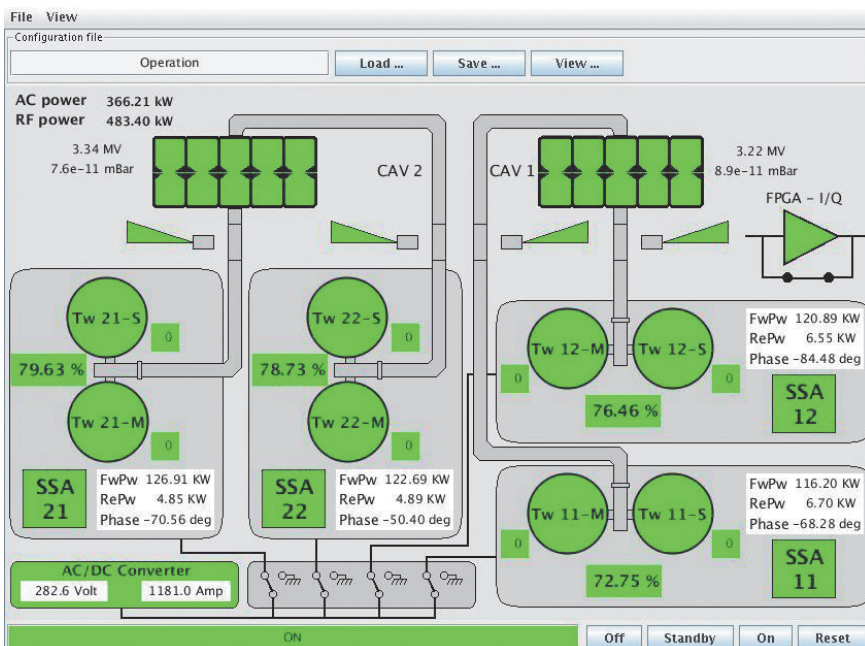


**Fig. 153:** Control synopsis of the new booster RF system with four SSAs powering the accelerating cavities.

The first four 352.2 MHz - 150 kW solid state amplifiers (SSA) were connected to the booster RF cavities during the long winter shutdown. They were brought into operation at the intermediary machine restart in March 2012. The system was debugged and calibrated in a few days. The new transmitter includes the SSAs delivered by ELTA/AREVA, two 400 kW - 280 V AC/DC power converters (one spare), implemented by the Power Supply Group and a new low level RF and control system built by the RF Group and the Accelerator Control Unit.

**Figure 153** shows the control synopsis of the booster RF system under typical operation conditions in pulsed mode at the 10 Hz repetition rate. A 3.2 F capacitor bank was installed on the 280 V DC

supply in order to smooth out the power drawn from the mains and limit the flicker at 10 Hz. Thanks to filtering, only 366 kW AC are drawn from the mains. Under similar operation conditions, this is about one third of the power demand of the former klystron transmitter for which such filtering was not possible.

After debugging and tuning, the new booster RF system has been operating very well since the machine restart in user mode in May 2012. So far, only one of about one thousand RF modules that compose the SSA has been in fault. Thanks to the built-in redundancy, this failure did not interrupt operation. Fine tuning is still ongoing with no impact on operation.

During the commissioning of the SSAs for the booster, some unforeseen effects were observed that are inherent to the combination of many RF amplifier modules operating at high power. Although these effects have no impact on the booster SSAs operated in pulsed regime, some modifications are necessary for the three SSAs still to be delivered by ELTA for operation in CW on the storage ring. The process of identifying and implementing these modifications has caused a substantial delay in the delivery of the next three SSAs. The revised schedule foresees their connection, in succession, to the three new HOM damped cavities on cell 23 in August 2013, January 2014 and March 2014, respectively.

## Low emittance project

In the past year, the Accelerator and Source Division has finalised its project for the Accelerator Phase II Upgrade. The project aims to greatly improve the brightness of the source by decreasing the horizontal equilibrium emittance of the storage ring from the present 4 nm to 150 pm. This will be possible by replacing the present 32 double-bend achromat (DBA) cells with a much more compact lattice based on hybrid 7-bend arc achromats (Figure 154). The smaller emittance, together with the development of shorter period smaller gap undulators and new beamline optics optimised to take full advantage of the new source, will allow a general improvement in performance by about a factor 100.

The scheme also provides the following advantages:

- the existing straight sections and beamlines can be maintained unchanged
- the present injection scheme and injection complex can be maintained unchanged
- the existing ARC hardware can be reused (e.g. power supplies, vacuum system components, diagnostics, etc.)
- operation costs can be reduced, especially wall plug power

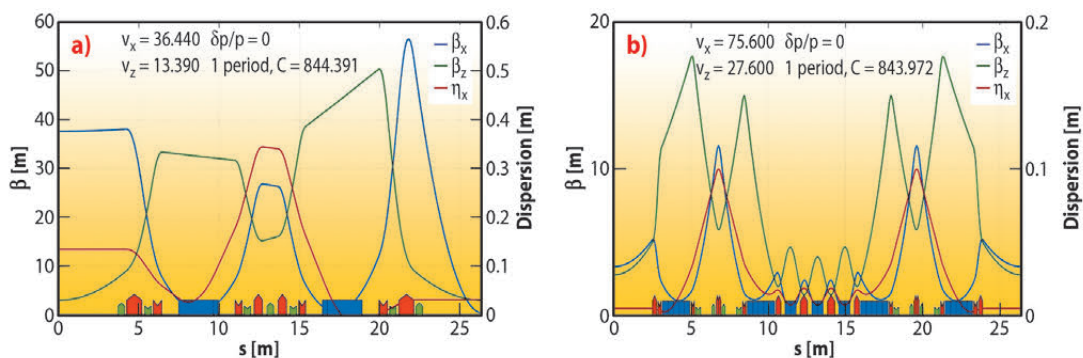


**Fig. 154:** The hybrid multi-bend (HMB) lattice. a) Existing cell (DBA) with a vertical emittance of 4 nm.rad. b) Proposed HMB cell with a vertical emittance of 150 pm.rad.

The technical aspects are challenging: very high gradient quadrupole magnets and tight tolerances are required. The vacuum system has to take full advantage of the new techniques developed in the last 10-20 years (e.g. NEG coating).

A white paper describing the general upgrade scheme and the science case has been submitted to the ESRF Council for approval of the technical design study phase, which is foreseen to be completed in two phases:

- Phase 1 at the end of 2014 to allow the beginning of the procurement phase
- Phase 2 at the end of 2016 to allow the beginning of the assembly phase

Installation is foreseen to start in the second half of 2018 and the user mode operations with the upgraded machine to be resumed in the second half of 2019.



# Facts and Figures

## Members and associate countries (as of February 2013)



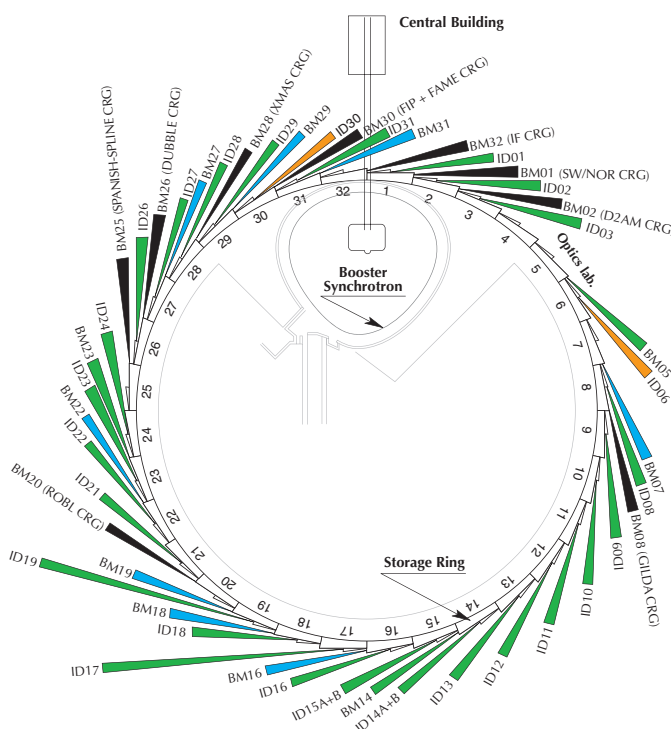
### Members' shares:

27.5%	France
25.5%	Germany
15%	Italy
14%	United Kingdom
4%	Spain
4%	Switzerland
6%	Benesync (Belgium, The Netherlands)
4%	Nordsync (Denmark, Finland, Norway, Sweden)

### Additional contributions

1%	Portugal
1%	Israel
1%	Austria
1%	Poland
1,05%	Centralsync (Czech Republic 0,55%, Hungary 0,25%, Slovakia 0,25%)

## The beamlines



Details of the public ESRF beamlines as well as those operated by Collaborating Research Groups (CRG) are given in **Tables 5 and 6**. **Figure 155** shows the location of the beamlines in the experimental hall.

- Public beamlines
- Instrumentation test and development beamlines
- CRG beamlines
- Free bending magnet ports

**Fig. 155:** Experimental hall showing location of the beamlines (public and CRG beamlines).



SOURCE POSITION	NUMBER OF INDEPENDENT END-STATIONS	BEAMLINE NAME	STATUS
ID01	1	Microdiffraction imaging	Operational since 07/97
ID02	1	High brilliance	Operational since 09/94
ID03	1	Surface diffraction	Operational since 09/94
ID08	1	Dragon	Operational since 02/00
ID09	1	White beam	Operational since 09/94
ID10	1	Soft interfaces and coherent scattering	Operational from 06/12
ID11	1	Materials science	Operational since 09/94
ID12	1	Circular polarisation	Operational since 01/95
ID13	1	Microfocus	Operational since 09/94
ID14A	1	Protein crystallography EH 1	Operational since 07/99
		Protein crystallography EH 2	Operational since 12/97
ID14B	1	Protein solution small-angle scattering EH 3	Operational since 12/98
		Protein crystallography EH 4	Operational since 07/99
ID15A	1	High energy diffraction	Operational since 09/94
ID15B	1	High energy inelastic scattering	Operational since 09/94
ID17	1	Medical	Operational since 05/97
ID18	1	Nuclear scattering	Operational since 01/96
ID19	1	Topography and tomography	Operational since 06/96
ID21	1	X-ray microscopy	Operational since 12/97
ID22	1	Microfluorescence	Operational since 12/97
ID23	2	Macromolecular crystallography MAD	Operational since 06/04
		Macromolecular crystallography microfocus	Operational since 09/05
ID24	1	Dispersive EXAFS	Operational since 02/96
ID26	1	X-ray absorption and emission	Operational since 11/97
ID27	1	High pressure	Operational since 02/05
ID28	1	Inelastic scattering II	Operational since 12/98
ID29	1	Multiwavelength anomalous diffraction	Operational since 01/00
ID31	1	Powder diffraction	Operational since 05/96
BM14	1	Macromolecular crystallography (MAD)	Operational since 01/10
BM23	1	X-ray absorption spectroscopy	Operational since 03/11
BM29	1	Bio SAXS	Operational since 06/12

**Table 5:** List of the ESRF public beamlines.

SOURCE POSITION	NUMBER OF INDEPENDENT END-STATIONS	BEAMLINE NAME	FIELD OF RESEARCH	STATUS
BM01	2	Swiss-Norwegian BL	X-ray absorption & diffraction	Operational since 01/95
BM02	1	D2AM (French)	Materials science	Operational since 09/94
BM08	1	Gilda (Italian)	X-ray absorption & diffraction	Operational since 09/94
BM20	1	ROBL (German)	Radiochemistry & ion beam physics	Operational since 09/98
BM25	2	SPLINE (Spanish)	X-ray absorption & diffraction	Operational since 04/05
BM26	2	DUBBLE (Dutch/Belgian)	Small-angle scattering	Operational since 12/98
			EXAFS	Operational since 06/01
BM28	1	XMAS (British)	Magnetic scattering	Operational since 04/98
BM30	2	FIP (French)	Protein crystallography	Operational since 02/99
		FAME (French)	EXAFS	Operational since 08/02
BM32	1	IF (French)	Interfaces	Operational since 09/94

**Table 6:** List of the Collaborating Research Group beamlines.



## ■ User operation

User operation of the facility for the year 2012 began after the first ever “long shutdown” since ESRF opened its beamlines to users in 1994. Following eighteen years of successful operation, the ESRF accelerator and beamlines were shut down on Monday 5<sup>th</sup> December 2011 for a 5-month period, during which time the construction works for the new EX2 experimental hall extension began. The accelerator and beamlines were restarted on schedule in early May 2012, and user operation resumed on 9<sup>th</sup> May 2012. The total beam time available for 2012 was reduced by 30% compared with a year of standard operation.

Major changes to the beamline portfolio have taken place through the Upgrade Programme: the EXAFS beamline ID24 was re-opened, beamlines ID10A/B/C were rebuilt as one beamline complex ID10, beamline ID16 was closed and the upgrade beamline is being rebuilt on ID20, and the Bio-SAXS beamline ID14-3 was moved to BM29. Beamline ID32 had to be closed to accommodate the upgrade beamline project UPBL7 following restrictions to the ESRF budget. In total, 28.25 ESRF publicly funded beamlines and 9 CRG beamlines were available for users in 2012. **Figure 156** shows the number of applications for beam time received since 2006. Since the beginning of the Upgrade Programme works in 2010, the number of applications received has evened off due to the unavailability of those beamlines undergoing upgrade and the closure of others. The small drop (6%) in the number of proposals received for 2012 was an expected consequence of the long shutdown. But this can also be attributed to the reduction in the number of beamlines available to users, down by more than 10% over the last 2 years (28.25 ESRF beamlines and 9 CRG beamlines in 2012 compared with 32 public and 10 CRG beamlines in 2010).

**Table 7:** Number of shifts of beam time requested and allocated for user experiments, year 2012.

Scientific field	Total shifts requested	Total shifts allocated
Chemistry	2 969	1 076
Hard Condensed Matter: Electronic & Magnetic Properties	3 859	1 113
Hard Condensed Matter: Crystals & Ordered Structures	3 718	1 173
Hard Condensed Matter: Disordered Systems	1 048	405
Applied Materials & Engineering	3 644	1 010
Environmental & Cultural Heritage Matters	2 279	657
Macromolecular Crystallography	3 221	1 846
Medicine	1 271	501
Methods & Instrumentation	685	219
Soft Condensed Matter	2 953	1 023
Surfaces & Interfaces	2 620	909
<b>Totals</b>	<b>28 267</b>	<b>9 932</b>

Despite this, there has been very little decrease in the number of proposals received, while the number of proposals received per operating beamline continues to increase.

Proposals for experiments are selected and beam time allocations are made through peer review. As in previous years, beam time for 2012 was allocated based on recommendations made by review committees of specialists, for the most part from European countries and Israel, set up in the following scientific areas:

- chemistry
- hard condensed matter: electronic and magnetic properties
- hard condensed matter: crystals and ordered systems
- hard condensed matter: disordered systems and liquids
- applied materials and engineering
- environmental and cultural heritage matters
- macromolecular crystallography
- medicine
- methods and instrumentation
- soft condensed matter
- surfaces and interfaces

The review committees met twice during the year, around six weeks after the deadlines for submission of proposals (1 September 2011 and 1 March 2012). They reviewed 1905 applications for beam time, and selected 719 (37.7%), which were then scheduled for experiments.

A new structure was put into place during 2012 for the proposal review process with the aim of allowing all proposals received for a particular beamline to be assessed by the same review committee. This gives the committees a better overall view of all the projects proposed for a single beamline, and allows them greater flexibility to optimise the selection

of proposals awarded beam time on each beamline. Beamlines of similar techniques or activities were grouped together to form ten new review committees. This new structure was used for the first time during the September-October 2012 proposal round where beam time is allocated for the first half of 2013.

Requests for beam time in 2012, which is scheduled in shifts of 8 hours, totalled 28 267 shifts or 226 136 hours, of which 9 932 shifts or 79 456 hours (35.1%) were allocated. The distribution of



shifts requested and allocated, by scientific area, is shown in **Table 7**.

The breakdown of shifts scheduled for experiments by scientific area in the first half of 2012 is shown in **Figure 157**. This same period (less than 3 months of beam time) saw 2091 visits by scientists to the ESRF under the user programme, to carry out 491 experiments. Overall, the number of users in each experimental team averaged just over 4 persons as in all previous years, and the average duration of an experimental session was 9 shifts as in 2011. This can be further broken down to show an average duration of 3 shifts for MX experiments and just over 14 shifts for non-MX experiments. The annual number of experimental sessions and user visits since 2006 is shown in **Figure 156**. The particularly high figures in the full year 2009 are mainly due to the fact that an extra week of beam time was made available to users during that year to compensate partly for the anticipated reduction in beam time available in later years following the start of the reconstruction work of the Upgrade Programme. The effect of the reduction in beam time available in 2011 due to the long shutdown is clearly visible in the lower-than-normal numbers of experimental sessions carried out and user visits, and we expect similar numbers for 2012 once the 2012/II scheduling period finishes at the end of February 2013.

One of the principle measurable output parameters of the ESRF is the number and quality of publications accepted in peer-reviewed journals. **Figure 158** shows how this number has been rising continuously over the past years, with a publication output systematically on a level of over one publication per experimental session and reaching a record number of nearly 1900 for the year 2011. The year 2012 promises to be equally fruitful, with 1777 publications already registered in the ILL/ESRF Library database. Since ESRF began user operation back in 1994, a total of 21,294 publications have been accepted in peer-reviewed journals. Of these, more than 200 every year are published in high impact factor journals.

User responses to questionnaires show once again that the ESRF continues to maintain its excellent reputation concerning the assistance and service given by scientists and support staff on beamlines, and travel and administrative arrangements, in addition to the quality both of the beam and of the experimental stations. Facilities on site, such as preparation

laboratories, the Guesthouse and a canteen open 7 days a week, also make an important contribution to the quality of user support.

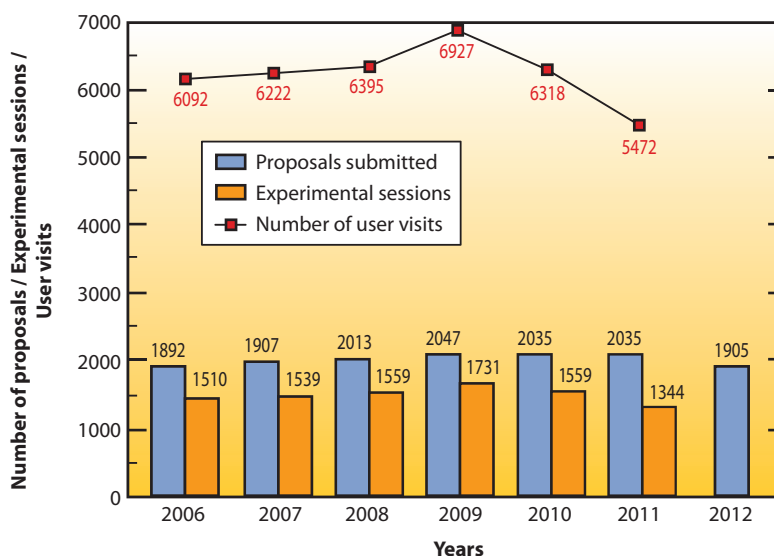


**Fig. 156:** Numbers of applications for beam time, experimental sessions and user visits, 2006 to 2012. N.B. Final numbers of experimental sessions and user visits for 2012 were not available at the time of going to press.

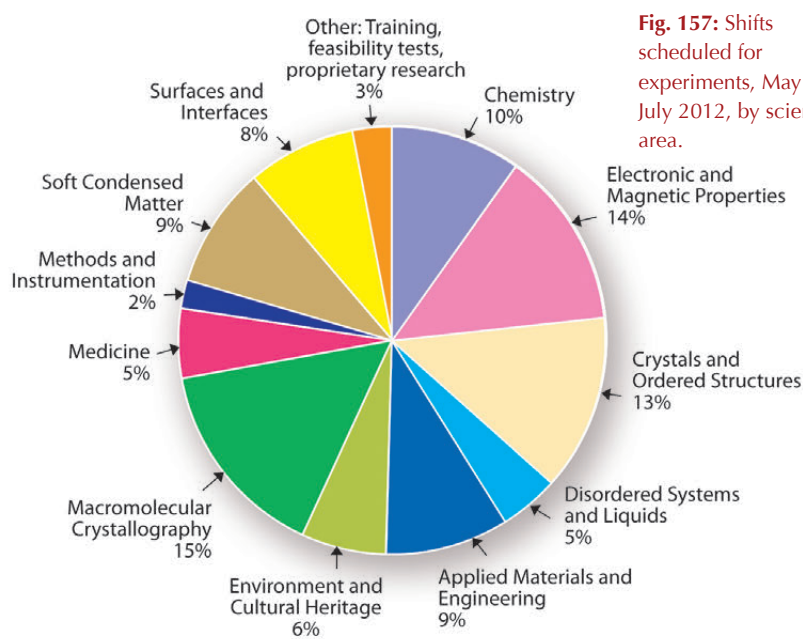


**Fig. 157:** Shifts scheduled for experiments, May to July 2012, by scientific area.

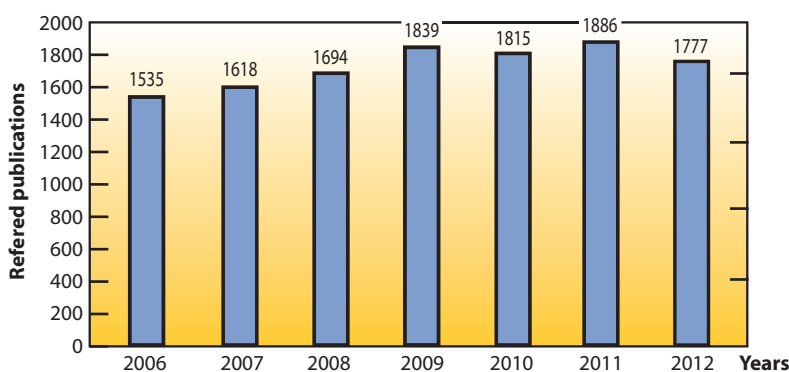


**Fig. 158:** Numbers of publications appearing in refereed journals reporting on data collected either partially or totally at ESRF, 2006 to 2012.



## Administration and finance

### Expenditure and income 2011

Expenditure	kEuro	Income	kEuro
Accelerator and Source		2011 Members' contributions	81 613
Personnel	5 626.9	Funds carried forward from 2010	8 756
Recurrent	1 294.7	Other income	
Operating costs	1 228.3	Scientific Associates	4 960
Other recurrent costs	66.4	Sale of beamtime	1 600
Capital	6 116.5	Compensatory funds	0
Accelerator and Source developments	6 116.5	Scientific collaboration and Special projects	3 060
Beamlines, experiments and in-house research		Income carried forward to 2012	539
Personnel	18 461.2		
Recurrent	5 301.7		
Operating costs	2 649.1		
Other Recurrent costs	2 652.6		
Capital	8 063.5		
Beamline developments	7 156.8		
Beamline refurbishment	906.7		
Technical and administrative supports			
Personnel	25 970.9		
Recurrent	11 641.1		
Capital	14 061.0		
Industrial and commercial activity			
Personnel	403.3		
Recurrent	50.0		
Unexpended committed funds			
Funds carried forward to 2012	3 537.0		
<b>Total</b>	<b>100 528</b>	<b>Total</b>	<b>100 528</b>

### Revised expenditure and income budget for 2012

Expenditure	kEuro	Income	kEuro
Accelerator and Source		2012 Members' contributions	83 666
Personnel	5 657	Funds carried forward from 2011	3 537
Recurrent	1 395	Income carried forward from 2011	539
Operating costs	1 325	Other income	
Other recurrent costs	70	Scientific Associates	5 111
Capital	4 964	Sale of beamtime	900
Accelerator and Source developments	4 964	Compensatory funds	2 650
Beamlines, experiments and in-house research		Scientific collaboration and Special projects	3 605
Personnel	18 000	Pre-financing	6 225
Recurrent	4 751		
Operating costs	1 236		
Other Recurrent costs	3 515		
Capital	14 996		
Beamline developments	14 302		
Beamline refurbishment	694		
Technical and administrative supports			
Personnel	26 746		
Recurrent	10 499		
Capital	18 830		
Industrial and commercial activity			
Personnel	300		
Recurrent	95		
<b>Total</b>	<b>106 233</b>	<b>Total</b>	<b>106 233</b>

The budget for 2012 includes additional contributions from Members and Scientific Associates of 15 531 kEuro dedicated to the Upgrade Programme. The Upgrade expenditure budget amounts to a total of 36 930 kEuro including 15 165 kEuro of ESRF operating budget.

#### Expenditure 2011 by nature of expenditure

	kEuro
<b>PERSONNEL</b>	
ESRF staff	48 500.0
External temporary staff	123.5
Other personnel costs	1 838.9
<b>RECURRENT</b>	
Consumables	7 308.7
Services	8 839.7
Other recurrent costs	2 139.0
<b>CAPITAL</b>	
Buildings, infrastructure	10 571.0
Lab. and Workshops	1 547.3
Accelerator and Source incl. ID's and FEs	6 116.5
Beamlines, Experiments	8 063.5
Computing Infrastructure	1 935.8
Other Capital costs	6.8
Unexpended committed funds	
Funds carried forward to 2011	3 537
<b>Total</b>	<b>100 528</b>

#### Revised budget for 2012 by nature of expenditure

	kEuro
<b>PERSONNEL</b>	
ESRF staff	48 739
External temporary staff	60
Other personnel costs	1 904
<b>RECURRENT</b>	
Consumables	6 050
Services	8 625
Other recurrent costs	2 065
<b>CAPITAL</b>	
Buildings, infrastructure	15 151
Lab. and Workshops	2 303
Accelerator and Source incl. ID's and FEs	4 964
Beamlines, Experiments	14 996
Computing Infrastructure	1 326
Other Capital costs	50
<b>Total</b>	<b>106 233</b>



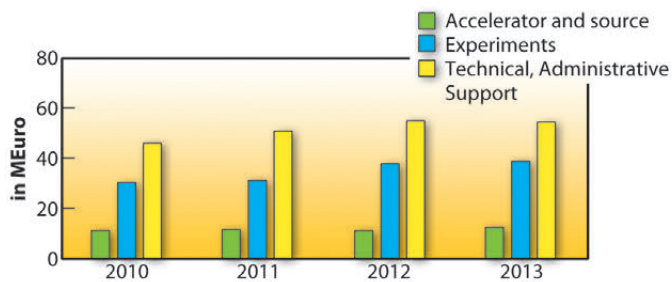
**2012 manpower (posts filled on 31/12/2012)**

	Scientists, Engineers, Senior Administrators	Technicians and Administrative Staff	PhD Students	Total
<b>Staff on regular positions</b>				
Accelerator and Source	27	38	3	68
Beamlines, instruments and experiments*	220	85.8	23.5	329.3
General technical services	30.6	50		80.6
Directorate, administration and central services	39.6	49.8		89.4
<i>Sub-total</i>	<i>317.2</i>	<i>223.6</i>	<i>26.5</i>	<i>567.3</i>
<b>Other positions</b>				
Short term contracts	12.7	11		23.7
Staff under "contrats de professionnalisation" (apprentices)		23		23
European Union grants	1		1	2
Temporary workers		3		3
<b>Total</b>	<b>330.9</b>	<b>260.6</b>	<b>27.5</b>	<b>619</b>
<i>Scientific collaborators and consultants</i>	<i>10</i>			<i>10</i>
<i>External funded research fellows</i>	<i>11</i>		<i>15</i>	<i>26</i>

\* Including scientific staff on time limited contract.

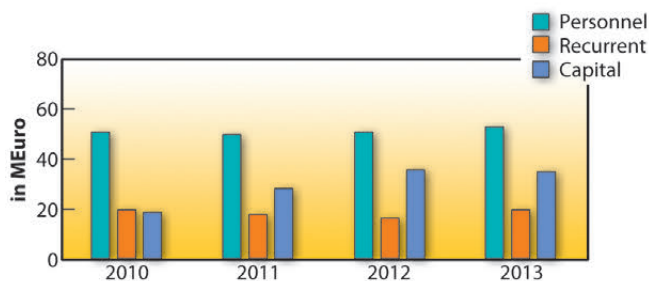
**Financial resources in 2010, 2011, 2012 and 2013, by major programme**

(current prices in MEuro for the respective years)



**Financial resources in 2010, 2011, 2012 and 2013, by nature of expenditure**

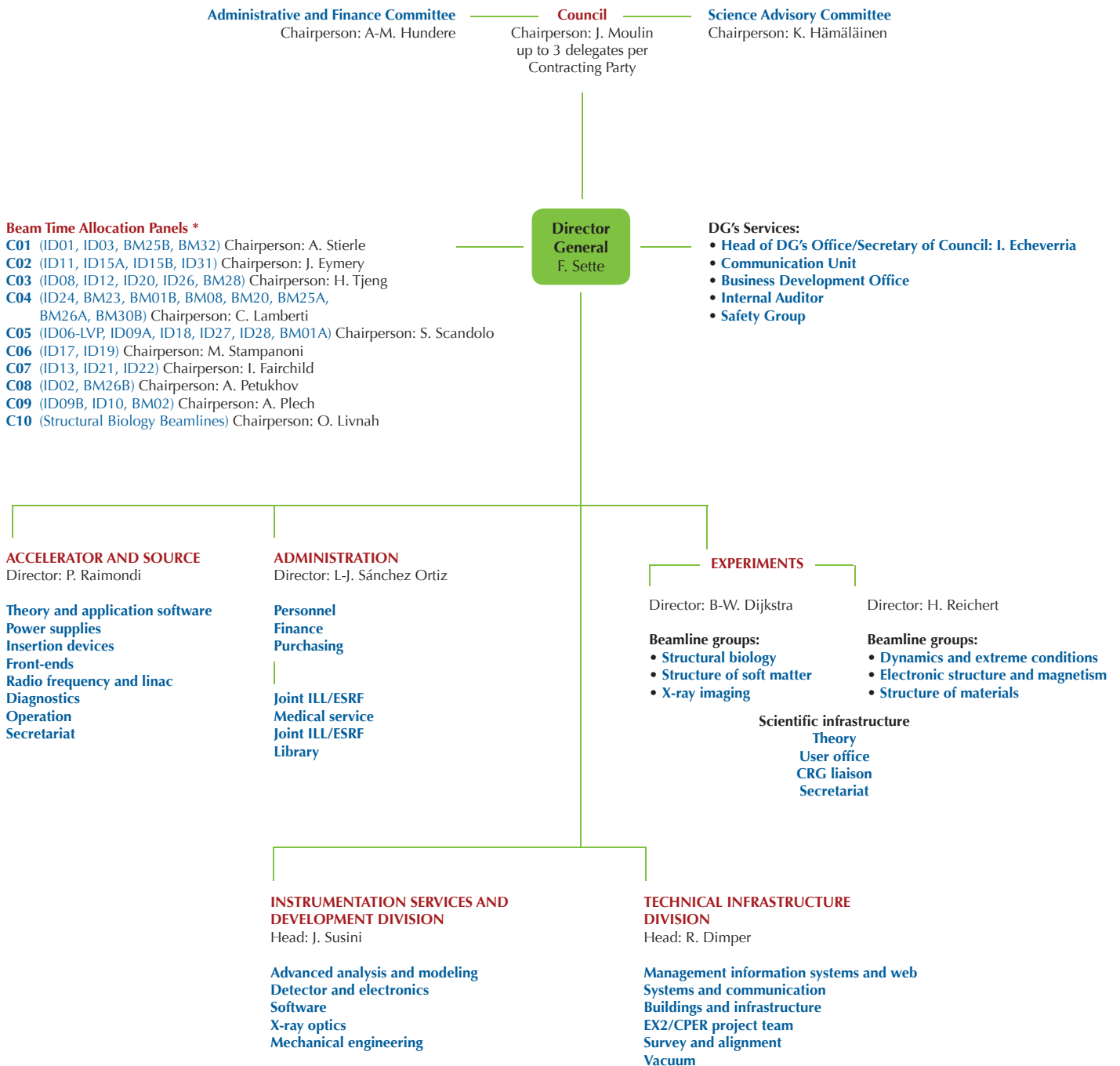
(current prices in MEuro for the respective years)





# Organisation chart of the ESRF

(as of January 2013)



\*The BTAPs were restructured during 2012 so that they are now based on beamlines rather than on scientific themes. Each BTAP reviews all proposals submitted for a subset of beamlines, as given above.



**We gratefully acknowledge the help of:**

C. Argoud, B. Boulanger, N.B. Brookes, K. Clugnet, K. Colvin, M. Cotte, E. Dancer, B. Dijkstra, R. Dimper, I. Echeverría, R. Felici, A. Fitch, K. Fletcher, S. Gerlier, C. Habfast, E.S. Jean-Baptiste, A. Kaprolat, M. Krisch, T. Lafford, G. Leonard, J. McCarthy, S. McSweeney, T. Narayanan, P. Raimondi, M. Regis, H. Reichert, S. Rio, F. Sette, J. Susini, G. Vaughan, K. Wong and all the users and staff who have contributed to this edition of the Highlights.



Editor

G. Admans

Layout

Pixel Project

Printing

Imprimerie du Pont de Claix

© ESRF • February 2013

Communication Group

ESRF

BP220 • 38043 Grenoble • France

Tel. +33 (0)4 76 88 20 56 • Fax. +33 (0)4 76 88 25 42

<http://www.esrf.eu>